MONASH University

Doctoral Thesis

Nucleosynthesis Models of the Intermediate Neutron-Capture Process

Melanie Hampel

A dissertation submitted for the degree of

Doctor of Philosophy

at the School of Physics and Astronomy,
Monash University, Australia

October 2021

Supervisor:	A. Prof. Amanda I. Karakas
Co-supervisors:	Dr. Simon W. Campbell
	Prof. John C. Lattanzio

Nucleosynthesis Models of the Intermediate Neutron-Capture Process

Thesis, School of Physics and Astronomy, Monash University, Australia.

Abstract

The majority of elements heavier than iron are produced by the *slow* (s) and *rapid* (r) neutron-capture processes. However, it has become clear that a separate neutron-capture process operating at conditions *intermediate* (i) to the s and r process produces a distinct heavy-element abundance pattern, which does not just resemble a mixture of s- and r-processed material.

Compelling observational evidence for i-process nucleosynthesis comes from carbon-enhanced metal-poor stars with enhancements of barium *and* europium which are representative elements of s- and r-process nucleosynthesis, respectively. These abundances cannot be succesfully explained as originating from separate s- and r-process nucelsosynthesis events and instead i-process nucleosynthesis models reproduce the abundance patterns much better (we will refer to these stars as CEMP-i stars).

Proton-ingestion episodes in various stellar evolution scenarios can lead to i-process nucleosynthesis, yet the stellar host site(s?) of i-process nucleosynthesis remains debated. To better understand the i process and to put constraints on where and how it operates, we presents nuclear-reaction network studies of i-process nucleosynthesis in this thesis.

At first we use observations of lead abundances in CEMP-i stars to constrain the time scales and neutron exposures of i-process nucleosynthesis. We find that neutron exposures of $\tau \gtrsim 2\,\mathrm{mbarn}^{-1}$ are required to reproduce the observed abundances of CEMP-i stars, which correspond to short time scales of weeks or even just days at i-process neutron densities. We also find that i-process abundance patterns can explain puzzlingly low abundances of Pb, which are observed in Magellanic post-AGB stars and could not be explained previously by s-process predictions.

We investigate the neutron production for i-process nucleosynthesis in detail and show how varying amounts of ingested protons and initial ^{12}C abundances in proton-ingestion episodes affect the production and recycling of neutrons, as well as the effects of nuclear reaction-rate uncertainties and variations of convective velocities. For the undelying thermodynamic properties we investigate three different potential i-process sites: an early thermal pulse of a low-mass, low-metallicity AGB star, a very late thermal pulse in a post-AGB star, and the core He flash in a low-mass ultra metal-poor star. We find that our models predict different abundance ratios, particularly for elements between the typical s-process peaks. Only very few CEMP-i stars have observed abundances for these elements. More complete abundance patterns of elements in this region have the potential to place meaningful limits on i-process models.

We also review a few characteristic i-process abundance signatures that can guide future observational studies to identify and distinguish s- and i-process heavy-element patterns. A strong prediction of the i process is an enhanced production of ^{135}I which decays into ^{135}Ba. This produces very high odd-isotope fractions of barium. Additionally, this feature is responsible for succesfully reproducing high abundance ratios between heavy and light s-process peak elements such as Ba/Sr, as well as high Ba/La ratios and generally higher Eu/Ba and Eu/La ratios compared to s-process models.

Declaration

I hereby declare that this thesis contains no material which has been accepted for the award of any other degree or diploma at any university or equivalent institution and that, to the best of my knowledge and belief, this thesis contains no material previously published or written by another person, except where due reference is made in the text of the thesis.

This thesis includes one original paper published in peer reviewed journals and one unpublished publications. The core theme of the thesis is i-process nucleosynthesis. The ideas, development and writing up of all the papers in the thesis were the principal responsibility of myself, the student, working within the School of Physics and Astronomy under the supervision of A. Prof. Amanda I. Karakas.

The inclusion of co-authors reflects the fact that the work came from active collaboration between researchers and acknowledges input into team-based research.

I have / have not renumbered sections of submitted or published papers in order to generate a consistent presentation within the thesis

In the case of Chapter §2 and Chapters §3 my contribution to the work involved the following:

- **Chapter 2**

  Publication title:
  Learning about the intermediate neutron-capture process from lead abundances

  Status: published

  Contribution (60 %): Model grid calculations, data analysis and visualisation, contribution to concept and project idea, manuscript authorship

  Co-authors (none are Monash students):

  - A. Prof. Amanda I. Karakas (10 %): contribution to concept and project idea, manuscript corrections and review
  - Dr. Richard J. Stancliffe (10 %): contribution to concept and project idea, manuscript corrections and review
  - Prof. Bradley S. Meyer (10 %): help with the code, manuscript review
  - Dr. Maria Lugaro (10 %): contribution to concept and project idea, manuscript corrections and review

- **Chapter 3**

  Publication title:
  Low proton fractions required for i-process nucleosynthesis in ingestion episodes

  Status: not submitted

  Contribution (60 %): Model grid calculations, data analysis and visualisation, contribution to concept and project idea, manuscript authorship

  Co-authors (none are Monash students):

  - A. Prof. Amanda I. Karakas (10 %): contribution to concept and project idea, manuscript corrections and review
  - Dr. Simon W. Campbell (10 %) contribution to concept and project idea, manuscript corrections and review
  - Dr. Richard J. Stancliffe (10 %): stellar model contribution, contribution to concept and project idea, manuscript corrections and review
  - Prof. Bradley S. Meyer (5 %): help with the code, manuscript review
  - Dr. Maria Lugaro (5 %): contribution to concept and project idea, manuscript corrections and review

Signature: _____

Print Name: Melanie Hampel

Date: _____

The undersigned hereby certify that the above declaration correctly reflects the nature and extent of the student's and co-authors' contributions to this work. In instances where I am not the responsible author I have consulted with the responsible author to agree on the respective contributions of the authors.

Signature: _____

Print Name: A. Prof. Amanda Karakas

Date: _____

> *The roots of the sciences come from the broad, abundant feeling of love.*
>
> — Toshiko Yuasa

Acknowledgements

Four years ago I moved to Melbourne to start my PhD at Monash and it is fair to say that I would not be at this point now without my awesome "Doktormutter"[1] Amanda Karakas. It was literally not even my idea to embark on this journey in the first place. Amanda, I am unbelievably thankful that you were convinced enough of my potential to approach me with the offer to come to Melbourne and that you did not lose the confidence in my abilities throughout the past years, particularly in the times when I did not have that confidence myself. The last four years threw incredible challenges at me and I would not have managed to see the other end of this PhD journey without your guidance and constant support as supervisor, mentor, and friend (or without all the coffees and occasional glasses of wine or Margarita).

I would also like to thank the amazing team of collaborators who have accompanied me through years of i-process nucleosynthesis studies. Firstly, thanks to my co-supervisor Simon Campbell for all the interesting discussions over coffee, the insights into proton-ingestion episodes, hydrodynamics, and the metal-free Universe. Additional thanks for your efforts regarding regular coffee breaks and SINS meetings and for being available with help and support whenever needed. Also a big thanks to John Lattanzio for your support and educating me not just on stellar but also many Earthly things, including AFL and fine wine. Richard, my i-process journey started many years ago as Master student in your group in Bonn. Thank you for the fun group meetings, the engaging and social atmosphere you brought to the institute, and all the many hours of i-process and CEMP discussions (and rants) — then and now. Thank you for all your support and friendship over the years. Maria, thank you for always welcoming me in Budapest and being such a generous host. Visiting you and working with you has always been a pleasure, not least because you always showed enthusiasm and encouragement for my ideas and are just overall an amazing role model. Brad, thank you so much for providing not only your code for my studies, but for always being helpful with troubleshooting and implementing new ideas. Carolyn, although we never really worked together you have always been helping me out with discussions, advice, a glass of wine, a chat through the whole night, as host in Budapest and even in Italy. Thank you for your contagious enthusiasm about stars and your friendship over the years. Carlo, thank you for all the good times in Canberra and Bonn. After leaving Bonn we didn't really keep in touch much, but you were still always there to help me out with questions and data about CEMP stars and even a thesis template.

[1] German for PhD supervisor. Literally translates to *doctoral mother* and, in my opinion, this term conveys Amanda's influence on my PhD journey much better than just calling her my supervisor.

Sarah, thank you for always being there, even though we are worlds apart. You are simply the best and I cannot put into words how much your friendship means to me!

A big thank you to all the (former) MoCA and SoPA students who I can gladly count as close friends today. You are what made Australia not just the place I've moved to, but a home. Especially to the "former generation", Hayley, Kate, Chloe, Conrad, Adelle, Dave, and Zac, who welcomed me when I first got here, made me feel right at home and taught me all about Aussie life. To Reinhold, Moritz, Avi, Isobel, Alejandro and Floor for your friendship, the coffee breaks and the laughs. A special thank you to Giulia and Vishnu who supported me through lockdown and made a special impact on my finishing this journey.

I gratefully acknowledge the financial support from the Monash Graduate Scholarship, the Monash International Postgraduate Research Scholarship, and the J. L. William Scholarship, as well as from the ARC Centre of Excellence for All Sky Astrophysics in 3 Dimensions (Astro 3D).

The biggest thanks goes to my family and most of all to my mom.
Danke für die unendliche Liebe und die Unterstützung meine Träume zu verwirklichen, selbst wenn das bedeutet, dass uns unzählige Kilometer und Zeitzonen trennen. Ohne dich, Mama, und ohne euch alle hätte ich diesen Weg nie gehen können.
Und zum Schluss: Julia, diese Arbeit ist für dich. Astrophysik war immer dein Traum, bestimmt schon bevor ich überhaupt wusste, was das Wort bedeutet. Du hast mich immer inspiriert und unglaublich stolz gemacht. Deine Leidenschaft war bewundernswert! Ich vermisse dich unendlich, doch die Sterne werden uns ewig verbinden.

Für Julia

Contents

> *Your reward will be the widening of the horizon as you climb. And if you achieve that reward, you will ask no other.*
>
> — Cecilia Payne-Gaposchkin

Chapter 1

Introduction

To date we know of 118 elements in the periodic table with ongoing searches for heavier and heavier elements in nuclear physics accelerator facilities around the world. In astronomer's jargon we refer to all of these elements as *metals*, with the exception of the two lightest species hydrogen (H) and helium (He). Only those two elements along with small amounts of lithium (Li) were produced in the Big Bang. The vast majority of elements heavier than He are created in the interior of stars and released into the Universe at the end of the star's life where they enrich the material from which new stars form. This creates an ongoing cosmic matter-recycling system and through many generations of stellar lifetimes the Universe has slowly been enriched in metals: each new generation of stars forms from the material that has been more enhanced in metals than the past generation. Some 4.6 billion years ago, by the time our Solar System was born, the metal content in the gas from which our Sun formed was already 1.4 % (by mass, Asplund et al., 2009).

It has not even been a century since Cecilia Payne proposed in her doctoral thesis that stars are primarily made up of H and He (Payne, 1925). A few decades later the famous B^2FH review paper on *Synthesis of the Elements in Stars* (Burbidge et al., 1957) described the "at least eight different types of synthesizing processes" that are required to reproduce the solar abundances. Along with separate work by Cameron (1957b,a), B^2FH paved the way for the research field of nucleosynthesis. More than 60 years later the origin of the elements is still not fully understood and is regularly considered one of the big scientific questions of our time. Consequently, among the six fundamental science questions guiding this decade's research direction for Australian Astronomy, one defining question is *"How are elements produced by stars and recycled through galaxies?"* (Australian Academy of Science, 2015).

As our understanding of the origin of the elements grows, astronomers have been able to create their own versions of the periodic table to visualise the origin and cosmic history of each element. Two different versions of the periodic table are shown in Figure 1.1. The first example in Figure 1.1a assigns one or multiple cosmic origins to each element and re-emphasises that the majority of these origins are stellar sources. In the second example in Figure 1.1b we can even see a time evolution of the contribution of different sources throughout the history of the Universe, based on models of Galactic Chemical Evolution (Kobayashi et al., 2020).

Our understanding of the origin of the elements comes from improvements in theoretical models of stellar evolution, nucleosynthetic processes, nuclear physics inputs, and computational capabilities combined with a growing number of observational constraints from abundance analyses of stellar atmospheric spectra and a wealth of information from dedicated surveys. However, with all these improvements over the last decades also come a variety of new challenges and puzzling new findings, which show that the current picture is not yet complete.

In this thesis we will address some of those puzzling findings posed by observations of elements heavier than iron (Fe) in old, metal-poor objects. Since the early Universe was less enriched in metals, the surviving old metal-poor stars still contain the imprints of the nucleosynthesis from the early Universe. Essentially, all of these are ingredients to understanding the formation history of our Milky Way Galaxy and our place in the cosmos. Building a reliable narrative about the assembly of our Galaxy is the main aim of the research field of Galactic archaeology (Freeman & Bland-Hawthorn, 2002). In analogy to archaeology on Earth, the old metal-poor stars are the fossils we set out to find and to analyse the story they tell us.

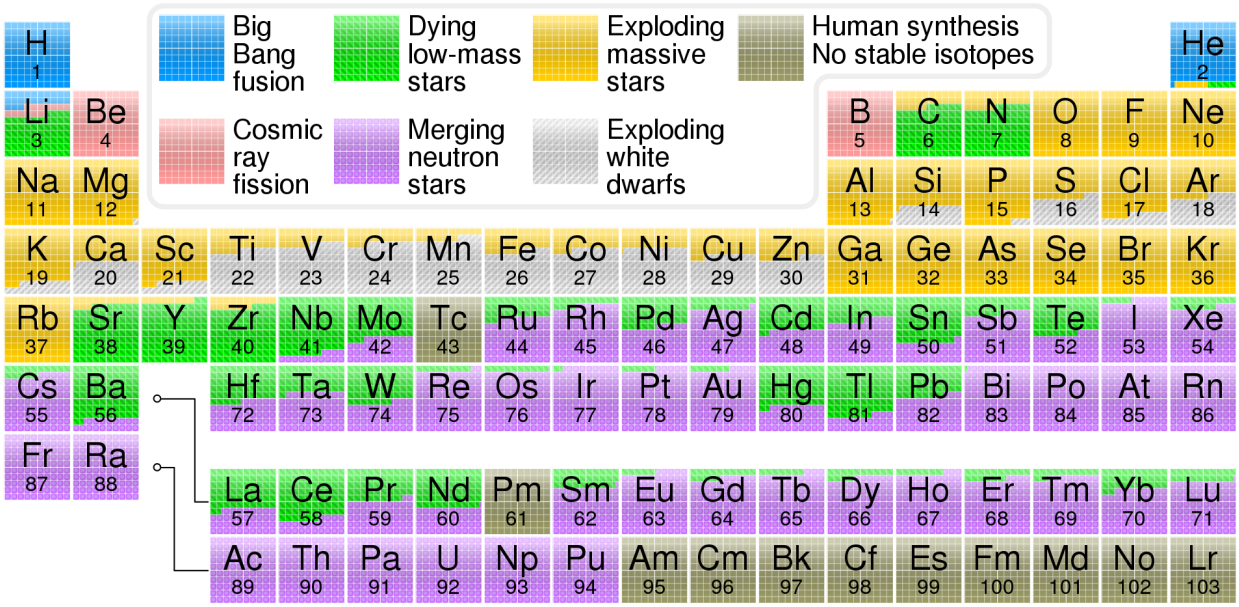

(a) The cosmic origins of the elements in the periodic table. This table shows the relative contributions of various origins to the abundances of the elements in the Solar System based on data by Jennifer Johnson. Image Credit: CMG Lee, CC BY-SA 3.0.

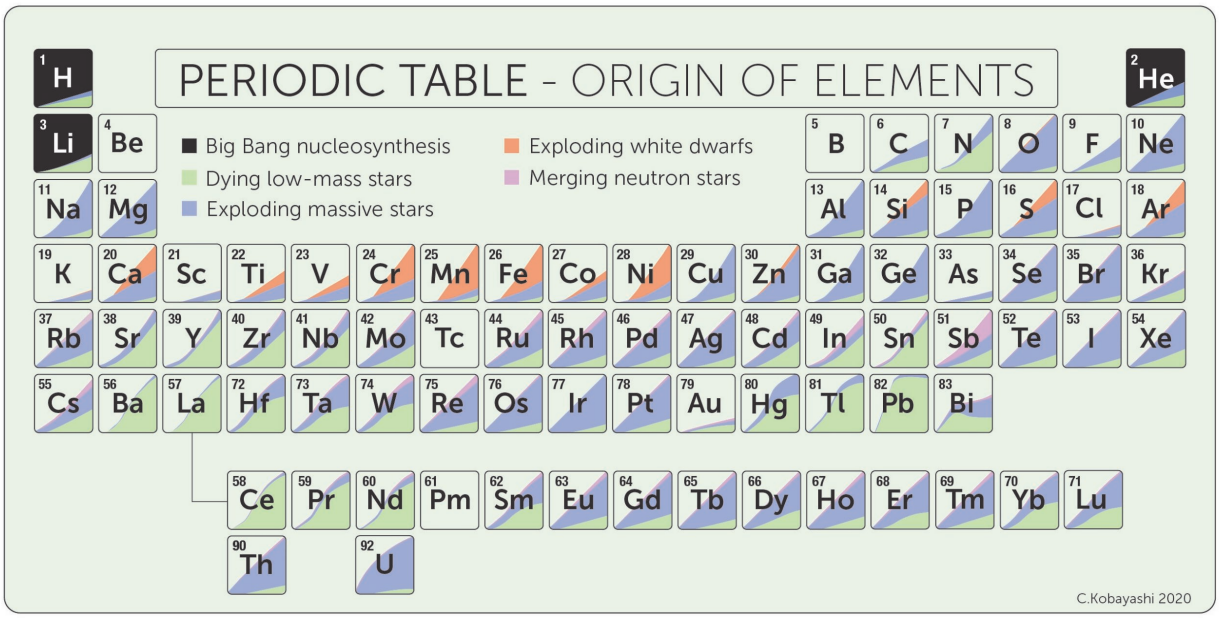

(b) Periodic table of the elements with time evolution of the contributions of various sources to the total abundance of each elements. This Figure was kindly provided by Chiaki Kobayashi (Kobayashi et al., 2020).

Figure 1.1: **Periodic tables visualising the origin of the elements.**

However, in order to gain information from the elements we observe in metal-poor stars, we have to understand how to link observed abundance patterns to the stellar sources responsible for their production. This brings us back around to the question about the origin of the elements. Ultimately, there is an intimate link between the quest to understand where the building blocks come from that are part of everything we know on Earth, including life itself, with studying the history of our Galaxy, the stars within the Galaxy, as well as the Universe as a whole.

1.1 Heavy-element production by s- and r-process nucleosynthesis

Stars are fuelled by nuclear fusion reactions, which create the energy to keep a star from collapsing under its own gravity. However, the process of fusing two (or more) light particles to a heavier one only provides energy for fusion reactions of elements up to iron (Fe). We will use the term *heavy elements* to refer to elements heavier than Fe with atomic numbers above $Z > 26$, whose formation does not occur by thermonuclear fusion reactions anymore. Instead, there are two processes responsible for the production of the majority of heavy elements: the slow (s) and rapid (r) neutron-capture process. *Slow* and *rapid* characterise the time scale of neutron-capture reactions relative to the β-decay time scale of the unstable neutron-rich isotopes created by neutron-capture reactions. This can be quantified in terms of neutron density regimes where $n \approx 10^7\,\mathrm{cm}^{-3}$ to $10^{10}\,\mathrm{cm}^{-3}$ leads to typical s-process conditions. In contrast, the r-process requires much higher neutron densities of $n \gtrsim 10^{20}\,\mathrm{cm}^{-3}$.

In a classical picture it is these two separate and independent processes which are required to explain the origin of the heavy neutron-capture elements[1] and each contributed approximately equal parts to the heavy-element content of our Sun (e.g., Burbidge et al., 1957; Cameron, 1957b,b; Sneden et al., 2008; Arnould & Goriely, 2020). The main site for s-process nucleosynthesis are stars on the asymptotic giant branch (AGB), a phase at the end of the life of low-mass stars similar to our Sun or even a few times more massive (up to approximately $8\,\mathrm{M}_\odot$). For an extensive review we refer the reader to a variety of review papers, such as Busso et al. (1999); Herwig (2005); Karakas & Lattanzio (2014). The s process, particularly the weak s-process which contributes to the production of elements up to a mass number of $A \approx 90$, can also occur in massive stars (Frischknecht et al., 2016; Prantzos et al., 2018, and references therein).

The main site (or sites?) for the r process is less clear and this topic remains debated in the literature. The r process requires very high neutron densities associated with extreme conditions and we refer the reader to the recent review by Cowan et al. (2021) and the refereces therein for a more detailed reflection on potential r-process sites. Two of the most likely candidates for r-process nucleosynthesis are magneto-hydrodynamically driven supernovae and the mergers of neutron stars. Neutron star merger events in particular gained a lot of attention in the past years as proposed r-process sites. In 2017 the detection of the gravitational wave event GW170817 by the LIGO/Virgo Collaboration was the first detected neutron star merger (Abbott et al., 2017). GW170817 not only confirmed the existence of such events in the first place but the associated kilonova AT2017gfo

[1] We know that there are proton-rich isotopes, which cannot be produced by neutron-capture reactions, neither slow nor rapid. Their origin is attributed to a separate p process (Wallerstein et al., 1997). For the remaining isotopes produced by neutron-capture reactions the s and r process are considered the primary contributors.

even allowed for direct proof of heavy-element nucleosynthesis through the identification of the neutron-capture element strontium (Watson et al., 2019). However, neutron-star mergers alone appear unable to provide a complete narrative of the origin of r-process elements (Sneden et al., 2008) and account for all observed evidence as, for example, found by Galactic Chemical Evolution studies (Côté et al., 2019; Kobayashi et al., 2020).

1.2 Why do we need the i process?

The s and r process are the extremes on a continuum of neutron-capture processes and have naturally provided a starting point for theoretical studies as they are easier to investigate with analytical studies (Clayton, 1968). However, since the neutron-density regimes of the s and r process are separated by many orders of magnitude, it is no surprise that neutron densities *intermediate* to the s- and r-process neutron densities eventually gained attention. At a first glance it may appear just as a curious, yet purely academic exercise to explore this intermediate (i) neutron-capture process. However, over the past decade the i process sparked a lot of interest in the nuclear-astrophysics community. The combination of technical advancements and improvements in both theoretical and observational studies provided the foundation and evidence on which the i process could be established as an actual nucleosynthetic process occuring in nature.

The idea of the i process goes back several decades to studies by Cowan & Rose (1977) where neutron densities of $n \approx 10^{15}\,\mathrm{cm}^{-3}$ to $10^{17}\,\mathrm{cm}^{-3}$ were encountered in their stellar models as "effects of mixing various amounts of hydrogen-rich material into the intershell convective region of red giants undergoing helium shell flashes". We will refer to these events as *proton-ingestion episodes* and today it is not only giant stars anymore, which are considered to provide the conditions for i-process nucleosynthesis. Several other stellar evolution scenarios have been identified as possible hosts for proton-ingestion episodes and potential i-process nucleosynthesis. These proposed host sites for proton-ingestion episodes include:

- low-mass, low-metallicity AGB stars at the beginning of their thermally-pulsing phase (Fujimoto et al., 2000; Iwamoto et al., 2004; Campbell & Lattanzio, 2008; Cristallo et al., 2009; Suda & Fujimoto, 2010; Stancliffe et al., 2011; Cristallo et al., 2016; Choplin et al., 2021),
- the core helium flash of metal-poor or metal-free low-mass stars (Fujimoto et al., 1990; Hollowell et al., 1990; Fujimoto et al., 2000; Schlattl et al., 2001; Campbell & Lattanzio, 2008; Suda & Fujimoto, 2010; Campbell et al., 2010; Cruz et al., 2013),
- very late thermal pulses of post-AGB stars (Iben et al., 1983; Miller Bertolami et al., 2006; Herwig et al., 2011),
- dredge-out events in super-AGB stars (Doherty et al., 2015; Jones et al., 2016),
- rapidly accreting white dwarfs (Denissenkov et al., 2017, 2019), and
- low-metallicity massive stars (Banerjee et al., 2018; Clarkson et al., 2018; Clarkson & Herwig, 2021).

When protons are mixed into He convective regions where ^{12}C is abundant as a product of He-burning, then high neutron densities in the i-process regime can be produced in a two-step

process (Cowan & Rose, 1977; Malaney, 1986; Jorissen & Arnould, 1989): (*i*) in a first step ^{12}C captures the protons to produce unstable ^{13}N, which decays into ^{13}C and (*ii*) in a second step ^{13}C releases a neutron in the alpha-capture reaction $^{13}\mathrm{C}(\alpha,\mathrm{n})^{16}\mathrm{O}$. The key for the production of i-process neutron densities is that this sequence of reactions occurs in the He convective region, where high temperatures (at least $T > 10^8\,\mathrm{K}$) at the bottom of the convective region lead to a sufficiently high reaction rate of the temperature-sensitive $^{13}\mathrm{C}(\alpha,\mathrm{n})^{16}\mathrm{O}$ reaction. It is this same sequence of reactions which also provides the neutron source for the main s process in AGB stars but under radiative conditions (Straniero et al., 1995). Partial mixing of protons into the upper layers of the intershell region between thermal pulses creates a so-called ^{13}C pocket, which then burns radiatively and generates the s-process neutron densities at lower temperatures compared to the temperatures reached in convective He-shell conditions. However, the exact mechanism of the partial mixing and the ^{13}C pocket formation still remain unknown (Karakas & Lattanzio, 2014; Lattanzio, 2019).

Identifying scenarios where i-process neutron densities are encountered during stellar evolution is only a first step in order to establish the i process as a separate nucleosynthetic process. The second step that led to the increased interest in i-process nucleosynthesis comes from observations of heavy-element abundance patterns, which are not compatible with an s- or r-process origin, or even a combination of both.

The i process has been invoked as source of the heavy elements observed in Sakurai's object (V4334 Sgr), a "born-again giant" that experienced a very late thermal pulse after its AGB evolution (Duerbeck et al., 2000). Over the period of only a few months the composition of Sakurai's object has been observed to change, including abundance changes of heavy elements, such as strontium (Asplund et al., 1999), which are most likely the result of i-process nucleosynthesis (Herwig et al., 2011). Another object with unusual heavy-element abundances is the metal-poor star HD 94028: it shows super-solar abundance ratios of arsenic to germanium, as well as enhancements of molybdenum and ruthenium, which cannot be explained by s- and/or r-process nucleosynthesis and can only be reproduced if an i-process component is also considered (Roederer et al., 2016).

The largest collection of observational evidence for i-process nucleosynthesis comes from carbon-enhanced metal-poor (CEMP) stars, which are subdivided based on their content of the elements barium (Ba) and europium (Eu) as representatives of s- and r-process nucleosynthesis, respectively (Beers & Christlieb, 2005). Some CEMP stars only show enrichments in Ba (CEMP-s stars) and are generally believed to have accreted their carbon (C) and heavy elements from a previous AGB star in a binary system (Lucatello et al., 2005; Masseron et al., 2010; Lugaro et al., 2012; Bisterzo et al., 2012; Starkenburg et al., 2014; Abate et al., 2015a,b; Hansen et al., 2016; Jorissen et al., 2016; Abate et al., 2018). However, this formation scenario cannot explain the simultaneous enrichments of Eu, which are observed alongside the Ba enhancements in some CEMP stars. Unsuccessfully, a variety of formation scenarios were proposed to explain the origin of these stars with complex pathways of separate s- and r-process pollution events, which are extensively discussed in the literature (e.g., Jonsell et al., 2006; Lugaro et al., 2009, 2012; Bisterzo et al., 2011; Abate et al., 2015b, 2016; Goswami et al., 2021, and references therein). Typically these formation scenarios are an extension of the formation scenario for the CEMP-s stars, where the C and Ba overabundances stem from accretion of material previously processed by a binary companion in its AGB phase. The additional r-process enhancement is usually considered to be either primordial to the binary system due to

pollution of the birth cloud (Bisterzo et al., 2011), or the result of pollution by the r-process rich ejecta of an explosive event. The progenitor for such an explosion could be, e.g., a third, massive star in a triple system (Cohen et al., 2003), or even the primary companion after its AGB phase as result of an accretion induced collapse (Qian & Wasserburg, 2003; Cohen et al., 2003) or a type 1.5 supernova (Zijlstra, 2004; Wanajo et al., 2006).

From an observational point of view, it is important to acknowledge that CEMP stars with enhancements in Ba and Eu show a correlation between the s- and r-process enrichments, which is not expected from independent pollution events (Lugaro et al., 2012; Abate et al., 2016). Moreover, the measured ratios between heavy and light s-process elements are higher than observed in CEMP-s stars and cannot be explained by typical s-process nucleosynthesis (e.g. Lugaro et al., 2012; Abate et al., 2015b, 2016). Finally, Abate et al. (2016) used population synthesis studies to examine the numbers of CEMP stars with Ba and Eu enrichment expected from the proposed formation scenarios, but found much lower frequencies of these CEMP stars than are actually observed.

In contrast to invoking separate s- and r-process events for the formation for the CEMP stars with Ba and Eu enhancements, the abundance patterns of these stars can be much better matched by i-process nucleosynthesis (Dardelet et al., 2014; Hampel et al., 2016). We were able to reproduce the heavy-element abundances of 20 CEMP stars that show Ba and Eu enhancements (CEMP-i stars) with the equilibrium abundances of i-process nucleosynthesis simulations at constant neutron densities of $n \approx 10^{14}\,\mathrm{cm}^{-3}$ (Hampel et al., 2016).

1.3 Motivation and outline of this thesis

The link between i-process nucleosynthesis and observed heavy-element abundances of CEMP stars demonstrated in Hampel et al. (2016) sets the scene for the research presented in this thesis. Identifying the i process as responsible for the enhancements in CEMP-i stars is only just the first step in understanding the underlying physics and mechanisms. Many open questions about the i process remain, or have even just been raised by identifying the i process as a source for heavy elements observed in CEMP-i stars. Where did the i process nucleosynthesis occur and what was the nature of its host site? Is there a dominant i-process site or are multiple different stellar evolution scenarios hosting i-process nucleosynthesis? What can we learn about the underlying nuclear and stellar physics from observed i-process patterns? Compared to CEMP-s stars, CEMP-i stars do not appear to be particularly rare. Is i-process nucleosynthesis a common occurrence? Did the i process play a significant role in galactic chemical evolution?

To start answering these questions we need a better idea of the physics that shapes the i-process abundance patterns. What can the observed abundances reveal to us about the underlying stellar and nuclear physics? To start learning about the stars that created the i-process elements, one important factor is to understand the time scale over which the heavy-element production takes place. Hampel et al. (2016) showed that the observed CEMP-i abundance patterns can be very well reproduced with the equilibrium abundance ratios that are created at constant neutron densities. In fact, it is surprising how well these simulations reproduce the observed abundances, particularly given the simplicity of the models, which may indeed be oversimplified and should be far from reality in many aspects–or at least from what we imagine the reality within a star should look like. If the equilibrium abundances match the observations so well, does that mean that the star can

generally provide enough neutrons for sufficiently long until these equilibrium ratios are reached? How long would a star need to be able to sustain these high i-process neutron densities? And what does "enough neutrons" even mean? The quantity that describes for how long which neutron density is sustained is the time-integrated neutron exposure τ, which is defined as

$$\tau = \int n\, v_T\, dt\,, \tag{1.1}$$

with neutron density n and thermal velocity v_T.

But where do these neutrons even come from? Under what conditions can a star produce high enough neutron densities and exposures for heavy-element nucleosynthesis? Once we have a better understanding of the time scales and neutron exposures that are required to produce the observed abundance patterns we can start constraining the thermodynamic properties that a physical environment needs to have to provide the i-process conditions. The production of neutrons for the i process is a key link through which the observed abundance patterns are connected with the thermodynamic environment and its fundamental parameters and physical mechanisms.

In this thesis we will present the use of nuclear network calculations to model i-process nucleosynthesis to further understand and constrain the conditions under which this process operates and the heavy-element abundance patterns it creates. Our method will be further described in each of the following chapters. The outline is as follows:

In **Chapter 2** we start with models at constant neutron densities and expand on the work from Hampel et al. (2016). Instead of just analysing the equilibrium abundances of heavy elements, we consider the time evolution of the abundances as the i process produces them. The element which does not get into equilibrium with the other heavy elements is lead (Pb), the heaviest stable element at the end of the neutron-capture path, which only gets produced in larger and larger quantity by the neutron-capture reactions over time. We take advantage of this i-process feature to use observed Pb abundances in CEMP-i stars for the investigation of the i-process time scales and to place limits on required neutron exposures.

We also discuss a further set of puzzling heavy-element observations, which cannot be explained with s- and/or r-process nucleosynthesis: the Pb abundances in post-AGB stars in the Magellanic Cloud are too low compared to their other heavy-element abundances and s-process predictions. In our investigation of i-process nucleosynthesis and the produced Pb abundances we also show how the puzzlingly low Pb abundances of these post-AGB stars are evidence for i-process nucleosynthesis.

For **Chapter 3** we then move on from modelling i-process nucleosynthesis with constant neutron densities and instead model the i-process *neutron production* in proton-ingestion episodes in a more self-consistent approach via the $^{12}\mathrm{C}(\mathrm{p},\gamma)^{13}\mathrm{N}(\beta)^{13}\mathrm{C}(\alpha,\mathrm{n})^{16}\mathrm{O}$ reaction chain. We adopt a temperature-density trajectory from the conditions during a proton-ingestion episode in a low-mass, low-metallicity AGB star to simulate how a parcel of material moves through the intershell convective region and test various ingested proton fractions. This allows us to lay out the fundamental sequence of CNO and hot-CNO cycle reactions, which are responsible for the neutron production and neutron recycling at i-process neutron densities and to place limits on the amount of ingested protons.

In **Chapter 4** we investigate systematically how uncertainties affect the i-process neutron production and heavy-element nucleosynthesis. We test nuclear-reaction rate uncertainties of the reactions in the CNO region that are involved in the neutron production. Additionally we address

further uncertainties resulting from the underlying stellar evolution. The intershell composition in low-metallicity AGB stars varies over time from pulse to pulse, particularly for the first few pulses when proton-ingestion episodes are most likely to happen, but also during the duration of a pulse. We present how variations of the ^{12}C abundance in the intershell affect the i process. An additional major uncertainty stems from the convective velocities we assume for our temperature-density trajectory. The convective velocities stem from a 1D stellar evolution model, which we know does not provide accurate treatments of convective mixing. Therefore, we test how sensitive our i-process models are to varying convective velocities.

Chapter 5 utilises a major advantage of single-zone nuclear-reaction networks: they are computationally cheap and allow for easy parameter variations to test the conditions for different stellar environments. We present the evolution of an additional low-mass, low-metallicity AGB model, which we compute with an independent code to show how varying conditions in this i-process host site affect the nucleosynthesis. Moreover, we test two further trajectories from stellar evolution models of two alternative proposed i-process sites: a very late thermal pulse in a post-AGB star and the core helium flash in an ultra-metal poor low-mass star.

Finally, in **Chapter 6** we review some abundance signatures of the i process, which we have identified in our models and throughout the investigations for this thesis and which may assist in directing the quest for new observational campaigns. In closing, we summarise our findings, conclusions and directions for further studies in **Chapter 7**.

> *If you're having troubles in your life, to quote myself—"If you meet with a blockage, find a way around it." You can do it.*
>
> — E. Margaret Burbidge

Chapter 2

Learning about the intermediate neutron-capture process from lead abundances

M. Hampel, A. I. Karakas, R. J. Stancliffe, B. S. Meyer, M. Lugaro

The Astrophysical Journal, 2019, ***887****, 11*

This paper is dedicated to the celebration of the 100th birthday of Margaret Burbidge, in recognition of her outstanding contribution to nuclear astrophysics.

Abstract

Lead (Pb) is predominantly produced by the slow neutron-capture process (s process) in asymptotic giant branch (AGB) stars. In contrast to significantly enhanced Pb abundances predicted by low-mass, low-metallicity AGB-models, observations of Magellanic post-AGB stars show incompatibly low Pb abundances. Observations of carbon-enhanced metal-poor (CEMP) stars whose s-process enrichments are accompanied by heavy elements traditionally associated with the rapid neutron-capture process (r process) have raised the need for a neutron-capture process operating at neutron densities intermediate to the s and r process: the so-called i process. We study i-process nucleosynthesis with single-zone nuclear-network calculations. Our i-process models can explain the heavy-element abundance patterns measured in Magellanic post-AGB stars including their puzzlingly low Pb abundances. Furthermore, the heavy-element enhancements in the post-AGB and CEMP-i stars, particularly their Pb abundance, allow us to characterise the neutron densities and exposures of the i process that produced the observed abundance patterns. We find that the lower-metallicity CEMP-i stars ([Fe/H] ≈ -2.5) have heavy-element abundances best matched by models with higher neutron densities and exposures ($\tau > 2.0\,\mathrm{mbarn}^{-1}$) compared to the higher-metallicity post-AGB stars ([Fe/H] ≈ -1.3, $\tau < 1.3\,\mathrm{mbarn}^{-1}$). This offers new constraints and insights regarding the properties of i-process sites and demonstrates that the responsible process operates on time scales of the order of a few years or less.

2.1 Introduction

The large majority of elements heavier than iron are formed by the slow (s) and rapid (r) neutron-capture processes. These processes differ in their characteristic neutron density which determines how likely it is that an unstable neutron-rich isotope captures an additional neutron before decaying (Burbidge et al., 1957; Meyer, 1994; Sneden et al., 2008). The resulting abundance patterns for these processes shift as their conditions change opening up different neutron capture paths.

The s process operates at low neutron densities of $n \lesssim 10^{11}\,\mathrm{cm}^{-3}$ and its main site is within asymptotic giant branch (AGB) stars (Käppeler et al., 2011). In this late evolutionary stage of low- and intermediate-mass stars with initial masses $\lesssim 8\,\mathrm{M}_{\odot}$, an AGB star experiences thermal pulses (TP) and sometimes dredge-up events, which mix the material from the intershell to the stellar surface including carbon and s-process elements. In the intershell, conditions may allow for the formation of a small (in mass) region that is rich in ^{13}C (also referred to as a ^{13}C "pocket"). Subsequent release of free neutrons via $^{13}\mathrm{C}\,(\alpha,\mathrm{n})^{16}\,\mathrm{O}$ and their captures on Fe seed nuclei produce typical s-process elements, such as Sr, Y, Zr, Ba, La, Ce, and Pb. Strong mass loss on the AGB releases these elements into the interstellar medium and makes AGB stars important contributors to the chemical evolution of galaxies. For details and reviews about AGB stars and the s process we refer the reader to Busso et al. (1999); Herwig (2005); Karakas & Lattanzio (2014) and references therein.

In contrast, the r process operates at high neutron densities of $n \gtrsim 10^{20}\,\mathrm{cm}^{-3}$ (Meyer, 1994). Typical elements produced by the r process include Eu, Os, Au and Pt. Different sites have been proposed to host the extreme conditions that are required for the r process, such as magneto-hydrodynamically driven supernovae (Ono et al., 2012; Winteler et al., 2012; Nishimura et al., 2015, 2017) and neutron star mergers (Lattimer & Schramm, 1974; Meyer, 1989; Thielemann et al., 2017; Kilpatrick et al., 2017; Côté et al., 2018).

Observational evidence for another neutron-capture process intermediate to the s and r process comes from observations of carbon-enhanced metal-poor (CEMP, Beers & Christlieb, 2005) stars with enhancements of Ba and Eu. Generally, it is believed that CEMP stars with Ba enhancements are formed in a binary system and that their C and s-process enhancements are the results of mass-transfer from an AGB companion. However, the additional Eu enhancements of some CEMP stars cannot be explained with this formation scenario and pollution from separate s- and r-process sites have been considered unsuccessfully (Jonsell et al., 2006; Lugaro et al., 2012; Bisterzo et al., 2012; Abate et al., 2016). It now seems likely that the observed abundance patterns are the result of a neutron-capture process that can occur in one single stellar site and operates at neutron densities intermediate to the s and r process ($n \approx 10^{14} - 10^{15}\,\mathrm{cm}^{-3}$) (e.g. Dardelet et al., 2014; Hampel et al., 2016): the intermediate neutron-capture process (i process, Cowan & Rose, 1977; Malaney, 1986).

Another example of objects with a puzzling heavy-element enrichment are post-AGB stars (e.g. van Winckel, 2003) in the Small and Large Magellanic Clouds (SMC and LMC). From the inferred absolute luminosities it is possible to constrain the initial masses of the progenitors to $1 - 1.5\,\mathrm{M}_{\odot}$ at metallicities between $-1 \leq [\mathrm{Fe/H}] \leq -1.3$ (De Smedt et al., 2012; van Aarle et al., 2013; De Smedt et al., 2014, 2016). Stellar models in this mass and metallicity range can produce high yields of s-process elements and due to fewer iron seeds at lower metallicities, the chain of neutron captures reaches all the way to the end of the neutron capture path at Pb (Gallino et al., 1998; De

Smedt et al., 2012). Measurements of the Pb abundance in post-AGB stars in the LMC and SMC are only able to provide upper limits. However, even these upper limits are lower than the high abundances predicted from AGB models with the required low progenitor mass and metallicity (De Smedt et al., 2012, 2014; van Aarle et al., 2013; Lugaro et al., 2015; Trippella et al., 2016).

In order to reconcile the predicted and observed Pb abundances, uncertainties and parameters in AGB models have been studied, in particular with respect to the ^{13}C pocket responsible for the production of free neutrons. These attempts were not able to resolve the discrepancies (e.g. Lugaro et al., 2015; Trippella et al., 2016). Lugaro et al. (2015) demonstrated that the full elemental pattern is incompatible with the s process and proposed that these abundance patterns might be better explained by i-process nucleosynthesis resulting from proton-ingestion episodes in the AGB progenitor. However, they did not explore this idea in detail with an appropriate nuclear network.

Hampel et al. (2016, from here on Paper I) studied the equilibrium heavy-element abundance patterns characteristic for different neutron densities up to $n = 10^{15}\,\mathrm{cm}^{-3}$. This deliberately excluded investigating Pb, which always gets produced as a function of time and does not reach equilibrium with Fe and the other heavy elements. Via comparisons to the abundance patterns in CEMP stars Paper I identified the i process as the best explanation for stars that show both Ba and Eu enrichments and renamed them CEMP-i stars (formerly known in the literature as CEMP-s/r and variations thereof). However, additional insight into the total amount of captured neutrons and the time scale of the process is also essential for further interpretation.

This study aims at extending Paper I by systematically studying the parameters that are responsible for shaping i-process abundance patterns and the production of Pb. This includes investigating the dependence on both the neutron density and the integrated neutron exposure, the latter as a proxy for the time evolution constrained by observed Pb abundances. By comparing our results to the observed heavy-element abundances, particularly those of Pb measured in CEMP-i and Magellanic post-AGB stars, we aim to (*i*) show if the puzzlingly low Pb abundances can be attributed to the i process and (*ii*) constrain the neutron densities and exposures characteristic for the i process in these two types of objects with different metallicities. This is an important step towards identifying the site at which the i process operated in our observed samples. Moreover, linking the abundance patterns from CEMP-i and Magellanic post-AGB stars to the characteristic properties of the underlying neutron captures, we can infer observational constraints on the metallicity dependence of the i process.

We describe our method in §2.2 and show the results of our nuclear-network calculations in §2.3. In §2.4 we present the data sample of CEMP-i and post-AGB stars that provides us the observational i-process probes for this study. We compare our simulations to the observations in §2.5 with separate evaluations of the CEMP-i and post-AGB star comparisons in §2.5.1 and §2.5.2, respectively. A discussion of these results is provided in §2.6 complemented by a final summary and concluding remarks in §2.7.

2.2 Method

As in Paper I, we study the production of heavy elements by the i process by feeding constant neutron densities into a one-dimensional, single-zone nuclear-reaction network using *NucNet Tools* (Meyer, 2012) and the JINA Reaclib database (Cyburt et al., 2010). We model heavy-element

production in conditions typical of the intershell region of a low-mass, low-metallicity AGB star in the presence of constant neutron densities of different magnitudes. Temperatures and densities in the range $1.0 \times 10^8\,\mathrm{K} \leq T \leq 2.2 \times 10^8\,\mathrm{K}$ and $800\,\mathrm{g\,cm^{-3}} \leq \rho \leq 3200\,\mathrm{g\,cm^{-3}}$ were investigated, corresponding to the AGB-intershell conditions used by Stancliffe et al. (2011). Compared to charged-particle reactions, neutron-capture reactions are less temperature sensitive. Consequently, we find that different temperatures and densities do not result in significant changes in the heavy-element abundance patterns. Therefore, in the following, we present one representative case with $T = 1.5 \times 10^8\,\mathrm{K}$ and $\rho = 1600\,\mathrm{g\,cm^{-3}}$. We note that the temperature and density significantly affect the activation of the neutron-producing charged-particle reactions, which are not studied in this work.

We use two different initial compositions for our calculations of possible i-process enrichment in the CEMP-i and post-AGB stars to account for the different metallicities of the observed objects. Such different initial compositions are used for consistency with the metallicities of the CEMP-i and post-AGB stars. However, for nuclear network calculations with imposed constant neutron densities, a different initial composition does not result in significantly different heavy-element abundance patterns. For the CEMP-i stars we use abundances from the intershell of a $1M_\odot$-AGB model with metallicity [Fe/H] $= -2.3$ at the second thermal pulse from Lugaro et al. (2012). For the post-AGB stars we use abundances from the intershell of a $1.7M_\odot$-AGB model with metallicity [Fe/H] $= -1.4$ from Karakas et al. (2014), also at the second thermal pulse. In particular, these authors assumed an initial scaled-solar composition with solar abundances from Asplund et al. (2009).

We expose the intershell material to constant neutron densities of $n = 10^{11}$, 10^{12}, 10^{13}, 10^{14}, and $10^{15}\,\mathrm{cm^{-3}}$ to study the detailed abundance patterns created by neutron-capture processes. Note that the original definition of the i process by Cowan & Rose (1977) refers to a neutron density of $n = 10^{15}\,\mathrm{cm^{-3}}$ and the lower neutron densities in our range up to $n = 10^{13}\,\mathrm{cm^{-3}}$ are known to occur as peak neutron densities in s-process simulations (e.g. Raiteri et al., 1991; Gallino et al., 1998; The et al., 2007; Pignatari et al., 2010; Fishlock et al., 2014). This level of neutron density is typically only reached for a short amount of time in s-process models (of the order of days, see e.g. Fishlock et al., 2014) and can be the result of the activation of the ^{22}Ne source. Despite being short these intense neutron bursts can impact the heavy-element abundance pattern by opening up specific s-process branching points. However, these peak-s-process neutron densities do not produce the distinct i-process patterns that form when the bulk of the neutron irradiation occurs at the higher neutron density, as we model here. It is not clear that the s- and i-process neutron densities are separated by a fixed boundary. Instead, we expect an overlap of the associated neutron-density regimes, depending on the actual physical i-process sites and the resulting neutron-capture time scales. In order to study the transition between "typical" s- and i-process abundance patterns it is important to cover all these neutron densities in a systematic study.

We use the time-integrated neutron exposure τ to quantify the total amount of captured neutrons and the time scale of the responsible process:

$$\tau = \int n\, v_T\, dt = \int n \sqrt{2\, k_B\, T / m_n}\, dt\,, \tag{2.1}$$

with neutron density n, thermal neutron velocity v_T, Boltzmann constant k_B, temperature T, and neutron mass m_n. Note that $\tau \propto t$ for our case of a constant neutron density. It is the combination

of neutron density and exposure that allows us to infer the detailed operation of the neutron producing reactions and will ultimately constrain the thermodynamic properties and structural details of the production site.

In Paper I all calculations were run until complete equilibrium was reached between the heavy elements lighter than Pb, which was ensured by an unnaturally large exposure of $\tau = 495$ mbarn^{-1}. This means that a steady flow between neighbouring species was reached when the reaction rates of production and destruction (neutron-capture reactions and β^- decays) reach equilibrium. Constant abundance ratios between species are created and result in heavy-element abundance patterns that are characteristic at each neutron density, and independent from the actual total neutron exposure. However, Pb is only produced by neutron captures but not significantly destroyed and therefore does not reach equilibrium with Fe or the other heavy elements.

Here we expand our previous study from Paper I by exploring different neutron exposures in order to investigate the evolution of the elements at the end of the neutron-capture chain and Pb in particular. In practice, we extract the simulated abundance patterns of the produced unstable, neutron-rich isotopes from the nuclear-network calculations at each time step and evolve their further evolution without additional neutron exposure for $t = 10\,\mathrm{Myr}$. This allows the long-lived unstable isotopes to decay; a longer decay time than 10 Myr only has a negligible effect on the observable elemental abundances. For each tested neutron density, this results in a series of time- (and thereby exposure-) dependent heavy-element patterns.

2.3 Results of the Nuclear Network Calculations

When modelling the production of heavy elements by neutron-capture reactions, isotopes with magic neutron numbers are of particular interest. Due to low neutron-capture cross sections relative to their neighbouring isotopes, nuclei with magic neutron numbers act as bottlenecks on the neutron-capture path and are produced in larger quantities than their neighbouring isotopes. For the s process this gives rise to the Solar s-process element abundance pattern with the light s-process (ls) peak with representative elements such as Sr, Y and Zr (atomic numbers $Z = 38$, 39, and 40, respectively); the heavy s-process (hs) peak with representative elements such as Ba, La, and Ce (atomic numbers $Z = 56$, 57, and 58, respectively); and the Pb ($Z = 82$) peak (e.g., Sneden et al., 2008; Karakas & Lattanzio, 2014). In Paper I we discussed how the i process operates, the resulting heavy-element abundance patterns, and how they differ from the typical s process. In the following section we focus on the time-dependence of the i-process nucleosynthesis and the production of Pb in particular.

Figure 2.1 shows the evolution of the relative heights of the s-process peaks in our simulations, where we use Sr and Ba as representatives of the ls and hs peak, respectively. Since the material in our simulation is exposed to large neutron fluxes, the evolution of the s-process peaks is independent of the initial compositions. The shown abundances refer to the final, post-decay abundances of the stable nuclei. For comparison, a simulation with a typical s-process neutron density of $n = 10^7\,\mathrm{cm}^{-3}$ is also included in Figure 2.1. To account for the different time scales on which neutron captures happen at different n, the Sr, Ba and Pb production ratios are shown as a function of the time-integrated neutron exposure τ. All the simulations show an initial phase of decrease in [Ba/Sr] and [Pb/Ba] until they reach a minimum and begin to rise. For each simulation the rise of [Pb/Ba]

starts after the rise in [Ba/Sr]. This shows that the main production of Sr, Ba and Pb follow one after the other in the respective order as expected.

The minimum [Ba/Sr] and [Pb/Ba] for the different simulations shows that models with higher n start their production phases of Ba and Pb at higher τ. This shift shows a slow down of the heavy-element production in terms of integrated neutron exposure in comparison to the s process. As the i-process neutron-capture path moves away from the valley of stability more neutron-rich isotopes are produced. On average, these have lower neutron-capture cross sections than isotopes with fewer neutrons which are closer to the valley of stability. With a decrease of the average neutron-capture cross section an increase in neutron exposures is required for the production of heavier isotopes and Pb in particular.

In more detail, Figure 2.1 also shows the heavy-element abundance patterns of the simulations with $n = 10^7$, 10^{13}, and $10^{15}\,\mathrm{cm}^{-3}$ at the same integrated neutron exposure $\tau = 2.0$ mbarn^{-1}. From the different distributions of the produced heavy elements, it can be seen that the neutron-capture paths have progressed to very different stages, although the same amount of neutrons per neutron-capture cross section have been provided. The simulation with $n = 10^{15}\,\mathrm{cm}^{-3}$ shows a peak for the elements Xe, Cs, and Ba ($Z = 54$, 55, and 56, respectively). The neutron-capture path just reaches the second bottleneck at the magic neutron number $N = 82$ and it mainly produces magic isotopes of elements a few atomic numbers lighter than the traditional s-process elements. This results in a predominant production of the radioactive isotope ^{135}I (with decays to ^{135}Cs and ^{135}Ba) instead of the stable magic s-process isotopes such as ^{138}Ba, ^{139}La and ^{140}Ce. Most of the heavy elements that have been produced at $n = 10^{15}\,\mathrm{cm}^{-3}$ due to this exposure of $\tau = 2.0$ mbarn^{-1} are lighter than Ba. Most notably, the main neutron-capture path has not reached the Pb peak yet and the stable decay products show [Pb/Ba] $= -2.9$.

In contrast, the neutron capture path of the simulation with $n = 10^{13}\,\mathrm{cm}^{-3}$ has passed the first bottlenecks at the magic neutron numbers $N = 50$ and $N = 82$ and has progressed to the third Pb peak. Pb is already produced at a level similar to that of the second magic neutron peak with [Pb/Ba] $= 0.2$. The simulation with $n = 10^7\,\mathrm{cm}^{-3}$ shows the fastest progression in terms of neutron exposure, where the neutron-capture path has reached the highest production of Pb with abundances as high as [Pb/Fe] > 7 and [Pb/Ba] > 1.5.

An important consequence is evident in Figure 2.1: the simulations at neutron densities with $n \geq 10^{11}\,\mathrm{cm}^{-3}$ cover regimes of [Ba/Sr]-[Pb/Ba] space that cannot be reached by standard s-process nucleosynthesis. With the exception of $n = 10^{15}\,\mathrm{cm}^{-3}$, all the simulations show an almost identical ratio of [Ba/Sr] ≈ 1.2 at $\tau \approx 1.6\,\mathrm{mbarn}^{-1}$. At the same neutron exposure, the simulations with different n cover a range of more than 3 dex in the corresponding [Pb/Ba] abundance ratios. More generally, even at different exposures Figure 2.1 shows that the different neutron densities only result in relatively small changes in [Ba/Sr] compared to the larger ones in [Pb/Ba]. This gives rise to the possibility of explaining a range of heavy-element abundance patterns and in particular the different relative ratios of the ls, hs and Pb-peak using a range of neutron densities and exposures.

Figure 2.1 does not show the final phase of the abundance evolution, where the ratio between two elements becomes constant as a steady flow between them brings their abundances into equilibrium (studied in Paper I). For [Ba/Sr] this happens at higher exposures than shown ($\tau \gtrsim 10$ mbarn^{-1} for $n = 10^7\,\mathrm{cm}^{-3}$ and even higher for increasing n) and [Pb/Ba] does not reach an equilibrium at all. The second panel in Figure 2.1 suggests that such an equilibrium may be reached for $n = 10^7\,\mathrm{cm}^{-3}$

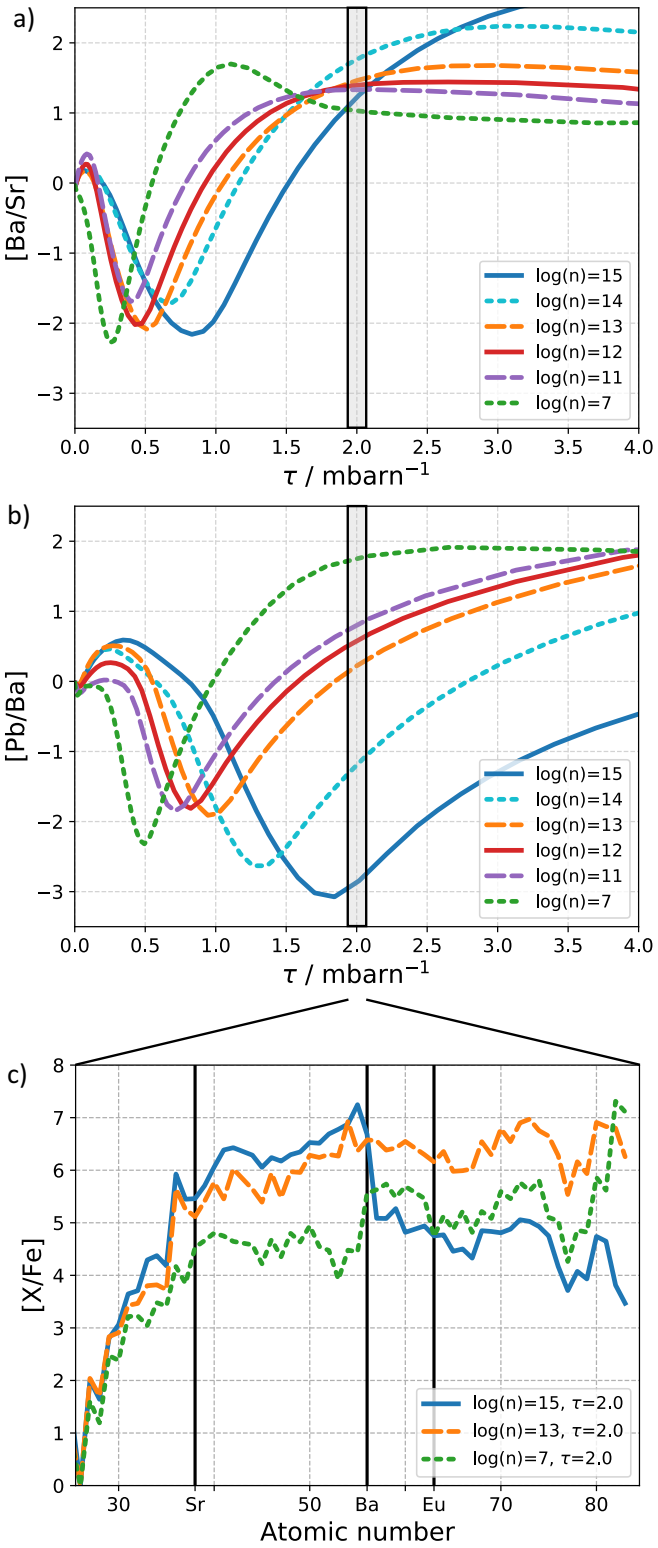

Figure 2.1: Heavy element abundances of s- and i-process calculations with different neutron densities n: a) and b) show the evolution of the relative abundances of the s-process peaks as a function of time integrated neutron exposure τ. c) Shows the heavy-element abundance patterns in the simulations with different neutron densities n at the same neutron exposure $\tau = 2.0$ mbarn^{-1}. The shown abundances refer to the final, post-decay abundances of the stable isotopes. Note that these are predicted, undiluted abundances and cannot be directly compared to observed [X/Fe] ratios. Further dilution with solar-scaled material will decrease the [X/Fe] ratios to the levels observed in CEMP-i and post-AGB stars (see section §2.5).

at $\tau \gtrsim 2.5$ mbarn^{-1}, which is not the case. Instead, [Pb/Ba] enters a phase of decrease before increasing again at higher τ. This is due to different production and destruction phases of Ba as it reaches equilibrium stages with other heavy elements, whereas the abundance of Pb keeps rising continuously and does not enter such steady-flow equilibria.

2.4 Observational Sample

We consider observed heavy-element abundance patterns from CEMP-i and post-AGB stars. The sample of CEMP-i stars is adapted from the sample compiled by Abate et al. (2015b) and used in Paper I. It comprises stars in the metallicity range of $-2.8 \leq$ [Fe/H] ≤ -1.8 from the SAGA database (Suda et al., 2008) and from Masseron et al. (2010) selected with the following criteria:

- [C/Fe] > 1 ,
- [Eu/Fe] > 1 and
- [Ba/Eu] > 0 .

We choose this CEMP-i definition for consistency with the definition of CEMP-rs from Masseron et al. (2010) and CEMP-s/r from Abate et al. (2015b). Note that some authors prefer more restrictive definitions by including an extra constraint on the upper limit on the relative abundance ratios of s- to r-elements, e.g. [Ba/Eu] < 0.5 (Beers & Christlieb, 2005) or [La/Eu] < 0.4 (Bisterzo et al., 2012). However, this restriction results in the misclassification of some stars as CEMP-s even though the heavy-element abundances are inconsistent with s-process nucleosynthesis and are better matched by i-process predictions (Paper I).

Out of the 20 stars from Abate et al. (2015b) we select the 16 stars with measured Pb abundances. We complement the sample with an additional 8 stars from the SAGA database (Suda et al., 2008), the JINABase (Abohalima & Frebel, 2018), Masseron et al. (2010), and Bisterzo et al. (2012). These additional stars were selected because they fulfil the criteria above and have a measurement or upper limit of the Pb abundance. They extend the metallicity range of our sources down to [Fe/H] $= -3$. For consistency with the compilation by Abate et al. (2015b) we adopt the same handling of multiple abundance and uncertainty measurements. We refer the reader to Abate et al. (2015b) for details regarding the data selection. Details of the 24 CEMP-i stars in our sample are listed in Table 2.1.

To investigate the puzzlingly low Pb abundances found in post-AGB stars, we consider the measured abundances and upper limits from five post-AGB stars in the LMC and SMC (De Smedt et al., 2012; van Aarle et al., 2013; De Smedt et al., 2014, 2015). We focus on the five post-AGB stars that show characteristics of being intrinsically enriched and exclude J053253, which instead has been suggested as a candidate for a young stellar object (van Aarle et al., 2013; Kamath et al., 2015). Due to its high metallicity of [Fe/H] $= -0.5$ we also exclude J051213. This makes our sample compatible with the study by Lugaro et al. (2015). Additionally, we include the two most metal-poor Galactic post-AGB stars from De Smedt et al. (2016) which have [Fe/H] < -0.7. A summary of the 7 post-AGB stars selected for this study is given in Table 2.1 where we show the full designations of the post-AGB stars considered in this study.

De Smedt et al. (2016) concluded that their upper limits for the Pb abundances of stars with [Fe/H] > -0.7 are compatible with predictions from AGB models. While the full abundance patterns were not tested for each individual star, it becomes evident from the [Pb/hs] and [Pb/ls] ratios (shown in their Figure 14) that [Fe/H] $= -0.7$ is the boundary below which the Pb discrepancy arises.

All together, this gives us a sample of 31 stars with Pb abundances or upper limits thereof, where we have 13 new i-process candidates and 16 stars that have been confirmed in Paper I to exhibit an i-process signature. Our sample spans a total metallicity range of $-0.8 \geq$ [Fe/H] ≥ -3.0.

2.5 Comparison to observations

To compare calculated heavy-element abundances to measured surface abundances of stars we assume some dilution with material of scaled-solar composition. Considering that we expect the i process to operate only in a small region of the star, it is justified to expect that further evolution, e.g., dredge-up episodes in the AGB phase or mass-transfers onto a companion star, will dilute the i-process material. For this we assume a solar-scaled heavy-element distribution of the dilution material and compute the final abundances X:

$$X = X_i \times (1 - d) + X_\odot \times d\,, \tag{2.2}$$

where X_i is the calculated i-process abundance of each element, $X_\odot$ the solar-scaled abundance[1] and d a dilution factor, which is a free parameter[2] with a value between 0 and 1. We compare the modelled abundances at different n to the sample of observed surface abundances of CEMP-i and post-AGB stars by varying the free parameters τ and d in order to find the minimal χ^2:

$$\chi^2 = \sum_Z \frac{\left([X_Z/\mathrm{Fe}]_\mathrm{obs} - [X_Z/\mathrm{Fe}]_\mathrm{mod}\right)^2}{\sigma^2_{Z,\mathrm{obs}}}\,, \tag{2.3}$$

where $[X_Z/\mathrm{Fe}]_\mathrm{obs}$ and $[X_Z/\mathrm{Fe}]_\mathrm{mod}$ are the observed and modelled abundances, respectively, of the element with atomic number Z and $\sigma_{Z,\mathrm{obs}}$ is the observational error of $[X_Z/\mathrm{Fe}]_\mathrm{obs}$. For these calculations, only the abundances of the heavy elements with $Z > 30$ are taken into account. Furthermore, for the post-AGB stars in the LMC and SMC, the observed Pb abundances are only upper limits and consequently cannot be considered in the χ^2 analysis of the fits. To put a special emphasis on the challenge that these Pb observations pose to nucleosynthesis models, we only consider models that do not produce Pb abundances above the observed upper limits.

In our analysis we use the absolute χ^2 to identify the best fit for each star. A standard approach to compare the goodness of fits is using the reduced $\chi^2_\mathrm{red} = \chi^2/\nu$, where ν is the number of degrees of freedom for the fit, which can only be reliably determined in the case of linear models without priors. Moreover, the observational data do not have uncorrelated Gaussian errors, which is why the statistical interpretation of χ^2_red does not apply here. The given $\sigma_{Z,\mathrm{obs}}$ still give useful measures of how to weight different elemental abundances for a fit to an individual star; however, it is not

[1] For this work and the presented results we use the solar abundances from Asplund et al. (2009).

[2] Physically, we motivate this dilution by combining unprocessed material with the i-processed material. However, we do not consider particular physical processes in detail, such as specific mixing mechanisms or mass-transfer scenarios. Therefore we refrain from a quantitative interpretation of the dilution parameter.

meaningful to derive the goodness of the fits and uncertainties of the determined fit parameters based on χ^2 statistics.

Figure 2.1 indicates that the fit parameters n and τ are correlated, where models with higher n also systematically require higher τ to produce the same abundance level. Moreover, Figure 2.1 suggests a certain degeneracy of the parameters where a different set of n and τ can result in similar abundance ratios. In the absence of a meaningful $\chi^2_{\rm red}$ measure to analyse the uncertainties and correlations of our parameters, we concentrate on presenting the best fitting models for each star. In some cases, almost equally good fits can be obtained from two models with different neutron densities, which we identify based on a 10%-variation of the minimal χ^2. We then also show the alternative fit to give an impression of how constrained the parameters are.

2.5.1 Comparison to carbon-enhanced metal-poor stars

We begin comparing our simulated abundance patterns to observations of the CEMP-i star LP625-44. This star has a metallicity of [Fe/H] $= -2.75$ and was discussed extensively in Paper I. Here we refit the elemental composition of LP625-44 using the method outlined in §2.2 which now includes the Pb abundance and an exposure dependence in the fit. Figure 2.2 shows the two best fits of the modified method, which come from the simulations with $n = 10^{13}\,\mathrm{cm}^{-3}$ and $n = 10^{14}\,\mathrm{cm}^{-3}$. For comparison, the best fit from Abate et al. (2015b) is also shown, which represents standard AGB evolution with s-process nucleosynthesis and binary interactions. We find the neutron density which reproduces the observed abundances of LP625-44 best is $n = 10^{13}\,\mathrm{cm}^{-3}$, which is lower than the previous result of $n = 10^{14}\,\mathrm{cm}^{-3}$ from Paper I. However, based on the corresponding values of $\chi^2 = 4.23$ and $\chi^2 = 4.27$, respectively, these fits are almost equally as good to describe the observed abundances. Moreover, as in Paper I a neutron density of $n = 10^{15}\,\mathrm{cm}^{-3}$ results in a significantly worse fit with $\chi^2 = 13.1$.

Our modified method shows that the neutron captures must occur over a relatively short time scale in order to match the data without overproducing Pb: for LP625-44, exposures as low as $\tau = 2.0$ mbarn^{-1} and $\tau = 2.4$ mbarn^{-1} at $n = 10^{13}\,\mathrm{cm}^{-3}$ and $n = 10^{14}\,\mathrm{cm}^{-3}$, respectively, result in the best fits to the observations and correspond to time scales of 15 and 1.7 days, respectively.

In contrast to the good fits from the i-process simulations, Figure 2.2 also shows that s-process simulations (data from Abate et al., 2015b; see also Figure 31 from Bisterzo et al., 2012) overproduce the Pb abundance in particular compared to the hs elements which are simultaneously underproduced. A less efficient s process, which is an assumption needed to better match the Pb observation, would also reduce the predicted hs abundances and hence even further increase the discrepancy that the hs measurements pose. It was already concluded in Paper I that the observations of LP625-44 show an abundance pattern that is best explained by i-process nucleosynthesis. The present additional consideration of the Pb enhancement of LP625-44, especially in comparison to the high enhancements of the elements with atomic numbers between $56 \leq Z \leq 72$, further strengthens this conclusion.

Figure 2.3 shows the abundance pattern of CEMP-i star CS31062-050, our best-fitting model, and the best s-process fit from Abate et al. (2015b). CS31062-050 has a metallicity of [Fe/H] $= -2.4$ and it has been the subject of multiple observational studies (e.g. Aoki et al., 2002b,a; Lai et al., 2004; Johnson & Bolte, 2004; Aoki et al., 2006; Lai et al., 2007) as well as i-process nucleosynthesis studies (Dardelet et al., 2014; Hampel et al., 2016; Denissenkov et al., 2019). The most comprehen-

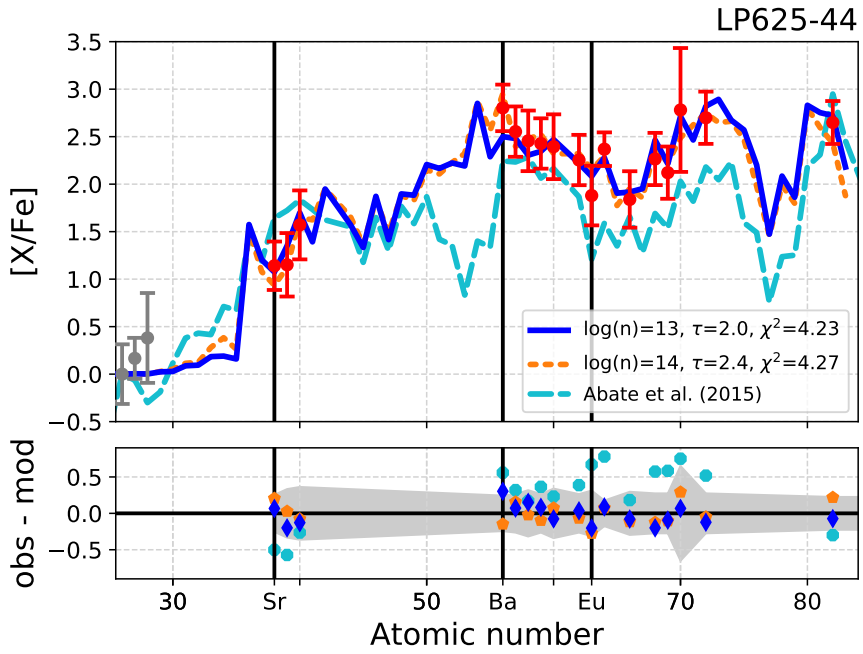

Figure 2.2: Best fits of the heavy-element abundance pattern of CEMP-i star LP625-44. The blue and orange line show the best fitting models with $n = 10^{13}\,\mathrm{cm}^{-3}$ and $n = 10^{14}\,\mathrm{cm}^{-3}$, respectively, which describe the observed abundances almost identically well based on the χ^2 value. For comparison the best fit of Abate et al. (2015b) is shown in cyan. The best fitting s-process models with initial r-process enhancement can be found in Fig. 31 of Bisterzo et al. (2012).

sive heavy-element abundance pattern is provided by Johnson & Bolte (2004) with measurements of 22 neutron-capture elements. Aoki et al. (2006) complemented this study by revising the uncertain abundance of Ba and deriving additional abundances for the interesting transition metals Os ($Z = 76$) and Ir ($Z = 77$).

Due to the high number of observed elements in CS31062-050 this star displays even more characteristics incompatible with s-process nucleosynthesis than already discussed for LP625-44, many of which have been pointed out by Johnson & Bolte (2004) and Bisterzo et al. (2012, see their Figure 26) but were not explicitly discussed in Paper I. This includes a high abundance ratio of Eu and Tb ($Z = 65$), where both of these elements are predominantly produced in the Solar System by the r process with a contribution of 98% and 94%, respectively (Sneden et al., 2008). However, the observed ratio of Eu/Tb = 3.1 cannot be reproduced by a pure r process (Eu/Tb = 1.52), a pure s process (Eu/Tb = 0.63), or any combination thereof. Contrary to these two standard neutron-capture processes, an i process with $n = 10^{14}\,\mathrm{cm}^{-3}$ yields Eu/Tb = 3.5 and can naturally explain this high observed abundance ratio. Similar discrepancies for Dy ($Z = 66$) and Ho ($Z = 67$) can also be resolved by the i process. Additionally, abundances for Pd, Lu, Os and Ir (atomic numbers $Z = 46$, 71, 76, and 77, respectively) are available for CS31062-050. Due to the observational challenges posed by the spectral lines of these elements (see, e.g., both Figures 1 of Johnson & Bolte, 2004 and of Aoki et al., 2006), they are infrequently studied in other CEMP stars. These rarely-measured elements provide valuable constraints on the heavy-element pattern between the three s-process peaks, all of which are well matched by our i-process models.

The best matching simulation for CS31062-050 requires a neutron exposure of $\tau = 3.4$ mbarn^{-1}

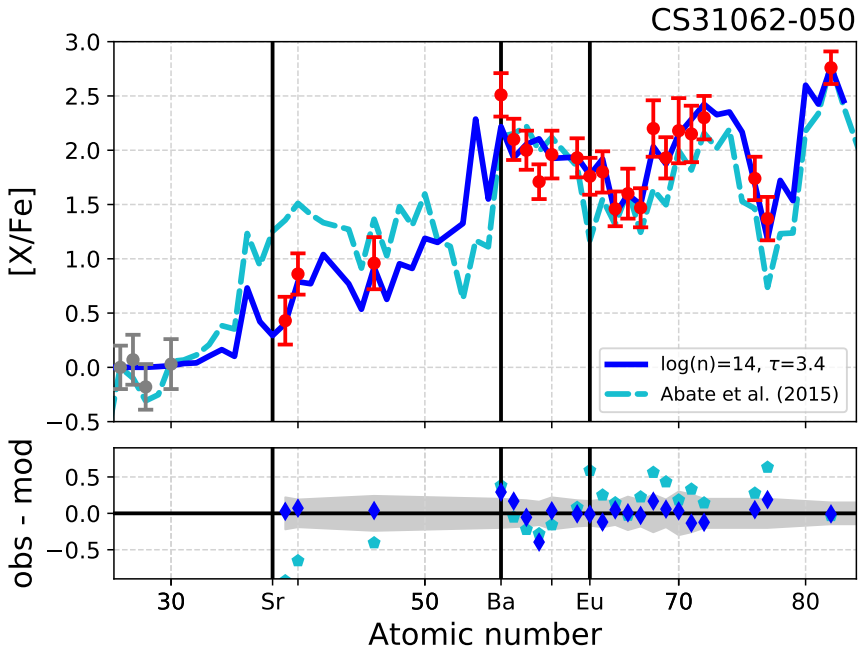

Figure 2.3: Best fits of the heavy-element abundance pattern of CEMP-i star CS31062-050. The blue line shows the best fitting i-process model with $n = 10^{14}\,\mathrm{cm}^{-3}$. For comparison the best fit of Abate et al. (2015b) is shown in cyan. The best fitting s-process models with initial r-process enhancement can be found in Fig. 26 of Bisterzo et al. (2012). The observational data are adapted from Johnson & Bolte (2004) with Ba, Os, and Ir abundances from Aoki et al. (2006).

at a density of $n = 10^{14}\,\mathrm{cm}^{-3}$ corresponding to a time of 2.5 days. The abundance pattern of CS31062-050 has also been the object of other i-process studies: Dardelet et al. (2014) reproduced the abundance pattern of CS31062-050 with single-zone i-process nucleosynthesis calculations at a neutron density of $n = 3 \times 10^{14}\,\mathrm{cm}^{-3}$ and $\tau = 40$ mbarn^{-1} (see their Figure 1). In comparison to our best-fitting model the neutron densities are of similar magnitude, while the required neutron exposures differ by more than an order of magnitude. With $\tau = 40$ mbarn^{-1}, our models overpredict the Pb abundance by at least 1.3 dex. However, it is not clear whether the observed Pb abundance was taken into account in the fits from Dardelet et al. (2014) and is reproduced by their high-exposure simulation. Denissenkov et al. (2019) show that the heavy-element abundances, including Pb, can be reproduced by the i process in their models of rapidly-accreting white dwarfs (see their Figure 12).

We find similar results for the neutron densities and exposures across the whole sample of studied CEMP-i stars. Table 2.2 lists the details of the best-fitting models for each of the stars and Appendix 2.A (online only) shows the individual abundance patterns in detail. For all of the 24 studied stars (16 revisited from Paper I), we find that the determined constant neutron density is either smaller than that found in Paper I (for 9 stars) or the same (for 7 stars). The majority of 13 stars can be fitted best by an abundance pattern produced by a neutron density of $n = 10^{13}\,\mathrm{cm}^{-3}$, five are best fitted by $n = 10^{14}\,\mathrm{cm}^{-3}$, and only one by $n = 10^{15}\,\mathrm{cm}^{-3}$. Despite $n = 10^{15}\,\mathrm{cm}^{-3}$ being the neutron density that is typically associated with the i process in the literature, we can rule out this neutron density as being characteristic for the CEMP-i stars.

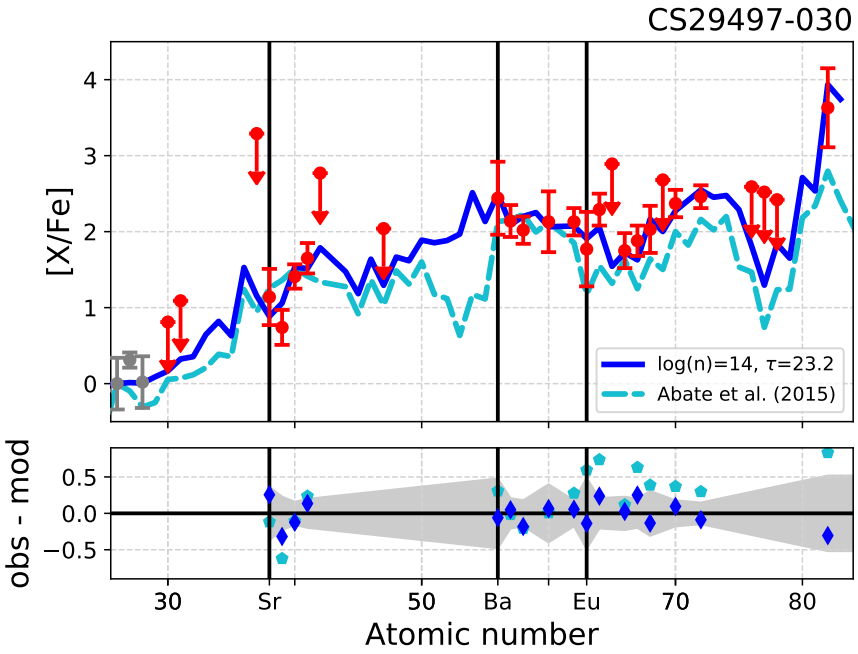

Figure 2.4: Best fits of the heavy-element abundance pattern of CEMP-i star CS29497-030. The blue line shows the best fitting i-process model with $n = 10^{14}\,\mathrm{cm}^{-3}$. For comparison the best fit of Abate et al. (2015b) is shown in cyan. The best fitting s-process models with initial r-process enhancement can be found in Fig. 18 of Bisterzo et al. (2012).

The integrated neutron exposures of the best-fitting models span a narrow range between $1.8 \leq \tau \leq 3.4$ mbarn^{-1} with 4 exceptions:

- CS29497-030 and CS22887-048 require much higher exposures of $\tau = 23.2$ mbarn^{-1} and $\tau = 12.0$ mbarn^{-1}, respectively,
- HE2258-6358 requires a high neutron exposure of $\tau = 7.7$ mbarn^{-1} but is also the only star with a best fit at $n = 10^{15}\,\mathrm{cm}^{-3}$, and
- HE0336+0113 can only be matched with a model of a particularly low exposure of $\tau = 1.1$ mbarn^{-1}.

CS29497-030 and CS22887-048 are the two stars with the highest Pb abundance amongst the studied CEMP-i stars ([Pb/Fe] = 3.5 for both), as well as the highest ratios between the Pb and hs peak. Consequently, high neutron exposures are needed to reproduce these high Pb abundances. As an example, Figure 2.4 shows the abundance pattern of CS29497-030 with the best fitting models from this work and from Abate et al. (2015b).

In contrast to CS29497-030 and CS22887-048, the abundance pattern of HE2258-6358, shown in Figure 2.5, does not show an extreme over abundance of Pb, which would naturally require a higher neutron expose. Instead, the exceptionally high required neutron exposure is due to the fact that the best fitting model has a neutron density of $n = 10^{15}\,\mathrm{cm}^{-3}$. As evident from Figure 2.1 and discussed in §2.3, the production of heavy elements needs higher exposures the higher the neutron densities. Figure 2.5 also shows the second best fit to the abundances of HE2258-6358, which occurs at the parameters $n = 10^{14}\,\mathrm{cm}^{-3}$ and $\tau = 2.6$ mbarn^{-1}. The χ^2 values of 28.8 and 30.1 for

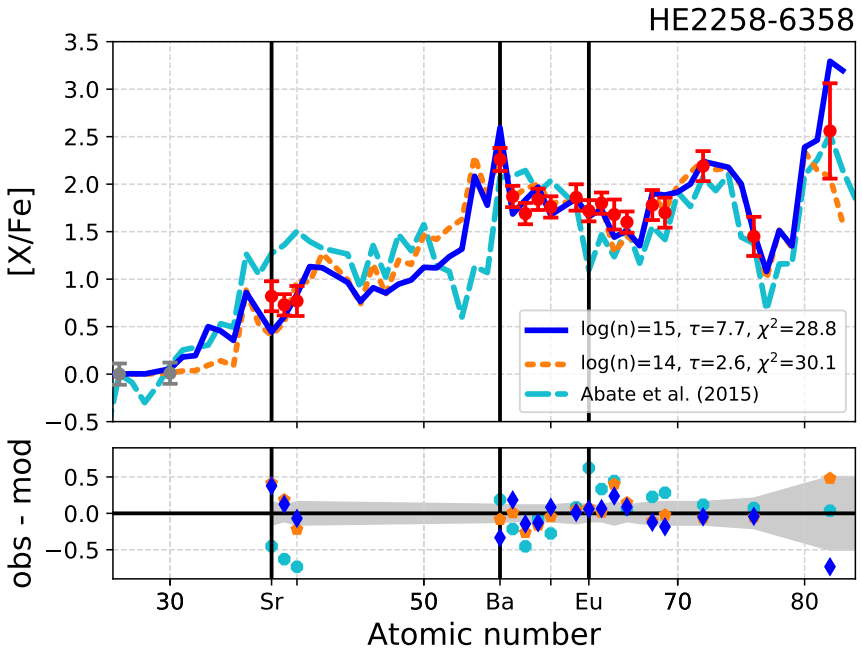

Figure 2.5: Best fits of the heavy-element abundance pattern of CEMP-i star CS29497-030. The blue and orange lines shows the best fitting i-process models with $n = 10^{15}\,\mathrm{cm}^{-3}$ and $n = 10^{14}\,\mathrm{cm}^{-3}$, respectively. For comparison the best fit of Abate et al. (2015b) is shown in cyan.

$n = 10^{15}\,\mathrm{cm}^{-3}$ and $n = 10^{14}\,\mathrm{cm}^{-3}$, respectively, show that the quality of the fits are comparable and that the parameters of the alternative fit lie within the expected range.

The CEMP-i star whose fit to its abundance pattern results in the lowest neutron exposure is HE0336+0113, shown in Figure 2.6. Not only does this fit indicate a low neutron exposure of $\tau = 1.1\ \mathrm{mbarn}^{-1}$ but also a low neutron density of $n = 10^{11}\,\mathrm{cm}^{-3}$. These parameters are very similar to those needed to match the post-AGB stars discussed in the next section, although the atmospheric parameters of $T = 5700 \pm 100\,\mathrm{K}$ and $\log g = 3.5 \pm 0.25$ identify it as a subgiant and not a post-AGB star. In fact, the abundance pattern of HE0336+0113 has more similarities with those of the post-AGB stars than with the other CEMP-i stars: it has the highest ls peak amongst the CEMP-i stars ([Sr/Fe] = 1.8) and a low [hs/ls] ratio combined with an upper limit of the Pb abundance at a particularly low level, which makes it the only CEMP star in the sample with [Pb/Ba] < 0. Moreover, it has a high overabundance of Ba compared to Eu of [Ba/Eu] = 1.3. In addition to these properties, which are more characteristic for s- than for i-process nucleosynthesis, Bisterzo et al. (2012, Figure 2) matched the abundance pattern of HE0336+0113 by s-process nucleosynthesis of an AGB star with initial mass of $1.4\,\mathrm{M}_\odot$ and an initial r-process enrichment of $[r/\mathrm{Fe}] = 0.5$. For comparison, Figure 2.6 also shows the best fit to our simulation with a neutron density of $n = 10^{7}\,\mathrm{cm}^{-3}$, which is typical for the s process. The resulting fit is not significantly worse than the one $n = 10^{11}\,\mathrm{cm}^{-3}$ and shows that determinations of the abundances of further elements, particularly of the heavy rare-earth elements, are desired to better constrain the nucleosynthetic history.

Our method for classifying CEMP-i stars did not have an upper limit for [Ba/Eu] ratios, although it is often used as criterion for s-process enrichment (see §2.4). In different classification schemes, e.g. [Ba/Eu] < 0.5 (e.g. Beers & Christlieb, 2005), HE0336+0113 would not be classified

as a CEMP-i star, but as a CEMP-s star instead. However, the same classification scheme would also classify 12 other stars from our CEMP-i sample as CEMP-s, although our fits from Paper I and Table 2.2 show that their abundance patterns can be better matched by i-process nucleosynthesis. For example, this includes the previously discussed stars LP625-44 (Figure 2.2) with [Ba/Eu] = 0.9 and CS31062-050 with [Ba/Eu] = 0.7 which have heavy-element abundances clearly incompatible with the s process and reproducible by i-process nucleosynthesis.

Although the limit of [Ba/Eu] < 0.5 does not accurately distinguish CEMP-i and CEMP-s stars, the example of HE0336+0113 might indicate that this highest ratio of [Ba/Eu] = 1.3 could indeed be seen as an s-process indicator. Comparison with Figure 1 of Masseron et al. (2010) emphasises this outlier status of HE0336+0113 in the Ba-Eu-abundance plane in comparison to other CEMP-i stars: with [Ba/Fe] = 2.6 and [Eu/Fe] = 1.3 it is the only CEMP-i star that lies above the dashed lines which correspond to pure s-process predictions from metal-poor AGB stars, the highest of which lies at [Ba/Eu] = 1.1 (see Masseron et al., 2010).

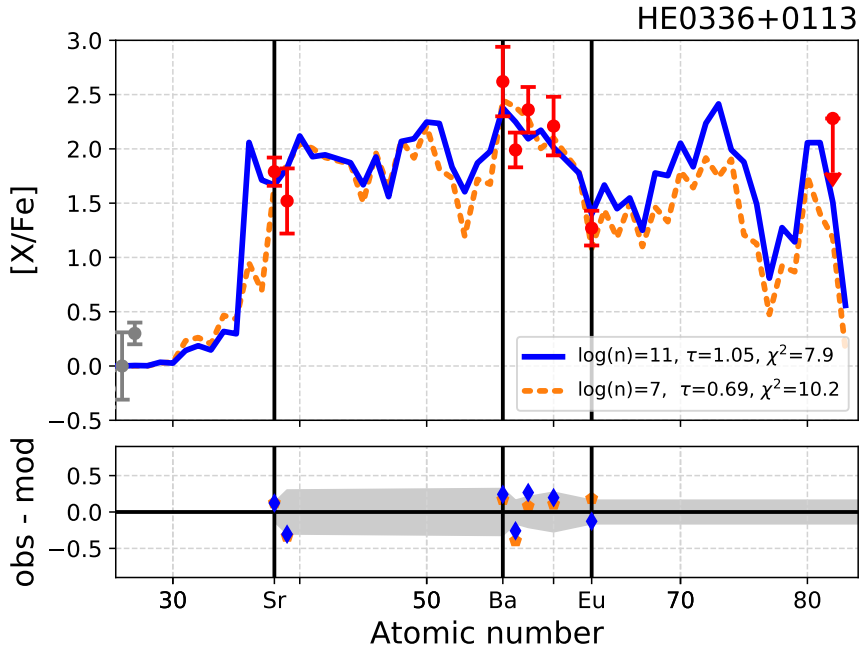

Figure 2.6: Best fits of the heavy-element abundance pattern of HE0336+0113. The blue and orange line show the best fitting models with $n = 10^{11}\,\mathrm{cm}^{-3}$ and $n = 10^{7}\,\mathrm{cm}^{-3}$, respectively. The best fitting s-process models with initial r-process enhancement can be found in Fig. 2 of Bisterzo et al. (2012).

2.5.2 Comparison to post-AGB stars

Figure 2.7 shows the abundance pattern of the Pb-deficient post-AGB star J052043 with our best-fitting model, while the fits for all other stars can be found in Appendix 2.B (online only). The best-fitting model was not only chosen by the minimal χ^2 value of the fit but also by the additional constraint that the observed upper limit of the Pb abundance should not be overproduced. The abundance pattern of J052043 can be best reproduced by simulations with a neutron density of $n = 10^{12}\,\mathrm{cm}^{-3}$ for 83.3 days, resulting in a neutron exposure of $\tau = 1.1$ mbarn^{-1}.

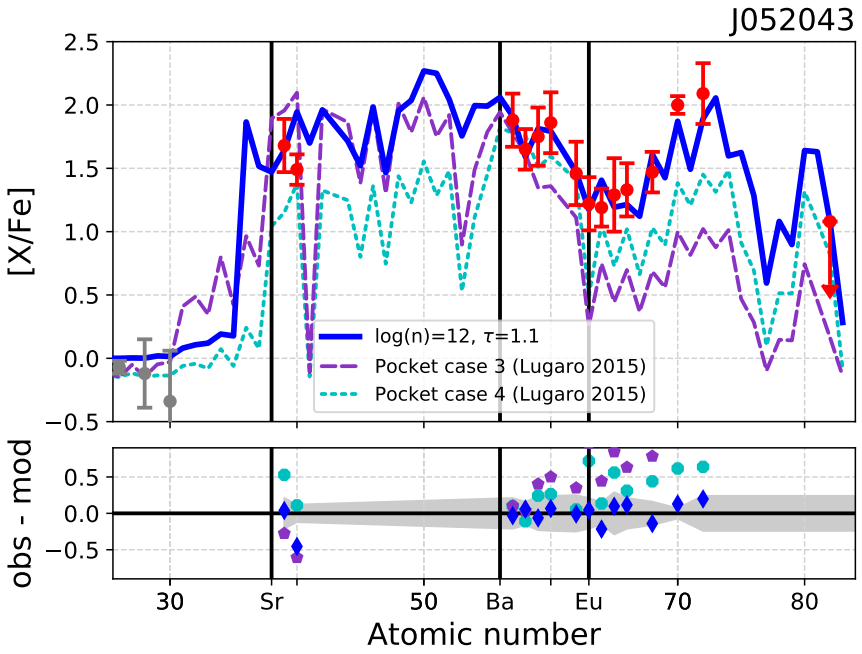

Figure 2.7: Best fits of the heavy-element abundance pattern of post-AGB star J052043. The blue line shows the best fitting model with $n = 10^{12}\,\mathrm{cm}^{-3}$. For comparison, the fits of Lugaro et al. (2015) are shown for modified ^{13}C pockets with two different proton fractions (normalised to La).

For comparison, s-process models from Lugaro et al. (2015) are also shown in Figure 2.7. These are the results of AGB evolution and nucleosynthesis of models with an initial mass of 1.3 $M_{\odot}$, metallicity [Fe/H] $= -1.3$ and ^{13}C pockets produced by two different constant proton abundances mixed into the intershell with $X\,(\mathrm{H})_{\mathrm{case3}} = 0.7 \times 10^{-4}$ and $X\,(\mathrm{H})_{\mathrm{case4}} = 1.05 \times 10^{-4}$. These two different ^{13}C pockets were fine-tuned to comply with the upper Pb limit and to match the hs abundances, but fail to reproduce the other characteristics of the observed abundance patterns. This can be clearly seen by the underproduction of the elements between the hs and Pb peak starting at Eu. The enhancement levels of these elements can be naturally matched by our simulation without overproducing Pb. Additionally, our simulations are successful at reproducing the observed ls- and hs-enhancements and the relative strengths of the s-process peaks.

The parameters for the best fitting i-process models for the studied post-AGB stars are summarised in Table 2.2. The abundance patterns and upper Pb limits of all 7 post-AGB stars can be fitted best by i-process models of $n = 10^{11}\,\mathrm{cm}^{-3}$ and $n = 10^{12}\,\mathrm{cm}^{-3}$, which is at the lower end of the tested neutron densities. Similar to the CEMP-i stars, our models show that the process responsible must have operated on short time scales. The required integrated neutron exposures for the post-AGB stars lie in the narrow range between $1.0 \leq \tau \leq 1.3\,\mathrm{mbarn}^{-1}$ leading to time scales between 0.2 and 2.5 years. Overall, the neutron densities and exposures found for the post-AGB stars are lower than those required to match the CEMP-i stars. The lower neutron densities in the i-process simulations allow for somewhat longer operation time scales in the post-AGB stars compared to CEMP-i stars. In general, the time scales of all of the best-fitting models are by far shorter than those of typical s-process nucleosynthesis in the ^{13}C pocket of the order of 10^4 yr: the longest of our simulations fitting the post-AGB stars requires only 2.4 years.

2.5.3 Summary of Results

Figure 2.8 shows the exposure and neutron density of the best fits to the observations as a function of their metallicity. Interestingly, our results show a bimodial distribution of parameters characterising the best-matching i-process conditions. The CEMP-i fits predominantly have higher neutron densities of $n = 10^{13}\,\mathrm{cm}^{-3}$ to $n = 10^{14}\,\mathrm{cm}^{-3}$ and higher integrated neutron exposures of $\tau \geq 1.8\,\mathrm{mbarn}^{-1}$ than the simulations matching the abundances of the Pb-poor post-AGB stars, which show lower neutron densities of $n = 10^{11}\,\mathrm{cm}^{-3}$ to $n = 10^{12}\,\mathrm{cm}^{-3}$ and lower integrated neutron exposures of $1.0 \leq \tau \leq 1.3\,\mathrm{mbarn}^{-1}$. A possible explanation of this bimodality is that these are the products of i-process nucleosynthesis occurring at two different sites where the specific i-process conditions give rise to slightly different characteristics. Alternatively, we could assume the same i-process site and that the reduction of n and τ is an effect of changing metallicity on the neutron production.

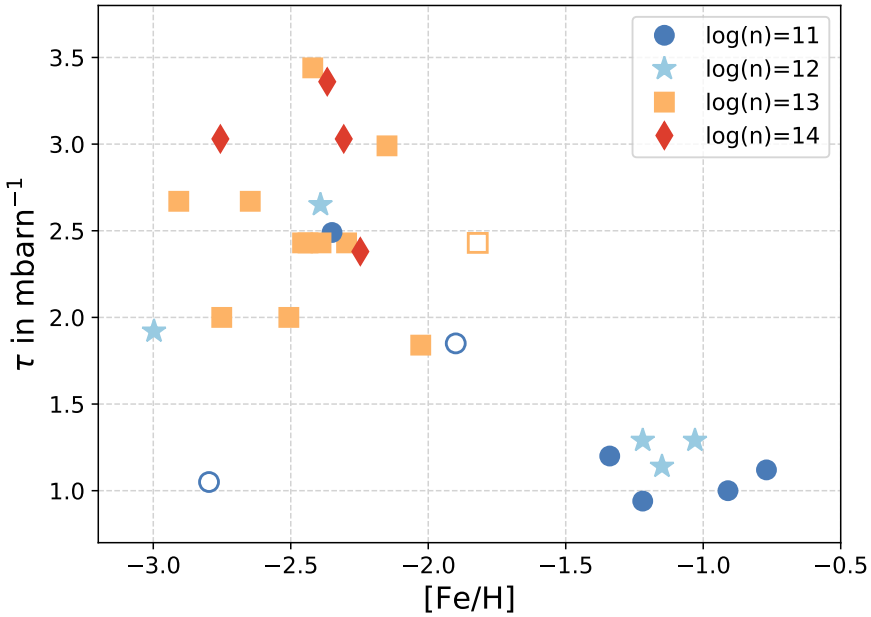

Figure 2.8: Neutron density and exposure of the best fitting models for each star as function of the metallicity. The empty symbols denote the least reliable fits due to only 7 or less measured heavy-element abundances. Note that only exposures up to $\tau = 3.5$ mbarn^{-1} are shown and the three CEMP-i stars with higher exposures are not included in this figure. See discussion in main text for further details, also about the outlying CEMP star HE0336+0113 at [Fe/H] $= -2.8$ and $\tau = 1.1$ mbarn^{-1}.

2.6 Discussion

The two fundamental questions regarding the i process are: *Does it happen in nature? And if so, where and how?* Despite the simplicity of our one-zone models, our results confirm that the observed abundance patterns of CEMP-i and Pb-poor post-AGB stars are best explained by i-process nucleosynthesis. This result can be used to help us shed light on possible i-process sites by considering which progenitors may be responsible for the observed i-process abundance patterns.

Let us start with the more obvious case: we know that the progenitors of the Pb-poor post-AGB stars are low-mass AGB stars and that their heavy-element enrichment is a direct result of their previous stellar evolution. Therefore our results imply that low-mass AGB stars with initial masses of approximately $1 - 1.5\,M_\odot$ at metallicities of $-1.3 \leq [Fe/H] \leq -0.7$ reach stages in their evolution that give rise to i-process conditions. Moreover, it seems that these progenitors have not experienced standard AGB s-process nucleosynthesis, as this would produce higher Pb abundances accompanying the other heavy-element enhancements (De Smedt et al., 2012, 2014; Lugaro et al., 2015; Trippella et al., 2016). From our results we cannot constrain the evolutionary phase in which the i-process nucleosynthesis occurred. Did it occur during the TP-AGB phase, replacing the s process, or is it the result of late He-shell flashes when the star has moved to the post-AGB?

The high neutron densities required for the i process could result from proton-ingestion episodes (PIEs). PIEs occur when protons are entrained into convective layers rich in He and C. This can lead to a neutron burst at i-process neutron densities via the $^{12}\mathrm{C}\,(\mathrm{p},\gamma)^{13}\,\mathrm{N}\,(\beta^{+}\nu)^{13}\,\mathrm{C}\,(\alpha,\mathrm{n})^{16}\,\mathrm{O}$ reaction chain (Cowan & Rose, 1977). A diversity of sites has been proposed to host PIEs and in extension i-process nucleosynthesis. These include core He flashes in low-metallicity low-mass stars (Campbell et al., 2010; Cruz et al., 2013), super-AGB stars (Doherty et al., 2015; Jones et al., 2016), very late thermal pulses (Herwig et al., 2011), rapidly-accreting white dwarfs (Denissenkov et al., 2017, 2019), and metal-poor massive stars (Clarkson et al., 2018; Banerjee et al., 2018). PIEs have also been predicted to occur in the first fully developed convective thermal pulse(s) in low-mass, low-metallicity AGB stars where the upper metallicity limit depends on mass and composition but tends to lie below $[Fe/H] \lesssim -2$ (Hollowell et al., 1990; Fujimoto et al., 1990; Iwamoto et al., 2004; Campbell & Lattanzio, 2008; Lau et al., 2009; Cristallo et al., 2009, 2016). While this metallicity is compatible with the studied CEMP-i stars, it is questionable whether this is also a realistic scenario to have occurred in the progenitors of the Pb-poor post-AGB stars of higher metallicity.

How could the i process occur in a post-AGB star with $[Fe/H] > -2$? Sakurai's Object (V4334 Sagittarii) is a born-again giant at solar metallicity and shows neutron-capture enrichments but only in the lightest elements such as Rb, Sr, Y, and Zr (Asplund et al., 1999). Similarly to the post-AGB stars in our sample, Sakurai's Object does not show the abundances that are expected from s-process nucleosynthesis during the TP-AGB phase at the observed solar metallicity. In particular, the measured abundances of the s-process peaks relative to each other pose challenges to standard s-process nucleosynthesis with a significantly higher observed overproduction of the ls peak. Without significant s-process contribution during the TP-AGB phase, the observed neutron-capture nucleosynthesis could be driven by a late He-shell flash which ingests the thin remaining H envelope. Herwig et al. (2011, 2014) studied such a (very) late He-shell flash in three-dimensional hydrodynamic simulations. The resulting i-process nucleosynthesis informed by the three-dimensional calculations can successfully explain the abundances in Sakurai's Object (Herwig et al., 2011).

The complicated details of different effects in the three-dimensional hydrodynamic simulations of proton-ingestion episodes are still debated and not fully understood. Stellar evolution models predict a prompt splitting of the convective zone prohibiting further mixing and i-process nucleosynthesis. Three-dimensional hydrodynamic simulations motivate that such a split can be delayed (Herwig et al., 2011) whereas Stancliffe et al. (2011) did not find evidence for convective zone splitting. Additionally, Herwig et al. (2014) observed that the proton ingestion can trigger global oscillations with uncertain consequences, such as enhanced entrainment rates or self-quenching.

Different to the post-AGB stars, the nature of the progenitor that hosted the i-process nucleosynthesis observed in CEMP-i stars is less clear. The observed abundance patterns of CEMP-i stars are assumed to show the products of nucleosynthesis in a companion star that have been accreted onto the lower-mass secondary in a binary system that we observe today. Therefore we do not know the initial mass and evolution of the progenitor. However, based on arguments from population-synthesis and from comparing the relative numbers of CEMP-s and CEMP-i stars, the formation-channel of CEMP-i stars is not expected to be much less common than that of CEMP-s stars, if not even equally as likely (Abate et al., 2016).

This scenario of pollution by a companion star is supported by the large binary fraction amongst the CEMP stars with Ba enrichment, which could be consistent with all these stars being in binaries (Lucatello et al., 2005; Starkenburg et al., 2014). However, Hansen et al. (2016) found a binary fraction of $\approx 80\%$ in their sample of CEMP-s and CEMP-i stars using a systematic and precise long-term radial-velocity monitoring program. While this study confirms a much higher binary fraction amongst CEMP stars with Ba enrichment compared to normal metal-poor giants, it also finds four CEMP-s stars without any signs of a companion. A population-synthesis study by Abate et al. (2018) shows that at least some or even all four of these apparently single CEMP-s stars could be undetected binaries with orbital periods of $P \gtrsim 10^4$ days. Alternatively, these stars could be single stars that require an alternative formation mechanism, e.g., pollution of their birth-clouds from previous-generation spinstars (Choplin et al., 2017). The mentioned studies are for CEMP stars with Ba enrichment in general, which include CEMP-s and CEMP-i stars. It will need larger samples of stars with consistent radial velocity monitoring in order to draw individual conclusions for CEMP-s and CEMP-i stars separately. Due to the limited data, the binary fraction of CEMP-i stars in particular remains unclear.

If the binary fraction of the CEMP-i stars is similar to that of CEMP-s and if the stars without radial-velocity variations from Hansen et al. (2015) are true single stars instead of undetected long-period binaries, then there may be the need for an i-process site that can account for a minority of single CEMP-i stars that are not polluted by a companion star. For instance, metal-free and metal-poor massive stars of $20 - 30\,M_\odot$ are considered as candidates for polluting the interstellar medium with i-process material from which a single CEMP-i star could subsequently form (Banerjee et al., 2018; Clarkson et al., 2018).

Alternatively, Denissenkov et al. (2017, 2019) investigated rapidly-accreting white dwarfs (RAWDs) as i-process sites and also as progenitors for single CEMP-i stars. Under certain conditions of stable and rapid mass transfer between white dwarfs in a multiple system, i-process nucleosynthesis could be hosted in the resulting He shell flashes. At decreasing metallicity, Denissenkov et al. (2019) find increasing mass retention efficiencies for RAWDs which opens a possible channel for supernova type Ia explosions. If such a RAWD system in a close binary is orbited by a companion in a wider tertiary, this companion could be polluted with i-process material from the RAWD. Moreover, if a subsequent supernova explosion leads to the ejection of this tertiary companion from the triple system, it could be observable today as a single CEMP-i star (Denissenkov et al., 2019).

The formation of CEMP-i stars by RAWDs requires a very specific sequence of events, which may be disfavoured by the stellar population. While the mechanism is possible, only population synthesis calculations can determine if it is probable. The i-process nucleosynthesis in RAWDs

only results from stable burning of accreted H, for which a very narrow range of accretion rates is required (Nomoto et al., 2007). So far the stable mass transfer has been imposed in the simulations by Denissenkov et al. (2017, 2019) but for low-metallicity systems with [Fe/H] < -1 stable mass transfer at this specific rate is predicted to be unlikely (Kobayashi et al., 1998). Moreover, it is not clear yet whether RAWDs are viable progenitors of CEMP-i stars, due to the low occurance rates of triple systems, in particular of such specific configurations that ultimately can form a close CEMP-i binary or are able to eject a CEMP-i single star from the system (Rastegaev, 2010; Hamers et al., 2013; De Marco & Izzard, 2017).

When using our parametric study to infer i-process parameters that reproduce the observed abundance patterns, one has to keep the simplicity of our models in mind. We utilised single-zone nuclear network calculations to study i-process nucleosynthesis detached from an actual stellar framework. While we used representative temperatures and densities derived from stellar evolution models, we still keep them constant throughout our calculations. Most significantly, we even detach the production of the neutrons not only from the stellar site and the physical conditions, but also from the ongoing nucleosynthesis. While this has the advantage that we can concentrate on the details of the heavy-element production, it means that we only study the influence of a constant neutron density. Important aspects as for example the production of neutrons, its metallicity and time dependence, the effect of mixing and the replenishment of neutron-capture seeds etc. remain untouched in this study.

Additionally, the nuclear data and reaction rates at the base of this study suffer from significant uncertainties. It is known that their effects on i-process abundance patterns can be large: Bertolli et al. (2013) found, for example, that predicted i-process abundances of [Ba/La] can change up to 1 dex depending on the theoretical nuclear physics models and effects of up to 0.3 dex were found to come from the (n, γ) reaction rate uncertainties of ls elements (Denissenkov et al., 2018). Therefore, it is important to systematically study the influences that nuclear physics uncertainties have on the simulated abundance patterns.

2.7 Conclusions

In this study we examined the observed heavy-element abundances of two types of objects that show enrichments in traditional s-process elements produced in AGB stars but whose abundance patterns are generally incompatible with s-process predictions: CEMP-i stars and Pb-poor post-AGB stars, with representative metallicities of [Fe/H] ≈ -2.5 and [Fe/H] ≈ -1.3, respectively. We can explain these abundance patterns, including the combination of puzzlingly low Pb enhancements and high rare-Earth element abundances, as results of i-process nucleosynthesis. We used nuclear-network calculations to study heavy-element production at different constant neutron densities up to $n = 10^{15}\,\mathrm{cm}^{-3}$. The constraints posed by measured Pb abundances in these objects allowed us to characterise the neutron densities and exposures of the process responsible for creating the observed heavy-element abundances.

We find that the patterns of the post-AGB stars are best explained by neutron-capture nucleosynthesis at relatively low neutron densities of $n = 10^{11}\,\mathrm{cm}^{-3}$ or $n = 10^{12}\,\mathrm{cm}^{-3}$ and exposures between $\tau = 1.0$ mbarn^{-1} and $\tau = 1.3$ mbarn^{-1}. In contrast, higher neutron exposures of at least $\tau > 2.0\,\mathrm{mbarn}^{-1}$ are required to reproduce the abundance patterns of CEMP-i stars as well as

higher neutron densities, mostly at $n = 10^{13}\,\mathrm{cm}^{-3}$ or $n = 10^{14}\,\mathrm{cm}^{-3}$. These results offer new constraints and insights regarding the properties of i-process sites and demonstrate that the responsible process operates on short time scales, of the order of a few years or less, depending on the neutron density, and requires lower bulk neutron densities than the initially characteristic i-process neutron density of $n = 10^{15}\,\mathrm{cm}^{-3}$ proposed by Cowan & Rose (1977).

That the n and τ parameters of the best fits to the abundance patterns of CEMP-i stars and Pb-poor post-AGB stars cluster in different regions of the parameter space might offer additional insights: there could be a metallicity dependence of the underlying process that leads to the neutron bursts, or this could indicate two different mechanisms or sites.

To understand which neutron density over which time scale is responsible for which abundance patterns is only a first step. Future work will need to study how representative these patterns are for more realistic neutron-density profiles, which are expected to reach some peak density and then decline afterwards. We still have to identify the main influences that shape the resulting abundance pattern and many questions remain unsolved: How does the lower neutron-density tail affect the final abundances after the peak density is reached? How quickly does the neutron source have to cease in order to maintain the characteristic i-process pattern formed at the peak neutron density before the exposure at lower neutron density reshapes the abundance patterns to resemble that of a typical s process? Can these effects (or the lack thereof) provide insights into the physical and structural properties of the i-process site? In order to understand the mechanisms responsible for i-process conditions, future theoretical i-process studies need to simulate heavy-element production in more realistic stellar environments, for example as presented for RAWDs by Denissenkov et al. (2019). A larger number of objects over a wider range of metallicities will improve the certainty with which we can constrain i-process properties and, of course, is fundamental to answering questions like *How common is i-process nucleosynthesis?* An increase in detected and (ideally homogeneously) analysed objects with i-process abundance patterns will therefore be very enriching for the field.

We are still at the beginning of understanding i-process nucleosynthesis and there are many open questions that require further theoretical and observational studies. Ultimately improving our understanding of the mechanisms leading to the conditions under which the i process operates will help us to complete our understanding of stellar physics, and the evolution and the origin of heavy elements in the Galaxy.

Table 2.1: The data sample. Temperatures, surface gravities and selected chemical properties of the studied 24 CEMP-i and 7 post-AGB stars.

ID	$T_{\rm eff}$ (K)	$\log g$	[Fe/H]	[C/Fe]	[Ba/Fe]	[La/Fe]	[Eu/Fe]	[Pb/Fe]	Reference
CEMP-i stars									
BS16080-175	6240	3.7	-1.9 ± 0.2	1.8 ± 0.2	1.5 ± 0.1	1.6 ± 0.1	1.1 ± 0.1	2.7 ± 0.1	1
BS17436-058	5690	2.7	-1.8 ± 0.1	1.6 ± 0.2	1.7 ± 0.1	1.6 ± 0.2	1.2 ± 0.1	2.3 ± 0.1	1
CS22183-015	5540	3.2	-2.9 ± 0.3	2.3 ± 0.2	2.0 ± 0.2	1.7 ± 0.2	1.6 ± 0.2	2.9 ± 0.1	1, 14, 15, 30
CS22887-048	6500	3.5	-1.8 ± 0.2	1.7 ± 0.3	1.9 ± 0.2	1.8 ± 0.1	1.5 ± 0.2	3.5 ± 0.1	1, 30
CS22898-027	6110	3.7	-2.3 ± 0.2	2.0 ± 0.4	2.3 ± 0.3	2.3 ± 0.2	2.0 ± 0.2	2.9 ± 0.2	4, 5, 28, 32
CS22948-027	4800	1.8	-2.5 ± 0.3	2.4 ± 0.4	2.4 ± 0.4	2.3 ± 0.2	1.9 ± 0.2	2.7 ± 0.1	7, 9
CS29497-030	6966	4.0	-2.6 ± 0.3	2.5 ± 0.2	2.4 ± 0.5	2.1 ± 0.2	1.8 ± 0.5	3.6 ± 0.5	25, 36, 37, 35
CS29497-034	4850	1.6	-3.0 ± 0.3	2.7 ± 0.2	2.2 ± 0.1	2.2 ± 0.1	1.9 ± 0.1	2.9 ± 0.1	7, 9
CS29526-110	6500	3.2	-2.4 ± 0.2	2.3 ± 0.4	2.1 ± 0.2	1.8 ± 0.2	1.8 ± 0.2	3.4 ± 0.2	4, 5
CS31062-012	6099	4.2	-2.8 ± 0.8	2.3 ± 0.4	2.1 ± 0.2	2.0 ± 0.3	1.6 ± 0.3	2.5 ± 0.2	3, 4, 5, 8, 33
CS31062-050	5500	2.7	-2.4 ± 0.2	1.8 ± 0.3	2.5 ± 0.2	2.1 ± 0.2	1.8 ± 0.2	2.8 ± 0.1	5, 6, 26, 28
HD187861	4960	2.0	-2.4 ± 0.5	2.0 ± 0.2	1.9 ± 0.3	2.1 ± 0.3	1.3 ± 0.2	3.1 ± 0.3	29, 39
HD209621	4450	1.5	-2.0 ± 0.3	1.3 ± 0.3	1.8 ± 0.3	2.2 ± 0.3	1.6 ± 0.3	1.9 ± 0.3	22, 31
HD224959	5050	1.9	-2.1 ± 0.2	1.8 ± 0.2	2.2 ± 0.2	2.2 ± 0.2	1.7 ± 0.1	3.1 ± 0.2	29, 39
HE0143-0441	6305	4.0	-2.4 ± 0.2	2.0 ± 0.2	2.4 ± 0.2	2.0 ± 0.2	1.7 ± 0.2	3.4 ± 0.3	13, 14
HE0243-3044	5400	3.2	-2.6 ± 0.2	2.4 ± 0.3	2.0 ± 0.2	2.5 ± 0.2	2.0 ± 0.2	3.1 ± 0.2	23
HE0336+0113	5700	3.5	-2.8 ± 0.3	2.5 ± 0.1	2.6 ± 0.3	2.0 ± 0.2	1.3 ± 0.2	< 2.3	14, 15
HE0338-3945	6161	4.1	-2.5 ± 0.2	2.1 ± 0.2	2.4 ± 0.2	2.3 ± 0.2	2.0 ± 0.2	3.0 ± 0.1	10, 27
HE0414-0343	4863	1.2	-2.3 ± 0.1	1.4 ± 0.3	1.9 ± 0.1	1.6 ± 0.1	1.3 ± 0.3	2.3 ± 0.1	24
HE1305+0007	4655	1.5	-2.2 ± 0.3	2.1 ± 0.4	2.6 ± 0.5	2.8 ± 0.3	2.2 ± 0.3	2.6 ± 0.3	11, 21
HE1405-0822	5220	1.7	-2.4 ± 0.1	1.9 ± 0.1	2.0 ± 0.2	1.5 ± 0.2	1.6 ± 0.2	2.3 ± 0.2	16
HE2148-1247	6380	3.9	-2.4 ± 0.2	2.0 ± 0.2	2.4 ± 0.1	2.3 ± 0.2	2.0 ± 0.1	3.1 ± 0.2	12
HE2258-6358	4900	1.6	-2.7 ± 0.1	2.4 ± 0.1	2.3 ± 0.1	1.9 ± 0.1	1.7 ± 0.1	2.6 ± 0.5	34
LP625-44	5500	2.6	-2.8 ± 0.3	2.3 ± 0.2	2.8 ± 0.2	2.6 ± 0.3	1.9 ± 0.3	2.6 ± 0.2	2, 3, 5, 6, 33
post-AGB stars									
IRAS07134+1005	7250	0.5	-0.9 ± 0.2	1.1 ± 0.2	1.8 ± 0.3	1.8 ± 0.2	0.6 ± 0.3	< 1.7	20
IRAS22272+5435	5750	0.5	-0.8 ± 0.1	1.0 ± 0.1	...	2.2 ± 0.1	1.1 ± 0.1	< 1.4	20
J004441.04-732136.4	6250	0.5	-1.3 ± 0.3	1.6 ± 0.4	...	2.7 ± 0.3	1.9 ± 0.2	< 2.3	17, 18
J050632.10-714229.8	6750	0.0	-1.2 ± 0.2	1.1 ± 0.1	1.2 ± 0.3	1.4 ± 0.2	0.5 ± 0.3	< 1.2	18, 38
J051848.86-700246.9	6000	0.5	-1.0 ± 0.1	1.1 ± 0.2	...	2.4 ± 0.2	1.3 ± 0.2	< 1.6	19
J052043.86-692341.0	5750	0.0	-1.1 ± 0.2	1.2 ± 0.2	...	1.9 ± 0.2	1.2 ± 0.2	< 1.1	18, 38
J053250.69-713925.8	5500	0.0	-1.2 ± 0.1	1.5 ± 0.2	...	1.9 ± 0.3	1.1 ± 0.2	< 1.4	18, 38

(1) Allen et al. 2012; (2) Aoki et al. 2000; (3) Aoki et al. 2001; (4) Aoki et al. 2002a; (5) Aoki et al. 2002b; (6) Aoki et al. 2006; (7) Aoki et al. 2007; (8) Aoki et al. 2008; (9) Barbuy et al. 2005; (10) Barklem et al. 2005; (11) Beers et al. 2007; (12) Cohen et al. 2003; (13) Cohen et al. 2004; (14) Cohen et al. 2006; (15) Cohen et al. 2013; (16) Cui et al. 2013; (17) De Smedt et al. 2012; (18) De Smedt et al. 2014; (19) De Smedt et al. 2015; (20) De Smedt et al. 2016; (21) Goswami et al. 2006; (22) Goswami & Aoki 2010; (23) Hansen et al. 2015; (24) Hollek et al. 2015; (25) Ivans et al. 2005; (26) Johnson & Bolte 2004; (27) Jonsell et al. 2006; (28) Lai et al. 2007; (29) Masseron et al. 2010; (30) Masseron et al. 2012; (31) Matrozis et al. 2012; (32) McWilliam et al. 1995; (33) Norris et al. 1997; (34) Placco et al. 2013; (35) Roederer et al. 2014; (36) Sivarani et al. 2004; (37) Sneden et al. 2003; (38) van Aarle et al. 2013; (39) van Eck et al. 2003.

Table 2.2: Fit parameters for each star: number of observed elements $N_{\rm obs}$ the fit is based on, neutron density n in cm^{-3} as found in this work and in Paper I for comparison, time t in seconds, integrated neutron exposure τ in mbarn^{-1}, dilution parameter d, and minimum χ^2.

ID	$N_{\rm obs}$	$\log(n)$ this work	$\log(n)$ Paper I	t (s)	τ (mbarn^{-1})	d	χ^2
CEMP-i stars							
BS16080-175	7	11	12	1.2×10^8	1.9	0.996	39.4
BS17436-058	4	13	13	1.5×10^6	2.4	0.996	0.6
CS22183-015	9	13		1.7×10^6	2.7	0.999	3.7
CS22887-048	7	13		7.6×10^6	12.0	0.983	4.1
CS22898-027	12	13	14	1.5×10^6	2.4	0.993	2.1
CS22948-027	10	13	13	1.3×10^6	2.0	0.996	10.8
CS29497-030	17	14	14	1.5×10^6	23.2	0.998	8.7
CS29497-034	10	12		1.2×10^7	1.9	0.999	30.3
CS29526-110	8	13	14	2.2×10^6	3.4	0.993	3.9
CS31062-012	8	14	14	1.9×10^5	3.0	0.999	1.3
CS31062-050	22	14	15	2.1×10^5	3.4	0.997	11.9
HD187861	9	11	12	1.6×10^8	2.5	0.996	2.2
HD209621	16	13		1.2×10^6	1.8	0.994	21.8
HD224959	9	13	13	1.9×10^6	3.0	0.992	1.1
HE0143-0441	9	12	14	1.7×10^7	2.7	0.992	5.9
HE0243-3044	14	13		1.7×10^6	2.7	0.997	22.6
HE0336+0113	7	11		6.7×10^7	1.1	0.997	7.91
HE0338-3945	17	13	14	1.5×10^6	2.4	0.995	10.5
HE0414-0343	14	14		1.9×10^5	3.0	0.999	12.0
HE1305+0007	11	14	14	1.5×10^5	2.4	0.980	6.6
HE1405-0822	19	13		1.5×10^6	2.4	0.999	54.4
HE2148-1247	13	13	14	1.5×10^6	2.4	0.993	6.2
HE2258-6358	18	15	14	4.9×10^4	7.7	0.998	28.8
LP625-44	17	13	14	1.3×10^6	2.0	0.997	4.2
post-AGB stars							
IRAS07134	14	11		6.3×10^7	1.0	0.984	7.7
IRAS22272	15	11		7.2×10^7	1.1	0.979	35.7
J004441	15	11		7.6×10^7	1.2	0.978	6.6
J050632	11	11		6.0×10^7	0.9	0.995	16.1
J051848	14	12		8.2×10^6	1.3	0.982	33.9
J052043	14	12		7.3×10^6	1.1	0.985	22.1
J053250	12	12		8.2×10^6	1.3	0.993	9.5

2.A Appendix: All fits – CEMP-i stars

This section shows the best fitting models for each of the CEMP-i stars that are not shown in section §2.5.1 in comparison to the observed abundance patterns in Figures 2.9 to 2.27. Details of each best fit (neutron density n and time-integrated neutron exposure τ) are shown in the right corner of the plots. For some stars two models at different neutron densities result in similarly good fits with their respective χ^2 values varying by less than 10%, in which case we provide both fits and χ^2 values (see also discussions in section §2.5). The lower panel shows the distribution of the residuals. The uncertainty of the observations $\sigma_{Z,obs}$ is indicated by errorbars in the upper panel and by the shaded region in the lower panel. The vertical lines show the location of Sr, Ba and Eu which are representatives of the ls and hs peak as well as the r process, respectively. For comparison the best fit from Abate et al. (2015b) is shown if available, which shows the result of binary evolution and AGB nucleosynthesis. We refer the reader to the corresponding figures of Bisterzo et al. (2012) for comparison to s-process models with initial r-process enhancement.

2.B Appendix: All fits – post-AGB stars

This section shows the best fitting models for each of the 7 post-AGB stars in comparison to the observed abundance patterns in Figures 2.28 to 2.34. As in Appendix 2.A, details of each best fit (neutron density n and time-integrated neutron exposure τ) are shown in the right corner of the plots. The lower panel shows the distribution of the residuals. The uncertainty of the observations $\sigma_{Z,obs}$ is indicated by errorbars in the upper panel and by the shaded region in the lower panel. The vertical lines show the location of Sr, Ba and Eu which are representatives of the ls and hs peak as well as the r process, respectively. For comparison the fits of pocket case 3 and 4 from Lugaro et al. (2015) are shown if available. These fits show the result of AGB nucleosynthesis with modified ^{13}C pockets to not overproduce the upper limit of the Pb abundance.

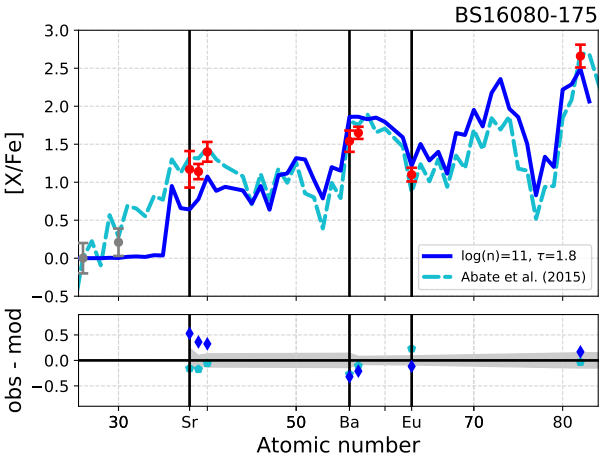

Figure 2.9: Best fitting model for CEMP-i star BS16080-175 compared to the best fit of s-process nucleosynthesis with binary evolution of Abate et al. (2015b). The best fitting s-process models with initial r-process enhancement can be found in Fig. 5 of Bisterzo et al. (2012).

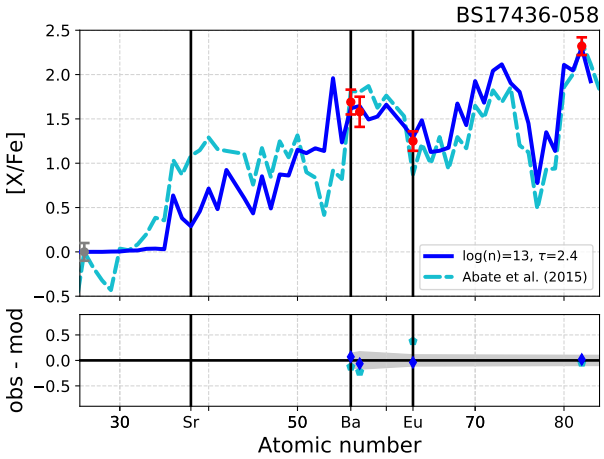

Figure 2.10: Best fitting model for CEMP-i star BS17436-058 compared to the best fit of s-process nucleosynthesis with binary evolution of Abate et al. (2015b). The best fitting s-process models with initial r-process enhancement can be found in Fig. 16 of Bisterzo et al. (2012).

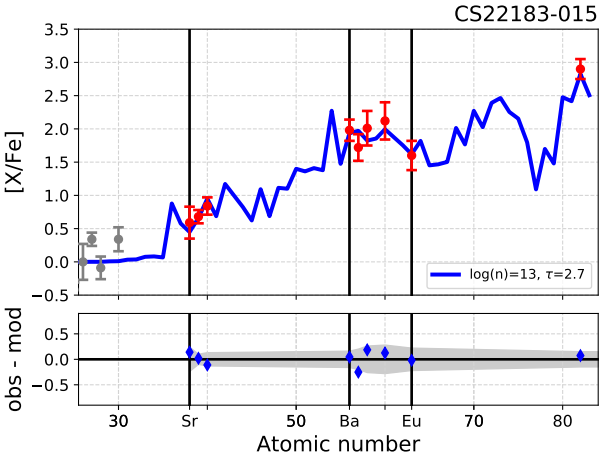

Figure 2.11: Best fitting model for CEMP-i star CS22183-015. The best fitting s-process models with initial r-process enhancement can be found in Fig. 32 of Bisterzo et al. (2012).

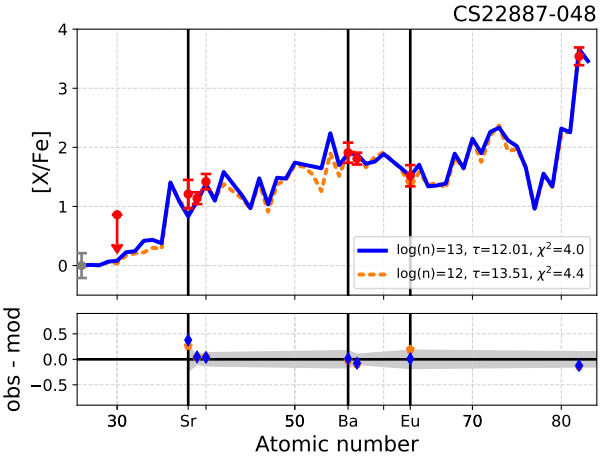

Figure 2.12: Best fitting models for CEMP-i star CS22887-048. The best fitting s-process models with initial r-process enhancement can be found in Fig. 36 of Bisterzo et al. (2012).

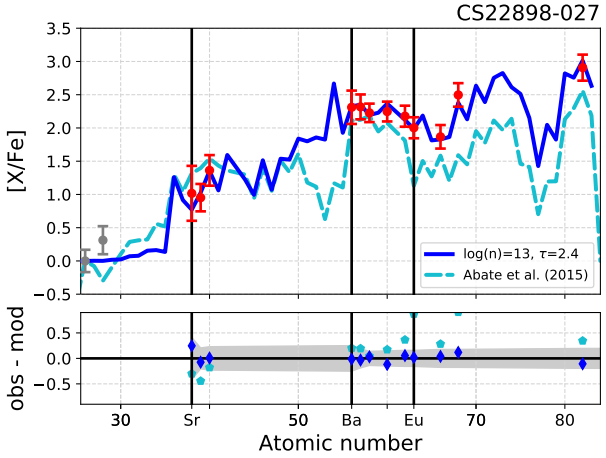

Figure 2.13: Best fitting model for CEMP-i star CS22898-027 compared to the best fit of s-process nucleosynthesis with binary evolution of Abate et al. (2015b). The best fitting s-process models with initial r-process enhancement can be found in Fig. 17 of Bisterzo et al. (2012).

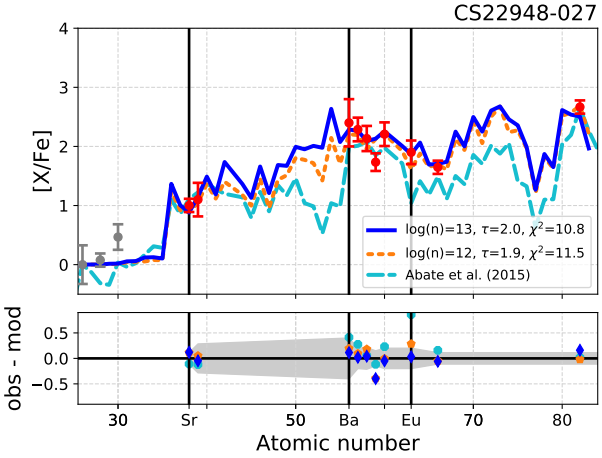

Figure 2.14: Best fitting models for CEMP-i star CS22948-027 compared to the best fit of s-process nucleosynthesis with binary evolution of Abate et al. (2015b). The best fitting s-process models with initial r-process enhancement can be found in Fig. 27 of Bisterzo et al. (2012).

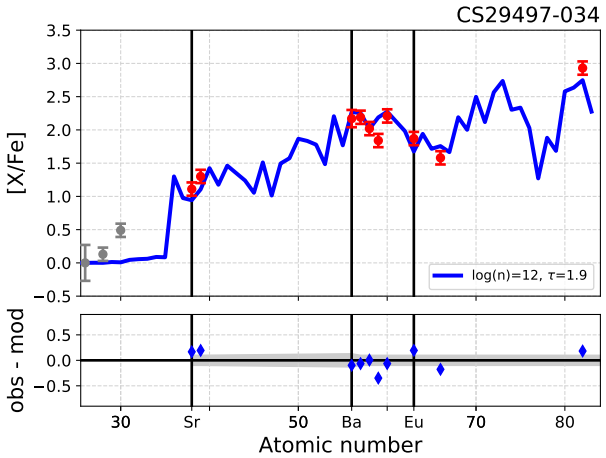

Figure 2.15: Best fitting model for CEMP-i star CS29497-034. The best fitting s-process models with initial r-process enhancement can be found in Fig. 24 of Bisterzo et al. (2012).

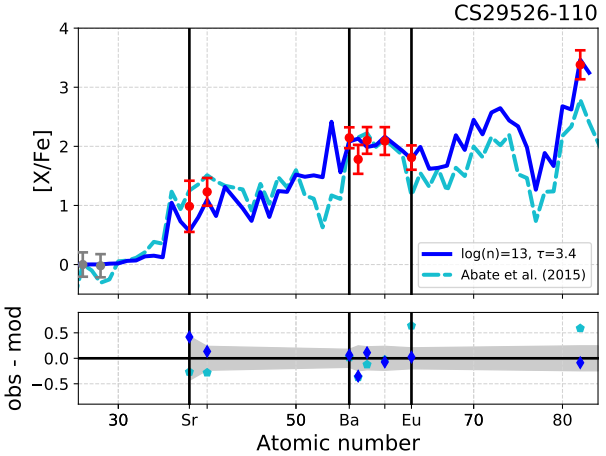

Figure 2.16: Best fitting model for CEMP-i star CS29526-110 compared to the best fit of s-process nucleosynthesis with binary evolution of Abate et al. (2015b). The best fitting s-process models with initial r-process enhancement can be found in Fig. 23 of Bisterzo et al. (2012).

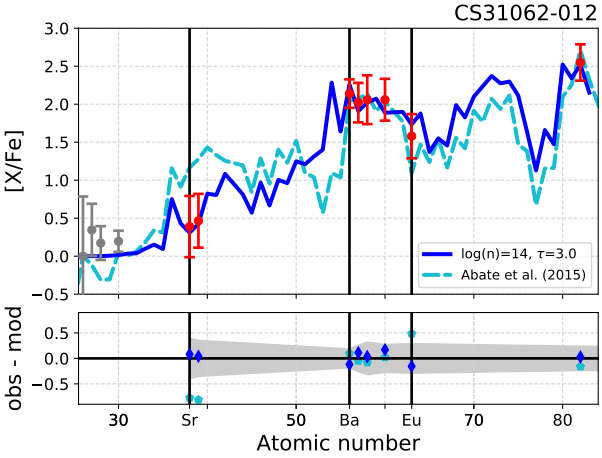

Figure 2.17: Best fitting model for CEMP-i star CS31062-012 compared to the best fit of s-process nucleosynthesis with binary evolution of Abate et al. (2015b). The best fitting s-process models with initial r-process enhancement can be found in Fig. 24 of Bisterzo et al. (2012).

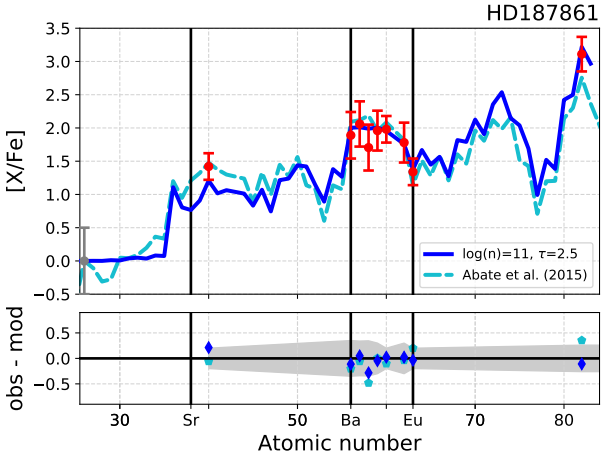

Figure 2.18: Best fitting model for CEMP-i star HD187861 compared to the best fit of s-process nucleosynthesis with binary evolution of Abate et al. (2015b). The best fitting s-process models with initial r-process enhancement can be found in Fig. 29 of Bisterzo et al. (2012).

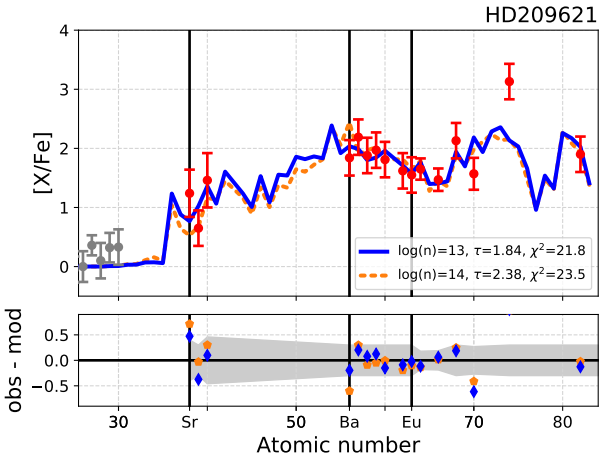

Figure 2.19: Best fitting models for CEMP-i star HD209621. The best fitting s-process models with initial r-process enhancement can be found in Fig. 35 of Bisterzo et al. (2012).

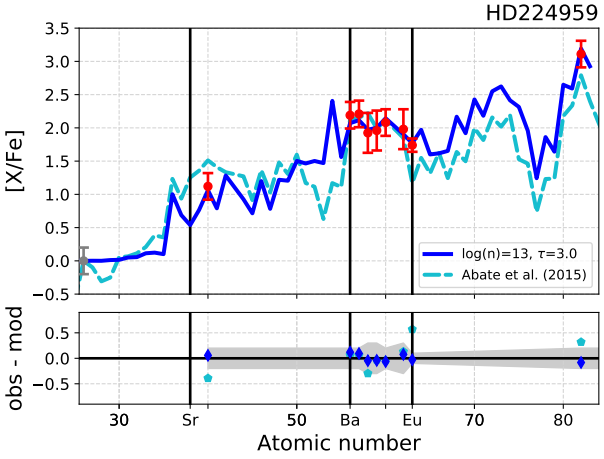

Figure 2.20: Best fitting model for CEMP-i star HD224959 compared to the best fit of s-process nucleosynthesis with binary evolution of Abate et al. (2015b). The best fitting s-process models with initial r-process enhancement can be found in Fig. 30 of Bisterzo et al. (2012).

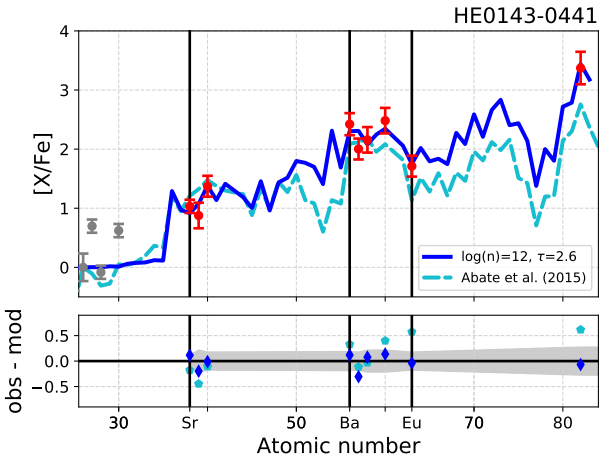

Figure 2.21: Best fitting model for CEMP-i star HE0143-0441 compared to the best fit of s-process nucleosynthesis with binary evolution of Abate et al. (2015b). The best fitting s-process models with initial r-process enhancement can be found in Fig. 33 of Bisterzo et al. (2012).

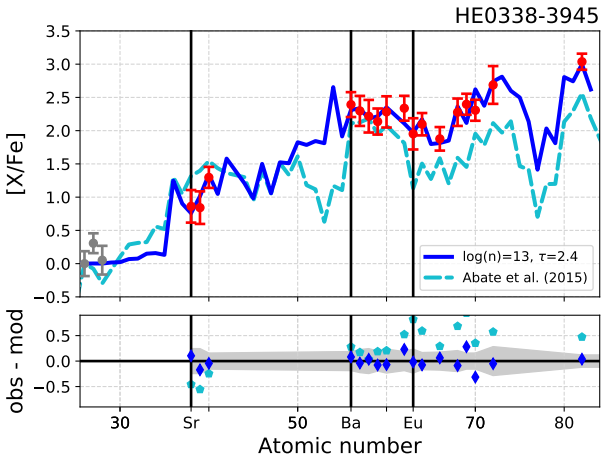

Figure 2.22: Best fitting model for CEMP-i star HE0338-3945 compared to the best fit of s-process nucleosynthesis with binary evolution of Abate et al. (2015b). The best fitting s-process models with initial r-process enhancement can be found in Fig. 19 of Bisterzo et al. (2012).

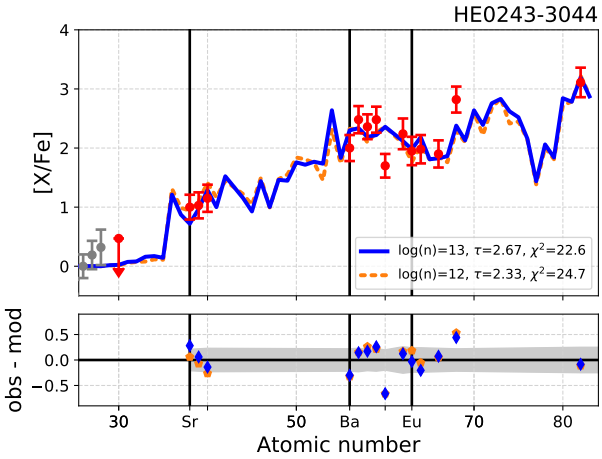

Figure 2.23: Best fitting models for CEMP-i star HE0243-3044.

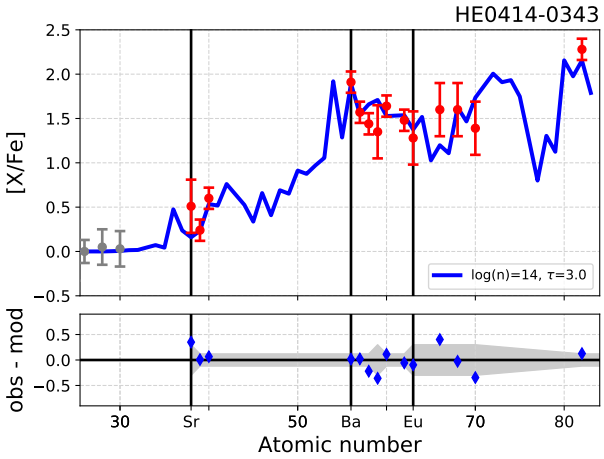

Figure 2.24: Best fitting model for CEMP-i star HE0414-0343.

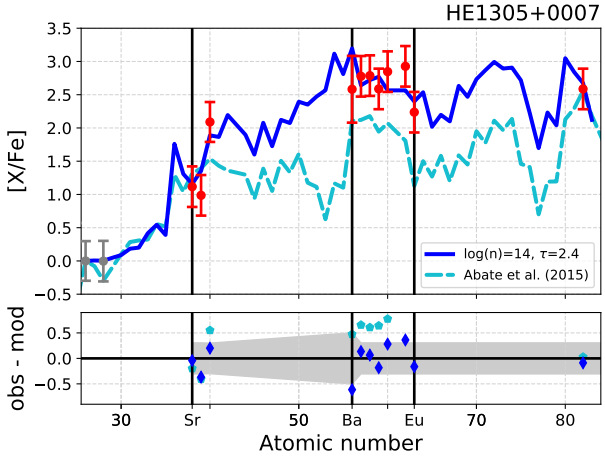

Figure 2.25: Best fitting model for CEMP-i star HE1305+0007 compared to the best fit of s-process nucleosynthesis with binary evolution of Abate et al. (2015b). The best fitting s-process models with initial r-process enhancement can be found in Fig. 22 of Bisterzo et al. (2012).

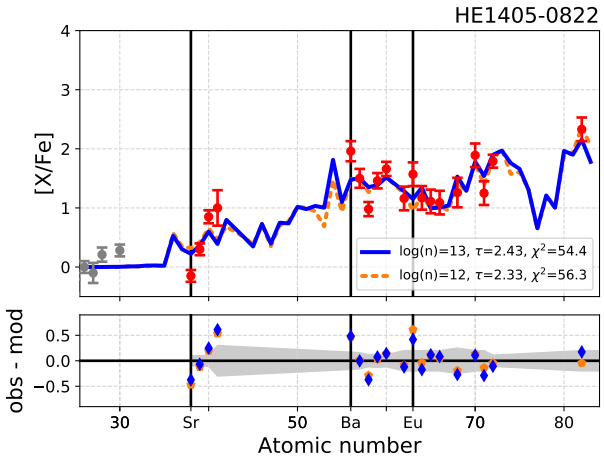

Figure 2.26: Best fitting models for CEMP-i star HE1405-0822.

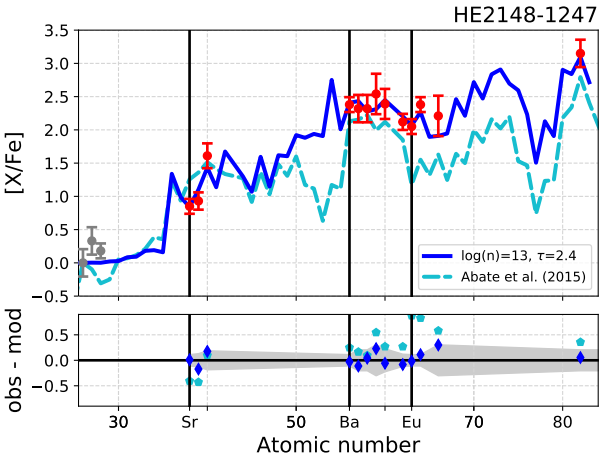

Figure 2.27: Best fitting model for CEMP-i star HE2148-1247 compared to the best fit of s-process nucleosynthesis with binary evolution of Abate et al. (2015b). The best fitting s-process models with initial r-process enhancement can be found in Fig. 21 of Bisterzo et al. (2012).

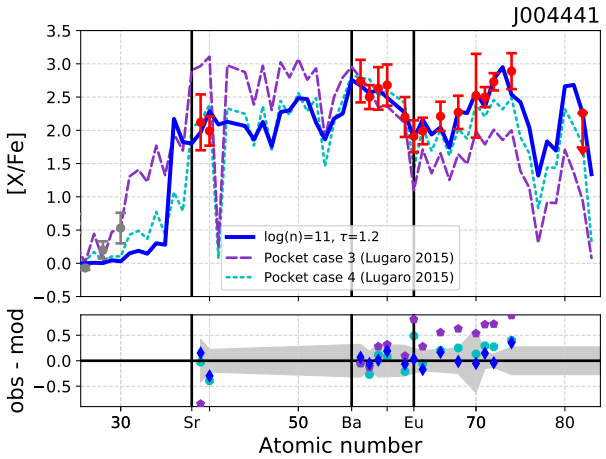

Figure 2.28: Best fitting model for post-AGB star J004441. The dashed and dotted lines show the fits of pocket case 3 and 4 from Lugaro et al. (2015), which represent AGB nucleosynthesis with modified ^{13}C pockets.

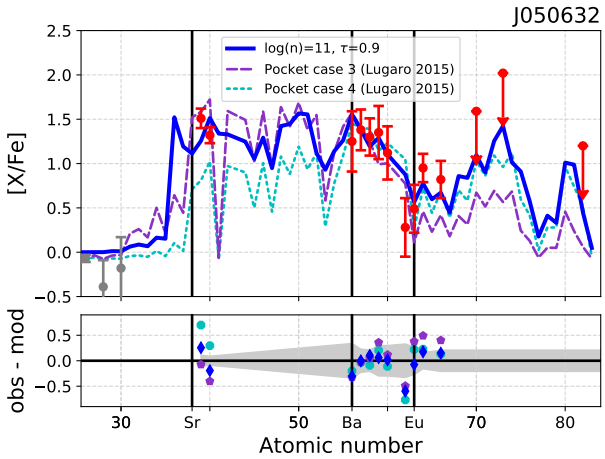

Figure 2.29: Best fitting model for post-AGB star J050632. The dashed and dotted lines show the fits of pocket case 3 and 4 from Lugaro et al. (2015), which represent AGB nucleosynthesis with modified ^{13}C pockets.

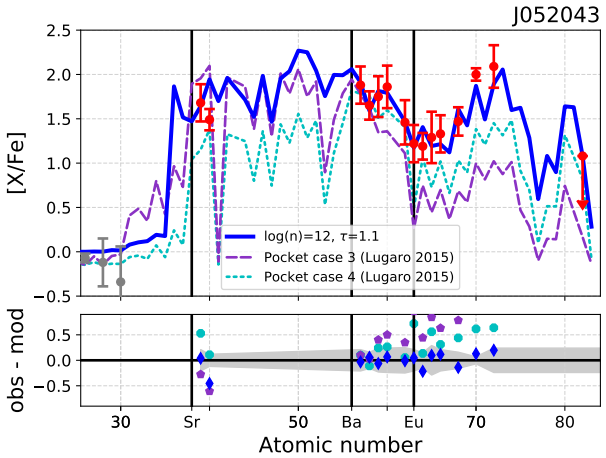

Figure 2.30: Best fitting model for post-AGB star J052043. The dashed and dotted lines show the fits of pocket case 3 and 4 from Lugaro et al. (2015), which represent AGB nucleosynthesis with modified ^{13}C pockets.

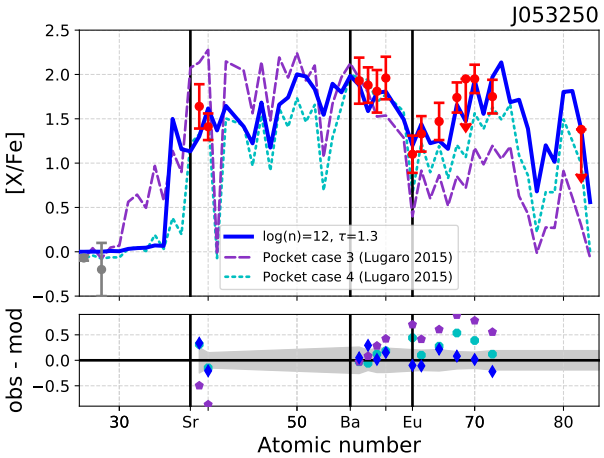

Figure 2.31: Best fitting model for post-AGB star J053250. The dashed and dotted lines show the fits of pocket case 3 and 4 from Lugaro et al. (2015), which represent AGB nucleosynthesis with modified ^{13}C pockets.

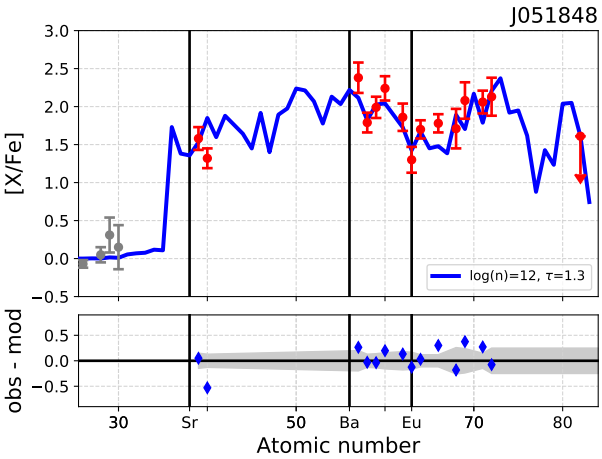

Figure 2.32: Best fitting model for post-AGB star J051848.

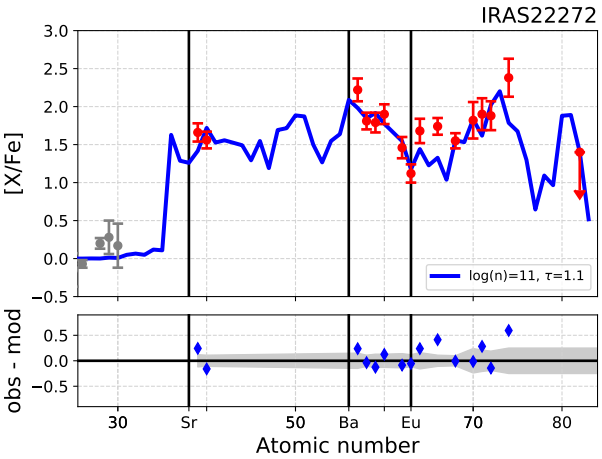

Figure 2.33: Best fitting model for post-AGB star IRAS22272.

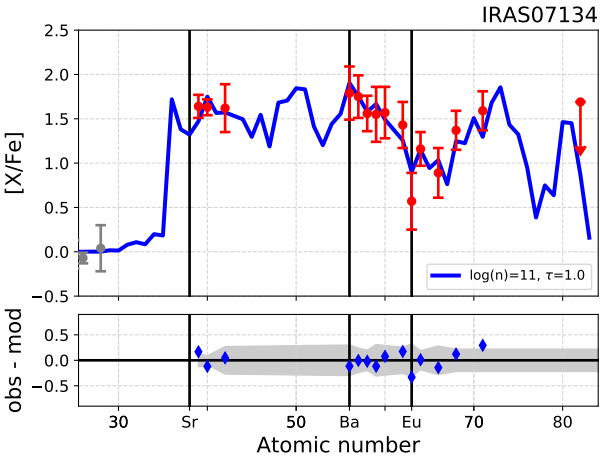

Figure 2.34: Best fitting model for post-AGB star IRAS07134.

> *There's something really beautiful about science, that human beings can ask these questions and can answer them. You can make models of nature and understand how it works.*
>
> — Margaret Geller

Chapter 3

Low proton fractions required for i-process nucleosynthesis in ingestion episodes

M. Hampel, A. I. Karakas, R. J. Stancliffe, S.W. Campbell, B. S. Meyer, M. Lugaro

not submitted

Abstract

The intermediate (i) neutron-capture process has been shown to create distinct heavy element patterns in nature. The site of the i process is unclear, although likely associated with proton-ingestion episodes (PIEs) into helium core- or shell-burning environments. We investigate how free neutrons for the i process are produced in a PIE. To constrain the conditions that lead to i-process nucleosynthesis we study the impact of differing amounts of ingested protons on the nuclear reaction chains responsible for releasing and recycling neutrons. To bridge current discrepancies between single-zone models with 1D stellar-evolution and full 3D hydrodynamic simulations we develop a single-zone model that uses a variable temperature and density trajectory from a 1D stellar-evolution model of a PIE in a low-mass, low-metallicity AGB star. Only proton fractions less than a few times 10^{-3} lead to neutron production high enough to result in i-process nucleosynthesis. Proton-capture reactions onto ^{13}N and ^{13}C compete with the production of ^{13}C, leading to a suppression of neutron production at higher proton fractions. Our results disagree with previous calculations where high proton fractions ≥ 0.1 are required in single-zone calculations for i-process nucleosynthesis. We find that much lower ingested proton fractions are suitable, in-line with more realistic simulations of PIEs. This result reinforces the value of computationally inexpensive single-zone calculations as a powerful complementary tool to study the i process.

3.1 Introduction

The intermediate neutron capture process (i process; Cowan & Rose, 1977; Malaney, 1986) operates at neutron densities of $n \approx 10^{12}$ to $10^{16}\,\mathrm{cm}^{-3}$, which are intermediate between those of the slow (s) and rapid (r) neutron-capture processes. The i process creates unique abundance patterns of the elements heavier than Fe observed in stars, such as carbon-enhanced metal-poor (CEMP) stars with abundance enhancements in typical s- and r-process elements (CEMP-i stars, Dardelet et al., 2014; Hampel et al., 2016; Denissenkov et al., 2019; Hampel et al., 2019; Karinkuzhi et al., 2021). Post-AGB stars such as Sakurai's Object and the Pb-deficient stars in the Magellanic Clouds may also be the result of an i-process (Herwig et al., 2011; Hampel et al., 2019).

The exact site(s) in which this nucleosynthetic process occurs is currently uncertain. The most likely sites are proton-ingestion episodes (PIEs), which occur when hydrogen is ingested into convective regions driven by He burning (e.g., Fujimoto et al., 1990). Potential astrophysical objects where PIEs can occur are low-mass, low-metallicity asymptotic giant branch (AGB) stars (Cristallo et al., 2009; Stancliffe et al., 2011), core He flashes in low-metallicity low-mass stars (Fujimoto et al., 1990; Campbell & Lattanzio, 2008; Campbell et al., 2010; Cruz et al., 2013), very late thermal pulses (Herwig et al., 2011), super-AGB stars (Doherty et al., 2015; Jones et al., 2016), rapidly-accreting white dwarfs (Denissenkov et al., 2017, 2019), and metal-poor massive stars (Clarkson et al., 2018; Banerjee et al., 2018). The result of a PIE is a complex convective-reactive event that involves the interplay between convective mixing, nuclear reactions, and the feedback from the burning onto the mixing flows and stellar structure itself—all on similar time scales. It has been recognised that 1D stellar codes alone are not well suited for simulating these events, since they rely on simplified descriptions of convection and mixing. Moreover, although PIEs are inherently 3D phenomena and progress has been made to understand their details using 3D hydrodynamic simulations, it is not yet computationally feasible to follow their full duration, especially with an i-process nuclear network (e.g., Mocák et al., 2010; Herwig et al., 2011; Stancliffe et al., 2011; Woodward et al., 2015). Therefore, it is beneficial to use computationally inexpensive single-zone nuclear network calculations as a bridge between observed i-process patterns and the underlying full 3D hydrodynamic picture. This offers the advantage of exploring a range of physical conditions in parametric studies to improve the constraints on the physical environments.

Single-zone nuclear network calculations of the i process have been successful at reproducing observed heavy-element patterns, however, they rely on simplifications to achieve the required high neutron densities. Either constant neutron densities are imposed manually (Hampel et al., 2016, 2019) or very high initial proton fractions[1] of $X_0(\mathrm{H}) \gtrsim 0.1$ are adopted to ensure neutron production (Dardelet et al., 2014; Denissenkov et al., 2018; McKay et al., 2020). Proton fractions of $X_0(\mathrm{H}) \gtrsim 0.1$ are much higher than those encountered in more realistic 1D or 3D multi-zone simulations, which typically result in ingestion of around $X_0(\mathrm{H}) \approx 10^{-4}$ or less, depending on the specifics of the simulations and stellar sites (Campbell et al., 2010; Stancliffe et al., 2011; Woodward et al., 2015).

When hydrogen-rich material is ingested into regions rich in He and C, the reaction chain $^{12}\mathrm{C}(\mathrm{p},\gamma)^{13}\mathrm{N}(\beta^+\nu)^{13}\mathrm{C}(\alpha,\mathrm{n})^{16}\mathrm{O}$ leads to production of neutrons. During the formation of the

[1] We use $X_0(\mathrm{H})$ to refer to the initial mass fraction of hydrogen throughout this chapter, as well as for the following chapters of this thesis.

"^{13}C pocket" in AGB stars (Karakas & Lattanzio, 2014), for example, these reactions are activated at temperatures around 40 MK. In contrast, the convective conditions of PIEs provide higher temperatures, which can exceed 200 MK at the bottom of the He-shell driven convective regions of AGB stars (hereafter intershell) and lead to a more rapid production of neutrons therefore reaching the i-process neutron densities. As a consequence of the higher temperatures, competing charged-particle reactions occur, particularly proton-capture reactions typical of the usual CNO and hot CNO cycle, such as ^{13}N(p, γ)^{14}O($\beta^+\nu$)^{14}N and ^{13}C(p, γ)^{14}N (e.g., Jorissen & Arnould, 1989). These reactions can interrupt the neutron-producing reaction chain and instead produce the neutron poison ^{14}N reducing the number of free neutrons for heavy element nucleosynthesis. Although the proton fractions in PIEs are too low for complete hot CNO cycling, the reaction chains indicated above are of importance to neutron production for the i process and their effects have to be included in the calculations. Furthermore, it is crucial to understand the delicate balance of the reactions that lead to i-process conditions if we are also to predict the abundance pattern of light elements such as C, N and O.

Here we present nuclear network calculations to investigate how free neutrons for the i process are released in PIEs. To bridge the divide between the results of 3D models and single-zone simulations, we develop a single-zone model with a variable temperature and density trajectory from a 1D stellar evolution model of a low-mass, low-metallicity AGB star that experiences PIEs. We study the reaction chains that lead to neutron production to constrain the proton fractions in PIEs that produce observed i-process heavy-element patterns. In particular, we investigate how varying amounts of ingested protons in PIEs affect the neutron density, the total integrated neutron exposure, and the formation of the heavy elements.

3.2 Method and code

We perform single-zone nuclear-network calculations with the *NucNet Tools* code (Meyer, 2012). The code and its inputs were previously described in Hampel et al. (2016, 2019). Here we use updated reaction rates provided by the default set from the JINA Reaclib database[2] (Cyburt et al., 2010).

Reactions of importance for the neutron production leading to the i process occur at different depths throughout the intershell, where temperature and density increase continuously with depth. This change in physical conditions results in variations of nuclear reaction rates throughout the convective region. Moreover, the abundance of protons changes throughout the convective region, where the mass fraction of ingested protons is highest at the top of the intershell and decreases as the protons burn while being mixed downwards. Particularly for the production of the neutron source ^{13}C as well as the neutron poison ^{14}N it is important to take this gradual change of the the physical conditions and the proton abundance into account. However, the release of neutrons for the i process via the ^{13}C(α, n)^{16}O reaction requires high temperatures to be activated and only occurs in a thin region at the bottom of the convective zone.

[2]The current JINA Reaclib default set now uses the *ka02* rates instead of *kd02*. As discussed in Hampel et al. (2016) some reactions with the label *kd02* underpredict crucial i-process neutron-capture rates at the temperatures relevant for nucleosynthesis in the He convective region, and the *ka02* reactions are more suitable for our investigation.

Single-zone nuclear-network calculations can only simulate the physical processes in stellar interiors by adopting a variety of simplifying assumptions. In particular, the effects of convective mixing are not accounted for in a single-zone simulation framework. Previous single-zone nuclear-network calculations of i-process nucleosynthesis use further simplifying assumptions of a constant temperature and density (Bertolli et al., 2013; Dardelet et al., 2014; Hampel et al., 2016; Denissenkov et al., 2018; Hampel et al., 2019; McKay et al., 2020; Denissenkov et al., 2021). The physical conditions correspond to those at the bottom of the convective intershell where the produced neutron densities are the highest. The required high i-process neutron densities are then achieved through further simplifications: Hampel et al. (2016, 2019) and Denissenkov et al. (2021) impose constant neutron densities up to $n = 10^{15}\,\mathrm{cm}^{-3}$ manually. While it is plausible that the lowermost zone in the convective region effectively gets exposed to approximately constant neutron densities, this approach does not take into account how and under which conditions the high neutron densities must first be produced. Moreover, this approach can only sensibly predict the abundance patterns of heavy elements because these are almost exclusively produced by neutron-capture reactions. However, the abundances of light elements, such as the CNO nuclei which constitute a much larger fraction of the mass, are significantly influenced by the charged-particle reactions, which lead to the production of neutrons in the first place. Therefore, this approach of simulating i-process nucleosynthesis with constant neutron densities cannot be used to study the abundance evolution of light elements.

An alternative approach used in single-zone studies (e.g., Bertolli et al., 2013; Dardelet et al., 2014; Denissenkov et al., 2018; McKay et al., 2020) injects large fractions of protons of $X_0(\mathrm{H}) \gtrsim 0.1$ directly into the lowermost zone at the bottom of the convective regions at $T \approx 200\,\mathrm{MK}$. This leads to conditions where unnaturally high amounts of protons react at very high temperatures, which are not usually encountered in typical hydrogen-burning environments. Recent insights from Denissenkov et al. (2021) clarify that this approach cannot self-consistently produce i-process neutron densities and instead the production of sufficiently high amounts of the neutron source ^{13}C has to be ensured by manual alterations of the nuclear-reaction network.

It becomes clear that the current methods to study i-process nucleosynthesis with single-zone simulations may be useful to study i-process heavy-element production with large nuclear-reaction networks in a computationally inexpensive way, yet they cannot account for self-consistent production of neutrons through charged-particle reactions of light elements. To improve the current single-zone simulations we propose a two-phase approach that combines aspects of both previous approaches to allow for a more realistic treatment of the neutron production and i-process nucleosynthesis.

One main assumption that remains from the previous approaches is that the region in the intershell where the i process produces heavy elements can be described by a single zone at the bottom of the convective intershell with a constant temperature and density. While this assumptions is not entirely accurate and the heavy-element production may in reality occur in a somewhat spatially-extended region, the steep temperature-dependence of the $^{13}\mathrm{C}(\alpha,\mathrm{n})^{16}\mathrm{O}$ reaction rate justifies the simplification that the produced neutron density is highest at the bottom of the intershell and that the dominant i-process abundance pattern is produced here. However, the heavy-element nucleosynthesis only constitutes the second phase of our two-phase method and we aim at determining the detailed isotopic composition of the i-process zone, including the production of ^{13}C, ^{14}N and neutrons, self-consistently in the first phase.

Figure 3.1 schematically shows the stages of our two-phase approach. Here we incorporate a gradual temperature and density increase for the first phase, which allows us to focus on the charged-particle reactions and ^{13}C production, where subsequent nuclear reactions occur under increasingly hotter and denser conditions. This first phase determines the composition, and particularly the abundances of the CNO isotopes, of the material from which neutrons then can be released in the second phase. To focus on the release of the neutrons and the i-process nucleosynthesis, we then move our attention to the thin layer at the bottom of the convective zone, where the highest temperatures are encountered and the highest neutron densities are produced.

To simulate this first phase and focus on the temperature-dependent proton-capture reactions, we construct a temperature and density trajectory from the stellar structure model of Stancliffe et al. (2011) at the point of the evolution of a $1\,M_\odot$ star with a metallicity of $Z = 10^{-4}$ in its second thermal pulse when it experiences a PIE. In our single-zone setup we consider a parcel of material at the top of the intershell and calculate how it moves inwards with a convective velocity taken from the stellar model. The trajectory covers temperatures between 30 and 230 MK, and densities between 84 and $3900\,\mathrm{g\,cm^{-3}}$ over a time period of $t = 13500\,\mathrm{s}$. The detailed trajectory is shown in Appendix 3.A. This period covers the phase of light-element nucleosynthesis when protons are ingested and get captured to produce ^{13}C as well as by-products such as ^{14}N.

After following our parcel of material down through the convective region and tracking the nucleosynthesis it experiences, we shift our attention to the second phase of the neutron production in which the formed ^{13}C captures the abundant α particles and releases neutrons leading to i-process heavy-element production. Once our parcel of material reaches the bottom of the intershell we use its composition as a representative initial composition for our i-process nucleosynthesis, which occurs almost exclusively in a single zone at the bottom of the intershell. To focus our i-process calculations on the very bottom region of the convective zone we keep the temperature and density constant and can thereby track the neutron densities that can be reached in this thin, hot layer of the star. Once the neutrons are released in this layer, the i-process neutron-capture reactions themselves have only weak temperature dependencies.

For the start of the proton-ingestion episode, we choose initial abundances that are typical for the intershell composition of our low-metallicity AGB model. In particular, the abundances for the key species are $X\left(^4\mathrm{He}\right) = 0.77$ and $X\left(^{12}\mathrm{C}\right) = 0.22$. To mimic the ingestion of protons we set an initial value of the mass fraction of hydrogen and analyse the results obtained by models calculated with different values in the range of $10^{-5} \leq X_0(\mathrm{H}) \leq 10^{-1}$.

3.3 Results

To highlight the basic sequence of reactions that lead to the production of neutrons, here we focus on two cases that exhibit very different behaviour: the first has an initial ingested hydrogen mass fraction of $X_0(\mathrm{H}) = 10^{-3}$ and the second $X_0(\mathrm{H}) = 10^{-2}$. The abundances of selected isotopes and their variation with time are shown in Figure 3.2. The first relevant isotope is ^{13}N, which is produced via proton captures onto the abundant ^{12}C. The rising abundance of ^{13}N is directly followed by a rise of ^{13}C as the unstable ^{13}N decays with a half life of $T_{1/2}\left(^{13}\mathrm{N}\right) = 598\,\mathrm{s}$. The short time scale of the proton captures allows ^{13}N and ^{13}C to also capture protons and produce ^{14}O and ^{14}N, respectively. In the simulation with an initial hydrogen fraction of $X_0(\mathrm{H}) = 10^{-2}$ this leads to

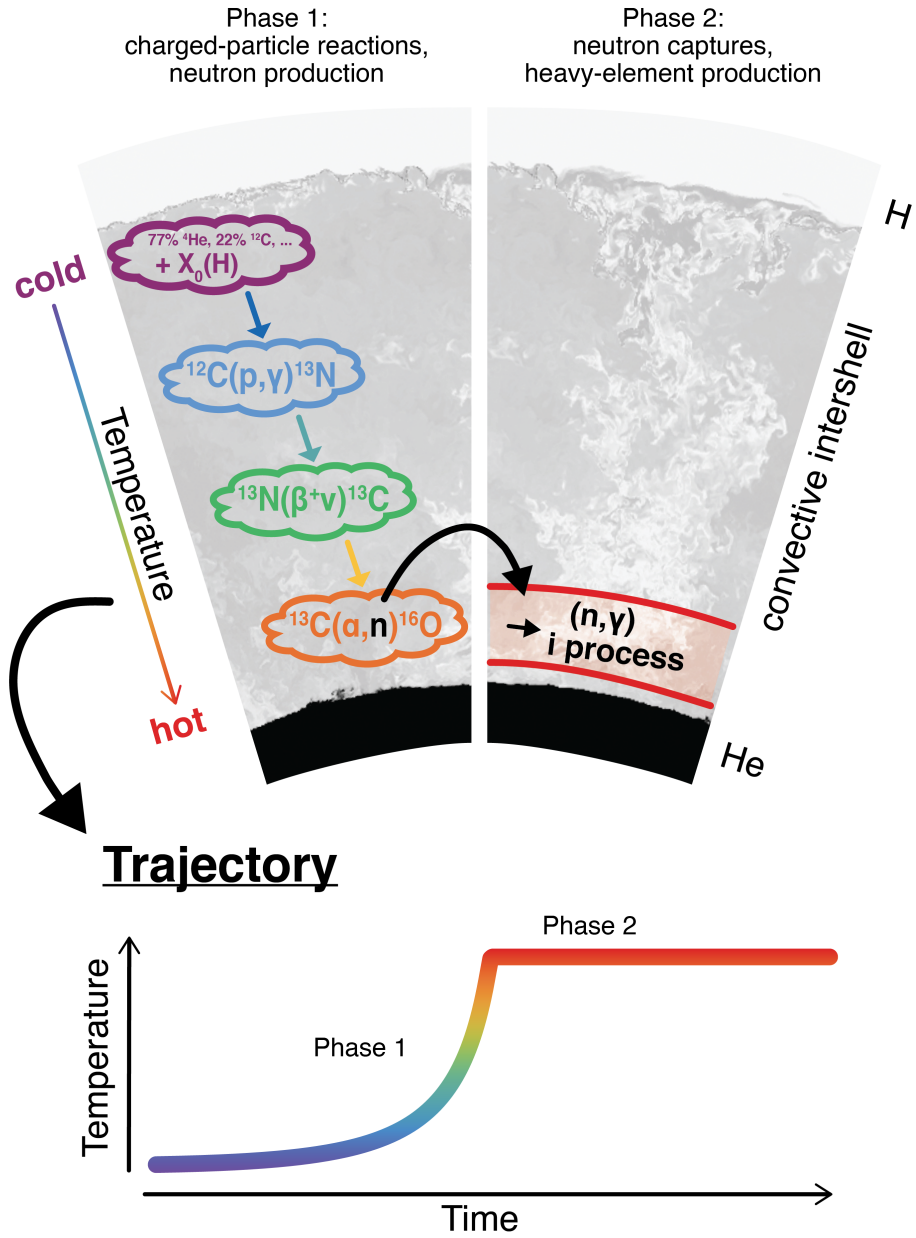

Figure 3.1: Schematic describing the two-phase approach used in this work to simulate the neutron production and i-process nucleosynthesis in a single-zone nuclear-network calculation. The upper part depicts a partial cross section of the stellar interior with the H-burning layer on the top (H) and the He-burning layer on the bottom (He) separated by the convective intershell. **Phase 1**: different reactions of the neutron-producing reaction chain occur at different depths throughout the intershell at increasing temperatures. From this a temperature (and density) trajectory can be constructed as a function of time (depicted in the lower part). In this phase the isotopic composition is calculated as initial composition for the point where neutrons are released. **Phase 2**: the i process occurs at the bottom of the convective intershell at the highest temperature (and density). The shift of focus from the neutron production (charged particle reactions in a moving convective parcel) to the i-process heavy-element nucleosynthesis (evolution of the composition of a single zone at the bottom of the intershell) is represented by the transition to a constant temperature in the trajectory.
Background image courtesy of S. W. Campbell. 2D slice of a 3D stellar hydrodynamics simulation using the PROMPI code, run on the Magnus supercomputer at the Pawsey Supercomputing Centre in Western Australia.

a significant production of ^{14}O, which reaches abundances $> 10^{-4}$ before decaying into ^{14}N with a half life $T_{1/2}\,(^{14}\mathrm{O}) = 71\,\mathrm{s}$. In the simulation with $X_0(\mathrm{H}) = 10^{-3}$, instead, the ^{14}O production is approximately 2 orders of magnitude lower.

After roughly $10^4\,\mathrm{s}$ the initially ingested proton fraction has dropped by one order of magnitude and the production of ^{14}N and ^{13}N stalls. At the time of maximum ^{13}N, the temperature of our trajectory has reached $T = 1.3 \times 10^8\,\mathrm{K}$, it then increases to $T = 2.2 \times 10^8\,\mathrm{K}$ in the next 2500 s, after which the maximum ^{13}C is reached. The increase in temperature and ^{13}C abundance leads to a rapid growth of the $^{13}\mathrm{C}(\alpha,\mathrm{n})^{16}\mathrm{O}$ reaction efficiency and results in neutron densities of $n \approx 10^{15}\,\mathrm{cm}^{-3}$ for $X_0(\mathrm{H}) = 10^{-3}$ and $n \approx 5 \times 10^{14}\,\mathrm{cm}^{-3}$ for $X_0(\mathrm{H}) = 10^{-2}$, as well as an increase in the abundance of ^{16}O in both cases.

In the simulation with $X_0(\mathrm{H}) = 10^{-3}$, the dominant neutron-capture reactions are $^{13}\mathrm{N}(\mathrm{n},\mathrm{p})^{13}\mathrm{C}$ and $^{12}\mathrm{C}(\mathrm{n},\gamma)^{13}\mathrm{C}$, which recycle neutrons back into ^{13}C from which more neutrons are subsequently produced. The released protons from the (n,p) reaction are also recycled for the most part by $^{12}\mathrm{C}(\mathrm{p},\gamma)^{13}\mathrm{N}$. There is a break-out of about 10% of the protons from this recycling, which are instead captured by ^{13}C to produce ^{14}N. This can be observed in the left panel of Figure 3.2 as a bump in the ^{14}N abundance at $t = 1.4 \times 10^4\,\mathrm{s}$. The flow of these neutron-recycling reactions outpace neutron captures by the typical neutron poison reaction $^{14}\mathrm{N}(\mathrm{n},\mathrm{p})^{14}\mathrm{C}$ by an order of magnitude. This leads to a plateau of the neutron density profile, and even a slight increase at $t \approx 3 \times 10^4\,\mathrm{s}$ as the ^{14}N abundance, and the neutron destruction, drops quicker than the abundance of ^{13}C. Finally at $t = 10^5\,\mathrm{s}$ the abundance of ^{13}C has dropped below $X\,(^{13}\mathrm{C}) < 10^{-5}$ and the neutron density below $n < 10^{12}\ \mathrm{cm}^{-3}$. This results in a total integrated i-process neutron exposure[3] of $\tau_\mathrm{i} = 4.7\,\mathrm{mbarn}^{-1}$.

The major difference in the simulation with $X_0(\mathrm{H}) = 10^{-2}$ is a larger production of ^{14}N. As a consequence, this simulation has a higher ratio of $^{14}\mathrm{N}/^{13}\mathrm{C}$, and reaches $X\,(^{14}\mathrm{N}) > X\,(^{13}\mathrm{C})$ from $t \approx 2 \times 10^4\,\mathrm{s}$ onwards. As soon as the peak neutron density is reached, the dominating neutron-capture reaction is $^{14}\mathrm{N}(\mathrm{n},\mathrm{p})^{14}\mathrm{C}$, and neutron recycling is less significant than in the simulation with $X_0(\mathrm{H}) = 10^{-3}$. In contrast, the abundance of ^{14}N is so low in the simulation with $X_0(\mathrm{H}) = 10^{-3}$ that further significant ^{14}N production is observed through break outs from neutron recycling reactions. The high level of ^{14}N in the simulation with $X_0(\mathrm{H}) = 10^{-2}$ not only leads to a lower peak neutron density but the neutron-density profile also drops faster. The i-process neutron densities of $n \geq 10^{12}\,\mathrm{cm}^{-3}$only lead to a total integrated neutron exposure of $\tau_\mathrm{i} = 1.05\ \mathrm{mbarn}^{-1}$, more than a factor 4 lower than in the simulation with $X_0(\mathrm{H}) = 10^{-3}$.

3.3.1 Neutron density trajectories and exposures

The upper panel of Figure 3.3 shows the neutron density as a function of time for our set of runs with different initial proton abundances. Once the maximum temperature is reached at $1.4 \times 10^4\,\mathrm{s}$ there is a steep initial rise in neutron densities above $10^{13}\,\mathrm{cm}^{-3}$. At first, increasing the ingested proton fraction results in higher peak neutron densities and the simulation with $X_0(\mathrm{H}) = 10^{-3}$ reaches the highest neutron densities of $n \approx 10^{15}\,\mathrm{cm}^{-3}$. Increasing the ingested proton fraction further beyond $X_0(\mathrm{H}) = 10^{-2}$ results in a drop in peak neutron density. This behaviour can be understood as a consequence of the reaction chains described in the previous subsection. In

[3]The integrated neutron exposure is defined as $\tau = \int n\, v_T\, dt = \int n \sqrt{2\, k_B\, T/m_n}\, dt$ with neutron density n, thermal neutron velocity v_T, Boltzmann constant k_B, temperature T, and neutron mass m_n. We use the notation τ_i to refer to the neutron exposure that is built up at i-process neutron densities with $n > 10^{12}\ \mathrm{cm}^{-3}$.

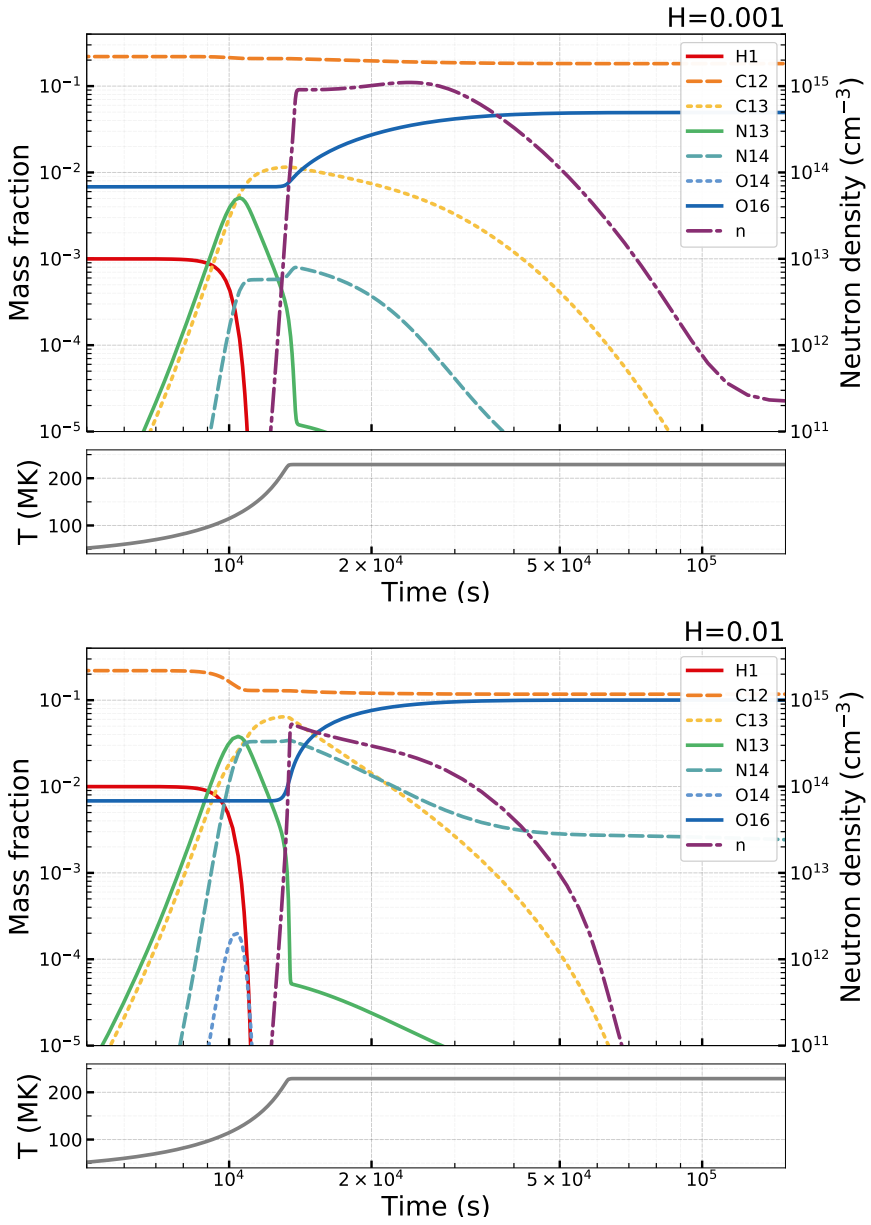

Figure 3.2: Development of the mass fractions of selected isotopes and neutron density for the simulations with and $X_0(\mathrm{H}) = 10^{-3}$ (upper panel) and $X_0(\mathrm{H}) = 10^{-2}$ (lower panel).

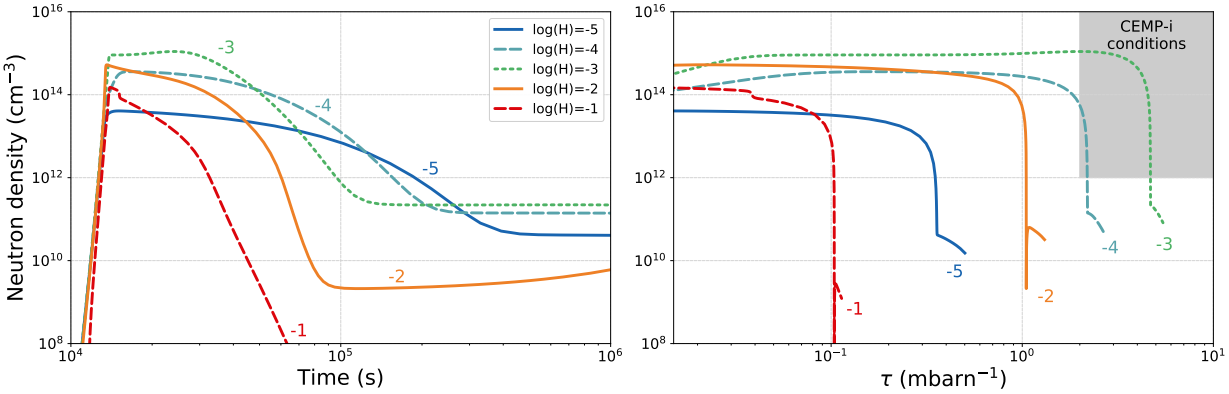

Figure 3.3: Neutron densities for various ingested proton fractions as function of time (left panel) and of the integrated neutron exposure τ (right panel). The shaded region in the right panel shows conditions with $\tau \geq 2\,\mathrm{mbarn}^{-1}$ and $n \geq 10^{12}$ cm^{-3}, which are typical for the production of the i-process heavy-element abundance patterns observed in CEMP-i stars (Hampel et al., 2019).

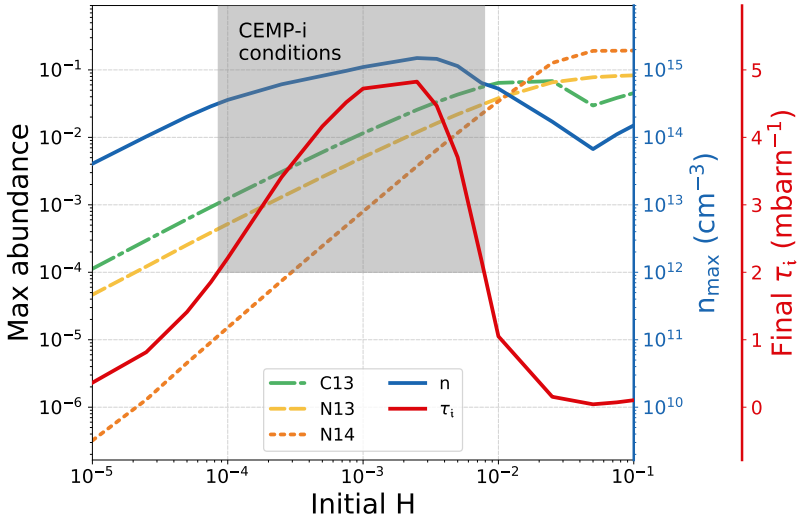

Figure 3.4: Maximum mass fraction of ^{13}C, ^{13}N, and ^{14}N, as well as maximum neutron density n and i-process exposure τ_i reached in each simulation with varying initial hydrogen mass fraction. The shaded region shows where an exposure with $\tau \geq 2$ is reached, which leads to conditions typical to reproduce the abundances in CEMP-i stars (Hampel et al. 2019).

particular the relative abundances of ^{13}C, ^{13}N, and ^{14}N are crucial for the relative importance of the neutron poisons and neutron recycling, which determine the peak neutron density and the shape of the neutron-density trajectory. Figure 3.4 shows the maximum abundance of ^{13}C, ^{13}N, and ^{14}N for each run as a function of the initially ingested proton fraction, as well their maximum neutron density and final i-process neutron exposure.

Simulations with $X_0(\mathrm{H}) \geq 10^{-2}$ show a rapid decline after reaching their peak neutron density (Figure 3.3), whereas the decline is slower for simulations with lower initial proton fractions, before the neutron density settles to levels below $n < 10^{12}\,\mathrm{cm}^{-3}$. The combination of high peak neutron density followed by a slow decline is essential to building up a high neutron exposure. Figure 3.3 shows that only the simulations with $X_0(\mathrm{H}) = 10^{-4}$ and $X_0(\mathrm{H}) = 10^{-3}$ reach exposures with

$\tau_{\rm i} > 2\,{\rm mbarn}^{-1}$, the characteristic exposure to reproduce the abundances in CEMP-i stars (Hampel et al., 2019). The simulation with $X_0({\rm H}) = 10^{-2}$ reaches an exposure of $\tau_{\rm i} \approx 1\,{\rm mbarn}^{-1}$, whereas all other cases stay well below unity. Once the neutron densities have settled to levels below $n < 10^{12}\,{\rm cm}^{-3}$ some additional neutron exposure builds up at this neutron density but below i-process levels.

3.4 Discussion and Conclusions

Using constant neutron density simulations, Hampel et al. (2019) have shown that the typical i-process abundance pattern observed in CEMP-i stars requires an integrated neutron exposure of $\tau \gtrsim 2\,{\rm mbarn}^{-1}$ at neutron densities of $\log(n) = 13 - 14$. From the current study only a limited range of initial proton fractions with $10^{-4} \lesssim X_0({\rm H}) \lesssim 8 \times 10^{-3}$ can lead to those conditions (see Figures 3.3 and 3.4). Lower initial proton fractions do not lead to a high enough production of ^{13}C, whereas higher initial proton fractions produce too much ^{14}N (see Figure 3.4). As a consequence there is a "sweet spot" of ingested proton fractions for i-process nucleosynthesis.

An early framework for analysing the nucleosynthesis accompanying the $^{13}{\rm C}(\alpha,{\rm n})^{16}{\rm O}$ neutron source (Jorissen & Arnould, 1989) focuses on regimes defined by relative reaction lifetimes. Conditions for i-process nucleosynthesis in this framework can develop when lifetimes of ingested protons against capture by ^{12}C ($\tau_{^{12}{\rm C}}(p)$) become shorter than the β-decay lifetime of ^{13}N ($\tau_\beta(^{13}{\rm N})$). Primarily caused by the gradual increase of temperature with time, our simulations do not stay stationary in such defined regimes, but develop $\tau_{^{12}{\rm C}}(p) < \tau_\beta(^{13}{\rm N})$ after 10^4 s. However, from our simulations it becomes obvious, that this alone is not a sufficient indicator for whether or not i-process heavy-element abundance patterns can develop. In particular, the importance of neutron-recycling reactions and the production of neutron poisons are highly dependent on the ingested proton fractions and are crucial factors for the integrated neutron exposure and the level of heavy-element production.

In this work we adapted a variable temperature and density profile to mimic the different physical conditions under which the studied chain of reactions occur in a convective parcel. Previous attempts to model neutron production and subsequent i process nucleosynthesis self-consistently, utilise constant temperature and densities (Bertolli et al., 2013; Dardelet et al., 2014; Denissenkov et al., 2018; McKay et al., 2020). These studies required large fractions of protons $X_0({\rm H}) \gtrsim 0.1$ burning at extremely high temperatures of $T \approx 200\,{\rm MK}$. In the ingestion scenario, however, the protons would not survive to the corresponding depth in the convective zone at which these high temperatures occur (see Figure 3.2) because the competing proton-capture reaction $^{13}{\rm N}({\rm p},\gamma)^{14}{\rm O}$ destroys a large fraction of ^{13}N before it can decay into ^{13}C, especially for high ingested proton fractions. In Appendix 3.B we investigate if the difference between these previous and the present results may be due to the use of constant versus variable temperature profiles by comparing the present results to nucleosynthesis calculations at constant temperature and density. While we do find slight variations in the resulting neutron densities and exposures, our conclusion holds that high proton fractions of $X_0({\rm H}) \gtrsim 10^{-2}$ are excluded for i-process nucleosynthesis. Therefore, we speculate that the difference between the previous and present results are instead related to different features of the nuclear network. In particular, as clarified by (Denissenkov et al., 2021), the manual suppression of the $^{13}{\rm N}({\rm p},\gamma)^{14}{\rm O}$ reaction is required to achieve high enough abundances of ^{13}C to

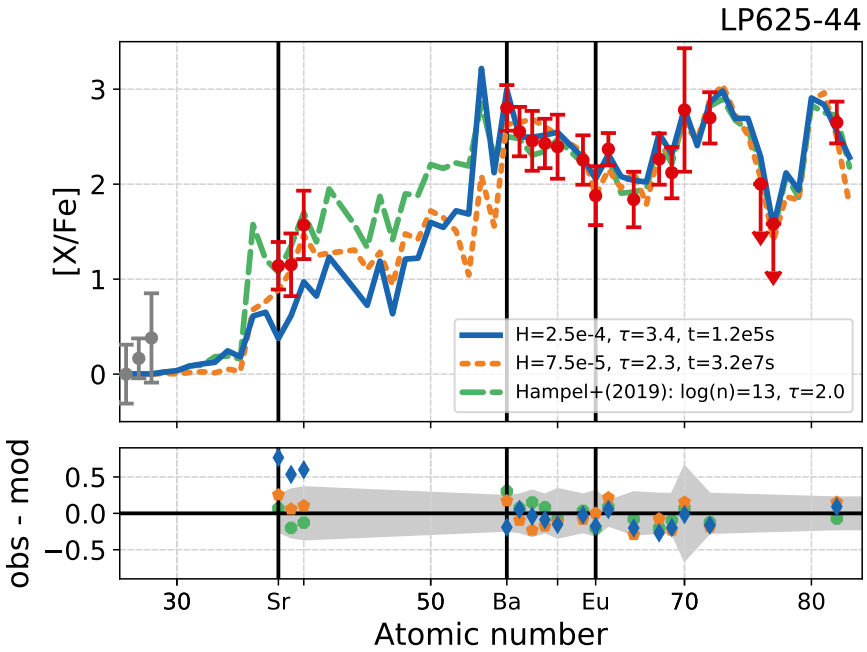

Figure 3.5: Abundance pattern of CEMP-i star LP625-44 with two fits from this work. The blue line provides the best fit if only i-process nucleosynthesis at neutron densities above $10^{12}\,\mathrm{cm}^{-3}$ are considered and the orange short-dashed line provides a better fit if further heavy-element production at neutron densities below i-process levels is taken into account. The best fit from Hampel et al. (2019, green long-dashed line) at constant neutron densities is shown for comparison.

produce i-process neutron densities at high proton fractions in the previous studies by Bertolli et al. (2013); Dardelet et al. (2014); Denissenkov et al. (2018); McKay et al. (2020).

Figure 3.5 shows the observational heavy-element abundance pattern of the representative CEMP-i star LP625-44 (Norris et al., 1997; Aoki et al., 2000, 2001, 2002c, 2006) and two fits from our simulations. The first fit (blue line) shows the best fit from our simulations considering only the time period when the neutron density is above $n > 10^{12}$ cm^{-3}, which is the case for approximately the first $\approx 10^5$ s. When we include the neutron-density drop (Figure 3.3) to s-process neutron densities below $n < 10^{12}$ cm^{-3} a better fit can be found (orange line in Figure 3.5).

The first (blue) fit at high neutron densities underproduces the light s-process peak (ls, at Sr), especially when compared to the heavy s-process peak (hs, at Ba), which is matched well. A high [hs/ls] ratio is a specific i-process signature and its value increases with neutron density. It has been shown that abundance patterns produced by neutron densities above $n > 10^{14}$ cm^{-3} overproduce this i-process feature and are incompatible with the abundance patterns of CEMP-i stars (Hampel et al., 2016, 2019). As most of our simulations build up the majority of their integrated neutron exposure at neutron densities above 10^{14} cm^{-3} (Figure 3.3) it is not surprising that the resulting abundance pattern show an [hs/ls] ratio that is too high to reproduce a typical CEMP-i pattern. This is especially true for LP625-44 as it is a star that has previously been matched with constant neutron density of $n = 10^{13}\,\mathrm{cm}^{-3}$, more than an order of magnitude lower.

The second (orange) fit shows that a subsequent exposure at lower neutron densities of $n < 10^{12}$ cm^{-3} can compensate for the high [hs/ls] ratio and provides a better match to the observations of LP625-44. However, at this lower neutron density it takes a longer time to produce additional

heavy elements, with the presented example indicating times exceeding $t > 10^7$ s. It is not clear whether such time scales are realistic. Some 1D stellar evolution models predict that the energy released by the nuclear reactions in PIEs results in an almost immediate splitting of the convective zone preventing further mixing throughout the intershell. However, some models report such a split to occur after 0.65 years (Cristallo et al., 2016), or even after 20 years, in the case of a PIE in a core-flash simulation by Campbell et al. (2010). In contrast to the common assumption of almost instantaneous convective-zone splitting in one-dimensional simulations, three-dimensional models indicate that such a split may be delayed (Stancliffe et al., 2011; Herwig et al., 2011, 2014). Prolonged neutron irradiation can then produce heavy-element patterns.

Alternatively, an improved fit to LP625-44 with a lower [hs/ls] ratio could be achieved under conditions that allow for most of the integrated neutron exposure to build up at slightly lower neutron densities than in our simulations, at $n \approx 10^{13}$ cm^{-3} (Hampel et al., 2019). Our simulations indicate that lower ingested proton fractions, e.g. the model with $X_0(\mathrm{H}) = 10^{-5}$, yield these more suitable neutron densities, however, it cannot sustain them for long enough to build up the needed neutron exposure for sufficient heavy-element production. Of importance here is that the proton ingestion in our simulations is simplified as the protons are ingested instantaneously. Instead, the proton ingestion probably occurs over an extended time or even repeatedly. Such extended or repeated proton ingestions at a lower proton fraction of $X_0(\mathrm{H}) \approx 10^{-5}$ could potentially lead to the conditions in which a neutron density of $n \approx 10^{13}$ cm^{-3} could be sustained long enough to better reproduce the characteristics of LP625-44. Previous work by Hampel et al. (2019) (green line in Figure 3.5) has shown that i-process nucleosynthesis resulting from constant neutron densities is successful at reproducing the observed abundance patterns of multiple CEMP-i stars and we plan on extending our work to further investigate whether more realistic models of PIEs, with extended proton ingestions, can provide such conditions.

Other uncertainties in the neutron production can influence the neutron density at which the main heavy-element abundance pattern is produced. In particular, the temperature profile over the first 10^4 to 10^5 s of the proton ingestion can strongly influence the rates at which the subsequent reactions occur and ultimately produce neutrons. In this work we only use one specific temperature-density trajectory for one potential i-process site, i.e., low-metallicity AGB stars. Different i-process sites will likely provide different physical conditions, such as temperature, density and initial abundance, and it is therefore expected that the resulting neutron-density profiles will differ. The extent of this will be addressed in a separate study, together with the impact of uncertainties on the relevant reaction rates (see Chapters §4 and §5).

Our two-phase approach incorporates the neutron production and isotopic abundance changes from charged-particle reactions to provide a more realistic and self-consistent initial composition for the i-process heavy-element nucleosynthesis compared to previous studies. However, this approach still relies on simplifying assumptions, which are unavoidable in the framework of a single-zone reaction-network simulation. The main caveat of our method is the neglect of mixing effects as well as the assumption of a single, instantaneous proton-ingestion event. Moreover, we followed our studied temperature-density trajectory according to convective velocities provided by mixing length theory (MLT), but it is uncertain how realistic these velocities are. It is conceivable that the parcel of material moves through the He-intershell at a rate different from the velocity predicted by MLT when viewed in the context of a three-dimensional convective environment. This will influence

the temperatures at which the specific sequences of nuclear reactions occur, which we will further address in Chapter §4.

In conclusion, we studied i-process neutron production as a function of ingested proton fractions spanning many orders of magnitude. Previous single-zone i-process models adopted high proton fractions of $X_0(\mathrm{H}) \approx 0.1$ to 0.2 (Dardelet et al., 2014; Denissenkov et al., 2018; McKay et al., 2020). In our simulations, such high proton fractions are unable to reproduce the neutron exposures required for heavy-element production. We achieve i-process conditions for $X_0(\mathrm{H}) \approx 10^{-3}$ and even lower ingested proton fractions of $X_0(\mathrm{H}) \approx 10^{-4}$ are favoured in reproducing the abundance pattern of CEMP-i star LP625-44. These proton fractions are comparable to those more commonly found in 1D and 3D stellar evolution models (e.g., Cristallo et al., 2009; Herwig et al., 2011; Stancliffe et al., 2011; Woodward et al., 2015; Denissenkov et al., 2019; Stephens et al., 2020). Our study validates single-zone nuclear network calculations as a helpful tool to understand the nuclear reactions at the heart of the processes that produce neutrons and heavy elements.

3.A Appendix: Temperature and density profile

In Figure 3.6 we show the details of the temperature and density trajectory that we use for this work. The temperature and density profile is constructed from the stellar structure of a evolution model of a $1\,\mathrm{M}_\odot$ star with a metallicity of $Z = 10^{-4}$, which experiences a PIE in its second thermal pulse (Stancliffe et al., 2011).

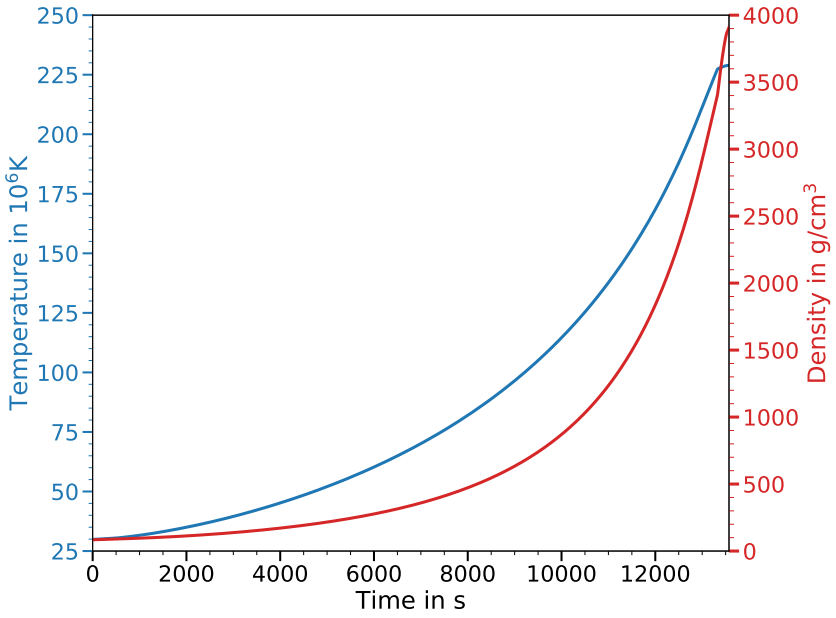

Figure 3.6: Temperature and density trajectory as function of time adapted from Stancliffe et al. (2011).

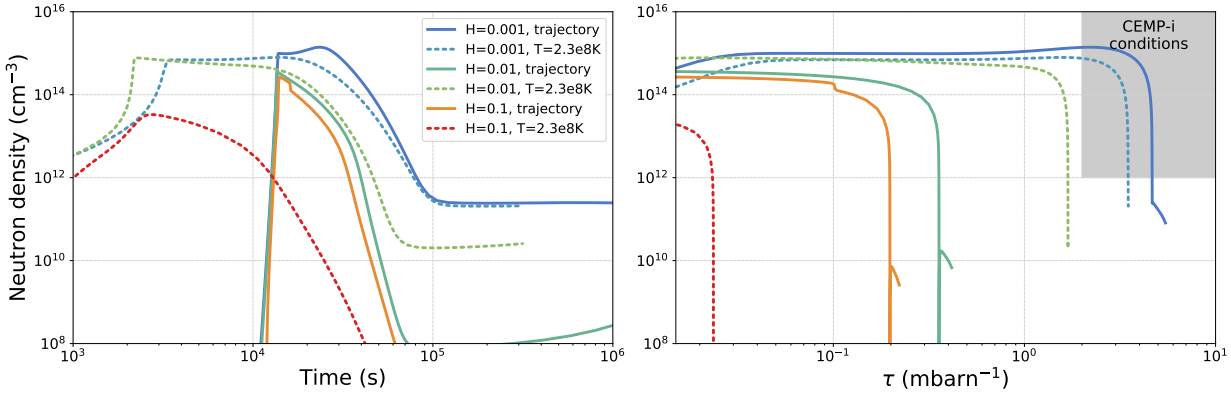

Figure 3.7: Comparison of neutron profiles over time and neutron exposure for different initially ingested proton fractions. The temperature and density for the simulations presented in this work increase with time following the trajectory in Figure 3.6 (solid lines labelled as *trajectory*). In comparison we show simulations with constant conditions of $T = 2.3 \times 10^8$ K and $\rho = 3900\,\mathrm{g\,cm^{-3}}$(dashed lines).

3.B Appendix: Comparison to simulations at constant temperature and density

Previous work that models the production of neutrons through the reactions $^{12}\mathrm{C(p,\gamma)^{13}N(\beta^+\nu)^{13}C(\alpha,n)^{16}O}$ in a single-zone context assumes a constant temperature and density for the whole reaction chain with high initially ingested proton fractions $X_0(\mathrm{H}) \approx 0.1$ to 0.2 (Dardelet et al., 2014; Denissenkov et al., 2018; McKay et al., 2020). In Figure 3.7 we compare our simulations where the temperature and density increase over time to the same simulations described in the main text, but at a constant temperature and density. The left panel shows that the cases with constant conditions already reach their maximum neutron densities after 2 to 3×10^3 seconds, whereas the cases with varying conditions only show neutron production after 10^4 seconds, which is the time needed to reach sufficiently high temperatures to activate the $^{13}\mathrm{C}(\alpha,\mathrm{n})^{16}\mathrm{O}$ reaction.

In the scenario of a proton-ingestion episode it becomes evident that the ingested protons will not immediately be exposed to the highest temperatures at the bottom of the convective region. Therefore the proton-capture reactions that produce ^{13}C and ^{14}N occur at different rates in the simulations with increasing temperature and density compared to those with a constantly high temperature and density. While this affects the final neutron exposure in the simulations (see right panel in Figure 3.7), we do not find that constant temperatures and densities can lead to i-process neutron exposures in simulations with high ingested proton fractions of $X_0(\mathrm{H}) \geq 0.1$. In fact, these simulations with high ingested proton fractions experience even more ^{14}N production through proton captures onto ^{13}N and ^{13}C and cannot maintain their maximum neutron density for a long enough time and high enough neutron exposure for i-process heavy-element production.

> *I was taught that the way of progress was neither swift nor easy.*

> *Nothing in life is to be feared, it is only to be understood. Now is the time to understand more, so that we may fear less.*
>
> — Marie Skłodowska Curie

Chapter 4

Parametric study of uncertainties in the neutron production for the i process

While single-zone models only provide a simplified picture of the nucleosynthesis occurring in the interiors of stars (and important effects such as mixing cannot be incorporated), they are computationally inexpensive and therefore well suited for a parameterised approach to quickly explore a range of physical conditions. A variety of physical situations and their effect on the resulting nucleosynthesis can be studied systematically.

In the previous Chapter §3, we studied how varying proton fractions, when ingested into a He-convective region, can result in neutron densities of $n \approx 10^{13} - 10^{15}\,\mathrm{cm}^{-3}$, which are typical values for the intermediate neutron-capture process. If these neutron densities are sustained long enough to reach integrated exposures of $\tau \gtrsim 2\,\mathrm{mbarn}^{-1}$, they can lead to the production of heavy elements as observed in CEMP-i stars (Hampel et al., 2019). We show that the neutron production and the heavy-element nucleosynthesis can indeed be studied self-consistently in a single-zone framework using *NucNet Tools* code (Meyer, 2012).

Here we want to expand on the previously presented simulations and explore how varying parameters of this model affect the resulting i-process neutron densities and nucleosynthesis. The variation of parameters is motivated by uncertainties encountered in the nuclear physics inputs and stellar evolution models. In particular we investigate the effects of different

- uncertainties in nuclear-reaction rates,
- initial abundances in the He-convective region, and
- convective velocities in the He-convective region.

We follow the method described in Chapter §3 and explore a range of initially ingested proton fractions for each of these tests. To remind the reader, we use a two-stage approach where the first step follows a parcel of material as it moves down through the He-convective region, by increasing the temperature and density with time. This allows us to study how the nuclear reactions in a proton-ingestion episode produce various isotopes in the CNO region, e.g. the neutron source ^{13}C and the neutron poison ^{14}N. Once the temperature and density have reached their maximum values this corresponds to the parcel having reached the bottom of the convective region. The second stage of our two-stage approach studies how these produced CNO isotopes contribute to the i-process neutron production and how the resulting i-process neutron densities lead to heavy-element production. This second stage can only take place in a narrow region at the bottom of the He-convective region, where the temperature is high enough to activate the release of neutrons via the $^{13}\mathrm{C}(\alpha,\mathrm{n})^{16}\mathrm{O}$ reaction. To focus on the nucleosynthesis that happens when the produced CNO isotopes reach this narrow, high-temperature region, we continue to keep the temperature and density constant (see Chapter §3).

4.1 Uncertainties in nuclear-reaction rates

In the last chapter, some key reactions were described that are important for the production of neutrons for i-process nucleosynthesis. Figure 4.1 shows important charged-particle reactions schematically on a section of the nuclide chart in the CNO region. In this section we will investigate the impact of each of these reactions further by considering their reaction-rate uncertainties and

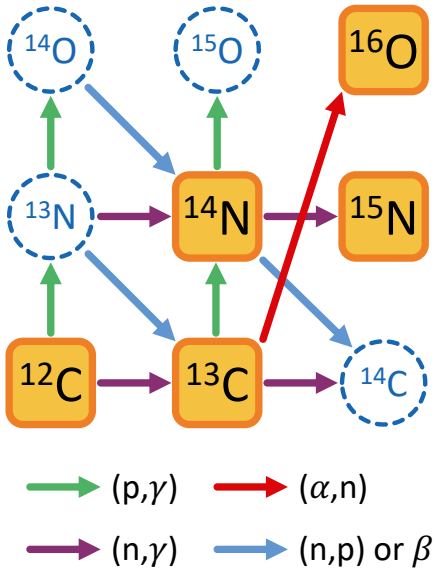

Figure 4.1: Reaction Schematic depicting the studied reaction rates in the CNO region, which can lead to i-process neutron production.

the implications for the i-process. In a first step in part §4.1.1 we will individually increase the reaction rates of the charged-particle reactions in the CNO region by a factor of two. This will allow us to examine in detail, which role each of the reactions has and how its rate influences and shapes the i-process neutron densities. In a next step in part §4.1.2 we will use the actual reaction rate uncertainties to assess the impact these uncertainties have on the neutron production. For a statistically meaningful representation of the reaction rate uncertainties, we use the so-called *factor uncertainties* which cover a probability of 68 % around the mean of a quantity following a log-normal probability distribution (Longland et al., 2010). Finally, we will show how the heavy-element abundance patterns of the i-process are affected by the reaction-rate uncertainties of the reactions involved in the neutron production.

4.1.1 Determining the roles of individual reactions through constant reaction-rate variations

To understand the role that individual reactions between the CNO isotopes play in the production and recycling of neutrons, we use the charged-particle reactions shown in Figure 4.1 and individually increase their rates by a factor of two. Figure 4.2 shows the evolution of the neutron density over time and as a function of neutron exposure for different proton fractions. The models for each of the proton fractions presented in the previous chapter, without modifications to the reaction rates, are also shown and serve as a reference simulation. For these reference simulations, Figure 4.3 shows the reaction flows in the CNO regions at the time when the maximum neutron density is reached.

Two interesting characteristics to assess the neutron production for the i process are the maximum reached neutron density $n_{\max}$ and the time integrated neutron exposure τ_{i} that can be built

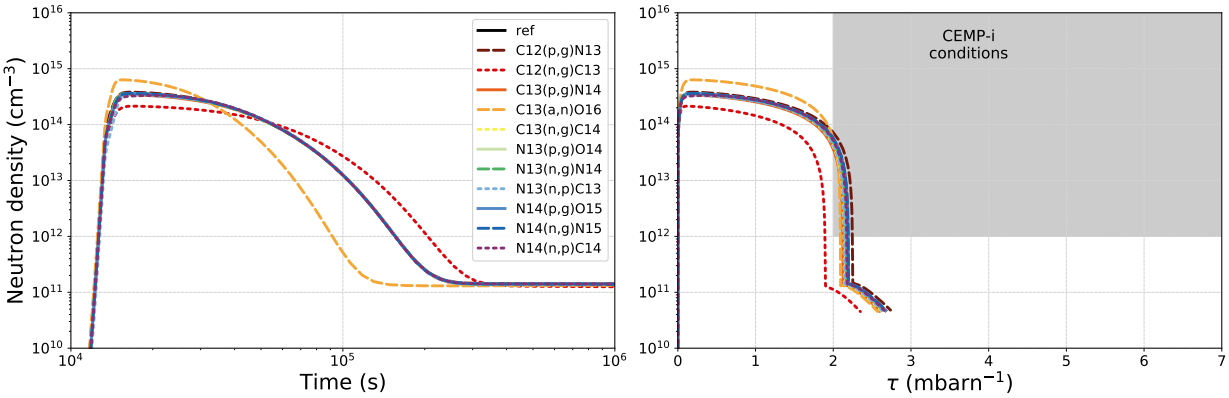

(A) Initially ingested proton fraction $X_0(\mathrm{H}) = 10^{-4}$.

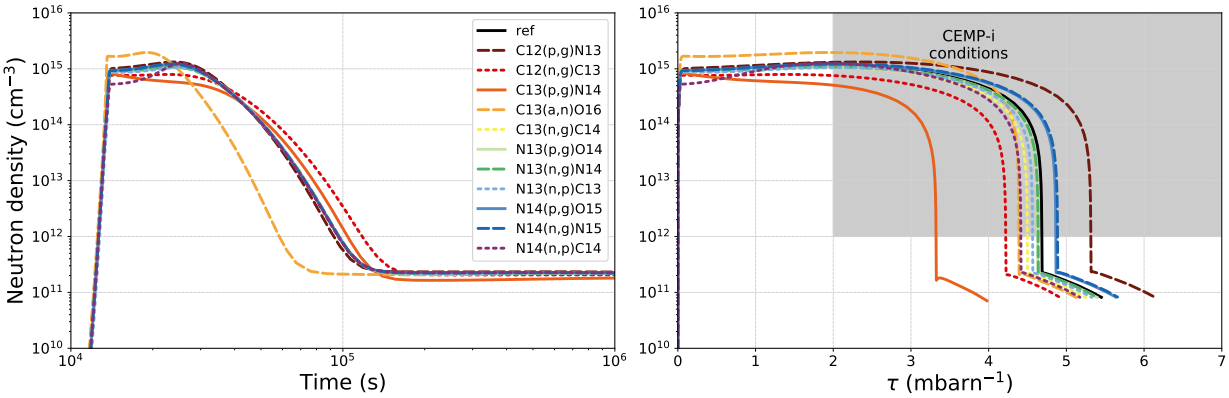

(B) Initially ingested proton fraction $X_0(\mathrm{H}) = 10^{-3}$.

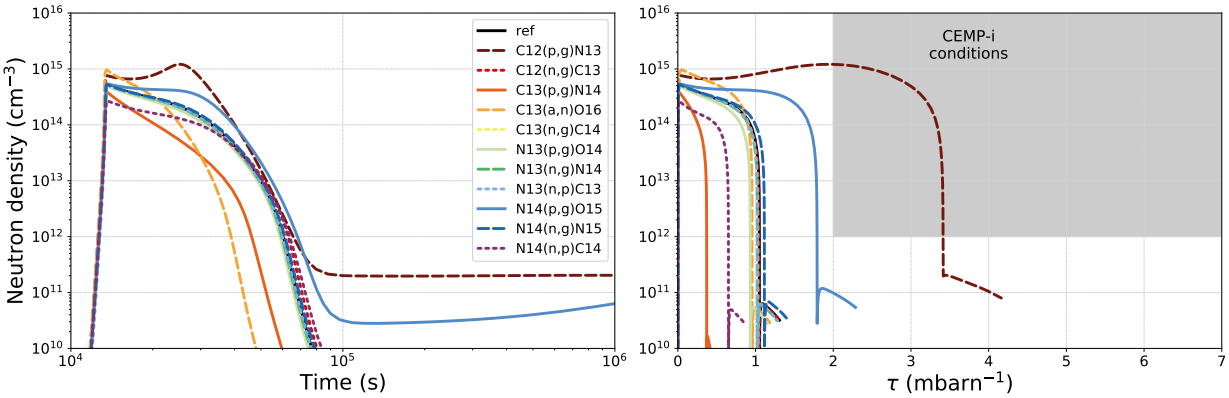

(C) Initially ingested proton fraction $X_0(\mathrm{H}) = 10^{-2}$.

Figure 4.2: Neutron densities for various ingested proton fractions as function of time (left panels) and of the integrated neutron exposure τ (right panels). For each initial proton fraction (subfigures a to c) the effect of increasing a single nuclear reaction rate by a factor of 2 is shown. The shaded region in the right panels indicates conditions with $\tau \geq 2\,\mathrm{mbarn}^{-1}$ and $n \geq 10^{12}$ cm^{-3}, which are typical for the production of the i-process heavy-element abundance patterns observed in CEMP-i stars (Hampel et al., 2019).

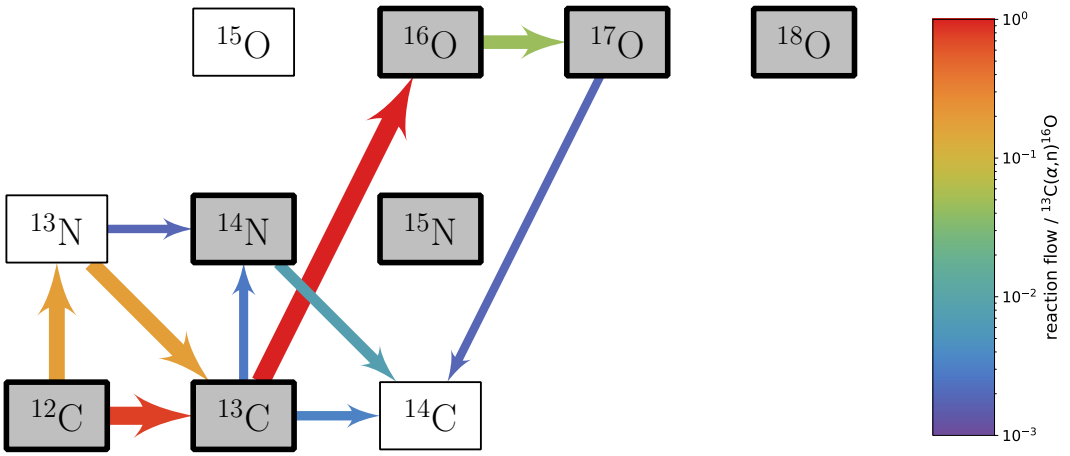

(A) Initially ingested proton fraction $X_0(\mathrm{H}) = 10^{-4}$.

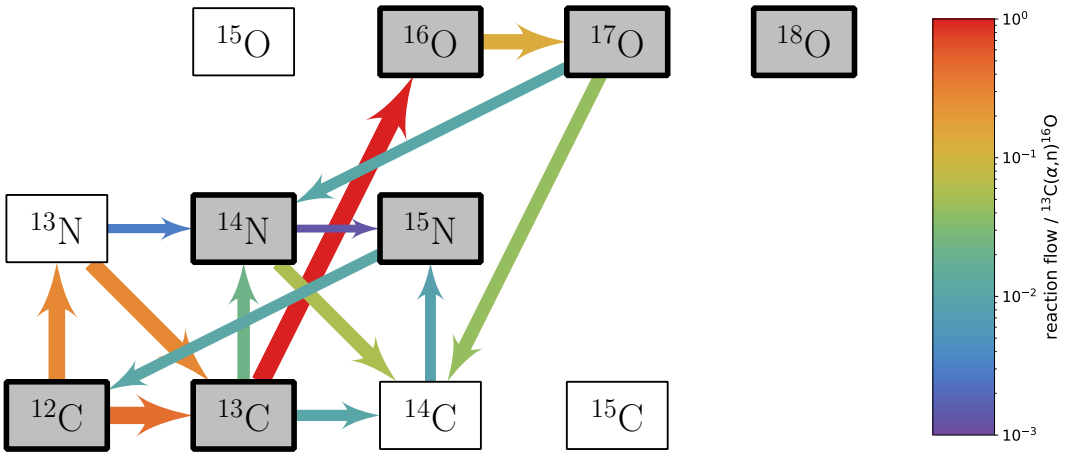

(B) Initially ingested proton fraction $X_0(\mathrm{H}) = 10^{-3}$.

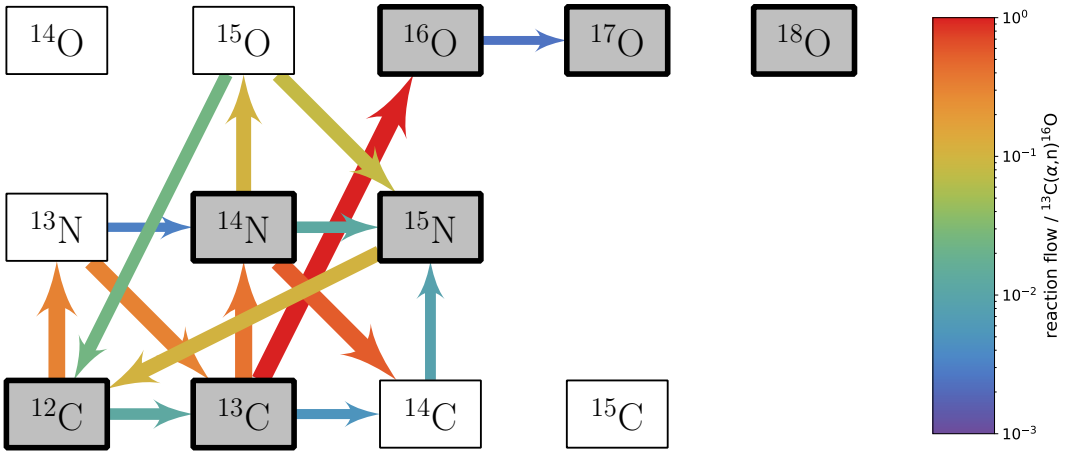

(C) Initially ingested proton fraction $X_0(\mathrm{H}) = 10^{-2}$.

Figure 4.3: **Flow charts of neutron recycling reactions in the CNO region for the reference simulations.** Reaction flows for the reference simulations at the time when maximum neutron density is reached. The colour and size of the arrow scales with the reaction flow, relative to the flow of $^{13}\mathrm{C}(\alpha,\mathrm{n})^{16}\mathrm{O}$. Stable isotopes are highlighted by bold black borders and grey colours.

Table 4.1: **Reaction-rate variations by a factor of two: $n_{\max}$ and $\tau_{\rm i}$ for $X_0(\mathrm{H}) = 10^{-4}$.** Maximum neutron density $n_{\max}$ and i-process neutron exposure $\tau_{\rm i}$ for simulations with ingested proton fraction $X_0(\mathrm{H}) = 10^{-4}$, when individual reaction rates are increased by a factor of two. $\Delta n_{\max}$ and $\Delta\tau_{\rm i}$ list the absolute differences of $n_{\max}$ and $\tau_{\rm i}$, respectively, between the reference simulation and the simulations with modified reaction rates. $\Delta n_{\max}$ (rel) and $\Delta\tau_{\rm i}$ (rel) give these differences relative to the reference value. $n_{\max}$ and $\Delta n_{\max}$ are in units of cm^{-3}. $\tau_{\rm i}$ and $\Delta\tau_{\rm i}$ are in units of mbarn^{-1}.

Reaction	$n_{\max}$ (cm^{-3})	$\Delta n_{\max}$ (cm^{-3})	$\Delta n_{\max}$ (rel) (%)	$\tau_{\rm i}$ (mbarn^{-1})	$\Delta\tau_{\rm i}$ (mbarn^{-1})	$\Delta\tau_{\rm i}$ (rel) (%)
reference	3.60×10^{14}	–	–	2.2	–	–
$^{12}\mathrm{C}(\mathrm{p},\gamma)^{13}\mathrm{N}$	3.81×10^{14}	2.12×10^{13}	5.9	2.2	0.1	3
$^{12}\mathrm{C}(\mathrm{n},\gamma)^{13}\mathrm{C}$	2.14×10^{14}	-1.46×10^{14}	−40.5	1.9	−0.3	−13
$^{13}\mathrm{C}(\mathrm{p},\gamma)^{14}\mathrm{N}$	3.44×10^{14}	-1.52×10^{13}	−4.2	2.1	−0.1	−3
$^{13}\mathrm{C}(\alpha,\mathrm{n})^{16}\mathrm{O}$	6.33×10^{14}	2.73×10^{14}	76.0	2.1	−0.1	−4
$^{13}\mathrm{C}(\mathrm{n},\gamma)^{14}\mathrm{C}$	3.57×10^{14}	-2.55×10^{12}	−0.7	2.1	−0.1	−2
$^{13}\mathrm{N}(\mathrm{p},\gamma)^{14}\mathrm{O}$	3.59×10^{14}	-9.71×10^{11}	−0.3	2.2	< 0.1	< 1
$^{13}\mathrm{N}(\mathrm{n},\gamma)^{14}\mathrm{N}$	3.60×10^{14}	8.46×10^{11}	0.2	2.2	< 0.1	−1
$^{13}\mathrm{N}(\mathrm{n},\mathrm{p})^{13}\mathrm{C}$	3.35×10^{14}	-2.43×10^{13}	−6.8	2.1	< 0.1	−2
$^{14}\mathrm{N}(\mathrm{p},\gamma)^{15}\mathrm{O}$	3.60×10^{14}	1.72×10^{11}	< 0.1	2.2	< 0.1	< 1
$^{14}\mathrm{N}(\mathrm{n},\gamma)^{15}\mathrm{N}$	3.61×10^{14}	1.81×10^{12}	0.5	2.2	< 0.1	< 1
$^{14}\mathrm{N}(\mathrm{n},\mathrm{p})^{14}\mathrm{C}$	3.33×10^{14}	-2.68×10^{13}	−7.5	2.2	< 0.1	−1

up at i-process neutron densities[1]. In Tables 4.1, 4.2, and 4.3 we list $n_{\max}$ and $\tau_{\rm i}$ for the reference run and each simulation with modified reaction rates for simulations with ingested proton fractions of $X_0(\mathrm{H}) = 10^{-4}$, 10^{-3}, and 10^{-2}, respectively. We also provide the change (absolute and relative) compared to the reference simulation at each proton fraction.

At low ingested proton fractions of $X_0(\mathrm{H}) = 10^{-4}$ the two reaction rates that have the strongest influence on the neutron production are $^{13}\mathrm{C}(\alpha,\mathrm{n})^{16}\mathrm{O}$ and $^{12}\mathrm{C}(\mathrm{n},\gamma)^{13}\mathrm{C}$. A factor of two increase in the reaction rates of $^{13}\mathrm{C}(\alpha,\mathrm{n})^{16}\mathrm{O}$ and $^{12}\mathrm{C}(\mathrm{n},\gamma)^{13}\mathrm{C}$ can increase the maximum neutron density by 76 % or decrease it by 40.5 %, respectively. Since $^{13}\mathrm{C}(\alpha,\mathrm{n})^{16}\mathrm{O}$ is the reaction that is ultimately responsible for the production of free neutrons once the available $^{13}\mathrm{C}$ reaches high enough temperatures, it is not surprising that its reaction rate is so closely linked to the reached neutron density. However, the effect that an increase in the $^{13}\mathrm{C}(\alpha,\mathrm{n})^{16}\mathrm{O}$ reaction rate has on the i-process neutron exposure is only very minor with a small decrease of just 4 %. In the first phase of the neutron production process, where $^{13}\mathrm{C}$ needs to be produced from the initial $^{12}\mathrm{C}$ and ingested protons while the temperature and density increase, the $^{13}\mathrm{C}(\alpha,\mathrm{n})^{16}\mathrm{O}$ reaction is not involved. Therefore, a change in $^{13}\mathrm{C}(\alpha,\mathrm{n})^{16}\mathrm{O}$ reaction rate does not affect the the amount of $^{13}\mathrm{C}$ that is available at the onset of the second phase, when the maximum temperature is reached and the $^{13}\mathrm{C}(\alpha,\mathrm{n})^{16}\mathrm{O}$ reaction can be activated to finally produce neutrons. As a consequence, the rate at which neutrons are released via the $^{13}\mathrm{C}(\alpha,\mathrm{n})^{16}\mathrm{O}$ reaction does not have a large influence on the total number of

[1]Recall the definition used in the previous Chapter §3 where $\tau_{\rm i}$ is defined as the neutron exposure that is built up at i-process neutron densities with $n > 10^{12}$ cm^{-3}.

Table 4.2: **Reaction-rate variations by a factor of two: n_{max} and τ_i for $X_0(H) = 10^{-3}$.** Same as Table 4.1 but for simulations with ingested proton fractions of $X_0(H) = 10^{-3}$.

Reaction	n_{max} (cm^{-3})	Δn_{max} (cm^{-3})	Δn_{max} (rel) (%)	τ_i ($mbarn^{-1}$)	$\Delta\tau_i$ ($mbarn^{-1}$)	$\Delta\tau_i$ (rel) (%)
benchmark	1.10×10^{15}	–	–	4.7	–	–
$^{12}C(p,\gamma)^{13}N$	1.32×10^{15}	2.23×10^{14}	20.2	5.3	0.6	13
$^{12}C(n,\gamma)^{13}C$	7.94×10^{14}	-3.08×10^{14}	−28.0	4.2	−0.5	−10
$^{13}C(p,\gamma)^{14}N$	8.39×10^{14}	-2.62×10^{14}	−23.8	3.3	−1.4	−29
$^{13}C(\alpha,n)^{16}O$	1.96×10^{15}	8.55×10^{14}	77.6	4.4	−0.3	−6
$^{13}C(n,\gamma)^{14}C$	1.06×10^{15}	-4.61×10^{13}	−4.2	4.5	−0.2	−4
$^{13}N(p,\gamma)^{14}O$	1.08×10^{15}	-2.15×10^{13}	−2.0	4.6	−0.1	−1
$^{13}N(n,\gamma)^{14}N$	1.08×10^{15}	-2.53×10^{13}	−2.3	4.6	< 0.1	−1
$^{13}N(n,p)^{13}C$	1.05×10^{15}	-5.10×10^{13}	−4.6	4.6	−0.1	−3
$^{14}N(p,\gamma)^{15}O$	1.19×10^{15}	8.96×10^{13}	8.1	4.9	0.2	4
$^{14}N(n,\gamma)^{15}N$	1.22×10^{15}	1.20×10^{14}	10.9	4.9	0.2	4
$^{14}N(n,p)^{14}C$	1.26×10^{15}	1.60×10^{14}	14.5	4.4	−0.3	−6

Table 4.3: **Reaction-rate variations by a factor of two: n_{max} and τ_i for $X_0(H) = 10^{-2}$.** Same as Table 4.1 but for simulations with ingested proton fractions of $X_0(H) = 10^{-2}$.

Reaction	n_{max} (cm^{-3})	Δn_{max} (cm^{-3})	Δn_{max} (rel) (%)	τ_i ($mbarn^{-1}$)	$\Delta\tau_i$ ($mbarn^{-1}$)	$\Delta\tau_i$ (rel) (%)
benchmark	5.27×10^{14}	–	–	1.0	–	–
$^{12}C(p,\gamma)^{13}N$	1.21×10^{15}	6.83×10^{14}	129.7	3.4	2.4	225
$^{12}C(n,\gamma)^{13}C$	5.20×10^{14}	-6.28×10^{12}	−1.2	1.0	< 0.1	< 1
$^{13}C(p,\gamma)^{14}N$	3.83×10^{14}	-1.43×10^{14}	−27.2	0.4	−0.7	−65
$^{13}C(\alpha,n)^{16}O$	9.63×10^{14}	4.37×10^{14}	82.9	1.0	−0.1	−9
$^{13}C(n,\gamma)^{14}C$	5.24×10^{14}	-2.70×10^{12}	−0.5	1.0	< 0.1	−2
$^{13}N(p,\gamma)^{14}O$	4.94×10^{14}	-3.31×10^{13}	−6.3	0.9	−0.1	−11
$^{13}N(n,\gamma)^{14}N$	5.27×10^{14}	3.06×10^{11}	0.1	1.0	< 0.1	−2
$^{13}N(n,p)^{13}C$	5.25×10^{14}	-1.80×10^{12}	−0.3	1.0	< 0.1	−2
$^{14}N(p,\gamma)^{15}O$	5.42×10^{14}	1.52×10^{13}	2.9	1.8	0.7	71
$^{14}N(n,\gamma)^{15}N$	5.26×10^{14}	-1.05×10^{12}	−0.2	1.1	0.1	6
$^{14}N(n,p)^{14}C$	2.68×10^{14}	-2.59×10^{14}	−49.1	0.7	−0.4	−38

neutrons that get produced in this single parcel of material. The exception to this is a secondary effect, where the amount of neutron recycling and breakouts from this recycling are influenced by the neutron density. Therefore a variation of the $^{13}\mathrm{C}(\alpha,\mathrm{n})^{16}\mathrm{O}$ reaction rate, and hence an increase in $n_{\max}$, leads to the small change in τ_{i} of only 4 %.

The situation is different for a change in the $^{12}\mathrm{C}(\mathrm{n},\gamma)^{13}\mathrm{C}$ reaction rate. Here an increase of the rate by a factor of two causes a decrease in both $n_{\max}$ and τ_{i} by 40.5 % and 13.5 %, respectively. This is because $^{12}\mathrm{C}(\mathrm{n},\gamma)^{13}\mathrm{C}$ is the dominant neutron-recycling reaction for simulations with $X_0(\mathrm{H}) = 10^{-4}$ during the neutron-release phase at the bottom of the convective zone where the maximum temperature is reached (see Figure 4.3a). Already for the reference simulation with the standard reaction rates, $^{12}\mathrm{C}(\mathrm{n},\gamma)^{13}\mathrm{C}$ dominates over $^{13}\mathrm{N}(\mathrm{n},\mathrm{p})$, which is contrary to the simulation for $X_0(\mathrm{H}) = 10^{-3}$ presented in the previous chapter (also compare Figure 4.3a and 4.3b). Since $^{12}\mathrm{C}(\mathrm{n},\gamma)^{13}\mathrm{C}$ is the reaction causing the highest absorption of neutrons, increasing its reaction rate immediately decreases the availability of free neutrons and therefore lowers $n_{\max}$. However, $^{12}\mathrm{C}(\mathrm{n},\gamma)^{13}\mathrm{C}$ is not a neutron-poison reaction in the classical sense. Although neutrons are absorbed by the $^{12}\mathrm{C}(\mathrm{n},\gamma)^{13}\mathrm{C}$ reaction, additional $^{13}\mathrm{C}$ is produced that can in return release neutrons, which leads to delayed neutron recycling. This neutron-recycling flow is not conserved completely, and instead breakouts via $^{13}\mathrm{N}(\mathrm{n},\gamma)^{14}\mathrm{N}$ and $^{13}\mathrm{C}(\mathrm{p},\gamma)^{14}\mathrm{N}$ produce the neutron poison $^{14}\mathrm{N}$. The magnitude of the breakout flux and of the $^{14}\mathrm{N}$ production, and hence of the decrease of total integrated neutron exposure τ_{i}, is determined by the overall flux of neutron-recycling reactions. Since $^{12}\mathrm{C}(\mathrm{n},\gamma)^{13}\mathrm{C}$ is the dominant neutron-recycling reaction, its change in reaction rate causes the highest decrease in τ_{i}. It is worth noting that the other reactions that absorb and recycle neutrons, such as $^{13}\mathrm{N}(\mathrm{n},\mathrm{p})$ or $^{14}\mathrm{N}(\mathrm{n},\mathrm{p})$, influence $n_{\max}$ and τ_{i} in a similar way, except to a much smaller degree (compare Figure 4.2 and Table 4.1). This is because in simulations with $X_0(\mathrm{H}) = 10^{-4}$ they are outpaced by the $^{12}\mathrm{C}(\mathrm{n},\gamma)^{13}\mathrm{C}$ reaction by orders of magnitudes.

As shown in Figure 4.2b and Table 4.2, an increase in individual reaction rates in the simulations with $X_0(\mathrm{H}) = 10^{-3}$ causes a larger spread in $n_{\max}$ and τ_{i} compared to the simulations with $X_0(\mathrm{H}) = 10^{-4}$. The maximum neutron densities range between $8 \times 10^{14} \leq n_{\max} \leq 2 \times 10^{15}$ cm^{-3} (which is an increase of 76 % and a decrease of 28 % compared to the reference simulation) and the i-process neutron exposures range between $3.3 \leq \tau_{\mathrm{i}} \leq 5.3\,\mathrm{mbarn}^{-1}$ (which is an increase of 13 % and a decrease of 29 % compared to the reference simulation). The effects that reaction-rate changes of $^{13}\mathrm{C}(\alpha,\mathrm{n})^{16}\mathrm{O}$ and $^{12}\mathrm{C}(\mathrm{n},\gamma)^{13}\mathrm{C}$ have on the neutron production are similar to those laid out for simulations with $X_0(\mathrm{H}) = 10^{-4}$. However, as becomes obvious from Figure 4.3b, for the reference simulation at $X_0(\mathrm{H}) = 10^{-3}$ the $^{12}\mathrm{C}(\mathrm{n},\gamma)^{13}\mathrm{C}$ reaction does not dominate the neutron recycling flow as much compared to the case at $X_0(\mathrm{H}) = 10^{-4}$, and other recycling reactions such as, e.g., $^{13}\mathrm{N}(\mathrm{n},\mathrm{p})$ and $^{14}\mathrm{N}(\mathrm{n},\mathrm{p})$ gain in relative significance.

The increased $^{13}\mathrm{N}(\mathrm{n},\mathrm{p})^{13}\mathrm{C}$ and $^{14}\mathrm{N}(\mathrm{n},\mathrm{p})^{14}\mathrm{C}$ reaction flows cause a higher proton flux, which lead to neutron-recycling in a delayed secondary step. It becomes crucial for the abundance of free neutrons, how the released neutrons get captured. Therefore, the two reactions whose increase in reaction rate can cause a large effect for the neutron production in the simulations with $X_0(\mathrm{H}) = 10^{-3}$ are $^{12}\mathrm{C}(\mathrm{p},\gamma)^{13}\mathrm{N}$ and $^{13}\mathrm{C}(\mathrm{p},\gamma)^{14}\mathrm{N}$. $^{12}\mathrm{C}(\mathrm{p},\gamma)^{13}\mathrm{N}$ is the starting point for the ingested protons to be eventually converted into neutrons, so it is not surprising that an increase of this reaction rate causes a significant increase in both $n_{\max}$ and τ_{i} by 20 % and 13 %, respectively. $^{13}\mathrm{C}(\mathrm{p},\gamma)^{14}\mathrm{N}$ on the other hand is the main producer of the classical neutron poison $^{14}\mathrm{N}$. Consequently, an increase

in its reaction rate leads to a significant decrease in $n_{\max}$ and $\tau_{\rm i}$ by 24 % and 29 %, respectively.

The effects that an increase of individual reaction rates have on the neutron production in simulations with $X_0(\mathrm{H}) = 10^{-2}$ is even more extreme than seen for the simulations with $X_0(\mathrm{H}) = 10^{-3}$ and $X_0(\mathrm{H}) = 10^{-4}$ (compare Figure 4.2c and Table 4.3). The higher ingested proton fractions lead to overall higher reaction flows such that the role of each reaction can be enhanced dramatically. In the case of the $^{12}\mathrm{C}(\mathrm{p},\gamma)^{13}\mathrm{N}$ reaction, a factor-of-two increase of the reaction rate more than doubles $n_{\max}$ and even triples $\tau_{\rm i}$. On the other hand, the previously observed role of $^{13}\mathrm{C}(\mathrm{p},\gamma)^{14}\mathrm{N}$ as a breakout reaction from the neutron recycling flow is also enhanced by its reaction rate modification and leads to an enhanced production of neutron poison ^{14}N, which causes a reduction of $\tau_{\rm i}$ by 65 %.

It was already pointed out in the previous section for the reference simulations, that the increases in the produced levels of ^{13}C and ^{14}N with increasing proton fractions do not follow the same proportionality (see Figure 3.4). For simulations with $X_0(\mathrm{H}) = 10^{-2}$ the role of the neutron poison ^{14}N has been elevated so much, that it becomes the limiting factor for building up i-process neutron exposures, although i-process neutron densities can still be achieved for short durations. The dominating role of ^{14}N can further be seen in Figure 4.2c. The $^{14}\mathrm{N}(\mathrm{n},\mathrm{p})^{14}\mathrm{C}$ and $^{14}\mathrm{N}(\mathrm{p},\gamma)^{15}\mathrm{O}$ reactions, whose reaction-rate variations only causes minor effects on $n_{\max}$ and $\tau_{\rm i}$ in the simulations with $X_0(\mathrm{H}) = 10^{-4}$ and $X_0(\mathrm{H}) = 10^{-3}$, now have more significant roles in the simulations with $X_0(\mathrm{H}) = 10^{-2}$. The factor-of-two increase of the neutron-recycling-reaction rate of the $^{14}\mathrm{N}(\mathrm{n},\mathrm{p})^{14}\mathrm{C}$ reaction decreases $n_{\max}$ and $\tau_{\rm i}$ by 49 % and 38 %, respectively. On the other hand, the variation of the $^{14}\mathrm{N}(\mathrm{p},\gamma)^{15}\mathrm{O}$ reaction rate increases $n_{\max}$ and $\tau_{\rm i}$ by 3 % and 71 %, respectively. Particularly this comparably large effect on $\tau_{\rm i}$ is notable. As evident from Figure 4.3c, the $^{14}\mathrm{N}(\mathrm{p},\gamma)^{15}\mathrm{O}$ reaction has a significant role in the destruction of ^{14}N in the simulation with $X_0(\mathrm{H}) = 10^{-2}$. An increase in the reaction rate of the $^{14}\mathrm{N}(\mathrm{p},\gamma)^{15}\mathrm{O}$ reaction strengthens this role and the increased destruction of the neutron poison ^{14}N results in higher densities of free neutrons. While this is only a minor effect at the time of the peak neutron density, Figure 4.2c shows how the increased ^{14}N destruction over time leads to a generally higher neutron density as time progresses after $n_{\max}$ has been reached. Consequently, the decrease of the neutron-density evolution is slowed down and this higher level of n over longer times causes the significant increase in the time-integrated i-process neutron exposure $\tau_{\rm i}$.

Overall, in this section we explore the roles that the individual charged-particle reactions have on the neutron production for i-process nucleosynthesis. In particular, we consider the effects that a factor-of-two increase of each reaction rate has at different ingested proton fractions, as the roles change for different $X_0(\mathrm{H})$. At low initial ingested proton fractions of $X_0(\mathrm{H}) = 10^{-4}$ the $^{12}\mathrm{C}(\mathrm{n},\gamma)^{13}\mathrm{C}$ reaction is a dominant neutron-recycling reaction, while the $^{13}\mathrm{N}(\mathrm{n},\mathrm{p})$and $^{14}\mathrm{N}(\mathrm{n},\mathrm{p})$reactions take over this role at $X_0(\mathrm{H}) \geq 10^{-3}$. Consequently, the role of the proton-capture reactions $^{12}\mathrm{C}(\mathrm{p},\gamma)^{13}\mathrm{N}$ and $^{13}\mathrm{C}(\mathrm{p},\gamma)^{14}\mathrm{N}$ gain importance in the neutron recycling process as starting point and breakout reaction, respectively, with increasing $X_0(\mathrm{H})$. Unsurprisingly, the main neutron producing reaction $^{13}\mathrm{C}(\alpha,\mathrm{n})^{16}\mathrm{O}$ has a significant impact on the maximum neutron density in all simulations. In comparison to the reaction flows and neutron-density evolutions of the reference simulations, this deepens and extends the understanding of neutron production and neutron recycling at i-process conditions presented in the previous chapter.

4.1.2 Realistic reaction-rate variations by factor uncertainties

While it is an instructive exercise to examine the changes in neutron production by varying reaction rates by a constant factor, it does not convey a realistic idea of the effects of physical reaction-rate uncertainties. Not all reaction rates are *"unknown by a factor of two"* and the statistical meaning of this statement remains unclear in the first place.

Thermonuclear-reaction rates are complex quantities, which incorporate many physical properties of the involved nuclei and their interactions. Simplifying this situation to a single reaction-rate value to be used at a given temperature is not trivial and involves many uncertainties. Traditionally, if reported at all, reaction rate uncertainties are presented in the form of upper and lower limits, whose statistical meaning is not well defined or even consistent. Over the past decade, efforts have been made to understand reaction rates as probability density functions with statistically meaningful uncertainties (Iliadis et al., 2015). Longland et al. (2010) first calculated such probability densities for reaction rates using Monte Carlo sampling techniques, which are discussed in a series of publications (see also Iliadis et al., 2010a,b,c) and included in the publicly available[2] STARLIB reaction rate library (Sallaska et al., 2013). In particular, recommended reaction rates and *factor uncertainties* are reported, where the reaction rate probability density function is approximated by a lognormal distribution. Analogous to the practice of reporting the standard deviation σ as uncertainty for quantities which follow a normal distribution, the reported factor uncertainties are a measure of the uncertainty of the reaction rates which follow a lognormal distribution. Even the specific statistical meaning of the factor uncertainty for a lognormal distribution is equivalent to the statistical meaning of the standard deviation for a normal distribution: the factor uncertainty with respect to the median describes the coverage probability of 68 % for the lognormal distribution. A comprehensive overview of addressing nuclear reaction rate uncertainties with statistical methods is given, e.g., by Longland et al. (2010), Iliadis et al. (2015) and Iliadis et al. (2016).

In Table 4.4 we list the previously discussed charged-particle reactions and their recommended reaction rates at a representative temperature of $T = 2 \times 10^8$ K from the JINA Reaclib database (Cyburt et al., 2010) and the STARLIB (Sallaska et al., 2013) database, as well as STARLIB's reported factor uncertainties for the same temperature. In most cases the recommended rates from the two databases are not the same and the extent of their differences varies. Particularly large differences arise for those reactions where STARLIB recommends the *taex* or *taly* rates. Both of these labels use the code TALYS (Koning et al., 2004, 2008; Goriely et al., 2008) to compute theoretical estimates for reaction rates based on the Hauser-Feshbach model, either to extrapolate experimentally determined rates (*taex*) or to provide a purely theoretical rate (*taly*). Note that a nominal factor-uncertainty value of 10 is recommended in STARLIB for the theoretical *taly* rates, which do not employ experimental cross section information.

In some cases the variation between the recommended Reaclib rates in our nuclear reaction network and the rates recommended in STARLIB vary by a factor that is larger than STARLIB's reported factor uncertainty. In these cases we adopt the discrepancy between both recommended rates as a more conservative measure for the factor uncertainty. The largest discrepancies arise for the $^{13}\mathrm{N}(\mathrm{n},\gamma)^{14}\mathrm{N}$ and $^{14}\mathrm{N}(\mathrm{n},\mathrm{p})^{14}\mathrm{C}$ reactions, where the STARLIB database recommends theoretical TALYS rates, which are a factor 87 lower and 309 higher, respectively, compared to the rates

[2] `http://starlib.physics.unc.edu/index.html`

recommended in Reaclib. Both of these reactions, as well as the ^{13}N(n, p)^{14}C reactions have theoretically predicted rates recommended by STARLIB and nominal factor uncertainties of 10. Due to the lack of experimental input and statistical meaning for the factor uncertainties of these rates, we exclude the ^{13}N(n, γ)^{14}N and ^{13}N(n, p)^{13}C factor uncertainties from the following discussion (but try to at least address variations of the ^{14}N(n, p)^{14}C reaction rate as outlined below).

Due to the high abundance and significant role of the neutron poison ^{14}N particularly for cases with high ingested proton fractions (see Chapter §3), it would be desirable to test the sensitivity of all relevant reaction rates, including the ^{14}N(n, p)^{14}C reaction, which absorbs neutrons but also provides protons that can lead to delayed neutron recycling instead of neutron poison. Instead of completely excluding this reaction with its factor uncertainty of 10 altogether, we compare the recommended Reaclib rate from Caughlan & Fowler (1988) in our network to the newer experimental data by Wallner et al. (2016). Using accelerator mass spectrometry measurements of the ^{14}N(n, p)^{14}C cross section, Wallner et al. (2016) found reaction rates that are about 15 to 20 % lower than the recommended Reaclib rate from Caughlan & Fowler (1988), which shows an even larger discrepancy to the theoretical TALYS rate recommended by STARLIB. We use this new experimental rate as motivation to include a hypothetical factor uncertainty of 1.2 for the ^{14}N(n, p)^{14}C reaction rate.

In Figure 4.4 we show the neutron-density evolution of our simulations where each reaction rate is varied by its factor uncertainty and in Tables 4.5, 4.6, and 4.7 we list the resulting $n_{\rm max}$ and $\tau_{\rm i}$. For the simulations with an ingested proton fraction of X_0(H) = 10^{-4} the maximum neutron densities vary between $2.4 \times 10^{14} \leq n_{\rm max} \leq 5.0 \times 10^{14}$ cm^{-3} around the reference value of $n_{\rm max} = 3.6 \times 10^{14}$ cm^{-3}. The i-process neutron exposures vary between $2.0 \leq \tau_{\rm i} \leq 2.4$ mbarn^{-1} around the reference value of $\tau_{\rm i} = 2.2$ mbarn^{-1}. For both quantities $n_{\rm max}$ and $\tau_{\rm i}$, it is the variation of the ^{12}C(n, γ)^{13}C reaction rate with the conservatively chosen factor uncertainty of 1.73 that causes the largest effect. This is not surprising given the important role that ^{12}C(n, γ)^{13}C has for the neutron-recycling flows at these low proton fractions, as discussed in the previous section.

Simulations with an ingested proton fraction of X_0(H) = 10^{-3} show a larger spread in $n_{\rm max}$ and $\tau_{\rm i}$. Here the maximum neutron densities vary between $8.2 \times 10^{14} \leq n_{\rm max} \leq 1.5 \times 10^{15}$ cm^{-3}around the reference value of $n_{\rm max} = 1.1 \times 10^{15}$ cm^{-3}and the i-process neutron exposures vary between $4.3 \leq \tau_{\rm i} \leq 5.3$ mbarn^{-1}around the reference value of $\tau_{\rm i} = 4.7$ mbarn^{-1}. As was the case for the reaction-rate variations by a constant factor of two, it is the ^{13}C(α, n)^{16}O rate whose rate changes have the largest effect on the maximum neutron density that can be reached, along with the reaction rate changes of ^{14}N(n, p)^{14}C, which have a similar effect. However, the large effects on $\tau_{\rm i}$ that were observed in the previous section when the ^{12}C(p, γ)^{13}N and ^{13}C(p, γ)^{14}N reaction rates were varied by a factor of two, are not observed here. This is because their factor uncertainties are relatively small compared to the other reactions and only indicate a 12 % and 17 % rate variations, respectively. Instead, the increase of the ^{13}C(n, γ)^{14}C reaction rate by its large adopted factor uncertainty of 3.10 leads to the lowest $\tau_{\rm i}$. The highest $\tau_{\rm i}$ on the other hand is a result of the decreased ^{14}N(n, p)^{14}C reaction rate, which is compatible with the measurements by Wallner et al. (2016).

Finally, the spread of $n_{\rm max}$ for simulations with X_0(H) = 10^{-2} extends between $2.7 \times 10^{14} \leq n_{\rm max} \leq 1.0 \times 10^{15}$ cm^{-3}around the reference value of $n_{\rm max} = 5.3 \times 10^{15}$ cm^{-3}. Both the highest and lowest $n_{\rm max}$ are the results of the reaction-rate variations of the ^{14}N(n, p)^{14}C reaction rate. The

Table 4.4: **Reaction-rate comparison.** Nuclear-reaction rates for important charged-particle reactions from our standard JINA Reaclib database compared to the STARLIB database with factor uncertainties *f.u.*. Rates are listed at the representative temperature $T = 2 \times 10^8$ K in units of $\mathrm{cm^3\,mol^{-1}\,s^{-1}}$.

	JINA Reaclib		STARLIB			
Reaction	rate	ref	rate	*f.u.*	ref	adopted *f.u.*
^{12}C(p,γ)^{13}N	9.7×10^{-3}	ls09	8.6×10^{-3}	1.11	nacr	1.12
^{12}C(n,γ)^{13}C	1.5×10^{3}	ka02	2.7×10^{3}	1.07	taex	1.73
^{13}C(p,γ)^{14}N	3.0×10^{-2}	nacr	2.9×10^{-2}	1.17	nacr	1.17
^{13}C(α,n)^{16}O	3.3×10^{-8}	gl12	3.8×10^{-8}	1.44	nacr	1.44
^{13}C(n,γ)^{14}C	1.2×10^{3}	ka02	3.8×10^{3}	1.19	taex	3.10
^{13}N(p,γ)^{14}O	2.3×10^{-3}	lg06	1.4×10^{-3}	1.39	nacr	1.58
^{13}N(n,γ)^{14}N	1.1×10^{6}	wies	1.3×10^{4}	10.00	taly	10.00
^{13}N(n,p)^{13}C	1.0×10^{8}	nacr	7.0×10^{8}	10.00	taly	10.00
^{14}N(p,γ)^{15}O	7.8×10^{-3}	im05	7.8×10^{-3}	1.05	im05	1.05
^{14}N(n,γ)^{15}N	7.5×10^{3}	ka02	6.9×10^{3}	2.46	taex	2.46
^{14}N(n,p)^{14}C	3.1×10^{5}	cf88	9.5×10^{7}	10.00	taly	1.2*

* We adopt this factor uncertainty for the ^{14}N(n,p)^{14}C reaction rate based on experimental rate measurements by Wallner et al. (2016) compared to Reaclib's recommended cf88 rate (see main text for discussion).

References – (cf88) Caughlan & Fowler (1988); (gl12) Guo et al. (2012); (im05) Imbriani et al. (2005); (ka02) Dillmann et al. (2006); (lg06) Li et al. (2006); (ls09) Li et al. (2010); (nacr) Angulo et al. (1999); (taex) Koning et al. (2004, 2008); Goriely et al. (2008); (taly) Koning et al. (2004, 2008); Goriely et al. (2008); (wies) Wiescher (2000)

same is true for the maximum i-process neutron exposures, where the ^{14}N(n, p)^{14}C reaction-rate variations cause a spread of $0.8 \leq \tau_{\mathrm{i}} \leq 1.7\,\mathrm{mbarn}^{-1}$around the reference value of $\tau_{\mathrm{i}} = 1.0\,\mathrm{mbarn}^{-1}$. As previously discussed, the influence of the neutron poison ^{14}N on the availability of free neutrons for the i process increases with higher ingested proton fractions. Therefore it is not surprising that the simulations with $X_0(\mathrm{H}) = 10^{-2}$ show such a large dependence of n_{max} and τ_{i} on the ^{14}N(n, p)^{14}C reaction rate.

4.1.3 Impact on heavy-element abundance patterns

The previous section has shown how realistic reaction rate uncertainties influence the i-process neutron production. An important question remains how these different neutron-density evolutions with their various n_{max} and τ_{i} impact the heavy-element production by the i process.

Figure 4.5 shows abundance patterns for the simulations with $X_0(\mathrm{H}) = 10^{-4}$ and $X_0(\mathrm{H}) = 10^{-3}$ with the factor-uncertainty variations to the reaction rates. The two times at which the abundance patterns for the different simulations are shown are (*i*) at the time when each simulation reaches a representative exposure of $\tau = 2.0$ mbarn^{-1} and (*ii*) when the neutron density of each simulation

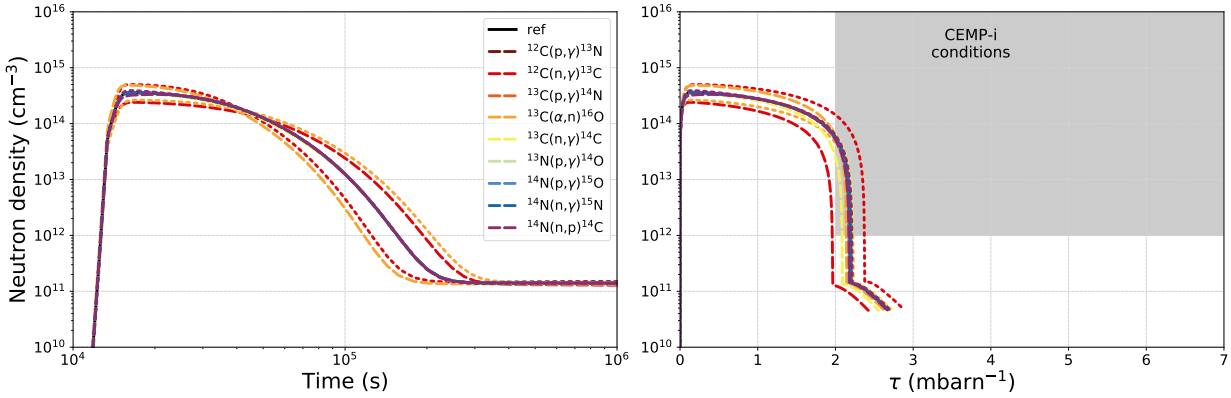

(A) Initially ingested proton fraction $X_0(\mathrm{H}) = 10^{-4}$.

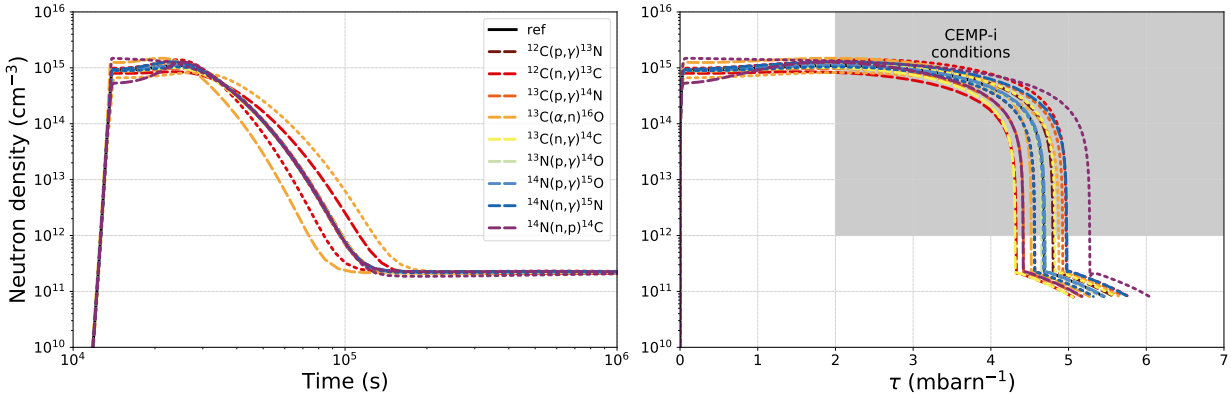

(B) Initially ingested proton fraction $X_0(\mathrm{H}) = 10^{-3}$.

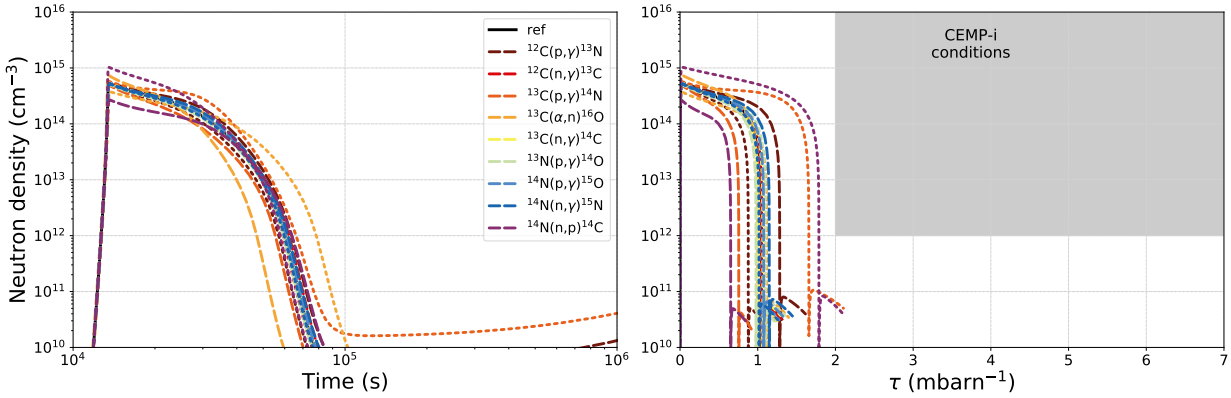

(C) Initially ingested proton fraction $X_0(\mathrm{H}) = 10^{-2}$.

Figure 4.4: **Reaction-rate variations by factor uncertainty: neutron-density evolution.** Same as Figure 4.2 but for variations of each reaction rate by its factor uncertainty. Dashed lines show the rate increase and dotted lines the rate decrease.

Table 4.5: **Reaction-rate variations by factor uncertainty: $n_{\max}$ and $\tau_{\rm i}$ for $X_0(\mathrm{H}) = 10^{-4}$.** Same as Table 4.1 but for reaction-rate variations by each reaction's factor uncertainty. An increased and decreased reaction rate is considered for each reaction (indicated as high and low rate in the rate column).

Reaction	rate	$n_{\max}$ (cm^{-3})	$\Delta n_{\max}$ (cm^{-3})	$\Delta n_{\max}$ (rel) (%)	$\tau_{\rm i}$ (mbarn^{-1})	$\Delta\tau_{\rm i}$ (mbarn^{-1})	$\Delta\tau_{\rm i}$ (rel) (%)
reference	–	3.60×10^{14}	–	–	2.19	–	–
$^{12}\mathrm{C}(\mathrm{p},\gamma)^{13}\mathrm{N}$	high	3.63×10^{14}	3.80×10^{12}	1.1	2.20	0.01	0.5
	low	3.56×10^{14}	-3.89×10^{12}	−1.1	2.18	−0.01	−0.6
$^{12}\mathrm{C}(\mathrm{n},\gamma)^{13}\mathrm{C}$	high	2.40×10^{14}	-1.19×10^{14}	−33.1	1.96	−0.23	−10.5
	low	5.01×10^{14}	1.41×10^{14}	39.2	2.37	0.18	8.4
$^{13}\mathrm{C}(\mathrm{p},\gamma)^{14}\mathrm{N}$	high	3.56×10^{14}	-3.46×10^{12}	−1.0	2.18	−0.01	−0.6
	low	3.63×10^{14}	3.26×10^{12}	0.9	2.20	0.01	0.5
$^{13}\mathrm{C}(\alpha,\mathrm{n})^{16}\mathrm{O}$	high	4.85×10^{14}	1.25×10^{14}	34.9	2.14	−0.05	−2.2
	low	2.64×10^{14}	-9.52×10^{13}	−26.5	2.23	0.04	1.7
$^{13}\mathrm{C}(\mathrm{n},\gamma)^{14}\mathrm{C}$	high	3.54×10^{14}	-5.13×10^{12}	−1.4	2.09	−0.10	−4.7
	low	3.61×10^{14}	1.75×10^{12}	0.5	2.22	0.04	1.6
$^{13}\mathrm{N}(\mathrm{p},\gamma)^{14}\mathrm{O}$	high	3.59×10^{14}	-5.28×10^{11}	−0.1	2.19	< 0.01	−0.1
	low	3.60×10^{14}	3.56×10^{11}	0.1	2.19	< 0.01	−0.1
$^{14}\mathrm{N}(\mathrm{p},\gamma)^{15}\mathrm{O}$	high	3.60×10^{14}	1.29×10^{10}	< 0.1	2.19	< 0.01	−0.1
	low	3.59×10^{14}	-1.24×10^{10}	< 0.1	2.19	< 0.01	−0.1
$^{14}\mathrm{N}(\mathrm{n},\gamma)^{15}\mathrm{N}$	high	3.62×10^{14}	2.63×10^{12}	0.7	2.19	0.01	0.2
	low	3.58×10^{14}	-1.08×10^{12}	−0.3	2.18	< 0.01	−0.2
$^{14}\mathrm{N}(\mathrm{n},\mathrm{p})^{14}\mathrm{C}$	high	3.33×10^{14}	-2.68×10^{13}	−7.5	2.17	−0.02	−0.8
	low	3.90×10^{14}	3.09×10^{13}	8.6	2.21	0.02	1.1

Table 4.6: **Reaction-rate variations by factor uncertainty: n_{max} and τ_i for $X_0(H) = 10^{-3}$.** Same as Table 4.5 but for simulations with ingested proton fractions of $X_0(H) = 10^{-3}$.

Reaction	rate	n_{max} (cm^{-3})	Δn_{max} (cm^{-3})	Δn_{max} (rel) (%)	τ_i ($mbarn^{-1}$)	$\Delta\tau_i$ ($mbarn^{-1}$)	$\Delta\tau_i$ (rel) (%)
reference	–	1.10×10^{15}	–	–	4.68	–	–
$^{12}C(p,\gamma)^{13}N$	high	1.14×10^{15}	3.97×10^{13}	3.6	4.80	0.11	2.4
	low	1.06×10^{15}	-4.15×10^{13}	−3.8	4.56	−0.12	−2.6
$^{12}C(n,\gamma)^{13}C$	high	8.51×10^{14}	-2.51×10^{14}	−22.7	4.33	−0.36	−7.7
	low	1.40×10^{15}	2.94×10^{14}	26.7	4.97	0.28	6.1
$^{13}C(p,\gamma)^{14}N$	high	9.76×10^{14}	-1.26×10^{14}	−11.4	4.42	−0.27	−5.7
	low	1.23×10^{15}	1.25×10^{14}	11.4	4.92	0.24	5.1
$^{13}C(\alpha,n)^{16}O$	high	1.48×10^{15}	3.83×10^{14}	34.7	4.52	−0.17	−3.5
	low	8.25×10^{14}	-2.77×10^{14}	−25.1	4.87	0.19	4.0
$^{13}C(n,\gamma)^{14}C$	high	1.01×10^{15}	-9.18×10^{13}	−8.3	4.31	−0.37	−8.0
	low	1.14×10^{15}	3.45×10^{13}	3.1	4.82	0.14	2.9
$^{13}N(p,\gamma)^{14}O$	high	1.09×10^{15}	-1.27×10^{13}	−1.2	4.65	−0.03	−0.7
	low	1.11×10^{15}	8.38×10^{12}	0.8	4.70	0.02	0.4
$^{14}N(p,\gamma)^{15}O$	high	1.11×10^{15}	4.66×10^{12}	0.4	4.69	0.01	0.2
	low	1.10×10^{15}	-4.79×10^{12}	−0.4	4.67	−0.01	−0.2
$^{14}N(n,\gamma)^{15}N$	high	1.28×10^{15}	1.77×10^{14}	16.0	4.98	0.29	6.2
	low	1.03×10^{15}	-6.89×10^{13}	−6.3	4.56	−0.12	−2.6
$^{14}N(n,p)^{14}C$	high	1.26×10^{15}	1.60×10^{14}	14.5	4.41	−0.27	−5.8
	low	1.48×10^{15}	3.83×10^{14}	34.8	5.27	0.59	12.6

Table 4.7: **Reaction-rate variations by factor uncertainty: n_{max} and τ_i for $X_0(H) = 10^{-2}$.** Same as Table 4.5 but for simulations with ingested proton fractions of $X_0(H) = 10^{-2}$.

Reaction	rate	n_{max} (cm^{-3})	Δn_{max} (cm^{-3})	Δn_{max} (rel) (%)	τ_i ($mbarn^{-1}$)	$\Delta\tau_i$ ($mbarn^{-1}$)	$\Delta\tau_i$ (rel) (%)
reference	–	5.27×10^{14}	–	–	1.05	–	–
$^{12}C(p,\gamma)^{13}N$	high	5.60×10^{14}	3.31×10^{13}	6.3	1.28	0.23	22.2
	low	4.96×10^{14}	-3.03×10^{13}	−5.8	0.88	−0.17	−16.3
$^{12}C(n,\gamma)^{13}C$	high	5.22×10^{14}	-4.60×10^{12}	−0.9	1.05	< 0.01	−0.2
	low	5.29×10^{14}	2.70×10^{12}	0.5	1.05	< 0.01	0.1
$^{13}C(p,\gamma)^{14}N$	high	4.89×10^{14}	-3.79×10^{13}	−7.2	0.76	−0.29	−28.0
	low	5.68×10^{14}	4.18×10^{13}	7.9	1.66	0.61	58.0
$^{13}C(\alpha,n)^{16}O$	high	7.26×10^{14}	1.99×10^{14}	37.9	1.00	−0.05	−5.0
	low	3.75×10^{14}	-1.52×10^{14}	−28.8	1.12	0.07	6.4
$^{13}C(n,\gamma)^{14}C$	high	5.21×10^{14}	-5.63×10^{12}	−1.1	1.00	−0.04	−4.3
	low	5.29×10^{14}	1.84×10^{12}	0.3	1.06	0.02	1.5
$^{13}N(p,\gamma)^{14}O$	high	5.08×10^{14}	-1.86×10^{13}	−3.5	0.98	−0.07	−6.9
	low	5.41×10^{14}	1.44×10^{13}	2.7	1.10	0.05	5.0
$^{14}N(p,\gamma)^{15}O$	high	5.27×10^{14}	4.96×10^{11}	0.1	1.08	0.03	2.6
	low	5.26×10^{14}	-6.31×10^{11}	−0.1	1.02	−0.03	−2.4
$^{14}N(n,\gamma)^{15}N$	high	5.26×10^{14}	-1.12×10^{12}	−0.2	1.15	0.10	9.4
	low	5.27×10^{14}	5.92×10^{11}	0.1	1.02	−0.03	−3.2
$^{14}N(n,p)^{14}C$	high	2.68×10^{14}	-2.59×10^{14}	−49.1	0.65	−0.40	−37.9
	low	1.02×10^{15}	4.98×10^{14}	94.6	1.79	0.74	70.3

has decreased to $n = 10^{12}$ cm^{-3}, i.e. the simulation has reached its $\tau_{\rm i}$ value. We show the abundance pattern at the given point in time in each simulation, as well as the "decayed" abundances, i.e. when a time of 10 Myr is considered for unstable species to decay into their stable isobars.

In Figure 4.5a it can be seen that the simulations with $X_0(\mathrm{H}) = 10^{-4}$ develop a spread of heavy-element abundances when they reach $\tau = 2$ mbarn^{-1}, where the largest spreads of up to 1.5 dex occur for the elements around $Z \approx 80$. Even when decays of unstable isotopes are taken into account, which rearranges the elemental abundances, spreads of approximately 1 dex remain, particularly for elements heavier than europium ($Z = 63$). Interestingly the various abundance patterns for the elements with $Z > 63$ show a constant offset between each other and the relative abundance ratios between the elements remains unaffected. Additionally, the abundances of the representative s-process elements Sr and Ba also show almost no variation.

The highest abundances are produced by the simulation with an increased $^{12}\mathrm{C}(\mathrm{n},\gamma)^{13}\mathrm{C}$ reaction rate. Recall from the previous sections that for proton fractions of $X_0(\mathrm{H}) = 10^{-4}$ this is the simulation with the lowest $n_{\rm max}$ and also the lowest n at the shown point in time of $\tau = 2$ mbarn^{-1}. As shown in Hampel et al. (2019), the neutron-capture path and the heavy-element production progresses faster (in terms of exposure) for lower neutron densities (see Figure 2.1), because the neutron-capture path stays closer to the valley of stability where the nuclei have higher neutron-capture cross sections compared to more neutron rich isotopes. Since the exposure of the simulation with an increased $^{12}\mathrm{C}(\mathrm{n},\gamma)^{13}\mathrm{C}$ reaction rate was built up mainly at lower neutron densities, the heavy-element production phase has progressed further at $\tau = 2$ mbarn^{-1} compared to the other simulations. Consequently, the opposite effect takes place for simulations with a decreased $^{12}\mathrm{C}(\mathrm{n},\gamma)^{13}\mathrm{C}$ reaction rate, which experience the highest $n_{\rm max}$ and show the lowest heavy-element abundances in Figure 4.5a.

Another effect of the different neutron-densities before and at the time of $\tau = 2$ mbarn^{-1} can be seen in Figure 4.5a around the second s-process peak, which traditionally is located around the element barium ($Z = 56$) but extends also to lighter elements for the i process. The simulation with an increased $^{12}\mathrm{C}(\mathrm{n},\gamma)^{13}\mathrm{C}$ reaction rate shows a peak at caesium ($Z = 55$), which is absent for the other simulations. In turn, the other simulations show higher abundances for the neighbouring lighter elements, particularly iodine ($Z = 53$), compared to the simulation with an increased $^{12}\mathrm{C}(\mathrm{n},\gamma)^{13}\mathrm{C}$ reaction rate. The elements at the second s-process peak have isotopes with the magic neutron number 82 on the neutron-capture path and act as bottlenecks for the neutron-capture flow and the successive production of heavier elements. For higher neutron densities the isotopes with magic neutron numbers will be reached at lighter elements, which causes a shift of the second s-process peak to lower Z. In particular, the lower neutron density of the simulation with an increased $^{12}\mathrm{C}(\mathrm{n},\gamma)^{13}\mathrm{C}$ reaction rate causes the neutron-capture path to stay closer to the valley of stability where the majority of isotopes with $N = 82$ are produced as stable ^{136}Xe ($Z = 54$), with a considerable production of unstable ^{137}Cs as well. In contrast to that, the other simulations with their higher neutron densities and a neutron-capture path further away from the valley of stability, produce a higher fraction of ^{135}I instead. However, Figure 4.5a (compare left to right panel) also shows that this difference in abundance pattern for the second s-process peak largely disappears after the unstable isotopes had time to decay, when the unstable ^{135}I is converted into stable ^{135}Ba and ^{137}Cs into ^{137}Ba. These decays also become apparent in Figure 4.5a as an increase in barium abundance for all simulations, when comparing the abundance pattern created while the neutron

source is active with the abundance pattern post decays.

Another way to compare abundance patterns from the simulations with varied reaction rates is shown in Figure 4.5b. Here each simulation is shown at its respective τ_{i} when the produced neutron density has decreased to $n = 10^{12}\,\mathrm{cm}^{-3}$ and further heavy-element production occurs only under more s-process-like conditions. The spread of abundances in this case is largest for the heaviest elements at the Pb peak, where abundance variations of approximately 0.8 dex occur. This is less than in the previous case where abundance patterns were compared at the same exposure of $\tau = 2$ mbarn^{-1}. The highest heavy-element abundances are produced in the simulation with a decreased $^{13}\mathrm{C}(\alpha,\mathrm{n})^{16}\mathrm{O}$ reaction rate, whereas the abundance spreads from the $^{12}\mathrm{C}(\mathrm{n},\gamma)^{13}\mathrm{C}$ reaction-rate variation noted at $\tau = 2$ mbarn^{-1} are reduced. As pointed out in previous sections, the variations of the $^{13}\mathrm{C}(\alpha,\mathrm{n})^{16}\mathrm{O}$ reaction rate influence the value of n_{max} while they only have minimal effects on τ_{i}, whereas the $^{12}\mathrm{C}(\mathrm{n},\gamma)^{13}\mathrm{C}$ reaction-rate variations influence both n_{max} and τ_{i}. Therefore the higher levels of heavy-element production, which the simulation with an increased $^{12}\mathrm{C}(\mathrm{n},\gamma)^{13}\mathrm{C}$ reaction-rate experiences due to the smaller n, evens out with less heavy-element production over time, as the total τ_{i} is reduced (and vice-versa for a reaction rate decrease). Without this simultaneous change in τ_{i}, the rate variations for the $^{13}\mathrm{C}(\alpha,\mathrm{n})^{16}\mathrm{O}$ reactions only influence the neutron-capture cross sections the neutron-capture path encounters, which leaves its imprints at the time of final τ_{i}.

For simulations with $X_0(\mathrm{H}) = 10^{-3}$ (see Figure 4.5c and 4.5d) a similar interplay between neutron density and neutron exposure can be seen, but to a much lesser extent. At $\tau = 2$ mbarn^{-1} the spread of abundances for elements heavier than barium is about 0.7 dex (both with active neutron production as well as for the decayed abundance pattern). At their respective τ_{i} the simulations show abundance patterns that only exhibit small spreads of 0.4 dex for the lead peak and the stable barium abundance, stemming from a spread in the abundance of unstable $^{135}\mathrm{I}$ previous to the decays.

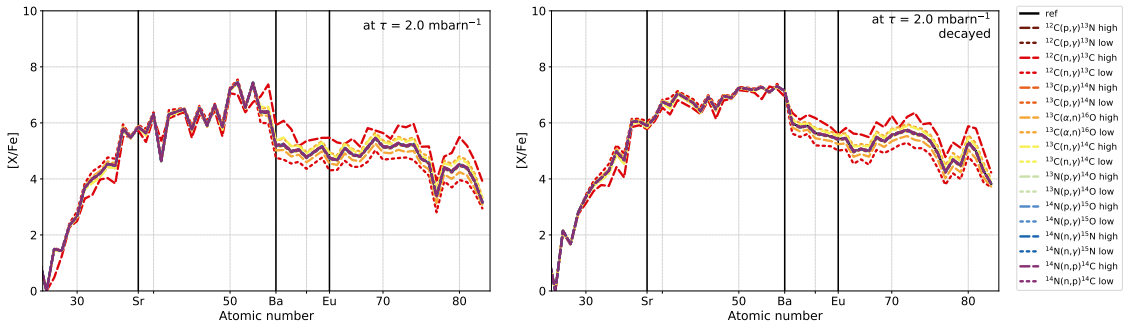

(A) $X_0(\mathrm{H}) = 10^{-4}$: abundance patterns at the same neutron exposure of $\tau = 2$ mbarn^{-1}.

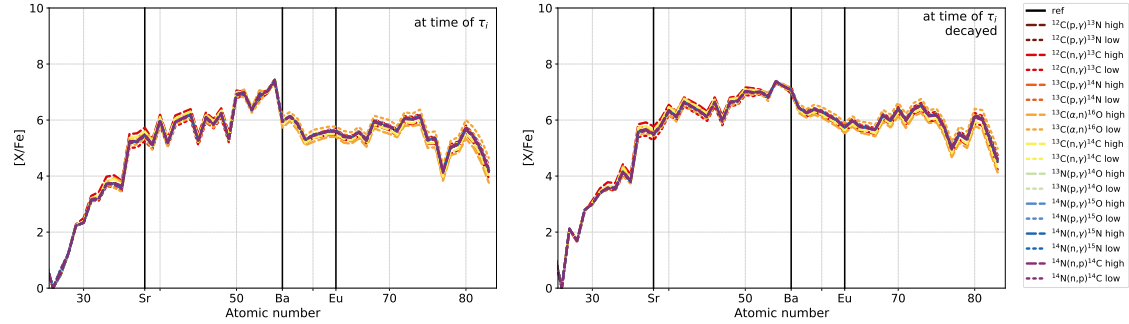

(B) $X_0(\mathrm{H}) = 10^{-4}$: abundance pattern shown at the respective τ_i (see Table 4.5) for each simulation.

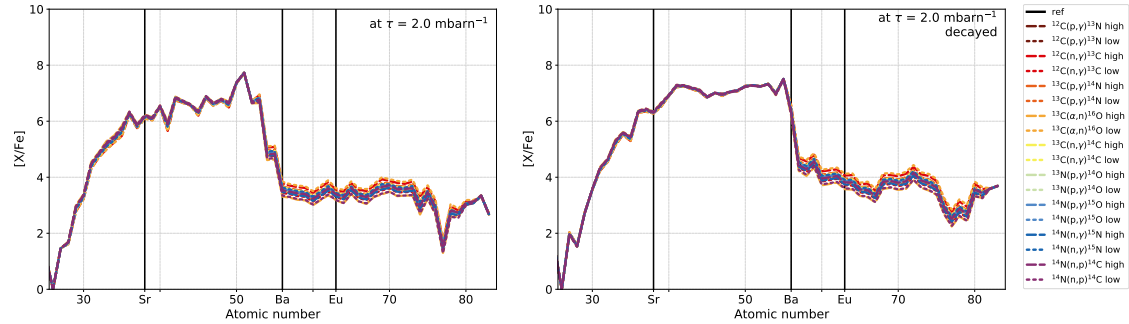

(C) $X_0(\mathrm{H}) = 10^{-3}$: abundance patterns at the same neutron exposure of $\tau = 2$ mbarn^{-1}.

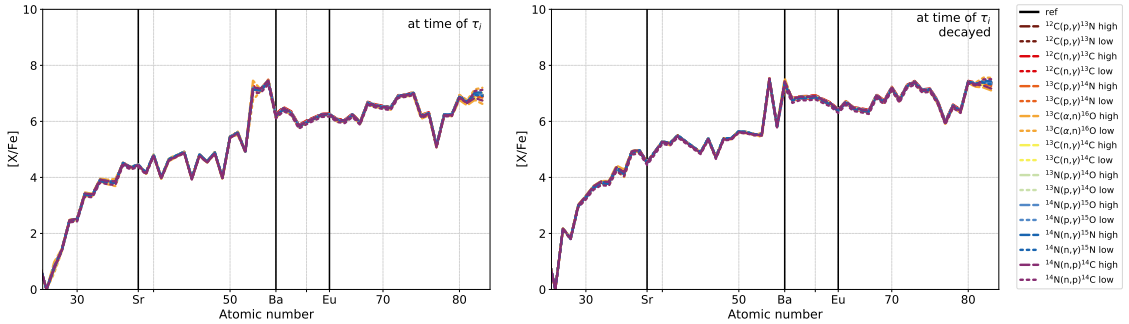

(D) $X_0(\mathrm{H}) = 10^{-3}$: abundance pattern shown at the respective τ_i (see Table 4.6) for each simulation.

Figure 4.5: **Reaction-rate variations by factor uncertainty: abundance patterns.** For simulations with ingested proton fractions of $X_0(\mathrm{H}) = 10^{-4}$ and $X_0(\mathrm{H}) = 10^{-3}$ and reaction rates varied by their factor uncertainties, the resulting heavy-element abundance patterns are shown. The abundances are shown when the neutron source is still active (left panel) and after 10Myr of decays (right panel). The abundances are shown at the time when each simulation reaches a representative neutron exposure of $\tau = 2$ mbarn^{-1} and when the neutron density has declined to $n = 10^{12}$ cm^{-3}.

4.2 Initial abundances

So far, the neutron-production and i-process simulations have been explored in the context of a proton-ingestion episode in a low-mass, low-metallicity AGB star. The initial abundances of some key species are $X_0(^4\mathrm{He}) = 0.77$, $X_0(^{12}\mathrm{C}) = 0.22$, and $X_0(^{16}\mathrm{O}) = 7 \times 10^{-3}$, representative of a standard AGB intershell composition (Karakas & Lattanzio, 2014). However, the abundances of AGB intershell regions, and of the ^{12}C abudnance in particular, can depend on multiple model-dependent factors. E.g., for low-metallicity stars in particular the ^{12}C abundance in the intershell needs to build up over time before reaching the typical value of $X_0(^{12}\mathrm{C}) \approx 0.2$ (Lugaro et al., 2012, e.g.,). This build up of ^{12}C increases from one thermal pulse to the next, but the abundance of ^{12}C also changes throughout each thermal pulse. Depending on when the proton-ingestion episode happens, a different amount of ^{12}C may be present in the intershell to capture the ingested protons. For proton-ingestion episodes which are likely to occur just shortly after the onset of one of the early thermal pulses the ^{12}C abundances in the intershell can be particularly low. Considering the opposite extreme, model-dependent parameters such as convective overshooting can significantly enhance the ^{12}C abundance in the intershell and may provide much higher ^{12}C abundances (e.g., Herwig, 2000; Kamath et al., 2012; Pignatari et al., 2016).

Here we want to address one of the many uncertainties concerning the exact conditions of i-process nucleosynthesis by investigating how a range of initial ^{12}C abundances affects the neutron production and subsequent heavy-element nucleosynthesis.

4.2.1 Variations of initial ^{12}C

Figure 4.6 shows the neutron-density evolutions for different initial abundances of ^{12}C in the range of $0.1 \leq X_0(^{12}\mathrm{C}) \leq 0.5$. For the simulations with the lowest ingested proton fraction of $X_0(\mathrm{H}) = 10^{-4}$ the maximum reached neutron density for each simulation increases with decreasing initial ^{12}C. Based on this higher n_{max} the final i-process neutron exposure τ_{i} also increases with decreasing initial ^{12}C. However, the maximum $\tau_{\mathrm{i}} = 2.2\mathrm{mbarn}^{-1}$ is reached for the reference simulation with $X_0(^{12}\mathrm{C}) = 0.22$ after which a further decrease of initial ^{12}C does not lead to further significant increase of τ_{i}. As described earlier and visible, e.g., from Figure 4.3a, the $^{12}\mathrm{C}(\mathrm{n},\gamma)^{13}\mathrm{C}$ reaction is the dominant neutron absorber at $X_0(\mathrm{H}) = 10^{-4}$ and the ^{12}C abundance thereby directly influences the density of free neutrons. Integrated over time, the higher neutron densities produced by simulations with lower $X_0(^{12}\mathrm{C})$ also lead to higher τ_{i}.

Besides the maximum neutron density, the simulations with different $X_0(^{12}\mathrm{C})$ also show different shapes of their neutron-density evolutions: the simulations with highest ^{12}C abundance show the slowest decline in neutron density and the evolution is stretched out over longer times. As a consequence, it takes approximately three times longer for the simulation with $X_0(^{12}\mathrm{C}) = 0.5$ until the neutron density drops below a characteristic value of $n = 10^{12}\,\mathrm{cm}^{-3}$, compared to the simulation with a low initial $X_0(^{12}\mathrm{C}) = 0.1$. This slower decline of the neutron density is an effect of enhanced neutron-recycling reactions. The neutron-recycling flows are also determined by the $^{12}\mathrm{C}(\mathrm{n},\gamma)^{13}\mathrm{C}$ reaction flow which is higher for larger $X_0(^{12}\mathrm{C})$. Therefore the depletion of ^{13}C by the $^{13}\mathrm{C}(\alpha,\mathrm{n})^{16}\mathrm{O}$ reaction can be counteracted more strongly through partial ^{13}C replenishment by higher $^{12}\mathrm{C}(\mathrm{n},\gamma)^{13}\mathrm{C}$ reaction flows and a higher neutron density can be sustained longer.

Due to the higher initial proton fraction compared to the previously discussed simulations with

$X_0(\mathrm{H}) = 10^{-4}$, the simulations with $X_0(\mathrm{H}) = 10^{-3}$ experience higher levels of ^{13}C and ^{14}N production. Particularly $^{14}\mathrm{N}(\mathrm{n},\mathrm{p})^{14}\mathrm{C}$ contributes to the neutron-recycling flow, which contributes to replenishing ^{13}C and keeping up i-process neutron exposures over a longer period of time. Compared to the simulations with $X_0(\mathrm{H}) = 10^{-4}$, the enhanced neutron-recycling flows have a stronger effect on the neutron exposures that can build up at high neutron densities and consequently the simulations with higher $X_0(^{12}\mathrm{C})$ can reach the highest τ_i.

For simulations at $X_0(\mathrm{H}) = 10^{-2}$, Figure 4.6c shows that both n_max and τ_i increase with initial ^{12}C abundance. As discussed in previous sections, the high ^{14}N abundances that get produced by the high initial proton fractions for the reference case with $X_0(^{12}\mathrm{C}) = 0.22$ lead to a relatively fast decline of the produced neutron density, such that only a low neutron exposure can build up at i-process neutron densities, which results in $\tau_\mathrm{i} = 1.1\,\mathrm{mbarn}^{-1}$. A decrease in initial ^{12}C abundance leads to an even lower ^{13}C to ^{14}N ratio, which results in lower n_max and consequently even lower τ_i. However, for initial ^{12}C abundances above $X_0(^{12}\mathrm{C}) \geq 0.3$ the produced ^{14}N abundance is low enough, such that ^{14}N is destroyed quicker than ^{13}C. This leads to a plateau in the neutron-density evolution and even a further neutron-production phase at around 3×10^4 s. This extended time at high neutron densities has a large influence on the total i-process neutron density, which increases up to $\tau_\mathrm{i} = 4.6\,\mathrm{mbarn}^{-1}$.

4.2.2 The importance of the proton to ^{12}C ratio

The relative abundances of ^{13}C to ^{14}N are an important factor for the production of free neutrons, and are largely determined by the initial proton to ^{12}C ratio[3] $Y_\mathrm{p}/Y(^{12}\mathrm{C})$. This is well known from studies on the formation and activation of ^{13}C pockets for the s process (e.g., Jorissen & Arnould, 1989; Gallino et al., 1998; Goriely & Mowlavi, 2000; Lugaro et al., 2003) . In a simplified scenario, the formation of a ^{13}C pocket for the s process requires a higher number of ^{13}C nuclei than ^{14}N nuclei, such that not all released neutrons can be captured by the neutron poison ^{14}N. More precisely, this idea leads to the requirement of a higher reaction flow of $^{13}\mathrm{C}(\alpha,\mathrm{n})^{16}\mathrm{O}$ compared to the sum of all neutron poison reactions, which is indeed dominated by the high neutron-capture cross section of ^{14}N. In order to have the required high ^{13}C to ^{14}N ratio at the activation of the ^{13}C pocket, the initial proton to ^{12}C number ratio is crucial. Typical values in the literature that are considered for efficient s-process nucleosynthesis are, e.g., $Y_\mathrm{p}/Y(^{12}\mathrm{C}) \leq 0.1$ (Gallino et al., 1998), $0.005 \lesssim Y_\mathrm{p}/Y(^{12}\mathrm{C}) \lesssim 2$ (Goriely & Mowlavi, 2000), or $Y_\mathrm{p}/Y(^{12}\mathrm{C}) \lesssim 0.3$ (Lugaro et al., 2003).

We have confirmed that these concepts known from s-process nucleosynthesis, such as requirements of the right $Y_\mathrm{p}/Y(^{12}\mathrm{C})$ and high ^{13}C to ^{14}N ratios, apply just as much to neutron production for i-process nucleosynthesis. However, the previous tests have also shown that the neutron-recycling flows and the various reactions that dominate those flows under different conditions can have effects on the overall neutron production and particularly on the neutron exposures that can be achieved at i-process neutron densities. We have seen in the previous chapter and sections, that the absolute magnitude of these neutron recycling flows, and also the consequent leak of neutrons, depends on the available neutron densities, as well as the abundances of the CN species that capture the protons and neutrons in the recycling reactions.

[3]Different nomenclatures are used in the literature to denote the proton to ^{12}C ratio. Here we adopt the notation by Goriely & Mowlavi (2000) where Y_p is the initial proton abundance and $Y(^{12}\mathrm{C}) = X(^{12}\mathrm{C})/12$ the abundance of ^{12}C by number.

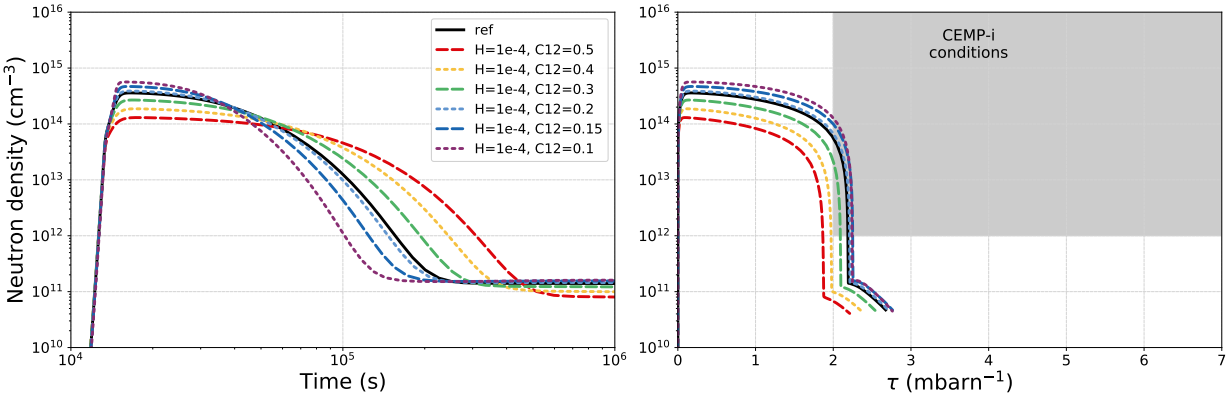

(A) Initially ingested proton fraction $X_0(\mathrm{H}) = 10^{-4}$.

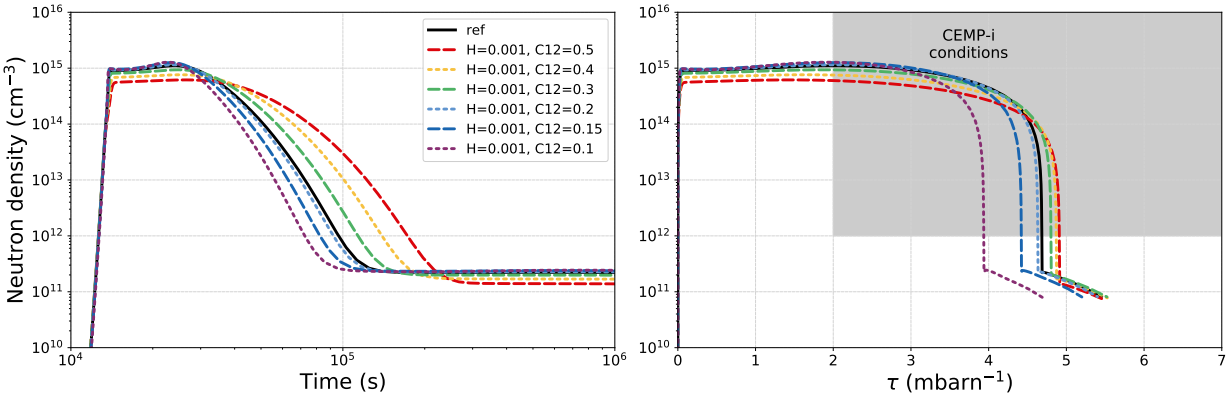

(B) Initially ingested proton fraction $X_0(\mathrm{H}) = 10^{-3}$.

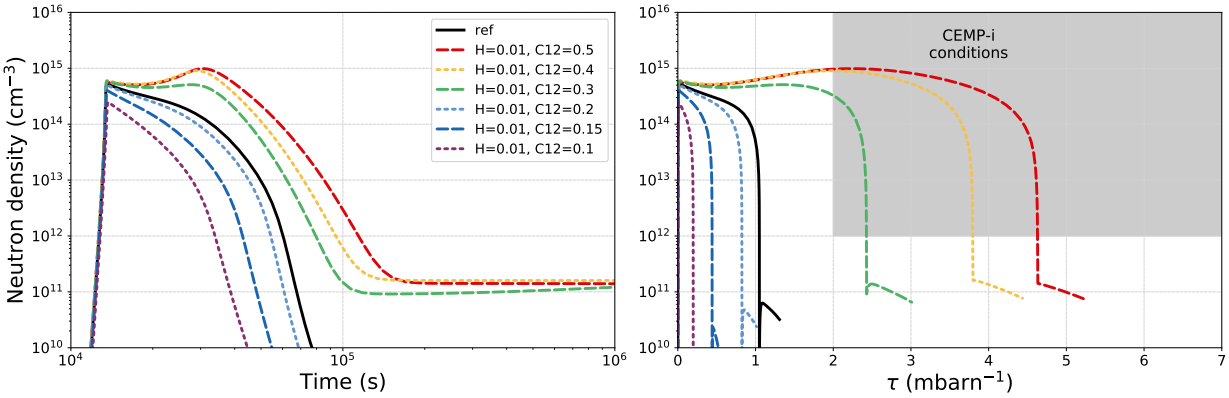

(C) Initially ingested proton fraction $X_0(\mathrm{H}) = 10^{-2}$.

FIGURE 4.6: **Initial abundance variation of ^{12}C: neutron-density evolution.** Same as Figure 4.2 but for variations of initial ^{12}C abundances.

In Figure 4.7 we show the previously introduced simulations with different initial $X_0(^{12}\mathrm{C})$ and $X_0(\mathrm{H})$, which naturally cover a range of initial $Y_\mathrm{p}/Y(^{12}\mathrm{C})$. Figure 4.7 summarises the discussed characteristics, such as $^{13}\mathrm{C}$ to $^{14}\mathrm{N}$ ratio, maximum neutron density n_max, and i-process neutron exposure τ_i as a function of their respective $Y_\mathrm{p}/Y(^{12}\mathrm{C})$. The $^{13}\mathrm{C}$ to $^{14}\mathrm{N}$ ratio (shown in both panels) is shown in two different ways: (*i*) the ratio is shown when our parcel of material reaches the highest temperature at the bottom of the convective zone, and (*ii*) the ratio of the overall maximum reached abundances of $^{13}\mathrm{C}$ and $^{14}\mathrm{N}$ are shown, which is not necessarily at the same point in time for the two isotopes. In particular, it can be seen that the simulations with the lowest initially ingested proton fractions have a lower $^{13}\mathrm{C}_\mathrm{max}/^{14}\mathrm{N}_\mathrm{max}$ abundance than the $^{13}\mathrm{C}$ to $^{14}\mathrm{N}$ ratio when first reaching the maximum temperature. This is because simulations with low proton fractions, whose neutron production is not dominated by high abundances of $^{14}\mathrm{N}$, can experience additional $^{14}\mathrm{N}$ production through neutron recycling and associated neutron leaking (see, e.g., Figure 3.2 and previous discussion). Since the simulations with lowest $X_0(\mathrm{H})$ also show the lowest production of $^{14}\mathrm{N}$ previous to the activation of the neutron source, this relative effect of additional $^{14}\mathrm{N}$ enhancement through neutron recycling increases with decreasing $X_0(\mathrm{H})$ and becomes visible in Figure 4.7.

The $^{13}\mathrm{C}$ to $^{14}\mathrm{N}$ ratios shown in Figure 4.7 follow the expected inverse trend with $Y_\mathrm{p}/Y(^{12}\mathrm{C})$ known from s-process studies. As discussed previously, for simulations with $X_0(\mathrm{H}) \leq 10^{-3}$ the maximum neutron densities increase with decreasing $X_0(^{12}\mathrm{C})$ (see Figure 4.6a and 4.6b). From Figure 4.7 it becomes clear that n_max scales not only with $X_0(^{12}\mathrm{C})$, but more broadly with $Y_\mathrm{p}/Y(^{12}\mathrm{C})$ and the associated changes in $^{13}\mathrm{C}$ to $^{14}\mathrm{N}$ ratios. At $Y_\mathrm{p}/Y(^{12}\mathrm{C}) = 0.2$ the highest n_max is reached at a $^{13}\mathrm{C}$ to $^{14}\mathrm{N}$ ratio of $X\left(^{13}\mathrm{C}\right)/X\left(^{14}\mathrm{N}\right) = 5$. This marks the critical point in our parameter space, where the transition occurs, so that the neutron-density evolution becomes dominated by the poisoning effects of $^{14}\mathrm{N}$, as shown in detail in the previous discussions of the simulations with $X_0(\mathrm{H}) = 10^{-2}$.

Unsurprisingly, similar results are well established in the s-process literature, where $Y_\mathrm{p}/Y(^{12}\mathrm{C})$ is generally considered the determining factor for the efficiency of s-process nucleosynthesis for a given composition and metallicity. However, for i-process nucleosynthesis and the production of characteristic i-process heavy-element abundance patterns it is crucial to not only produce a high maximum neutron density, but to sustain a sufficiently high neutron density for long enough, such that a characteristic heavy-element pattern can develop. In contrast to s-process studies, it therefore becomes particularly important to pay close attention to the neutron-recycling reactions, which can influence τ_i as shown in Figure 4.6.

The lower panel of Figure 4.7 shows the final exposures at i-process neutron densities τ_i for the different simulations with varying $X_0(\mathrm{H})$ and $X_0(^{12}\mathrm{C})$ as a function of the respective $Y_\mathrm{p}/Y(^{12}\mathrm{C})$. In contrast to n_max in the upper panel, τ_i does not show a smooth variation with $Y_\mathrm{p}/Y(^{12}\mathrm{C})$ or with the associated $^{13}\mathrm{C}$ to $^{14}\mathrm{N}$ ratios. Since it is also the absolute abundances of the involved isotopes, not only their ratios, that have a high influence on the magnitude of the neutron-recycling flows, the final τ_i shows a much more complex behaviour that cannot be simplified as a dependence on the initial ratios between protons and $^{12}\mathrm{C}$. This leads to the consequence that simulations with the same $Y_\mathrm{p}/Y(^{12}\mathrm{C})$ but different absolute $X_0(\mathrm{H})$ and $X_0(^{12}\mathrm{C})$ can show different behaviours, in particular with respect to their final i-process exposures and the heavy-element production that can occur in this time.

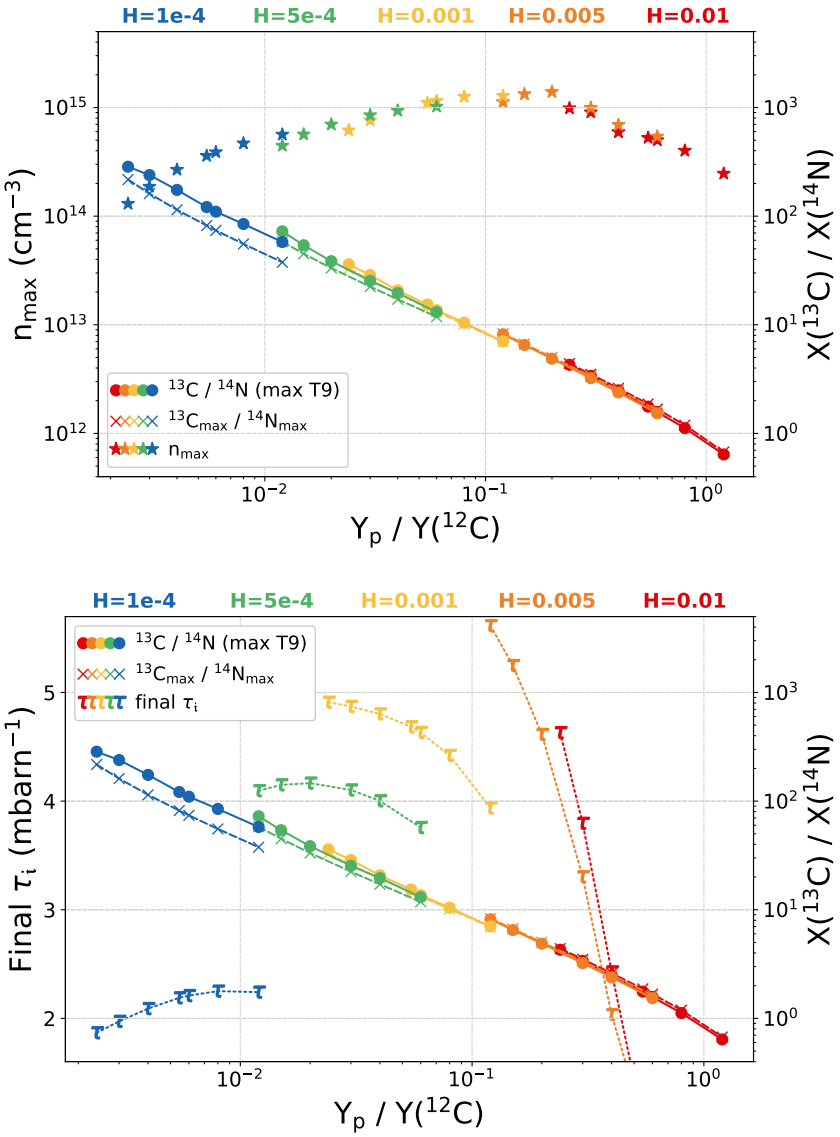

FIGURE 4.7: **Initial abundance variation of ^{12}C: resulting ratios of ^{13}C to ^{14}N as function of $Y_\mathrm{p}/Y(^{12}\mathrm{C})$.** Shown with the respective maximum neutron densities n_max (upper panel) and i-process neutron exposure τ_i (lower panel) ^{13}C to ^{14}N ratios are shown at the time when first reaching the maximum temperature (max T9) and as ratios of the overall maximum produced abundances ($^{13}\mathrm{C}_\mathrm{max}/^{14}\mathrm{N}_\mathrm{max}$). The simulations with different initial X_0(H) are colour-coded. Note that ^{13}C to ^{14}N ratios are by mass fraction, whereas $Y_\mathrm{p}/Y(^{12}\mathrm{C})$ fractions are by number.

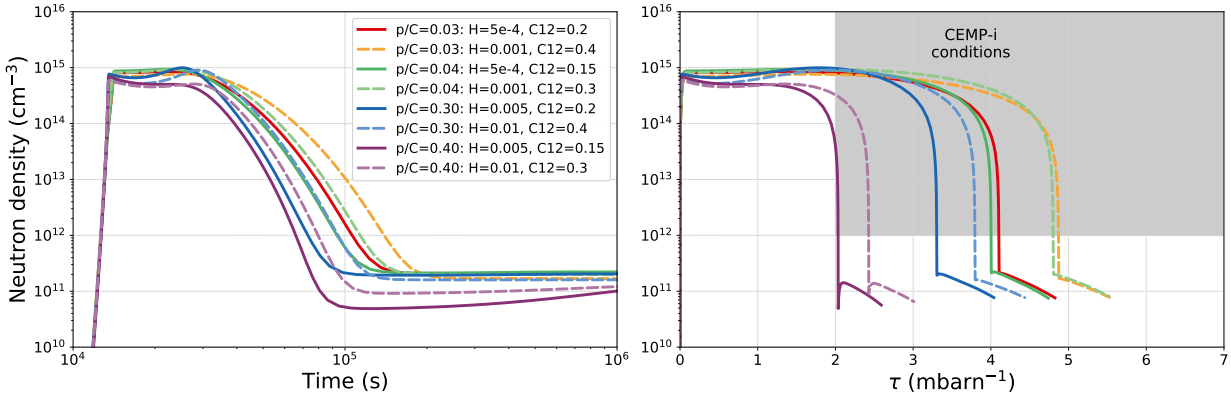

Figure 4.8: **Initial abundance variation of ^{12}C: neutron-density evolutions for selected pairs with same $Y_\mathrm{p}/Y(^{12}\mathrm{C})$.** Same as Figure 4.6 but a subset of simulations is selected, such that pairs with constant $Y_\mathrm{p}/Y(^{12}\mathrm{C})$ are shown. In the legend, p/C represents the number fraction $Y_\mathrm{p}/Y(^{12}\mathrm{C})$, whereas H and C12 denote the mass fractions of initial $X_0(\mathrm{H})$ and $X_0(^{12}\mathrm{C})$, respectively.

To emphasise the dependence of the i-process neutron-density evolution on the actual values of $X_0(\mathrm{H})$ and $X_0(^{12}\mathrm{C})$ and not just their ratio $Y_\mathrm{p}/Y(^{12}\mathrm{C})$, Figure 4.8 shows four pairs of simulations. Both simulations in each pair have the same $Y_\mathrm{p}/Y(^{12}\mathrm{C})$, but values of $X_0(\mathrm{H})$ and $X_0(^{12}\mathrm{C})$ that vary by a factor of 2. For each pair of simulations with the same $Y_\mathrm{p}/Y(^{12}\mathrm{C})$ the main differences arise in the phase of neutron-density decline after n_max was reached. The simulation of each pair that has the higher proton and ^{12}C abundances shows a slower neutron-density decline, which consequently results in a higher neutron exposure. This is because the simulations with higher proton and ^{12}C abundances can also produce higher absolute abundances of ^{13}C and ^{14}N compared to their counterpart with the same $Y_\mathrm{p}/Y(^{12}\mathrm{C})$, which causes higher neutron-recycling flows. As pointed out in the previous section, the neutron-recycling flows can partially replenish ^{13}C and increase τ_i significantly, such that for each pair in Figure 4.8 the simulation with higher $X_0(^{12}\mathrm{C})$ reaches the higher τ_i.

To examine the effect that the different neutron-density evolutions have on the heavy-element production at i-process neutron density, Figure 4.9 shows heavy-element abundance patterns, analogous to those presented in section §4.1.3. The abundance patterns in Figure 4.9b show the heavy-element production at the point in time when each simulation has experienced the same neutron exposure of $\tau = 2$ mbarn^{-1}. Despite having had the same exposure of neutrons, the simulations with $Y_\mathrm{p}/Y(^{12}\mathrm{C}) = 0.4$ show higher heavy-element enhancements. As discussed previously, and visible in Figure 4.8, these simulations with $Y_\mathrm{p}/Y(^{12}\mathrm{C}) = 0.4$ have built up their neutron exposure at lower neutron densities, which results in a neutron-capture path that lies closer to the valley of stability where the isotopes have higher average neutron-capture cross sections and allow for a faster progression of the i process. For the elements past the second s-process peak around barium, this can lead to abundance differences exceeding 1 dex. Even for the two simulations with the same $Y_\mathrm{p}/Y(^{12}\mathrm{C}) = 0.4$, the resulting abundances show a spread of up to 0.5 dex.

The simulations with $Y_\mathrm{p}/Y(^{12}\mathrm{C}) = 0.4$ not only have the lowest neutron densities, they also have the lowest exposures τ_i at the time when their neutron density drops below $n = 10^{12}\,\mathrm{cm}^{-3}$. It can be seen from Figure 4.9b that this leads to abundance patterns with the least progressed neutron-capture process, as evident from abundance spreads exceeding $\Delta[\mathrm{X/Fe}] > 3.5$ dex for

the lead-peak nuclei. The difference in $\tau_{\rm i}$ directly influences how far the neutron-capture paths have progressed to different production stages, where the simulations with the lowest $Y_{\rm p}/Y(^{12}{\rm C})$ show advanced heavy element production at the lead peak, while the simulations with the highest $Y_{\rm p}/Y(^{12}{\rm C})$ have just reached the bottlenecks at the second s-process peak around barium. This has direct consequences for how well the characteristic i-process features in the abundance patterns have been developed. Example characteristics typical for observed abundances in CEMP-i stars, are a high ratio of heavy to light s-process peak elements, as well as an overabundance of barium and europium. Both of these features have developed in the abundance patterns for simulations with $Y_{\rm p}/Y(^{12}{\rm C}) \leq 0.3$ while they have not been well-developed in the simulations with $Y_{\rm p}/Y(^{12}{\rm C}) = 0.4$. However, as shown in Hampel et al. (2019) a signature of Magellanic post-AGB stars incompatible with s-process models but better matched with i-process models of low exposures, is a relatively low abundance of lead, particularly when compared to other heavy rare-earth elements. This feature is well developed in the simulations with $Y_{\rm p}/Y(^{12}{\rm C}) = 0.4$, although the actual extent still varies. The two simulations with the same $Y_{\rm p}/Y(^{12}{\rm C}) = 0.4$ show a very similar production of elements at the second s-process peak, but still show a difference of Δ[Pb/Fe] = 1 dex and even show abundance variations of the first s-process peak elements of more than 0.5 dex.

In comparison to these simulations with high proton-to-carbon ratios, the simulations with the lowest proton-to-carbon ratios of $Y_{\rm p}/Y(^{12}{\rm C}) = 0.03\,{\rm and}\,0.04$ appear to show less variation in their final i-process heavy-element abundances, despite having the larger exposure variations of $\Delta\tau_{\rm i} = 0.8{\rm mbarn}^{-1}$. At the considered low values of $Y_{\rm p}/Y(^{12}{\rm C})$ both simulations of each pair reach high enough i-process neutron exposure to produce heavy elements past the bottleneck at the second s-process peak. Therefore the extra exposure that the simulations with the higher absolute proton and ^{12}C reach, does not influence the general progress of the neutron-capture path anymore. Instead, the extra neutron exposure mainly leads to an additional production of Pb-peak elements. While the rest of the heavy-element abundance patterns remains largely unaffected, the simulation-pairs with $Y_{\rm p}/Y(^{12}{\rm C}) = 0.03\,{\rm and}\,0.04$ still show abundance variations of Δ[Pb/Fe] = 0.4 dex, between the simulations of each pair.

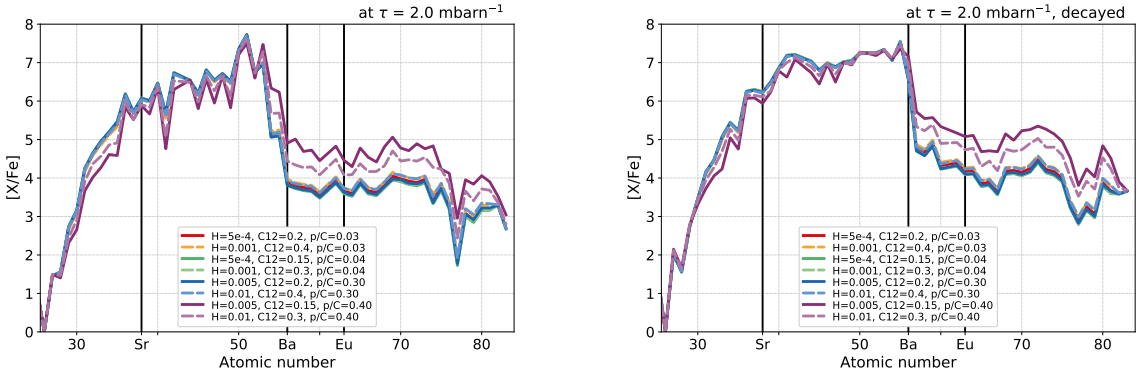

(A) Abundance patterns at the same neutron exposure of $\tau = 2$ mbarn^{-1}.

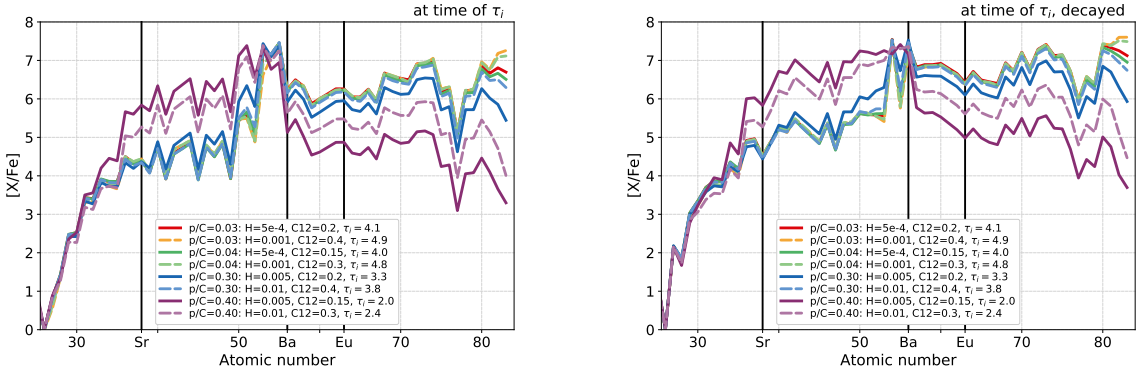

(B) Abundance pattern shown at the respective $\tau_{\rm i}$ for each simulation.

Figure 4.9: **Initial abundance variation of ^{12}C: abundance-pattern evolutions for selected pairs with same $Y_{\rm p}/Y(^{12}{\rm C})$.** Like Figure 4.5 but for selected simulations with varying ratios between the initial abundances of protons and ^{12}C, with legend nomenclature as in Figure 4.8.

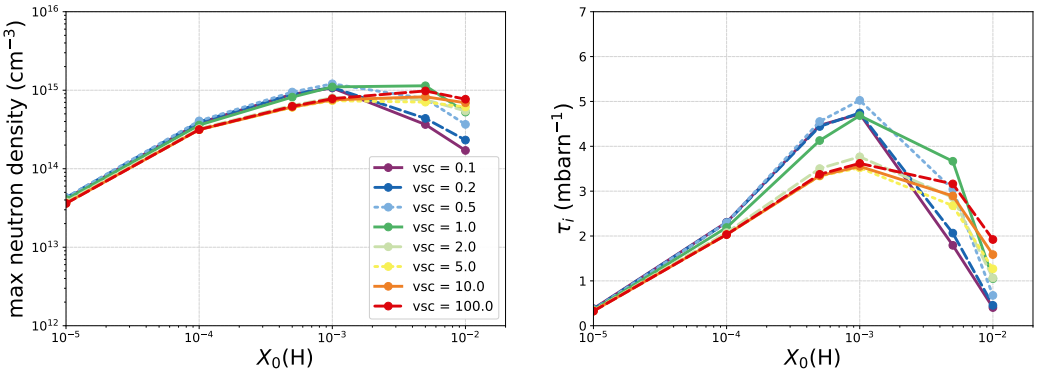

FIGURE 4.10: **Velocity scaling: resulting $n_{\max}$ and τ_i.** Effects of velocity scaling factors on the maximum neutron density (left) and integrated i-process neutron exposure (right) reached at various initially ingested proton fractions.

4.3 Varying the convective velocities in the He-convective regions

Our simulations adopt a method, which imitates the movement of a parcel of material through the He-convective region, where the temperature and density increase with depth. In 1D stellar evolution models a proper treatment of convection, which is an inherently 3D phenomenon, is not possible. Instead we use the velocities predicted by mixing-length theory and/or diffusive processes. It is well known that this does not necessarily describe the actual behaviour and velocity that individual parcels of material travel with and that not all parcels travel with the same velocity in the first place. Therefore, here we adjust our trajectories by introducing a velocity scaling factor vscthat speeds up ($vsc > 1$) and slows down ($vsc < 1$) our convective bubble by up to an order of magnitude. This means that the convective bubble moves along the temperature-density trajectory over a changed time scale and also reaches the maximum temperature and density at a different time. A scaling factor of $vsc = 1$ represents the reference simulations we previously discussed.

Figure 4.10 shows the maximum neutron densities $n_{\max}$ and final i-process neutron exposures $\tau_{\rm i}$ for various initially ingested proton fractions and different velocity scaling factors. For small proton fractions of $X_0(\mathrm{H}) \leq 10^{-4}$ the different scalings only have minor effects on $n_{\max}$ and $\tau_{\rm i}$, which both only vary approximately 10 % compared to the reference simulation. Despite only being a small effect, a trend can be observed, that smaller scaling factors result in larger $n_{\max}$ and $\tau_{\rm i}$ and vice-versa. At $X_0(\mathrm{H}) = 10^{-3}$ the maximum neutron density also remains largely unaffected by the velocity scaling factor, while $\tau_{\rm i}$ shows variations between 3.5 and 5.0 mbarn^{-1}. This variation in $\tau_{\rm i}$ for $X_0(\mathrm{H}) = 10^{-3}$ appears almost bimodal, where scaling factors of $vsc < 1$, which mimic slower convective velocities than the reference case, do not affect the final $\tau_{\rm i} \approx 4.7$mbarn^{-1} much. In contrast to that, scaling factors of $vsc > 1$, which mimic faster convective velocities than the reference case, reduce the exposure built up at high neutron densities to $\tau_{\rm i} \approx 3.5$mbarn^{-1}. At larger proton fractions of $X_0(\mathrm{H}) > 10^{-3}$ the variations in $n_{\max}$ and $\tau_{\rm i}$ become even larger and show a complex non-uniform behaviour.

To further investigate how a change in velocity scaling impacts the neutron production and the

i process, Figure 4.11 shows the detailed evolution of the neutron density for a range of X_0(H) and scaling parameters. Figure 4.12 shows the abundances of ^{13}C, ^{13}N and ^{14}N for the same X_0(H) and *vsc*at two different times. These two times are (*i*) when the simulation reaches the maximum temperature t_{maxT} and (*ii*) when the species reaches its maximum abundance in each simulation, which may be at different times for each isotope and simulation. We can make a few observations for different *vsc* and X_0(H) regimes, which will help us understand the underlying connections that are the main drivers for the different behaviours of the neutron production and consequently n_{max} and τ_{i}:

(a) For all cases it can be seen, e.g. in Figure 4.11, increasing the velocity scaling leads to an earlier rise of the neutron density. For $vsc > 1$ this results in a "dent" in the neutron-density evolution, which indicates a two-step process, where a fast rise of n to a medium level can be observed first, followed by a slower rise to the i-process neutron densities.

(b) The ^{13}N abundance at t_{maxT} (Figure 4.12, green dots) is very small at low *vsc* (i.e., $X(^{13}\mathrm{N}) < 10^{-4}$, $vsc \lesssim 1$) and experiences a jump-like increase of 2 to 3 orders of magnitude when the scaling factor reaches unity.

(c) The opposite trend to (b) can be seen in the t_{maxT} abundances of ^{13}C and ^{14}N (blue and red circles, respectively, in Figure 4.12), which decrease for $vsc > 1$.

(d) At low velocity-scaling factors $vsc \lesssim 1$, Figure 4.12 shows a correlation between the maximum ^{13}N abundance (light green crosses) and the velocity scaling, where the lowest *vsc* result in the lowest maximum ^{13}N abundances.

(e) At low velocity-scaling factors $vsc < 1$, Figures 4.12a and 4.12b show for low ingested proton fractions of $X_0(\mathrm{H}) \leq 10^{-3}$ that the t_{maxT} abundances of ^{13}C (blue dots) are almost the same as the maximum ^{13}C abundances (light blue crosses). In contrast to that, Figures 4.12c and 4.12d show that in the simulations with higher ingested proton fractions $X_0(\mathrm{H}) \geq 5 \times 10^{-3}$ a discrepancy between the maximum ^{13}C abundances and the t_{maxT} abundances of ^{13}C arises for $vsc \lesssim 1$. For the lowest $vsc = 0.1$ cases, the maximum ^{13}C abundances are more than double the abundances of ^{13}C at t_{maxT}.

The general behaviour described in (a), where the time at which the rise in neutron density occurs increases with *vsc*, simply emphasises the role that *vsc* and the adopted convective velocities have for our simulations: the convective velocity determines how quickly the temperature and density increase for our parcel of material, as its movement from the outer to the inner boundary of the intershell is mimicked. Therefore, *vsc* is a direct scaling factor of the time t_{maxT} when the highest temperature at the bottom of the convective region is reached. Because the main neutron release can only happen efficiently when the high temperatures close to the bottom of the convective region are reached, the time at which the neutron density starts increasing scales just as closely with *vsc* as t_{maxT}. To understand the "dent" in the neutron-density evolutions (described in a) as well as the behaviour described in (d) and (e), a separate consideration for low for velocity scalings $vsc < 1$ is needed, which will be given in §4.3.2. However, for simplicity we will first address the more obvious behaviour described in (b) and (c), which is based on consideration for high velocity scalings $vsc > 1$, given in §4.3.1.

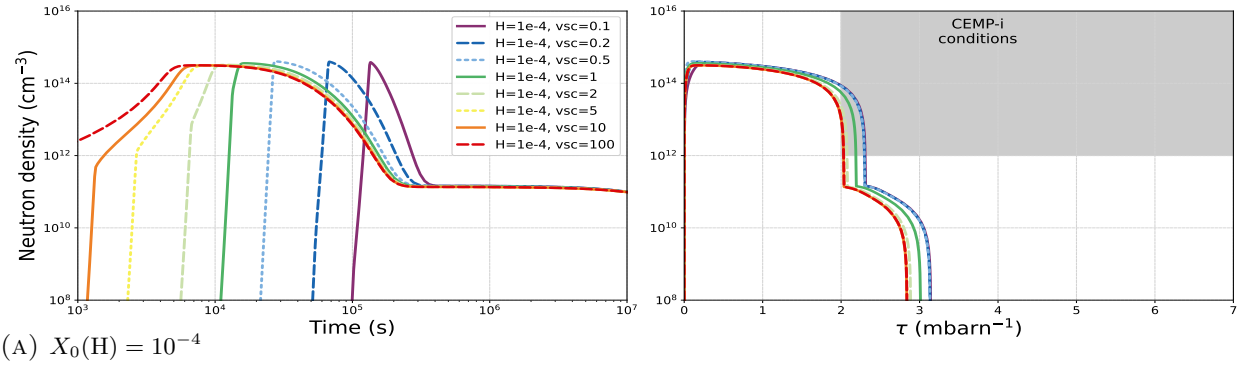

(A) $X_0(\mathrm{H}) = 10^{-4}$

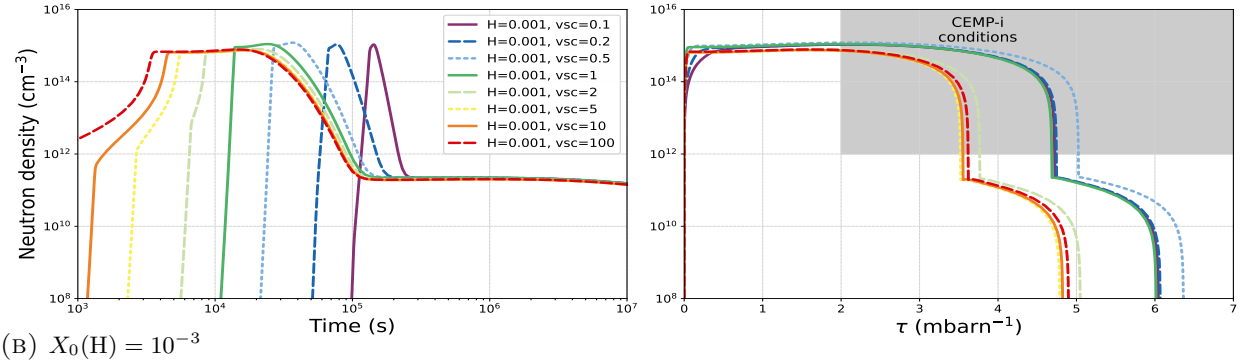

(B) $X_0(\mathrm{H}) = 10^{-3}$

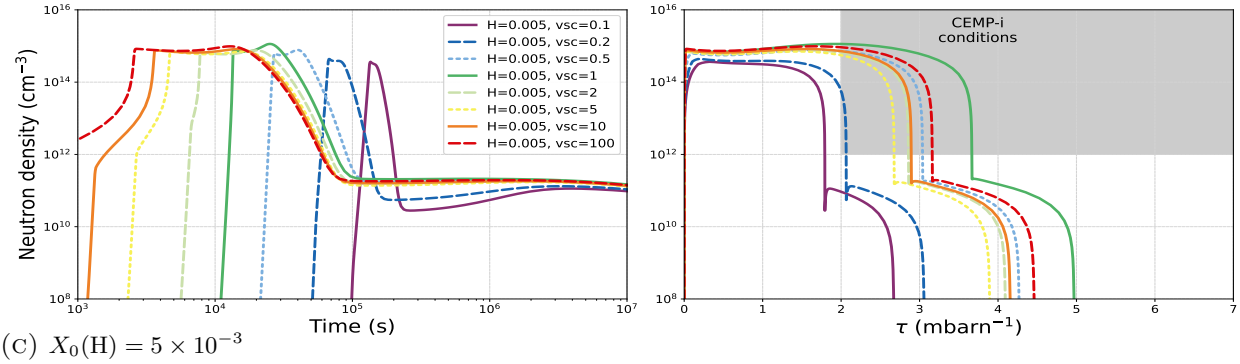

(C) $X_0(\mathrm{H}) = 5 \times 10^{-3}$

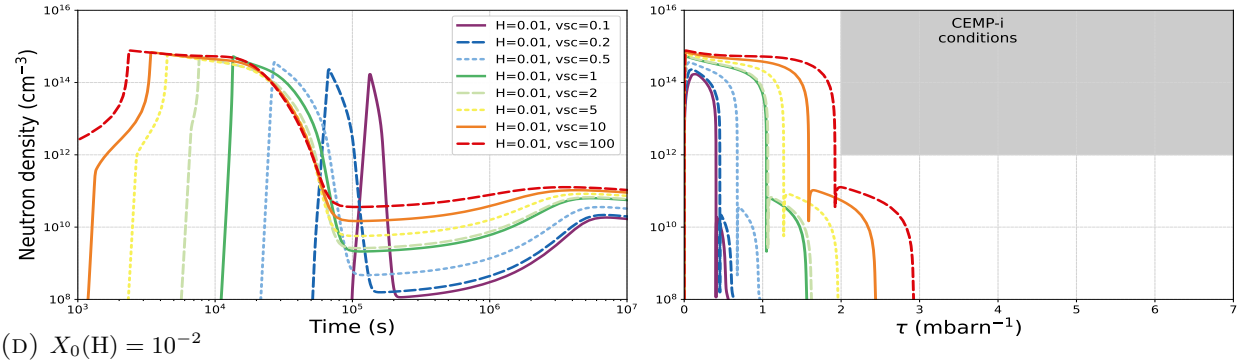

(D) $X_0(\mathrm{H}) = 10^{-2}$

FIGURE 4.11: **Velocity scaling: neutron-density evolution.**
Same as Figure 4.2 but for variations of the velocity-scaling factor.

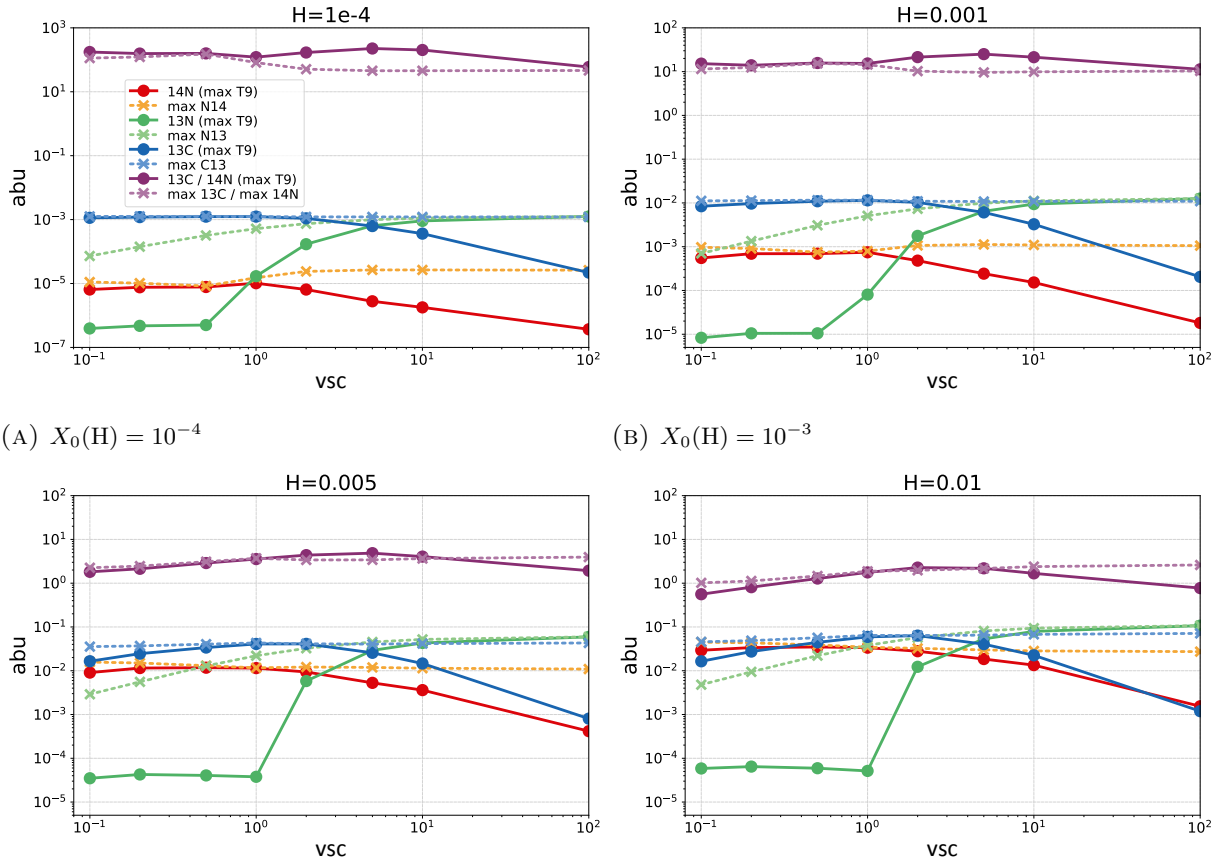

(A) $X_0(\mathrm{H}) = 10^{-4}$

(B) $X_0(\mathrm{H}) = 10^{-3}$

(C) $X_0(\mathrm{H}) = 5 \times 10^{-3}$

(D) $X_0(\mathrm{H}) = 10^{-2}$

Figure 4.12: **Velocity scaling: abundances of ^{13}C, ^{13}N and ^{14}N.** Abundances are shown at the time when the maximum temperature is reached, as well as the maximum abundance throughout the simulation. Note that the abundance scale for panel (a) differs from the scale used the other three panels, while the legend in panel (a) applies to all of the panels.

4.3.1 Fast convective velocities with $vsc > 1$

The majority of ingested protons can be successfully converted into ^{13}C via $^{12}\mathrm{C}(\mathrm{p},\gamma)^{13}\mathrm{N}(\beta^{+}\nu)^{13}\mathrm{C}$, such that a sufficiently high abundance of ^{13}C is present to be activated as neutron source to reach i-process conditions, once high enough temperatures are reached. This does not hold true any longer if the maximum temperatures are reached before the majority of the produced ^{13}N had time to decay into ^{13}C. For the reference simulations, Figure 3.2 shows that it takes just over 10^4 seconds until the ingested protons are captured by ^{12}C and the maximum ^{13}N abundance is reached. There is a delay of approximately $\Delta t \approx 3000$ seconds, between the time when the ^{13}N abundance is at its maximum and the time when the highest temperature at the bottom of the convective intershell region is reached. This leaves enough time for the majority of ^{13}N, which has a half life of 598 seconds, to decay.

As the scaling factors increase and the maximum temperature is reached quicker, the time between the production of ^{13}N and the activation of the $^{13}\mathrm{C}(\alpha,\mathrm{n})^{16}\mathrm{O}$ reaction decreases. At a scaling factor of $vsc = 5$ this time delay has decreased to $\Delta t \approx 400$ seconds, and for $vsc = 10$ this time delay is less than $\Delta t \lesssim 200$ seconds. As a consequence, the fraction of ^{13}N that has decayed to ^{13}C before t_{maxT} decreases with increasing scaling factor. This leads to a clear distinction between the cases where almost all of the produced ^{13}N has time to decay, resulting in low ^{13}N abundances at t_{maxT} ($vsc \lesssim 1$), and those cases where substantial amounts of ^{13}N are still present when the neutron source is activated ($vsc > 1$).

The lower abundances of ^{13}C at t_{maxT} are directly responsible for the "dent" in the neutron-density evolutions in Figure 4.11. For the simulations with $vsc > 1$ the first quick rise of n cannot reach as high neutron densities as the other cases because less ^{13}C is present for the $^{13}\mathrm{C}(\alpha,\mathrm{n})^{16}\mathrm{O}$ reaction. Only after some additional time for further ^{13}N decays can the i-process neutron-density levels be reached.

The increase of the t_{maxT} abundance of non-decayed ^{13}N with faster convective velocities, particularly for $vsc > 1$, directly influences the abundance of ^{13}C that has been created until t_{maxT}. Additionally, this means that less ^{13}C is present to have undergone $^{13}\mathrm{C}(\mathrm{n},\gamma)^{14}\mathrm{N}$ before t_{maxT}, consequently resulting in a lower t_{maxT} abundance of ^{14}N. Not only does this directly impact the $^{13}\mathrm{C}(\alpha,\mathrm{n})^{16}\mathrm{O}$ reaction flow and the produced neutron density, the non-decayed ^{13}N also impacts the neutron-recycling reactions once the neutron production starts. A higher ^{13}N abundance then leads to neutron absorption and recycling via $^{13}\mathrm{N}(\mathrm{n},\mathrm{p})^{13}\mathrm{C}$ but can also interrupt some neutron recycling via $^{13}\mathrm{N}(\mathrm{p},\gamma)^{14}\mathrm{O}(\beta^{+}\nu)^{14}\mathrm{N}$ which instead produces more neutron poison.

For low proton fractions $X_0(\mathrm{H}) \leq 10^{-3}$, the higher scaling factors and hence the higher ^{13}N and lower ^{13}C abundances at t_{maxT}, lead to both lower n_{max} and lower τ_{i} compared to the reference case, as seen in Figures 4.10 and 4.11. While the effect is still relatively small at $X_0(\mathrm{H}) = 10^{-4}$, it leads to the bimodal behaviour for the cases with $X_0(\mathrm{H}) = 10^{-3}$, where the simulations in which almost all of the produced ^{13}N has time to decay ($vsc \leq 1$) can reach τ_{i} that are approximately $1\,\mathrm{mbarn}^{-1}$ higher compared to the cases where substantial amounts of ^{13}N are still present when the neutron source is activated ($vsc > 1$), which reduces n_{max} and τ_{i}.

For higher ingested proton fractions $X_0(\mathrm{H}) \geq 5 \times 10^{-3}$ a reversed trend between high scaling factors ($vsc > 1$) and neutron production can be seen in Figures 4.10 and 4.11, where higher vsc lead to higher n_{max} and τ_{i}. It became apparent previously (see, e.g., Figure 4.9) that simulations

with $X_0(\mathrm{H}) = 5 \times 10^{-3}$ mark the transition at which the produced neutron poison ^{14}N starts to dominate the behaviour of the neutron-density evolution. These ^{14}N-dominated simulations benefit from delayed neutron-recycling in the sense that higher neutron-recycling flows can prolong the time a relatively high neutron density can be sustained, which can enhance the overall i-process neutron exposure (analogous to the discussion in the previous section §4.2, e.g. for Figure 4.6c), through partial replenishment of ^{13}C. Particularly in the simulations with $X_0(\mathrm{H}) = 10^{-2}$, this behaviour becomes obvious as it increases τ_i by 50% and 83% for scaling factors of 10 and 100, respectively, when compared to the reference simulation. In this context it is worth noting that the test cases with constant temperature and density in Appendix 3.A of the previous Chapter §3, can be interpreted as the limit case of infinitely high scaling factors, i.e. reaching the bottom of the convective region instantaneous with $t_\mathrm{maxT} \to 0$. Therefore it is not surprising that the very fast case with $vsc = 100$ can reach almost the same final exposure of $\tau_\mathrm{i} = 1.9$, as the constant temperature test case in Appendix 3.A.

4.3.2 Slow convective velocities with $vsc < 1$

When we are dealing with cases that have slow convective velocities and scaling factors $vsc < 1$, there is a substantial time delay between the ^{13}N production and reaching t_maxT. This allows the majority of ^{13}N to decay into ^{13}C before the neutron-production and neutron-recycling reactions are activated. However, in cases with low vsc the β-decay time scale of ^{13}N is still of importance. In contrast to the previously discussed cases with high vsc it is the ^{13}N production vs. destruction time scale that is crucial to understanding how vsc affects the neutron-density evolution and the i-process characteristics n_max and τ_i.

To remind the reader, the relevant features at low vsc in Figure 4.12 are observations (d) and (e) from the start of this section: for all $X_0(\mathrm{H})$ the maximum abundance of ^{13}N decreases with decreasing vsc. For high ingested proton fractions $X_0(\mathrm{H}) \geq 5 \times 10^{-3}$ the t_maxT abundance of ^{13}C also decreases significantly with decreasing vsc, with values deviating further from the respective maximum ^{13}C as vsc decreases and/or $X_0(\mathrm{H})$ increases.

At the start of the proton ingestion, the reaction responsible for the production of ^{13}N is $^{12}\mathrm{C}(\mathrm{p},\gamma)^{13}\mathrm{N}$, while ^{13}N is mainly destroyed by β-decays and a minor contribution of the $^{13}\mathrm{N}(\mathrm{p},\gamma)^{14}\mathrm{O}$ reaction, depending on the proton abundances and temperatures. A decrease in vsc leads to a slower temperature rise for the parcel of material in our simulations. While the time scale of the ^{13}N β-decay remains unaffected by the rise in temperature, the ^{13}N production occurs via a proton-capture reaction, which is highly temperature sensitive. This slower rise in temperature for decreasing vsc also slows down the rate at which the ^{13}N production increases, while the ^{13}N destruction rate remains the same. As a consequence, there is less accumulation of ^{13}N for lower vsc, due to the relatively higher destruction rates when compared to the production rate. The maximum ^{13}N that can build up is therefore less and results in the decreasing trends in Figure 4.12.

In a simplistic consideration, where the ^{13}C production only depends on the $^{12}\mathrm{C}(\mathrm{p},\gamma)^{13}\mathrm{N}(\beta^+\nu)^{13}\mathrm{C}$ reaction chain, the abundance of ^{13}C should only depend on how many protons can be captured by ^{12}C and not on the relative reaction time scales and the maximum ^{13}N abundance in between, where ^{13}C is "locked up" temporarily. This is approximately true for low ingested proton $X_0(\mathrm{H}) \leq 10^{-3}$ fractions and can be seen as constant ^{13}C abundances (both

maximum and t_{maxT}) in Figures 4.12a and 4.12b. However, we know that this simplified view gets significantly altered at higher ingested proton fractions of $X_0(\mathrm{H}) \geq 5 \times 10^{-3}$, when the $^{13}\mathrm{C}(\mathrm{p},\gamma)^{14}\mathrm{N}$ reaction destroys the neutron source ^{13}C and produces the neutron poison ^{14}N. The rate of this reaction does not only depend on the available proton abundance, but also on the abundance of ^{13}C. While ^{13}C is still locked up in ^{13}N, this reaction pathway does not produce ^{14}N. The alternative proton captures by ^{13}N (which can produce ^{14}N via $^{13}\mathrm{N}(\mathrm{p},\gamma)^{14}\mathrm{O}(\beta^{+}\nu)^{14}\mathrm{N}$) have a cross section, which is more than an order of magnitude smaller than the proton captures by ^{13}C.

Putting these considerations together, the net effect is that more of neutron poison ^{14}N can be produced at the expense of the neutron source ^{13}C when the velocity scaling factor is lower. For the neutron production this means that the simulations with the slowest convective velocities also show the lowest n_{max} and τ_{i}. However, this effect is only significant for the simulations with high ingested proton fractions of $X_0(\mathrm{H}) \geq 5 \times 10^{-3}$, which are dominantly affected by the neutron poison ^{14}N in the first place.

4.4 Summary

In this chapter we investigated how the neutron production for the i process is impacted by uncertainties in parameters for single-zone simulations, which were introduced in the previous chapter §3. While it can be seen as a disadvantage and oversimplification that our single-zone nucleosynthesis model is parametric and detached from an actual stellar evolution code, we can use this parametric approach to our advantage. As presented in this chapter, the model setup allows us to vary parameters individually and the comparably low computational effort of the single-zone simulation allows us to study the parameter space systematically.

The parameters that were tested in this chapter cover uncertainties related to nuclear reaction rates, initial abundances and varying proton-to-carbon fractions, and relative time-scale variations of reaction rates due to changes in convective velocities. We examine the roles of different neutron-recycling reactions and provide a detailed investigation into the neutron-production.

Nuclear-reaction rates

Through varying individual reaction rates by a constant factor of two, the role of individual reactions for the neutron production and recycling became apparent. For low ingested proton fractions of $X_0(\mathrm{H}) = 10^{-4}$, neutron recycling through the $^{12}\mathrm{C}(\mathrm{n},\gamma)^{13}\mathrm{C}$ reaction is dominant and determines the further evolution of the neutron densities. When considering more realistic uncertainties of reaction rates as described by their factor uncertainties, it became apparent that the uncertainties in the $^{12}\mathrm{C}(\mathrm{n},\gamma)^{13}\mathrm{C}$ reaction can influence the maximum neutron density by approximately $\Delta n_{\max} \approx 35\,\%$ and the i-process neutron density by approximately $\Delta\tau_{\mathrm{i}} \approx 10\,\%$. The differences in the neutron production caused by the $^{12}\mathrm{C}(\mathrm{n},\gamma)^{13}\mathrm{C}$ reaction-rate uncertainty can propagate into abundance variations of heavy elements that can reach spreads of up to 1.5 dex when considering the abundance pattern after the same neutron exposure. However, when considering the i-process abundance pattern at τ_{i}, that was produced before the neutron density drops and further heavy-element production with s-process characteristic might occur, abundance spreads of up to 0.8 dex can still be noted. The spreads of the final i-process abundances at τ_{i} occur in different regions of the abundance pattern, where the variations around the first s-process peak for elements with $(36 \leq Z \leq 40)$ are dominated by the uncertainty in the $^{12}\mathrm{C}(\mathrm{n},\gamma)^{13}\mathrm{C}$ reaction rate, while the variations around the Pb peak ($Z = 82$) are dominated by the uncertainty in the $^{13}\mathrm{C}(\alpha,\mathrm{n})^{16}\mathrm{O}$ reaction rate.

For higher ingested proton fractions, the simulations at $X_0(\mathrm{H}) = 10^{-3}$ show a shift in the relative importance of the various neutron-recycling reactions. Since the higher proton abundance also leads to higher abundances of $^{13}\mathrm{N}$ and $^{14}\mathrm{N}$, the (n,p) reactions and particularly the $^{13}\mathrm{N}(\mathrm{n},\mathrm{p})^{13}\mathrm{C}$ reaction start to be significant and even dominate the neutron recycling. With higher fluxes of released protons that participate in the recycling of neutrons, the proton-capture reactions, particularly the $^{12}\mathrm{C}(\mathrm{p},\gamma)^{13}\mathrm{N}$ and $^{13}\mathrm{C}(\mathrm{p},\gamma)^{14}\mathrm{N}$ reactions, gain influence. However, these proton-capture reactions have relatively well constrained reaction rates and low factor uncertainties. Therefore it is the higher uncertainties of the $^{13}\mathrm{C}(\alpha,\mathrm{n})^{16}\mathrm{O}$ and $^{14}\mathrm{N}(\mathrm{n},\mathrm{p})^{14}\mathrm{C}$ reactions that drive the neutron-production uncertainty altogether. For the produced heavy elements, these reaction rate uncertainties can propagate into abundance spreads of several tenth of a dex. When considering abundances at the same neutron exposure for all simulations, the production of typical elements such as Sr, Ba, and

Pb is almost unaffected. Interestingly, the elements heavier than Ba show abundance spreads of 0.7 dex, despite showing the same abundances for elements lighter than Ba. When letting each simulation run until its final i-process neutron exposure is reached self-consistently, these abundance spreads of the heavy elements between Ba and Pb even out and instead propagate into a spread of abundances for the elements at the end of the neutron-capture path. Here the abundances of the Pb-peak elements still show differences of approximately 0.4 dex, dominated by the uncertainty in the $^{13}\mathrm{C}(\alpha,\mathrm{n})^{16}\mathrm{O}$ reaction rate.

The simulations with high ingested proton fractions of $X_0(\mathrm{H}) = 10^{-2}$, show yet again a different behaviour of neutron-recycling reactions. The high proton fractions lead to significant production of ^{14}N from the $^{13}\mathrm{C}(\mathrm{p},\gamma)^{14}\mathrm{N}$ reaction, such that the $^{14}\mathrm{N}(\mathrm{p},\gamma)^{14}\mathrm{C}$ reaction has significant influence on the availability of free neutrons and particularly on the total i-process exposures. Only the simulations where the reaction rates of those reactions are lowered by their factor uncertainty, can yield i-process neutron exposures of $\tau_\mathrm{i} = 1.5\,\mathrm{mbarn}^{-1}$ to $1.7\,\mathrm{mbarn}^{-1}$ that could at all allow for heavy-element production past the second s-process peak.

Initial abundances

When studying the production of neutrons for the i process in proton-ingestion episodes, not only the abundance of ingested protons is of importance, but also the abundance of ^{12}C, which is responsible for capturing the ingested protons. As well known from s-process studies, the ratio of protons to carbon mainly determines in which ratio ^{13}C and ^{14}N can be produced, which sets important constraints for the number of free neutrons that can be produced. Systematically varying both, initial proton and ^{12}C fractions, we also confirmed for i-process conditions that the maximum neutron density that can be reached in each simulation increases with increasing proton-to-carbon ratio, largely independent of the absolute proton and ^{12}C abundances. However, this is only true for proton-to-carbon ratios up to $Y_\mathrm{p}/Y(^{12}\mathrm{C}) \leq 0.2$. Our simulation with $X_0(\mathrm{H}) = 5 \times 10^{-3}$ and $X_0(^{12}\mathrm{C}) = 0.3$ (i.e. $Y_\mathrm{p}/Y(^{12}\mathrm{C}) = 0.2$ for both) reaches the maximum neutron abundances of $n_\mathrm{max} = 1.4{\times}10^{15}\,\mathrm{cm}^{-3}$, after the produced ^{13}C and ^{14}N reached a favourable ratio of $^{13}\mathrm{C}/^{14}\mathrm{N} = 0.5$. A further increase in the proton-to-carbon ratio leads to lower ^{13}C-to-^{14}N ratios which reduce the maximum neutron densities that the simulations can reach.

When evaluating the exposure τ_i that can built up at i-process neutron density, we found that it is not only the initial proton-to-carbon ratio that determines the amount of i-process nucleosynthesis that can occur. Instead, the absolute abundances of protons and ^{12}C highly influence the final τ_i. This is because the absolute proton fraction largely determines the absolute abundance levels of the produced isotopes such as ^{13}N, ^{13}C, and ^{14}N, which are important for the neutron recycling. It is the absolute abundance of these CN isotopes, that sets the level of neutron-recycling flows and thereby largely influences how long the high neutron-density level for i-process nucleosynthesis can be maintained.

With different combinations of initial proton and carbon fractions, we could test how the neutron production and the heavy-element nucleosynthesis varies between two simulations that have the same initial proton-to-carbon ratio, but different absolute proton and ^{12}C abundances. Although both simulations with the same proton-to-carbon ratio also reach the same maximum neutron densities, the differences in their i-process neutron exposures can exceed $1\,\mathrm{mbarn}^{-1}$. The different τ_i can influence the heavy-element production and can determine how pronounced i-process charac-

teristics in the abundance patterns are. The simulations with low proton-to-carbon ratios, e.g., $Y_{\rm p}/Y(^{12}{\rm C}) = 0.03$ and 0.04 reach high enough $\tau_{\rm i}$ for substantial i-process nucleosynthesis regardless of their absolute proton and ^{12}C abundances. For these simulations the difference in $\tau_{\rm i}$ results in abundance variations at the end of the neutron-capture path, and the simulations with the same proton-to-carbon ratio still show Δ[Pb/Fe] = 0.4 dex. In contrast, the two simulations with $Y_{\rm p}/Y(^{12}{\rm C}) = 0.4$ show a vastly different progression of their neutron-capture path. Although both simulations have the same abundance of Ba at the second s-process peak, their production of first s-process peak elements varies by Δ[Sr/Fe] = 0.6 dex and the production of Pb-peak elements by Δ[Pb/Fe] = 1.1 dex.

Convective velocities

Adopting different convective velocities for our parcel of material to travel along its temperature-density trajectory, can change the relative time scales between reactions. In our simplified model, where the production of ^{13}C and ^{14}N occurs on the way down through the He-convective region, the changes in time scale do not affect the reaction time scales of the neutron-producing reactions or the neutron-recycling reactions. Instead the reaction time scales of important reactions prior to reaching the maximum temperature and density are affected, such as the $^{12}{\rm C}({\rm p},\gamma)^{13}{\rm N}(\beta^+\nu)^{13}{\rm C}$ reaction chain. In this reaction chain, the production of ^{13}N via proton captures by ^{12}C is temperature sensitive and affected by differences in the rate of the temperature increase. In contrast, the destruction of ^{13}N via β-decays is not affected. It is an important factor, how much time the produced ^{13}N has to decay into ^{13}C before the maximum temperature is reached, which can activate the neutron source.

For slow convective velocities (those of our reference simulation from Chapter §3 or lower, i.e. scaling factors $vsc \leq 1$) the majority of produced ^{13}N has decayed into ^{13}C by the time the maximum temperature are reached. In contrast, for simulations with high convective velocities (larger than in our reference simulation, i.e. scaling factors $vsc > 1$) a significant amount of ^{13}N is still present when the maximum temperatures are reached. Non-decayed ^{13}N still present when the main neutron production starts can then influence the neutron recycling via the $^{13}{\rm N}({\rm n},{\rm p})^{13}{\rm C}$ reaction, or it can absorb released protons and produce neutron poison via $^{13}{\rm N}({\rm p},\gamma)^{14}{\rm O}(\beta^+\nu)^{14}{\rm N}$. The detailed effects that the changes in convective velocities, relative reaction time scales, and neutron recycling have on the i-process neutron densities depends on various factors, including the ingested proton fractions and the ^{13}N abundance variations. These convoluted dependencies lead to complex behaviour of the neutron production when the convective velocities are varied. The variations of maximum neutron densities and exposure do not necessarily follow smooth trends, particularly at points in the parameter space where transitions between dominating effects occur.

Especially for fast convective velocities we expect our single-zone model to become less reliable. Despite neglecting mixing and dilution effects that can alter the composition of our convective bubble as it moves downwards through the He-convective region, this simplified model still performs reasonably robust in predicting the important ratios of, e.g., ^{13}C to ^{14}N that can be encountered at the bottom of the H-convective region where the subsequent neutron production can occur. This scenario uses the implicit assumption that the parcels of material that move from the top to the bottom of the convection region, have a very similar nucleosynthesis history and hence comparable composition at the time when reaching the hottest temperatures. This assumption

forms an important basis of our two step approach, where we separate the production of the C and N isotopes during the downward movement of our convective bubble from the neutron production and recycling that occurs at the bottom of the He-convective region. However, for fast convective velocities, when not all of the produced ^{13}N had time to decay to ^{13}C, it may become more significant to consider individual convective bubbles to experience multiple convective turn overs. Even for a single parcel of material, a repeated cycle of temperate and density increases and decreases will influence the time, which produced ^{13}N has to decay to ^{13}C before reaching the conditions again, at which ^{13}C can be activated.

> *The answer to not going crazy with worry is to me to think on a much larger scale than the Earth; the stars are comforting.*
>
> — Beatrice Hill Tinsley

Chapter 5

Neutron production and i-process nucleosynthesis at different stellar sites

One major uncertainty for simulations of i-process nucleosynthesis is the actual stellar site (or combination of multiple sites) at which the i process occurs in nature. There are multiple stellar evolution scenarios that can lead to proton-ingestion events and subsequent i-process nucleosynthesis. So far the nucleosynthesis models studied in Chapter §3 and §4 adopt the temperature-density structure of a proton-ingestion episode in a low-mass, low-metallicity AGB star.

Our approach of using single zone nuclear-reaction networks to detach the detailed nucleosynthesis from the stellar evolution calculations brings the big advantage of testing parameter variations independently from one another. To investigate how the neutron production and i-process nucleosynthesis varies in different stellar sites, we will adopt temperature and density profiles from the stellar structures of three additional stellar models. Using the convective velocities predicted by each stellar model we construct a temperature-density trajectory as a function of time, as previously described for the AGB model in chapter §3. The additional scenarios and stellar models, which we will explore further in the coming sections, are:

- a $1.3\,\mathrm{M}_\odot$, $Z = 10^{-4}$ AGB star computed with the Monash-Stromlo stellar evolution code,
- a Magellanic post-AGB star with initial mass of $1.3\,\mathrm{M}_\odot$ and [Fe/H] $= -1.3$ from Lugaro et al. (2015), and
- the core helium flash of an ultra metal-poor ($Z = 2 \times 10^{-6}$) star with an initial mass of $0.8\,\mathrm{M}_\odot$ (Campbell, S. W. 2020, private communication).

5.1 Early thermal pulse of a low-mass, low-metallicity AGB star

5.1.1 Evolution of a 1.3 $\mathrm{M}_\odot$, $Z = 10^{-4}$ stellar model

To show a reasonable variation of the thermodynamic structure of the intershell region that can be expected during the early thermal pulses of low-mass, low-metallicity AGB stars, we evolve a separate model with a different code to complement the temperature-density trajectory from Stancliffe et al. (2011), which we have been using so far. We will be referring to the previous trajectory, which Stancliffe et al. (2011) calculated with the Stars code, as the Stars-trajectory, in contrast to the Monash-trajectory, from the new model described in the following.

Here we present the stellar-evolution model of a $1.3\,\mathrm{M}_\odot$ star with a scaled-solar composition[1] and a metallicity of $Z = 10^{-4}$. We use the Monash-Stromlo stellar-evolution code to calculate the stellar evolution from the zero-age main sequence to the end of the AGB phase. This code has a long history of development and modifications, details of which can be found, e.g., in Lattanzio (1986) and Frost & Lattanzio (1996). More recent updates are, e.g., described in Kamath et al. (2012); Karakas (2014); Constantino et al. (2014); Fishlock et al. (2014) and references therein. In particular, we use the C- and N-rich low-temperature ÆSOPUS opacities from Marigo & Aringer (2009), which are based on Lodders (2003) solar abundances, and the OPAL tables (Iglesias & Rogers, 1996) updated to the same solar composition for consistency. To include mass-loss on the RGB we use the Reimers (1975) prescription with $\eta_\mathrm{R} = 0.4$ and for the AGB we use the Vassiliadis

[1] We adopt a solar metallicity of $Z = 0.014$ and solar abundances from Asplund et al. (2009).

& Wood (1993) mass-loss prescription. Convective regions are modelled with the standard mixing length theory (Böhm-Vitense, 1958) using the mixing-length parameter $\alpha = 1.86$.

The stellar evolution code includes the most important energy-generating nuclear reactions and only calculates the abundance evolution of H, ^{3}He, ^{4}He, ^{12}C, ^{14}N, ^{16}O. In a separate post-processing approach, we use the stellar structure information from the calculated evolutionary sequence to model the nucleosynthesis of additional light elements in more detail (Cannon, 1993; Lugaro et al., 2004). The used nuclear network includes 77 species as described in Karakas (2010) with updated reaction rates from the 2016 JINA Reaclib database (Cyburt et al., 2010). The species are mainly isotopes between hydrogen and sulphur but also some iron-peak isotopes (cobalt, iron, and nickel) and a virtual neutron-capture "sink" particle, which accounts for neutron-capture reactions of species heavier than nickel.

In Figure 5.1 we show the evolution of our stellar model on the Hertzsprung-Russel diagram. The evolution of the first four thermal pulses is shown in more detail in Figure 5.2. The first two thermal pulses are relatively weak with He-burning luminosities below $10^{6}\,\mathrm{L}_{\odot}$. During the third thermal pulse the He-burning luminosity reaches a maximum of $L_{\mathrm{He}} = 5.9 \times 10^{6}\,\mathrm{L}_{\odot}$. Figure 5.3 shows this third thermal pulse in more detail in a Kippenhahn diagram including the convective instability in the intershell region. We extract the stellar structure of the model when the convective region reaches its largest extent. At this point the temperature and density at the outer boundary of the intershell-convective region are $T = 2.3 \times 10^{7}\,\mathrm{K}$ and $\rho = 34\,\mathrm{g\,cm^{-3}}$and reach up to $T = 2.3 \times 10^{8}\,\mathrm{K}$ and $\rho = 2500\,\mathrm{g\,cm^{-3}}$at the inner boundary of the intershell-convective region.

The temperature and density trajectory as function of time is shown in Figure 5.4, along with the trajectories of the other models used in this chapter, which we will discuss in the following sections. We list characteristics of each trajectory in Table5.1, such as the maximum temperature and density at the bottom of the convective region, the time until the maximum conditions are reached, and the composition of the convective region. Comparing the Monash- to the Stars-trajectory shows that the maximum temperature at the bottom of the convective region is very similar with only a slight variation between the models of $\Delta T = 1.5\,\mathrm{MK}$ (0.6 %). At the maximum temperatures of $T_{\mathrm{max,Stars}} = 2.289 \times 10^{8}\,\mathrm{K}$ for the Stars-trajectory and $T_{\mathrm{max,Monash}} = 2.275 \times 10^{8}\,\mathrm{K}$ for the Monash-trajectory, the temperature difference propagates into a reaction rate difference of 10 % for the main neutron-releasing $^{13}\mathrm{C}(\alpha,\mathrm{n})^{16}\mathrm{O}$ reaction. This reaction-rate difference is less than the variations discussed in the previous chapter, e.g., the factor uncertainty of the rate itself, or even just the difference between the rates for this reaction recommended by the Starlib and JINA Reaclib databases (see Table 4.4).

The main differences between the Monash- and the Stars-trajectory are the densities throughout the convective region and the time it takes to reach the maximum temperature and density. The maximum density of the Monash-trajectory is 35 % lower compared to the Stars-trajectory, while it takes 2.5 times as long for the Monash-trajectory to reach the maximum conditions at the bottom of the convective region. Moreover, the intershell abundances which we adopt as initial composition for the i-process nucleosynthesis are not identical. For our reference simulations with the Stars-trajectory we use a standard composition with the most abundant isotopes $X_0(^{4}\mathrm{He}) = 0.77$, $X_0(^{12}\mathrm{C}) = 0.22$, and $X_0(^{16}\mathrm{O}) = 7 \times 10^{-3}$. In contrast, the composition of the intershell in our model calculated with the Monash code is $X_0(^{4}\mathrm{He}) = 0.83$, $X_0(^{12}\mathrm{C}) = 0.16$, and $X_0(^{16}\mathrm{O}) = 4 \times 10^{-3}$ at the time when the trajectory is extracted.

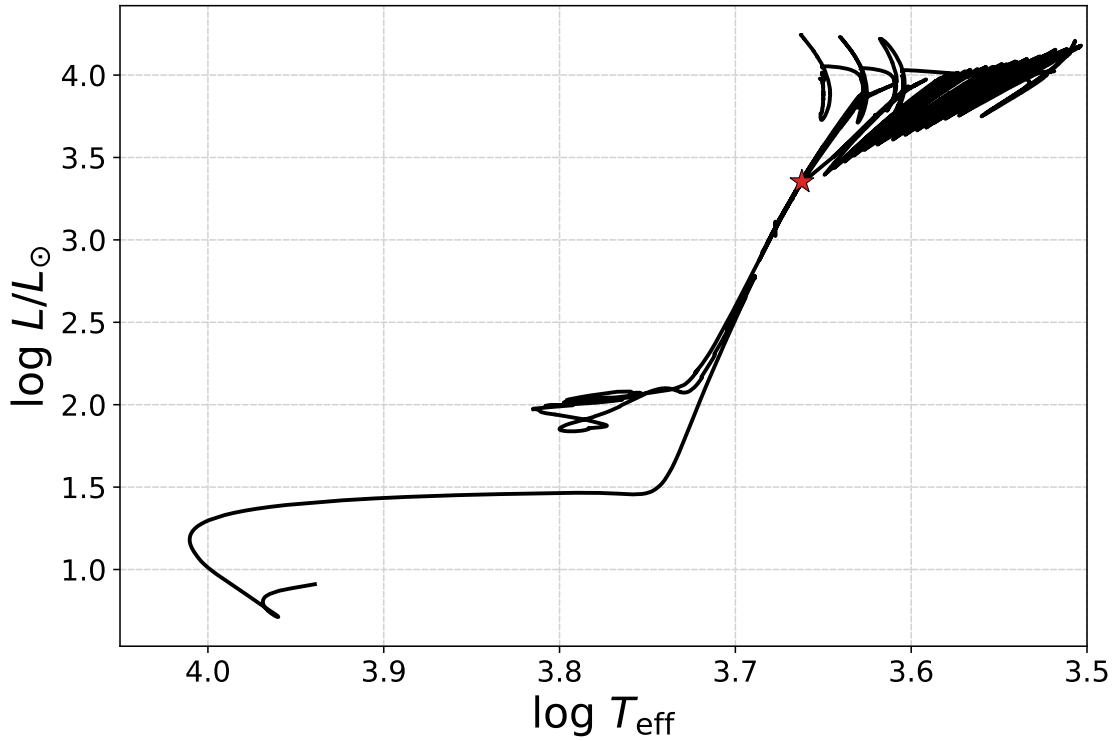

Figure 5.1: **Hertzsprung-Russel diagram** showing the evolution of our 1.3 $M_\odot$ model with an initial metallicity of $Z = 10^{-4}$. The red star highlights the chosen point in the evolution at which we extract the model. Note that luminosity peaks on the AGB during the thermal pulse (i.e. where the luminosity of He burning exceeds $10^5\,L_\odot$) are not shown for illustrative purposes.

Table 5.1: **Temperature-density trajectory characteristics**. Comparison of the maximum temperature $T_{\rm max}$ and maximum density $\rho_{\rm max}$ at the bottom of the convective region for the four models, as well as the time $t_{\rm max}$ each trajectory requires to reach these maximum conditions. The initial mass fraction X_0 of the three most abundant species ^{4}He, ^{12}C, and ^{16}O is also listed.

	$T_{\rm max}$ (10^8 K)	$\rho_{\rm max}$ (10^3 g/cm^3)	$t_{\rm max}$ (10^3 s)	$X_0(^4{\rm He})$	$X_0(^{12}{\rm C})$	$X_0(^{16}{\rm O})$
AGB (Stars)	2.3	3.9	14	0.77	0.22	7×10^{-3}
AGB (Monash)	2.3	2.5	34	0.83	0.16	4×10^{-3}
Post-AGB	2.8	4.0	6	0.76	0.23	8×10^{-3}
Core He flash	2.1	7.9	45	0.95	0.05	6×10^{-6}

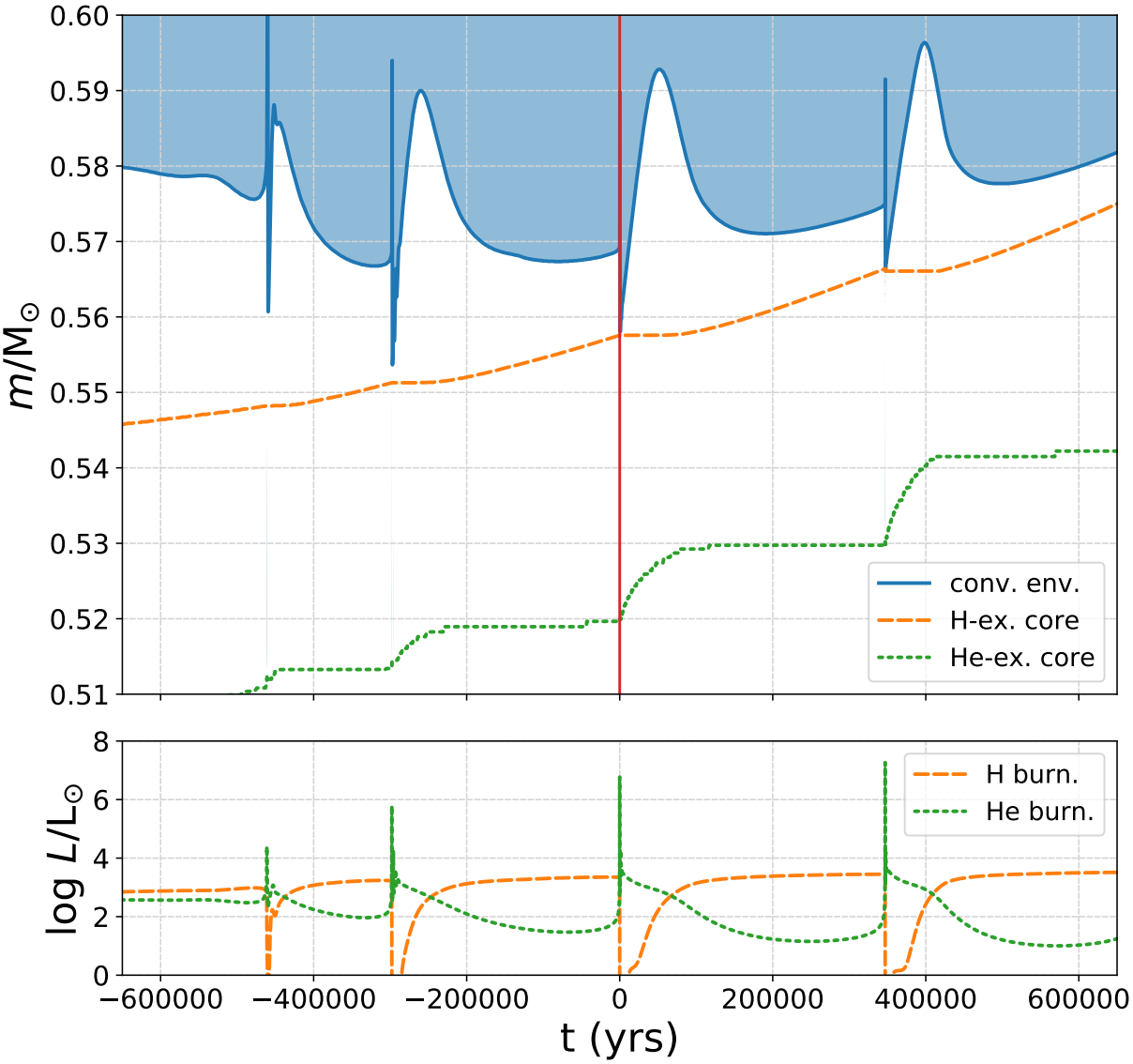

Figure 5.2: **Evolution of the first four thermal pulses on the AGB**. The time axis is offset by 2.66 Gyr. Time of zero is the time at which we extract the structure for the trajectory, highlighted by the red line. The upper panel shows a Kippenhahn diagram where blue shading indicates convection and lines show the locations of the edge of the convective envelope (blue line), the outer edge of H-exhausted core (orange dashed line), and the outer edge of the He-exhausted core (green dotted line). The lower panel shows the evolution of the H- and He-burning luminosities.

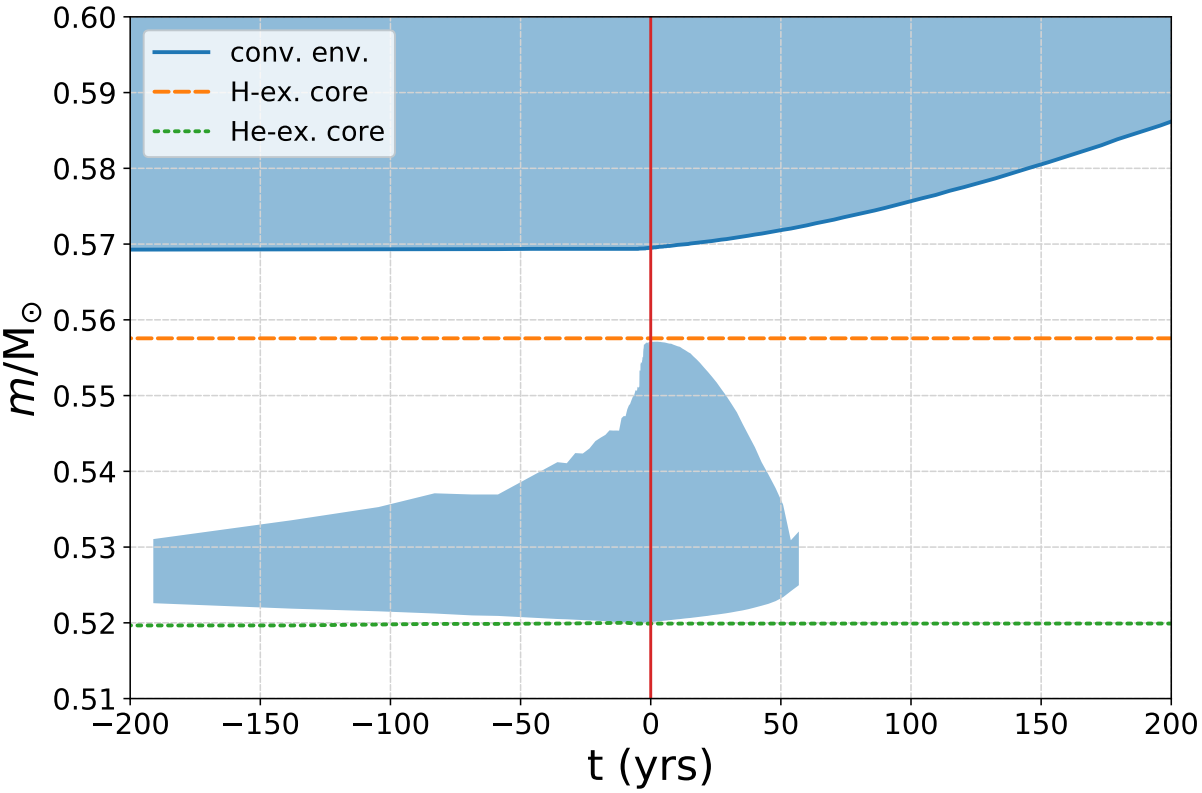

Figure 5.3: **Kippenhahn diagram of the third thermal pulse on the AGB**. Same as the upper panel in Figure 5.2 but zoomed in on the third thermal pulse and the flash-driven intershell convection.

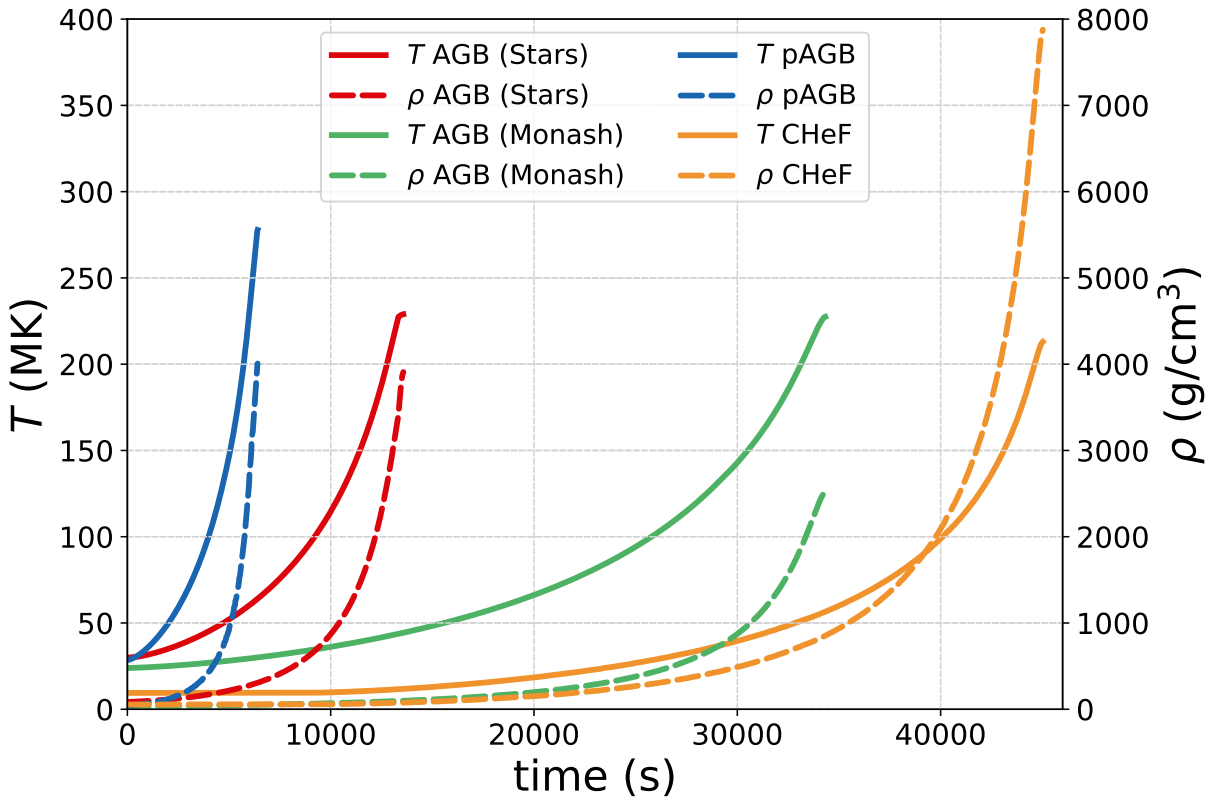

Figure 5.4: **Comparison of temperature-density trajectories.** The four separate stellar models refer to (*i*) AGB (Stars): the reference model of a He flash in a 1 $M_\odot$, $Z = 10^{-4}$ AGB star computed with the Stars code (Stancliffe et al., 2011), (*ii*) AGB (Monash): our model of a He flash in a 1.3 $M_\odot$, $Z = 10^{-4}$ AGB star computed with the Monash Stromlo code, (*iii*) pAGB: a 1.3 $M_\odot$, [Fe/H] $= -1.3$ post-AGB star (Lugaro et al., 2015), and (*iv*) CHeF: a core-helium flash model of a 0.8 $M_\odot$ ultra metal-poor star (Campbell, 2020). See main text for details.

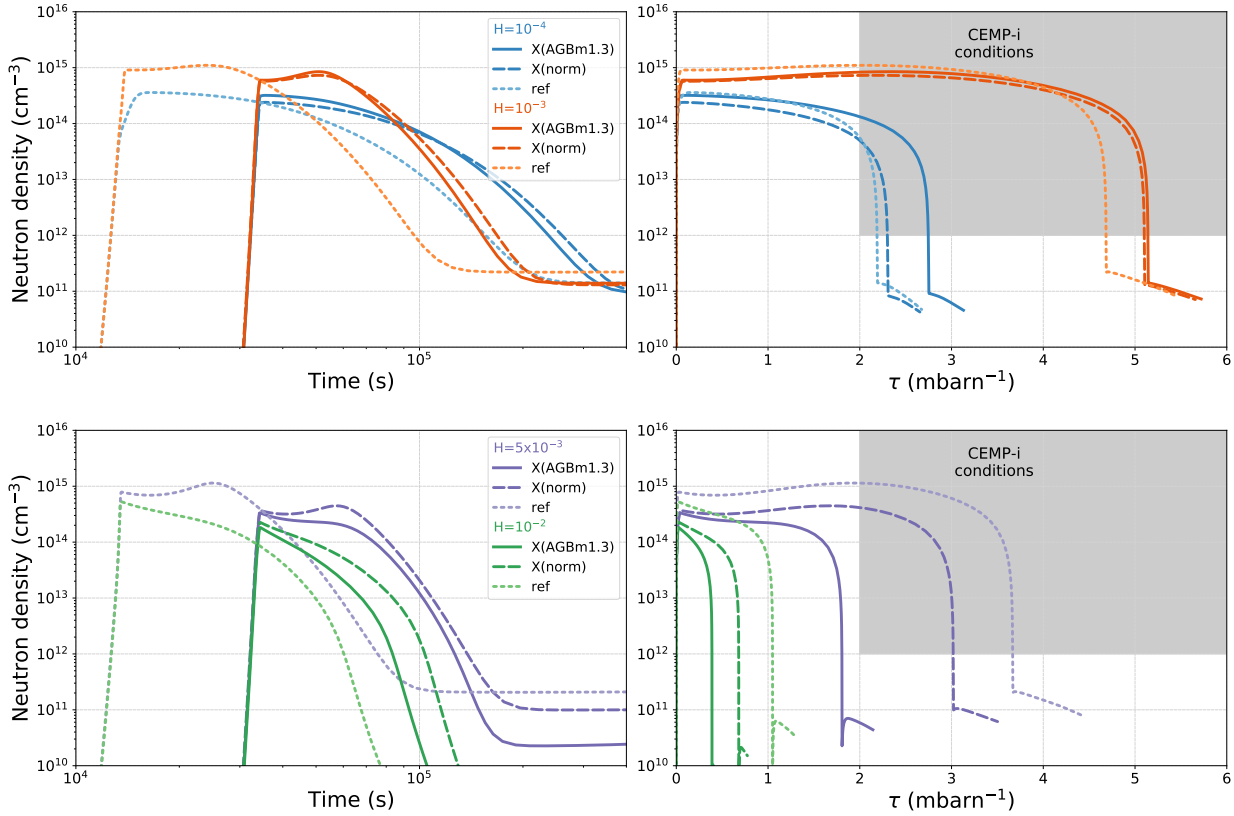

Figure 5.5: **Neutron-density evolution for the simulations using the Monash-trajectory.** Neutron densities for various ingested proton fractions are shown as function of time (left panels) and of the integrated neutron exposure τ (right panels). Two different initial compositions are compared: the self-consistent abundances from the post-processing of the AGB model labelled as X(AGBm1.3), and the standard composition from the previously presented reference simulations labelled as X(norm). The reference simulations with the Stars-trajectory and standard initial composition is also shown for comparison and labelled as ref. The shaded region in the right panels indicates conditions with $\tau \geq 2\,\mathrm{mbarn}^{-1}$ and $n \geq 10^{12}$ cm^{-3}, which are typical for the production of the i-process heavy-element abundance patterns observed in CEMP-i stars (Hampel et al., 2019).

5.1.2 Neutron production with the Monash-trajectory

In Figure 5.5 we show the neutron production resulting from our simulations using the Monash-trajectory and ingesting various initial proton fractions. We run each calculation twice with two different initial abundances to compare effects caused by the different temperature-density trajectory and those due to the differences in initial abundances. The first time we use the same standard initial abundance, which was previously used in the reference models with the Stars-trajectory. The second time we use the abundances of the intershell predicted by our stellar-evolution model and its post-processing nucleosynthesis calculations. The resulting maximum neutron densities and i-process neutron exposures are listed in Table 5.2.

Two major effects become obvious in Figure 5.5 when comparing the neutron-density evolution from the Monash- to the Stars-trajectory: (*i*) the time at which the neutron density rises is later for the models with the Monash-trajectory compared to the models with the Stars-trajectory, and (*ii*) the maximum neutron densities are lower for the models with the Monash-trajectory

Table 5.2: **Comparison of $n_{\max}$ and $\tau_{\rm i}$ results using four different trajectories**. For various initial proton fractions the resulting maximum neutron density $n_{\max}$ and total i-process neutron exposure $\tau_{\rm i}$ from each trajectory are compared to the reference simulations with the Stars-trajectory. Two different initial compositions for the Monash-trajectory are compared: the self-consistent abundances from the post-processing of the AGB model (AGB comp.), and the standard composition from the reference simulations (norm comp.).

	$X_0(\mathrm{H}) = 10^{-4}$		$X_0(\mathrm{H}) = 10^{-3}$		$X_0(\mathrm{H}) = 5 \times 10^{-3}$		$X_0(\mathrm{H}) = 10^{-2}$	
trajectory	$n_{\max}$ $(10^{14}\,\mathrm{cm}^{-3})$	$\tau_{\rm i}$ (mbarn^{-1})	$n_{\max}$ $(10^{14}\,\mathrm{cm}^{-3})$	$\tau_{\rm i}$ (mbarn^{-1})	$n_{\max}$ $(10^{14}\,\mathrm{cm}^{-3})$	$\tau_{\rm i}$ (mbarn^{-1})	$n_{\max}$ $(10^{14}\,\mathrm{cm}^{-3})$	$\tau_{\rm i}$ (mbarn^{-1})
Stars	3.6	2.19	11.0	4.68	11.4	3.67	5.3	1.05
Monash (AGB comp.)	3.2	2.75	8.5	5.14	3.3	1.81	1.8	0.39
Monash (norm comp.)	2.4	2.30	7.3	5.10	4.5	3.02	2.3	0.68
pAGB	9.1	0.35	65.4	1.83	111.0	2.22	89.3	1.07
CHeF (UMP comp.)	6.8	5.11	7.3	3.61	1.3	0.16	0.3	0.03

compared to the models with the Stars-trajectory. In Figure 5.5 the models with low ingested proton fractions of $X_0(\mathrm{H}) \leq 10^{-3}$ are shown in the upper panel, separated from models with higher ingested proton fractions of $X_0(\mathrm{H}) \geq 5 \times 10^{-3}$, which are shown in the lower panel. The choice of trajectory and initial composition has different effects on the i-process neutron exposure τ_{i} depending on the ingested proton fraction, which leads to two additional effects: (*iii*) for low ingested proton fractions ($X_0(\mathrm{H}) \leq 10^{-3}$) the models with the Monash-trajectory yield a higher τ_{i} compared to the models with the Stars-trajectory, and (*iv*) for high ingested proton fractions ($X_0(\mathrm{H}) \geq 5 \times 10^{-3}$) the models with the Monash-trajectory yield a lower τ_{i} compared to the models with the Stars-trajectory.

The time at which the neutron density rises is closely linked to the time it takes our parcel of material to reach the hottest conditions at the bottom of the convective intershell. In Figure 5.4 we can see that this takes 2.5 times longer for the Monash- compared to the Stars-trajectory. A direct consequence is a later rise of the neutron densities in the models with the Monash-trajectory. We have already examined similar behaviour in Chapter §4.3 where the convective velocities were slowed down by a scaling factor. In particular, the behaviour of the Monash-trajectory corresponds to an effective velocity scaling factor of $vsc = 0.4$ in terms of the time it takes to reach the maximum temperature and density compared to the reference simulation. However, this is not directly due to higher convective velocities in the Stars-trajectory, but rather due to a more extended convective region in the Monash-model, which is almost twice as large in mass and despite its lower density still approximately 50 % larger in radius..

By neglecting the differences in initial composition we gain the most insight into the differences in neutron production between the Monash- and and the Stars-trajectory. Therefore, we will first focus on the models where we combine the Monash-trajectory with the standard initial composition from the reference simulations. While the maximum temperature is comparable between the Monash- and the Stars-trajectory, the density given by the Monash-trajectory remains about a third lower. This significantly slows down the nuclear reactions, since the reaction rates depend on the number densities of the respective reactants. Even more importantly, we have to keep in mind that the neutron density shown in Figure 5.5 is directly proportional to the density of our parcel of material. Therefore it is no surprise that the Stars-trajectory with higher densities than the Monash-trajectory also results in higher n_{max}. However, the higher neutron-density values that the Stars-trajectory yields do not necessarily reflect a higher neutron abundance, or even a more favourable $^{13}\mathrm{C}/^{14}\mathrm{N}$ ratio. In fact, it is only for models with high ingested proton fractions of $X_0(\mathrm{H}) \geq 5 \times 10^{-3}$ that the models with the Stars-trajectory have a higher neutron abundance and higher $^{13}\mathrm{C}/^{14}\mathrm{N}$ ratio compared to the models from the Monash-trajectory when the maximum temperatures and densities are reached.

To understand the difference between the neutron production in the Monash- and Stars-trajectory we have to take the slower rise in temperature for the Monash-trajectory into account. In Chapter §4.3.2 we already examined the neutron production in models with slow convective velocities with $vsc < 1$. The Monash-trajectory is an example of such a model with an effective $vsc = 0.4$ and we can directly transfer the arguments about how the slower increase in temperature affects the neutron production. Such models with $vsc < 1$ experience higher $^{14}\mathrm{N}$ production prior to the main neutron production phase, particularly at high ingested proton fractions of $X_0(\mathrm{H}) \geq 5 \times 10^{-3}$. This leads to a lower $^{13}\mathrm{C}/^{14}\mathrm{N}$ fraction for the Monash-trajectory compared to the

same high proton fractions for the Stars-trajectory. Consequently, we see the similar behaviour in the models with Monash-trajectory, which we previously saw in Chapter §4.3.2, where the final i-process neutron exposure $\tau_{\rm i}$ increases for low proton fractions of $X_0({\rm H}) \leq 10^{-3}$ and decreases for high proton fractions of $X_0({\rm H}) \geq 5 \times 10^{-3}$.

Figure 5.5 and Table 5.2 show that the two simulations with the Monash-trajectory and different initial abundances enhance the variations in the neutron production which arise between the Monash- and Stars-trajectory with the same initial abundances: for low proton fractions of $X_0({\rm H}) \leq 10^{-3}$ the models with the self-consistent initial abundance from the intershell of the Monash-AGB model yield even higher $n_{\rm max}$ and $\tau_{\rm i}$ than the models with the standard initial composition. This is reversed for models with high proton fractions of $X_0({\rm H}) \geq 5 \times 10^{-3}$, where the standard initial composition lead to the higher $n_{\rm max}$ and $\tau_{\rm i}$. When comparing the reference models with the Stars-trajectory and the standard composition to the models with the Monash-trajectory and the self-consistent Monash-intershell composition, the models with an ingested proton fraction of $X_0({\rm H}) = 5 \times 10^{-3}$ show the largest differences in the neutron production. In the models with the Stars-trajectory $\tau_{\rm i}$ is twice as large and $n_{\rm max}$ even three times larger compared to the models with the Monash-trajectory.

The self-consistent intershell abundance from the Monash-model has a lower content of ^{12}C of $X_0(^{12}{\rm C}) = 0.16$ compared to the standard composition with $X_0(^{12}{\rm C}) = 0.22$. In the models where we use this self-consistent abundance as initial abundance for the i-process calculations, the models automatically have a higher proton-to-carbon ratio $Y_{\rm p}/Y(^{12}{\rm C})$ compared to the reference simulations with the same ingested proton fraction. The effects of different initial ^{12}C abundances were previously examined in Chapter §4.2. We have already seen that an increase in $Y_{\rm p}/Y(^{12}{\rm C})$ leads to higher $n_{\rm max}$ up to $Y_{\rm p}/Y(^{12}{\rm C}) \leq 0.2$, after which a further increase in $Y_{\rm p}/Y(^{12}{\rm C})$ leads to a decrease in $n_{\rm max}$ again (see Figure 4.7). In our simulations with the initial $X_0(^{12}{\rm C}) = 0.16$ from the Monash-model, the low ingested proton fractions of $X_0({\rm H}) = 10^{-4}$ and 10^{-3} result in $Y_{\rm p}/Y(^{12}{\rm C}) = 0.0075$ and 0.075, respectively. The models with higher ingested proton fractions of $X_0({\rm H}) = 5 \times 10^{-3}$ and 10^{-2} result in $Y_{\rm p}/Y(^{12}{\rm C}) = 0.375$ and 0.75, respectively. This shows that the models with the Monash-trajectory, the Monash-AGB initial abundances, and low ingested proton fractions of $X_0({\rm H}) \leq 10^{-3}$ fall into the $Y_{\rm p}/Y(^{12}{\rm C})$ regime where the higher $n_{\rm max}$ and $\tau_{\rm i}$ compared to the standard initial abundances can be explained by the increase of $Y_{\rm p}/Y(^{12}{\rm C})$. Analogously, the high ingested proton fractions of $X_0({\rm H}) \geq 5 \times 10^{-3}$ lead to $Y_{\rm p}/Y(^{12}{\rm C})$ ratios in the regime where the higher $Y_{\rm p}/Y(^{12}{\rm C})$ of the Monash-AGB initial abundances compared to the standard composition cause the drop in $n_{\rm max}$ and $\tau_{\rm i}$ shown in Figure 5.5 and Table 5.2.

Altogether we have seen that the temperature-density trajectory extracted from the third thermal pulse of our Monash-AGB model of a 1.3 $M_\odot$, $Z = 10^{-4}$ star leads to differences in the neutron production compared to the trajectory of a 1.0 $M_\odot$, $Z = 10^{-4}$ stellar model computed with the Stars code. Despite covering a very similar temperature range, the maximum density of the Monash-trajectory is lower when compared to the Stars-trajectory and a larger convective region contributes to a longer time needed until maximum temperature and density are reached. Additionally, the initial composition inferred from the Monash-AGB model has a lower $X_0(^{12}{\rm C})$ compared to the standard AGB-intershell composition used in the reference simulations with the Stars-trajectory. Particularly the effects of a slower temperature increase and a variation in initial ^{12}C abundances are tested as individual parameters in the previous chapter. The simulations us-

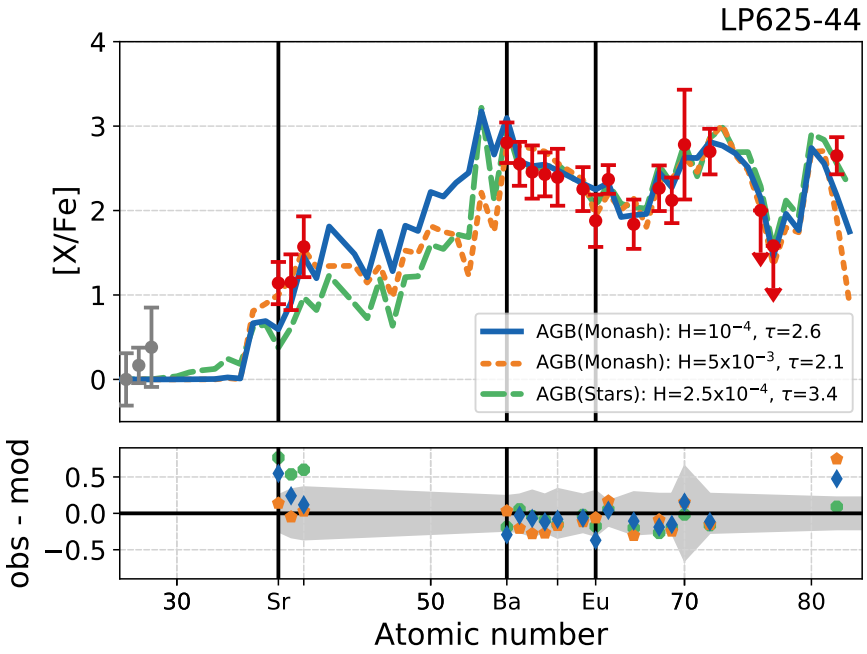

Figure 5.6: **Best fits of the heavy-element abundances of CEMP-i star LP625-44**. The blue and orange line show the best fitting models using the Monash-trajectory with $X_0(\mathrm{H}) = 10^{-4}$ and $X_0(\mathrm{H}) = 5 \times 10^{-3}$, respectively. For comparison the best fitting model from the reference simulations with the Stars-trajectory is shown as well. Exposure values in the label are given in mbarn^{-1}.

ing the Monash-trajectory show how these combined effects are encountered in a different stellar model and influence the neutron production in a slightly different environment. At an ingested proton fraction of $X_0(\mathrm{H}) = 5 \times 10^{-3}$ this can lead to a significant difference in $n_{\max}$ and τ_{i}, where the models with the Stars-trajectory yield an i-process exposure that is twice as large as the τ_{i} from the respective model with the Monash-trajectory, at a maximum neutron density that is even three times larger.

5.1.3 Heavy-element abundances from the Monash-trajectory

Here we discuss the heavy-element abundance patterns from the i-process nucleosynthesis in the models with the Monash-trajectory. For this purpose we use observational constraints from two well-studied CEMP-i stars LP625-44 and CS31062-050. In Figure 5.6 we show the heavy-element abundances observed in LP625-44 and the two best fitting abundance patterns predicted by the models with the Monash-trajectory and the self-consistent AGB-intershell composition. The best fitting abundances result from the models with ingested proton fractions of $X_0(\mathrm{H}) = 10^{-4}$ and $X_0(\mathrm{H}) = 5 \times 10^{-3}$. Based on their χ^2 evaluation, these two models describe the observed abundance pattern almost identically well. For comparison we also show the best fit from the models with the Stars-trajectory, which was previously presented and discussed in Chapter §3 (see Figure 3.5).

When comparing the three heavy-element models presented in Figure 5.6 it becomes obvious that they deviate most from each other in the region between the first and second s-process peak (elements between Zr and Ba). The abundances of the elements in this region do not have observational constraints and the predicted abundances for these elements can deviate up to 1 dex between the three presented models.

The two best fits from the Monash-models occur at very different stages in the nucleosynthesis evolution of the respective model, which can partly be seen in the vastly different time scales needed for the heavy-element production of the best-fitting abundances: the model with $X_0(\mathrm{H}) = 10^{-4}$ reaches the presented fit at $\tau = 2.6\,\mathrm{mbarn}^{-1}$ after 1.3×10^5seconds. In contrast, the model with $X_0(\mathrm{H}) = 5 \times 10^{-3}$ takes 4.9×10^7 seconds to reach the presented fit after a neutron exposure of $\tau = 2.2\,\mathrm{mbarn}^{-1}$. Both models reach similarly high neutron densities with $n_{\mathrm{max}} = 3.2 \times 10^{14}\,\mathrm{cm}^{-3}$ and $n_{\mathrm{max}} = 3.3 \times 10^{14}\,\mathrm{cm}^{-3}$ for the cases with $X_0(\mathrm{H}) = 10^{-4}$ and $X_0(\mathrm{H}) = 5 \times 10^{-3}$, respectively (see Figure 5.5 and Table 5.2). The main difference is that the model with $X_0(\mathrm{H}) = 10^{-4}$ can uphold this high neutron density much longer and build up a neutron exposure of $\tau_{\mathrm{i}} = 2.8\,\mathrm{mbarn}^{-1}$ before n drops to levels below $10^{12}\,\mathrm{cm}^{-3}$. This means that the presented best fit occurs at the stage of high neutron density during the i-process nucleosynthesis, which is at the relatively early time of ca. 10^5 seconds. This is not the case for the model with $X_0(\mathrm{H}) = 5 \times 10^{-3}$. It can only build up an i-process exposure of $\tau_{\mathrm{i}} = 1.8\,\mathrm{mbarn}^{-1}$ before the neutron density drops to levels below $10^{12}\,\mathrm{cm}^{-3}$. The presented best fit occurs at a higher neutron exposure and at a much later time ($> 10^7$ seconds), so that the model has additional time to produce heavy elements at neutron densities below i-process levels.

Given the simplicity of our models and particularly the lack of mixing effects, it is uncertain whether the low neutron-density tail (see Figure 5.5) after the main i-process neutron exposure is predicted correctly by our models. The i-process neutron production via $^{13}\mathrm{C}(\alpha, \mathrm{n})^{16}\mathrm{O}$ at the high temperature at the bottom of the convective region not only provides high neutron densities but also produces ^{16}O. Although the doubly-magic isotope ^{16}O has a relatively small neutron capture cross section (e.g., ca. 100 times lower than the $^{14}\mathrm{N}(\mathrm{n}, \mathrm{p})$ cross section and ca. 500 times lower than the $^{56}\mathrm{Fe}(\mathrm{n}, \gamma)$ cross section) the high abundance of both neutrons and ^{16}O ultimately leads to the production of ^{17}O via $^{16}\mathrm{O}(\mathrm{n}, \gamma)^{17}\mathrm{O}$. In our model with $X_0(\mathrm{H}) = 5 \times 10^{-3}$ a mass fraction as high as $X(^{17}\mathrm{O}) = 2 \times 10^{-3}$ has built up by the time the the ^{13}C neutron source is exhausted and the neutron density drops below $10^{12}\,\mathrm{cm}^{-3}$ at $\tau_{\mathrm{i}} = 1.8\,\mathrm{mbarn}^{-1}$. At the high temperatures at the bottom of the convective region some of the abundant ^{17}O can produce neutrons via $^{17}\mathrm{O}(\alpha, \mathrm{n})^{20}\mathrm{Ne}$. This feature is not unique to our Monash-trajectory or the models with $X_0(\mathrm{H}) = 5 \times 10^{-3}$. E.g., we have already seen in Chapter §3 (see Figure 3.5) that the models with the Stars-trajectory provide a better fit to the abundances observed in LP625-44 when further neutron exposure at lower neutron densities of $n < 10^{12}\,\mathrm{cm}^{-3}$ is taken into account.

The additional neutron exposure after the main i-process nucleosynthesis occurs at lower-than-i-process neutron densities of $n < 10^{12}\,\mathrm{cm}^{-3}$. This impacts the time scale of further heavy-element production and alters the i-process abundance pattern. A major uncertainty of proton-ingestion episodes regards the feedback on the stellar structure and the further evolution by the energy released from the nuclear reactions. The time scale of heavy-element nucleosynthesis after the ingestion of protons appears to be limited by the occurrence of a split in the convective region, caused by a temperature inversion when the energy released by the nuclear reactions in the proton-ingestion episode exceeds the He-burning energy. Although this split is generally considered to occur almost immediately, the exact time and consequence for the stellar evolution varies between models. For example, Cristallo et al. (2009) and Cristallo et al. (2016) find a convective zone splitting 1.65 years (5×10^7 seconds) and 0.65 years (2×10^7 seconds), respectively, after the start of the proton-ingestion episode, followed by a particularly deep third dredge-up episode. Afterwards

the star resumes a standard AGB evolution including multiple thermal pulses and third dredge-ups. In very recent models, Choplin et al. (2021) find that the convective zone in their 1 $M_\odot$, [Fe/H] $= -2.5$ stellar model splits after 1.18 years (3.6×10^7 seconds). The upper part of the convective region then merges with the envelope after 8 years. In this simulation the enhanced carbon abundance in the envelope raises the opacity so much that strong mass loss occurs and prevents further thermal pulses. These considerations show that nucleosynthesis time scales of a few 10^7 seconds after the start of the proton-ingestion episode may indeed be reasonable. Additionally, three-dimensional simulations indicate that the convective-zone split may be delayed compared to one-dimensional models (Stancliffe et al., 2011; Herwig et al., 2011, 2014).

At the very least the uncertainty about the further stellar evolution allows us to speculate about the possibility of further heavy-element nucleosynthesis after the main production by the i process. This could, but does not necessarily have to, take place in the neutron-density tail after the maximum i-process neutron densities have been reached. However, too much further processing by the s process, as would be the case if the proton-ingestion episode is followed by a standard AGB evolution, bears the risk that the i-process heavy-element abundance pattern gets erased and replaced by a typical s-process pattern instead.

The abundance comparison to CEMP-i star LP625-44 shows that there is the option of complementing the heavy-element production from the i process with further nucleosynthesis at lower neutron densities in order to reproduce the observations. This is also the case, albeit to a different extent and effect, when comparing our models to observations of CEMP-i star CS31062-050. In Figure 5.7 we show the heavy-elements observed in CS31062-050 compared to two fits from our models with the Monash-trajectory and in comparison to the best fit from the models with the Stars-trajectory. The two models from the Monash- and the Stars-trajectory with $X_0(\mathrm{H}) = 10^{-4}$ both describe the observed abundances very well for most elements. The exception is the abundance of Pb, which is underpredicted by both models but the worse prediction is given by the model with the Monash-trajectory with Δ[Pb/Fe] $= 0.5$. Another discrepancy between the models can again be found in the abundance levels of elements between the first and second s-process peak. However, the measurements of CS31062-050 provide some constraints for this region due to the measurement of Mo (Z=43), which is reasonably matched by both models.

In Figure 5.7 we also present a fit to the observed elements in CS31062-050 with $Z \geq 56$ (Ba to Pb) from the model with the Monash-trajectory and $X_0(\mathrm{H}) = 10^{-3}$. This model provides the best fit to the elements with $Z \geq 56$ but does not predict much enhancements for the lighter elements before the second s-process peak. The model with the Monash-trajectory and $X_0(\mathrm{H}) = 10^{-3}$ is one of the most extreme trajectories presented so far and reaches the highest i-process neutron exposures. In Figure 5.8 we show the evolution of the heavy-element abundance pattern at three different times. The first pattern shows the initial abundances (blue line). The second pattern shows the heavy-element production after 4.2×10^4 seconds when a neutron exposure of $\tau = 1\,\mathrm{mbarn}^{-1}$ is reached (orange dashed line). At this point the the heavy elements around the first s-process peak around Sr have been produced as well as some heavier elements past the first peak. However, the neutron-capture path has not fully reached the second s-process peak around Ba yet. Finally, the third line shows the abundance pattern at the final i-process neutron exposure of $\tau_\mathrm{i} = 5.1\,\mathrm{mbarn}^{-1}$ after 1.5×10^5 seconds. The heavy elements of the second s-process peak and beyond have been produced at the expense of the previously produced isotopes around the

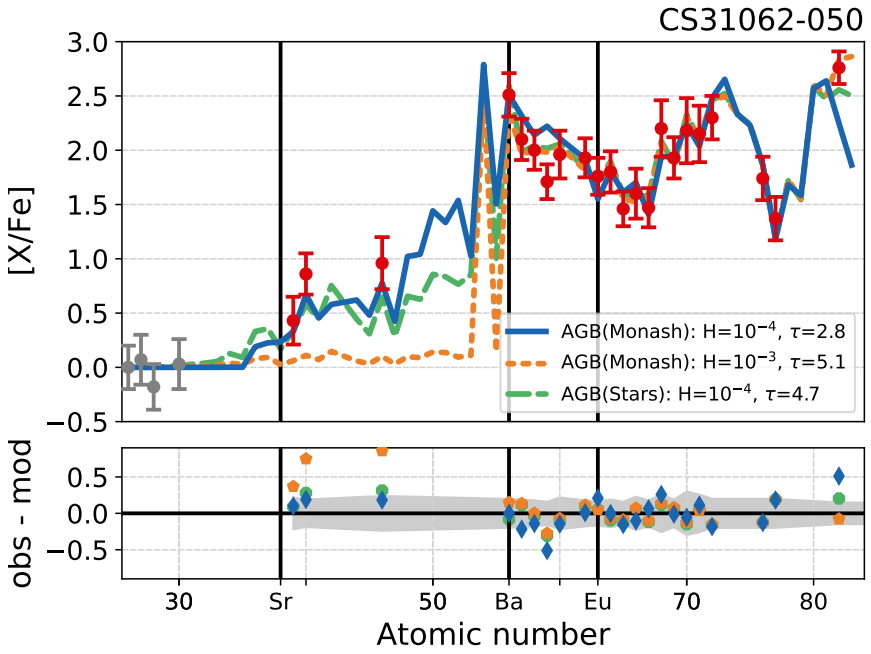

Figure 5.7: **Best fits of the heavy-element abundances of CEMP-i star CS31062-050**. The blue line shows the best fitting model using the Monash-trajectory with $X_0(\mathrm{H}) = 10^{-4}$. The orange line shows the model with the Monash-trajectory and $X_0(\mathrm{H}) = 10^{-3}$ at the final i-process neutron exposure τ_i. For comparison the best fitting model from the reference simulations with the Stars-trajectory is shown as well. Exposure values in the label are given in mbarn^{-1}.

first s-process peak. Particularly high abundances of xenon, barium and lead can be seen with $X(\mathrm{Xe}) = 7.4 \times 10^{-6}$, $X(\mathrm{Ba}) = 4.3 \times 10^{-6}$, and $X(\mathrm{Pb}) = 1.5 \times 10^{-5}$. Compared to their initial abundances, this corresponds to enhancements by 4.5 to 5 dex. In contrast, the abundance of the first s-process peak element Sr is only $X(\mathrm{Sr}) = 3 \times 10^{-9}$, which means an enhancement of barely 1 dex compared to its initial abundance. Interestingly, one can also see in Figure 5.8 how the main neutron-capture seeds around the Fe peak get depleted at first, but replenished again by production from neutron-capture reactions onto the lightest elements. In Figure 5.7 we take the heavy element abundance pattern at the model's final i-process exposure of $\tau_\mathrm{i} = 5.1\,\mathrm{mbarn}^{-1}$ with its strong enhancements in the elements of Xe, Ba, and above, and scale it to the abundances observed in CS31062-050. This results in a strongly diluted mixture (d=0.9968 as defined in Hampel et al. (2019) in Equation 2.2), where the strong enhancements of Xe, Ba, and heavier elements show up as clear signatures. The comparatively light enhancements of elements lighter than Xe, e.g. the first s-process peak elements, do not leave a notable imprint in the final abundance pattern.

The presented evolution of the heavy-element abundances produced in the model with the Monash-trajectory and $X_0(\mathrm{H}) = 10^{-3}$ shows how strong enhancements and characteristics of the heaviest elements can be produced without simultaneously affecting the abundances of the first s-process peak elements. Potentially, this opens another possibility to explain observed abundance patterns of CEMP-i stars as a combination of a strong i-process event, followed by milder heavy-element nucleosynthesis responsible for producing the first s-process peak signatures in the subsequent evolution. We want to stress that these options are presented as speculations, not as clear conclusions of this work. As already mentioned, the subsequent evolution of the star following

a proton-ingestion episode remains uncertain. Additionally, our single-zone models do not include the effects of mixing. Particularly for the last presented abundance pattern, the constant mixing with unprocessed material can replenish the neutron-capture seeds (e.g., Fe), which may enhance the signatures of the first s-process peak elements.

5.1.4 Summary

In this section we present the stellar evolution model of a 1.3 $M_\odot$, $Z = 10^{-4}$ star computed with the Monash-Stromlo evolution code. The star in this model is more massive than the 1 $M_\odot$, $Z = 10^{-4}$ stellar evolution model computed with the Stars code by Stancliffe et al. (2011), which we base the thermodynamic properties for our i-process nucleosynthesis studies in the previous chapters on. To show how the conditions in an early thermal pulse of a low-mass, low-metallicity star can vary, we have complemented the previously used Stars-trajectory with a new temperature-density trajectory, the Monash-trajectory, extracted from the third thermal pulse of our new model, when the flash-driven convective region is at its largest extent. We find that the maximum temperatures at the bottom of the convective shell of both trajectories are almost identical. The density in the Monash-trajectory is lower than in the Stars-trajectory, but the travel time from the top of the convective region to reach the maximum conditions at the base of the intershell is longer in the Monash-trajectory due to its higher mass and radius compared to the Stars-trajectory.

The nucleosynthesis post-processing of our stellar evolution model predicts an intershell composition where the carbon abundance with $X_0(^{12}\mathrm{C}) = 0.16$. This abundance of ^{12}C is lower than the standard composition with $X_0(^{12}\mathrm{C}) = 0.22$, which we adopt as initial composition for the i-process nucleosynthesis calculations in the previous chapters utilising the Stars-trajectory and the lower is ^{12}C composition is more realistic for the intershell composition of an early thermal pulse in a metal-poor star. Using the Monash-trajectory and the self-consistent intershell abundances as initial composition, we find very efficient neutron production where the highest i-process exposures of $\tau_\mathrm{i} = 5.1\,\mathrm{mbarn}^{-1}$ are achieved in the model with $X_0(\mathrm{H}) = 10^{-3}$.

Comparing the models with the Monash-trajectory to those with the Stars-trajectory, we find that the neutron production is affected by a combination of aspects studied in the previous Chapter §4. In particular, we find that the lower initial $X_0(^{12}\mathrm{C})$ of the Monash-trajectory combined with its longer duration to reach the maximum temperatures and densities (which can be interpreted like a velocity scaling factor examined previously) lead to higher i-process neutron exposures for low ingested proton fractions of $X_0(\mathrm{H}) \leq 10^{-3}$ compared to the models with the Stars-trajectory. The opposite trend becomes apparent for high ingested proton fractions of $X_0(\mathrm{H}) \geq 5\times10^{-3}$, where the i-process neutron exposure from the models with the Monash-trajectory are significantly lower by a factor of 2 to 3, compared to the models with the Stars-trajectory.

We compare the i-process heavy-element abundance patterns produced in the models with the Monash-trajectory to the observed abundances of CEMP-i stars LP625-44 and CS31062-050 and to the best fits for these patterns from the models with the Stars-trajectory. Amongst the models, which describe the observed abundances best we find two main distinctions: (*i*) for elements in the region between the first and second s-process peak (Zr to Ba) the different models predict abundances varying by up to 1 dex. Therefore more complete observational abundance patterns and particularly more abundance measurements of the elements between Zr and Ba are desirable. The measurements of these additional elements have high potential to deliver additional constraints

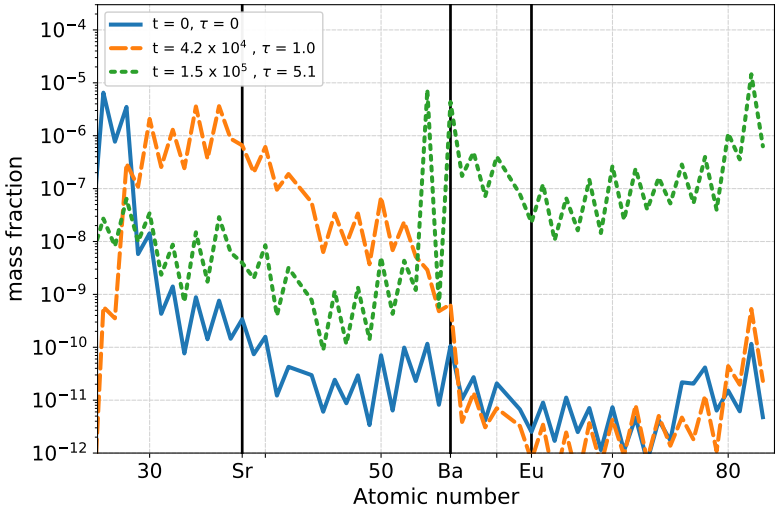

Figure 5.8: **Heavy-element abundance evolution for the model with the Monash-trajectory and $X_0(\mathrm{H}) = 10^{-3}$.** The initial abundances are shown, as well as the abundance patterns at two later times after a neutron exposure of $\tau = 1.0\,\mathrm{mbarn}^{-1}$and at the final i-process exposure of $\tau_\mathrm{i} = 5.1\,\mathrm{mbarn}^{-1}$. The time t of the model is given in the label in units of seconds and the neutron exposure τ in mbarn^{-1}.

to distinguish between i-process models. Particular differences between the models, which lead to these diverging abundance predictions, are related to the progress of the nucleosynthesis model in its heavy-element production. This relates to another major distinction between the best-fitting models: (*ii*) While some models reproduce the observed abundance patterns best while still in the phase of i-process nucleosynthesis at high neutron densities, other models achieve a better fit when additional heavy-element production occurs after the main i-process event at lower neutron densities below $n < 10^{12}$ cm^{-3}. In our models this subsequent nucleosynthesis occurs on a time scale of a few 10^7 seconds, which may be consistent with the time delay between the proton-ingestion and the quenching of the i-process nucleosynthesis due to a split in the convective zone. However, the uncertainties of how the proton-ingestion episode influences the star's structure and its further evolution only leaves us speculating if and how the i-process abundance pattern gets processed further before being observed at the surface of a CEMP-i star. Does additional significant heavy-element nucleosynthesis occur in the tail of the i-process neutron density, or as part of the star's further AGB evolution, or in an unrelated nucleosynthesis event, or maybe not at all? Hopefully, improved stellar models and more observational heavy-element abundances, including measurements for elements between Zr and Ba, will shed light on the formation history of CEMP-i stars and the history of the heavy elements in their atmospheres.

5.2 Very late thermal pulse during post-AGB phase

Post-AGB stars with (very) late thermal pulses have been suggested to host proton-ingestion episodes and potentially i-process nucleosynthesis (e.g., Herwig et al., 2011; Lugaro et al., 2015). We show in Hampel et al. (2019), that the abundances observed in Magellanic post-AGB stars, which

challenge s-process nucleosynthesis with puzzlingly low Pb abundances (De Smedt et al., 2012; van Aarle et al., 2013; De Smedt et al., 2014), are compatible with i-process nucleosynthesis. The progenitors of these objects are 1 to 1.5 $M_\odot$ stars at observed metallicities of $-1.34 \leq$ [Fe/H] ≤ -1.15 (van Aarle et al., 2013). Lugaro et al. (2015) computed a 1.3 $M_\odot$ stellar model with [Fe/H] $= -1.3$ and modelled a proton-ingestion episode during the 13th thermal pulse, after the star had already left the AGB track. We use the structure and nucleosynthesis of the model from Lugaro et al. (2015) to construct a temperature-density trajectory and determine the appropriate initial composition (see Lugaro et al., 2015, and references therein for details of the model and their Figure 1 for an overview of the evolution on the Hertzsprung-Russel diagram). We will refer to this trajectory as the pAGB-trajectory. The pAGB-trajectory is shown in Figure 5.4 in comparison to the trajectories of the previously discussed AGB thermal pulses (the Monash- and Stars-trajectory) and the conditions during a core helium flash which we will present in the next chapter. In Table 5.1 we list characteristics of the trajectory as well as the composition of the model's convective region.

Among the presented trajectories, the pAGB-trajectory provides the highest temperature at the bottom of the convective region, which reaches up to $T_{\max} = 2.8 \times 10^8$ K. The maximum density is almost the same as for the Stars-trajectory. Compared to the convective region in the thermal pulses of the previously discussed AGB models, this post-AGB star model has a relatively small convective region and higher convective velocities. This results in a temperature-density trajectory where the maximum conditions at the bottom of the convective region are reached quicker than in the other trajectories. Compared to the Stars-trajectory, the pAGB-trajectory reaches the maximum temperature and density five times faster. Therefore the pAGB-trajectory represents the situation of $vsc = 5$ when the trajectory's faster crossing time through the convective region is interpreted in the velocity-scaling framework from Chapter §4.3. The composition of the post-AGB star's convective region (see Table 5.1 for abundances of the most abundant species and Lugaro et al. (2015) for more details), which we use as initial composition for the i-process nucleosynthesis calculations, is very similar to the standard intershell composition which we have previously adopted for the reference models with the Stars-trajectory. This is at least the case for the light elements due to the previous processing through CNO-cycling and He-burning, while the abundances of the heavier elements are an order of magnitude higher due to the higher metallicity of the post-AGB star model.

In Figure 5.9 we show the evolution of the neutron densities in our i-process simulations with the pAGB-trajectory and different ingested proton fractions. Additionally, we list $n_{\max}$ and $\tau_{\rm i}$ for each simulation in Table 5.2. Note that we define $\tau_{\rm i}$ here as the exposure at the time when the neutron density drops to $n = 10^{12}\,\mathrm{cm}^{-3}$ for the first time after reaching $n_{\max}$. In a subsequent stage the simulations with the pAGB-trajectory experience i-process neutron densities of $n > 10^{12}\,\mathrm{cm}^{-3}$ in the neutron-density tail, which we discuss later and do not include in the considerations for $\tau_{\rm i}$ at this point. Compared to the reference simulations with the Stars-trajectory, all models with the pAGB-trajectory reach the neutron production phase earlier due to the short time needed for the pAGB-trajectory to reach the maximum temperature. The maximum neutron densities in the models with the pAGB-trajectory are higher for all X_0(H) compared to the respective model with the Stars-trajectory, while the opposite is true for the i-process neutron exposures. The model with the pAGB-trajectory and an ingested proton fraction of $X_0(\mathrm{H}) = 5 \times 10^{-3}$ reaches the highest neutron density in the presented simulations with $n_{\max} = 1.1 \times 10^{16}\,\mathrm{cm}^{-3}$, close to a

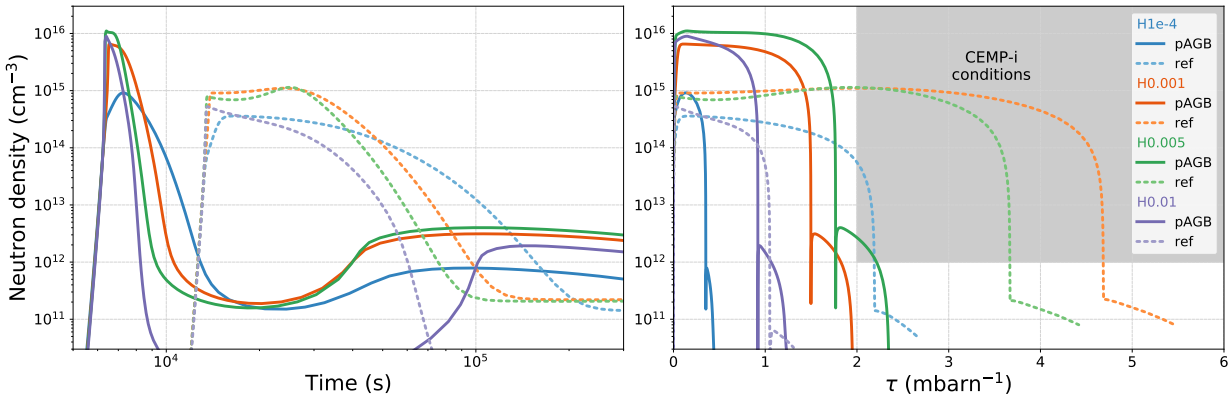

Figure 5.9: **Neutron-density evolution for the simulations using the pAGB-trajectory.** Neutron densities for various ingested proton fractions are shown as function of time (left panels) and of the integrated neutron exposure τ (right panels). The reference simulations with the Stars-trajectory (labelled as ref) are also shown for comparison. The shaded region in the right panels indicates conditions with $\tau \geq 2\,\mathrm{mbarn}^{-1}$ and $n \geq 10^{12}$ cm^{-3}, which are typical for the production of the i-process heavy-element abundance patterns observed in CEMP-i stars (Hampel et al., 2019).

whole magnitude higher than in the reference simulation. This is also the model amongst those with the pAGB-trajectory, which reaches the highest i-process neutron exposure of $\tau_{\mathrm{i}} = 1.8\,\mathrm{mbarn}^{-1}$ although this is ca. $\Delta\tau_{\mathrm{i}} = 1.5\,\mathrm{mbarn}^{-1}$ lower than the exposure reached in the reference simulation, despite the opposite trend for n_{max}.

A major difference between the models with the pAGB-trajectory and the reference simulations with the Stars-trajectory is the maximum temperature at the bottom of the convective region. Since the $^{13}\mathrm{C}(\alpha,\mathrm{n})^{16}\mathrm{O}$ reaction is highly temperature sensitive, the change in maximum temperature has a direct influence on the rate at which neutrons can be released. This temperature difference alone converts into a reaction-rate difference of more than a factor of 25 for the $^{13}\mathrm{C}(\alpha,\mathrm{n})^{16}\mathrm{O}$ reaction. Additionally, from our considerations of models with the Stars-trajectory and $vsc > 1$ in Chapter §4.3.1 we know that a complex interplay between different reaction rates and the rate of temperature increase influences the neutron production as well. In the simulations with the pAGB-trajectory these effects are enhanced since the time to reach the maximum temperature is five times shorter than for the reference simulations.In combination with the higher maximum temperature the rate of the temperature increase is even higher than in either variation alone. Neither of these variations has significant influence on the β-decay rate of $^{13}\mathrm{N}$, leading to the same situation encountered in Chapter §4.3.1 for simulations with $vsc > 1$: a large fraction of $^{13}\mathrm{N}$ has not decayed to $^{13}\mathrm{C}$ yet, when the highest temperature at the bottom of the convective region is reached and the $^{13}\mathrm{C}(\alpha,\mathrm{n})^{16}\mathrm{O}$ reaction is activated. Due to the higher maximum temperatures the simulations with the pAGB-trajectory still reach higher neutron densities than the reference simulations, but the higher temperatures and neutron densities also impact the neutron-recycling reactions. As a consequence the high neutron densities drop very quickly below i-process neutron densities and the i-process neutron exposures are lower than in the reference simulations.

The model's metallicity is an additional effect that has to be taken into account for the interpretation of the simulations with the pAGB-trajectory. Compared to the reference models, the heavy elements that capture the free neutrons are 1 dex more abundant due to the higher metallicity of

the initial composition. At the same neutron densities, a composition with higher metallicity has a lower neutron-to-seed ratio. The free neutrons get captured by the 10-times more abundant seed nuclei, which decreases the heavy-element enhancements and the progression of the neutron-capture path. Additionally, the higher neutron densities from the models with the pAGB-trajectory cause the neutron-capture path to produce heavy elements further away from the valley of stability, where the average neutron-capture cross sections are lower, such that the progression of the heavy-element nucleosynthesis is slowed down in terms of neutron exposure (see, e.g., Figure 2.1 and discussion in previous chapters).

In Figure 5.10 we show the heavy-element abundances that are produced in our simulations with the pAGB-trajectory for ingested proton fractions between $10^{-4} \leq X_0(\mathrm{H}) \leq 10^{-2}$ at the time of their respective τ_i. The heavy-element production is not very advanced at this time for any of the ingested proton fractions, due to the combination of the low τ_i, the high n_max, and the high metallicity of the initial composition. For the simulations with $X_0(\mathrm{H}) = 10^{-4}$ and $X_0(\mathrm{H}) = 10^{-2}$, which have $\tau_\mathrm{i} < 1\,\mathrm{mbarn}^{-1}$, the neutron-capture path has barely started producing the elements of the first peak. The shown simulations with $X_0(\mathrm{H}) = 10^{-3}$ and $X_0(\mathrm{H}) = 5 \times 10^{-3}$ reach higher neutron exposures of $\tau_\mathrm{i} = 1.5\,\mathrm{mbarn}^{-1}$ and $\tau_\mathrm{i} = 1.8\,\mathrm{mbarn}^{-1}$ respectively, such that the neutron-capture path has at least passed the elements around the first peak, but has still not advanced enough to start the production of the second-peak elements.

It becomes clear that the models with the pAGB-trajectory do not reach conditions where efficient i-process nucleosynthesis takes place before the ^{13}C source is exhausted and the neutron density drops below $n = 10^{12}\,\mathrm{cm}^{-3}$. Already at $t = 2 \times 10^4\,\mathrm{s}$ the neutron density in all models with the pAGB-trajectory has dropped to $n \approx 2 \times 10^{11}\,\mathrm{cm}^{-3}$ or even lower. However, just like in the previously discussed cases with the Monash- and Stars-trajectory the simulations with the pAGB-trajectory show a neutron density tail, which is sustained by neutron production via the $^{17}\mathrm{O}(\alpha, \mathrm{n})^{20}\mathrm{Ne}$ reaction after the ^{13}C source is exhausted. After a few times $10^4\,\mathrm{s}$ the majority of the abundant neutron poison ^{14}N is consumed and the neutron density even begins rising again. Due to the high temperature at the bottom of the convective zone this second phase of neutron production can reach i-process neutron densities again. For the simulations with $X_0(\mathrm{H}) = 10^{-3}$ and $X_0(\mathrm{H}) = 5 \times 10^{-3}$ this leads to a build up of neutron exposures up to $\tau = 1.8\,\mathrm{mbarn}^{-1}$ and $\tau = 2.2\,\mathrm{mbarn}^{-1}$, respectively, at i-process neutron densities of a few times $10^{12}\,\mathrm{cm}^{-3}$. In Figure 5.10 we also show two additional abundance patterns of the simulation with $X_0(\mathrm{H}) = 10^{-3}$ and $X_0(\mathrm{H}) = 5 \times 10^{-3}$, where the effect of this additional exposure at $n > 10^{12}\,\mathrm{cm}^{-3}$ is shown. The abundance patterns after the additional exposure show that the neutron-capture path has proceeded much further than at the time of the respective τ_i when the neutron density dropped below i-process levels for the first time. These more advanced patterns show that elements of the second peak as well as the Pb peak have been produced. However, the heavy-element nucleosynthesis has still not proceeded far enough into a regime where the enhancements of the second peak outweigh those of the first peak.

In Figure 5.11 we show the abundance pattern with the most advanced i-process heavy-element nucleosynthesis of the simulation using the pAGB-trajectory with $X_0(\mathrm{H}) = 5 \times 10^{-3}$ and $\tau = 2.2\,\mathrm{mbarn}^{-1}$ in comparison to the observations of Magellanic post-AGB star J004441. The observed abundances of J004441 show higher enhancements of the elements of the second peak compared to those of the first peak (e.g., [La/Y] > 0). None of our simulations reach conditions that allow the

neutron-capture path to advance enough to reach a production of [La/Y] > 0 at i-process neutron densities, even from a larger grid of simulations with additional values of ingested proton fractions spaced between the ones presented in Figure 5.9 and Table 5.2. When we consider further heavy-element production over longer time scales in the neutron-density tail with $n < 10^{12}\,\mathrm{cm}^{-3}$, we can find good fits to the observed abundances of J004441. We also show the two best fits amongst our simulations in Figure 5.11, which are produced by our modes with $X_0(\mathrm{H}) = 7.5 \times 10^{-3}$ and $X_0(\mathrm{H}) = 5 \times 10^{-3}$ at $\tau = 2.3\,\mathrm{mbarn}^{-1}$ and $\tau = 2.6\,\mathrm{mbarn}^{-1}$, respectively. Both of these fits show an almost identical abundance pattern, only with a small difference in the abundances of the elements around the first peak. These best-fitting abundance patterns both require additional heavy-element nucleosynthesis on the time scale of a few times 10^8 s at neutron densities below i-process level. Note that these further advanced simulations require higher dilution factors $d = 0.99$ (as defined in Hampel et al. (2019) in Equation 2.2) to fit the heavy-element enhancement levels observed in J004441 compared to the less advanced simulation using the pAGB-trajectory with $X_0(\mathrm{H}) = 5 \times 10^{-3}$ and $\tau = 2.2\,\mathrm{mbarn}^{-1}$, which shows a best fit at $d = 0.83$. The different dilution factors allow all three models shown in Figure 5.11 to reproduce the same abundance of, e.g., [Ba/Fe] despite the different heavy-element content produced in the simulations.

We show in Hampel et al. (2019) that models with constant neutron densities best reproduce the observed abundances of the Pb-poor Magellanic post-AGB stars at neutron densities of $n = 10^{11}\,\mathrm{cm}^{-3}$ and $n = 10^{12}\,\mathrm{cm}^{-3}$ with neutron exposures up to $\tau = 1.3\,\mathrm{mbarn}^{-1}$, which is significantly less than the neutron exposures of $\tau = 2.3\,\mathrm{mbarn}^{-1}$ and $\tau = 2.6\,\mathrm{mbarn}^{-1}$ required for the simulations with the pAGB-trajectory to match the abundances of J004441 shown in Figure 5.11. However, this is not surprising since the simulations with the pAGB-trajectory have much higher neutron densities and produce heavy elements along a different neutron-capture path further away from the valley of stability, compared to the simulations with constant neutron densities of $n = 10^{11}\,\mathrm{cm}^{-3}$ and $n = 10^{12}\,\mathrm{cm}^{-3}$. Figure 5.10 shows that the heavy-element production in the simulations with the pAGB-trajectory responsible for reproducing the observed abundance pattern of J004441 is largely built up after the initial high neutron burst at exposures of $\tau > \tau_\mathrm{i}$. A large fraction of the initial i-process neutron exposure up to τ_i builds up the enhanced abundance levels of elements with $Z \lesssim 50$, but it is the following neutron exposures at neutron densities of only a few times $10^{12}\,\mathrm{cm}^{-3}$ and below, which produce the enhancements of the elements around the second peak, the heavy rare-earth elements and eventually the non-pronounced Pb peak.

In summary, we have used the conditions from the model of a very late thermal pulse of a post-AGB star with initial mass of $1.3\,\mathrm{M}_\odot$ and [Fe/H] = −1.3 from Lugaro et al. (2015) to describe how the temperature and density increase in a proton-ingestion episode as a parcel of material travels from the top to the bottom of the convective region. This pAGB-trajectory has a significantly higher temperature at the bottom of the convective zone compared to the previously studied Monash- and Stars-trajectory and needs less time to reach the maximum conditions. Nucleosynthesis simulations of a proton ingestion episode following this pAGB-trajectory lead to a high-intensity burst of neutrons creating neutron densities of up to $10^{16}\,\mathrm{cm}^{-3}$. However, the neutron density drops rapidly and cannot build up high enough neutron exposures to drive significant heavy-element production. The majority of heavy-element production occurs only after the ^{13}C source responsible for the main neutron burst is exhausted. The responsible neutrons are produced via $^{17}\mathrm{O}(\alpha,\mathrm{n})^{20}\mathrm{Ne}$ from a reservoir of ^{17}O created by the previous neutron burst. Only these subsequent neutron

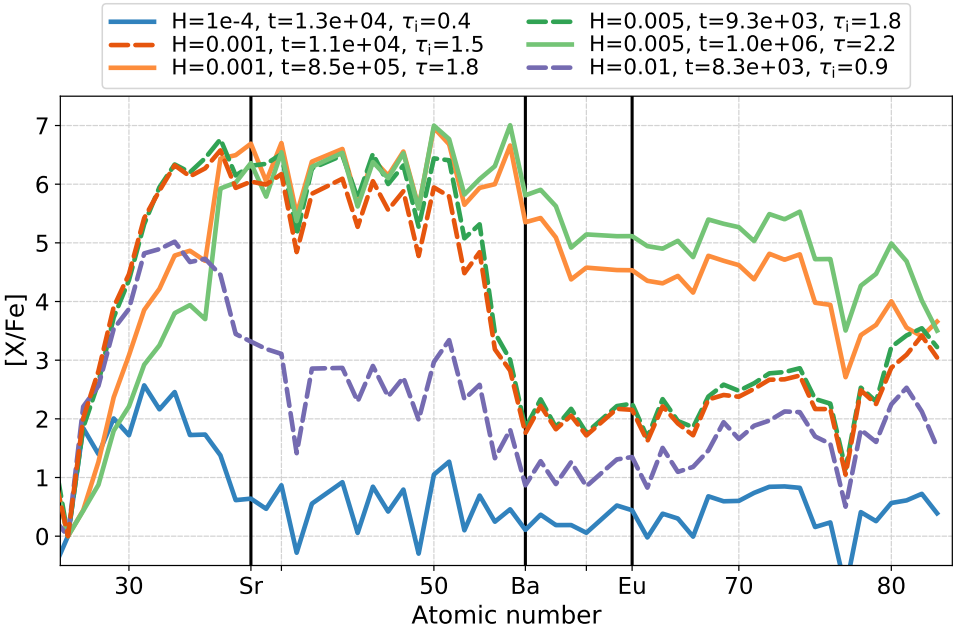

Figure 5.10: **Heavy-element abundances for the models with the pAGB-trajectory**. We show the abundance patterns for various ingested proton fractions at the time of τ_i. For $H = 0.001$ and $H = 0.005$ we also show an abundance pattern at a later time after additional neutron exposure. The time t of the model is given in the label in units of seconds and the neutron exposures τ and τ_i in mbarn^{-1}.

captures at densities around $10^{12}\,\mathrm{cm}^{-3}$ and below can reproduce the heavy-element abundance patterns observed in Pb-poor post-AGB stars.

In our simulations the quick drop of the peak neutron density as well as the rise to high levels afterwards may not be modelled accurately with the simplistic single-zone models and an instantaneous ingestion of protons at the start of the simulations, particularly for this trajectory, which reaches a very high temperature at the bottom of the convective zone very quickly. In this case it is likely a more extended region of the intershell, where the temperatures are high enough to activate the $^{13}\mathrm{C}(\alpha,\mathrm{n})^{16}\mathrm{O}$ reaction, instead of just a thin zone at the very bottom of the convective region. The quick rise of the temperature in the pAGB-trajectory does not leave sufficient time for a large fraction of ^{13}N to decay into ^{13}C before reaching the hottest temperatures. In combination with a prolonged proton-ingestion episode it is likely that the supply of ^{13}C in hot enough regions for neutron production is actually higher than estimated here. In turn, it is not certain whether the abundance of ^{17}O at the thin bottom layer of the convective region is as high as predicted here and leads to i-process conditions in the neutron-density tail.

With these caveats in mind, we can conclude that the observed abundance patterns of Pb-poor Magellanic post-AGB stars can be reproduced by heavy-element nucleosynthesis where at least the final few tenth of mbarn^{-1}of exposure occur at neutron densities of $10^{12}\,\mathrm{cm}^{-3}$ and below, which is not inconsistent with our findings in Hampel et al. (2019). However, the high temperatures at the bottom of the convective zone in this post-AGB star model may influence the neutron production significantly potentially leading to short intense neutron bursts instead, which by themselves cannot explain the observed abundance patterns.

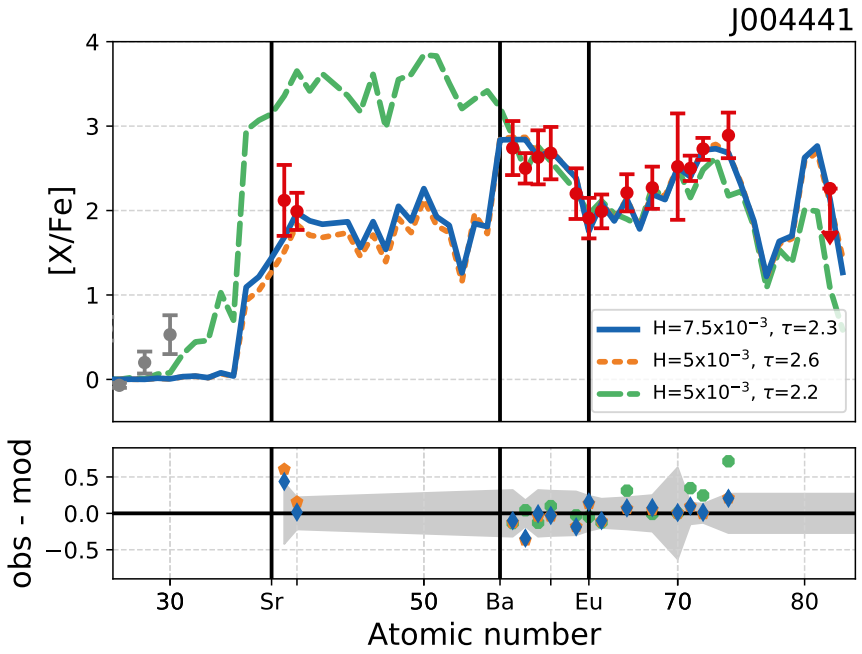

Figure 5.11: **Best fits of the heavy-element abundances of Magellanic post-AGB star J004441**. The blue and orange line show the best fitting models using the pAGB-trajectory with $X_0(\mathrm{H}) = 7.5{\times}10^{-3}$ and $X_0(\mathrm{H}) = 5{\times}10^{-3}$, respectively, after additional heavy-element nucleosynthesis below i-process neutron densities. For comparison we show the best fitting model with $X_0(\mathrm{H}) = 5 \times 10^{-3}$ at $\tau = 2.2\,\mathrm{mbarn}^{-1}$.

5.3 Core helium flash in an ultra metal-poor star

Low-mass stars that are extremely metal-poor (EMP, [Fe/H] < -3) or even metal-free can experience the ingestion of protons into a convective He-rich region during the core helium flash (CHeF) at the tip of the Red Giant Branch. Although the exact limits on stellar mass and metallicity for which a proton-ingestion episode during the CHeF occurs are model-dependent, the phenomenon itself is a robust prediction in one-dimensional stellar evolution codes (e.g., Fujimoto et al., 1990; Hollowell et al., 1990; Fujimoto et al., 2000; Schlattl et al., 2001; Weiss et al., 2004; Picardi et al., 2004; Campbell & Lattanzio, 2008; Campbell et al., 2010; Suda & Fujimoto, 2010; Cruz et al., 2013). Here we want to complement our parametric study of i-process nucleosynthesis with models that adopt the physical conditions of a proton-ingestion episode during the CHeF.

We use the model of a $0.8\,\mathrm{M}_\odot$ ultra metal-poor (UMP, $Z = 2 \times 10^{-6}$) star (Campbell, S. W. 2020, private communication) calculated with the Modules for Experiments in Stellar Astrophysics (MESA, Paxton et al., 2011, 2013, 2015, 2018, 2019). In Figure 5.12 we show the Hertzsprung-Russel diagram of our model's evolution until just after the CHeF at the tip of the red giant branch. Just after the off-center ignition of He during the flash, the star experiences a proton-ingestion episode. We extract the structure and composition during the proton-ingestion episode to construct a temperature-density trajectory with the respective initial composition for our i-process nucleosynthesis simulation.

In Figure 5.4 we show the temperature-density trajectory constructed from the CHeF-model, the CHeF-trajectory, alongside the previously discussed trajectories. Additionally, we list some

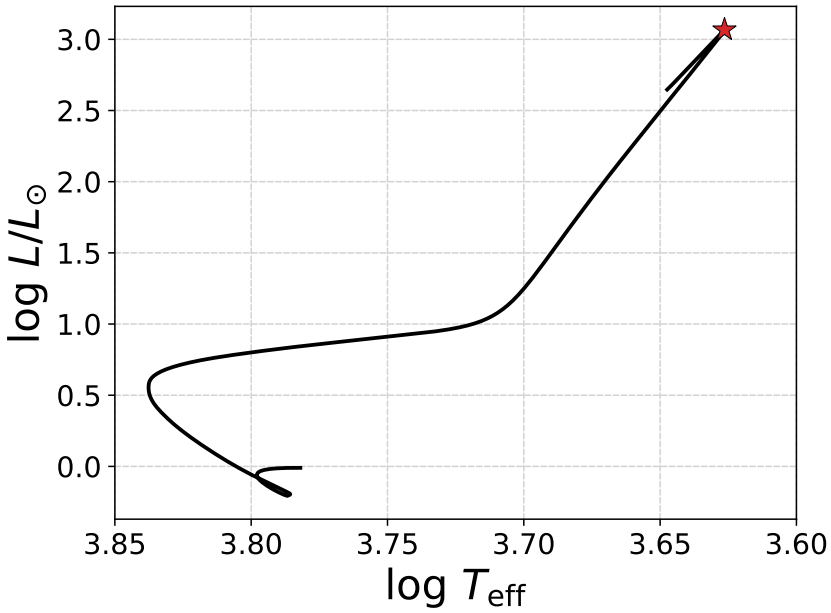

Figure 5.12: **Hertzsprung-Russel diagram** showing the evolution of our $0.8\,\mathrm{M}_\odot$ model with initial metallicity $Z = 2 \times 10^{-6}$. The red star highlights the chosen point in the evolution during the proton-ingestion episode following the CHeF at the tip of the red giant branch.

characteristics of the CHeF-trajectory and the respective chemical composition in Table 5.1. Compared to the other trajectories, the CHeF-trajectory provides the highest density environment at the bottom of the convective region, about two-times higher than the maximum density of the Stars-trajectory and the pAGB-trajectory and more than three-times higher compared to the Monash-trajectory. In contrast, the maximum temperature $T_{\rm max} = 2.1 \times 10^8\,\mathrm{K}$ at the bottom of the convective region in the CHeF-trajectory is the lowest amongst the trajectories. The temperature difference of $\Delta T_{\rm max} = 16\,\mathrm{MK}$ compared to the Stars-trajectory lowers the reaction rate of the neutron-producing $^{13}\mathrm{C}(\alpha,\mathrm{n})^{16}\mathrm{O}$ reaction by a factor of four at the bottom of the convective region. Compared to the other more evolved models, the early evolutionary stage of our CHeF-model has two more consequences for the initial conditions of our i-process nucleosynthesis models: (i) the convective region is more extended in mass and as a result it takes our trajectory more than three times longer to reach the maximum conditions at the bottom of the convective region, and (ii) the burning of He has just been ignited in the CHeF and there has not been much previous burning to produce $^{12}\mathrm{C}$. Therefore, the initial $^{12}\mathrm{C}$ abundance of $X_0(^{12}\mathrm{C}) = 0.05$ is the lowest amongst the considered scenarios.

In Figure 5.13 we show the neutron-density evolution for various ingested proton fractions using the CHeF-trajectory as well as the reference simulations with the Stars-trajectory for comparison. We also list the characteristic values for the maximum neutron density $n_{\rm max}$ and the final i-process exposure $\tau_{\rm i}$ in Table 5.2. Compared to the reference simulations with the Stars-trajectory the neutron densities in the simulations with the CHeF-trajectory start being produced at a later time due to the longer time needed to reach the maximum conditions at the base of the convective region. Among the simulations with the CHeF-trajectory the highest neutron densities of $n_{\rm max} = 7.4 \times 10^{14}\,\mathrm{cm}^{-3}$ and $n_{\rm max} = 6.8 \times 10^{14}\,\mathrm{cm}^{-3}$ are reached at ingested proton fractions of $X_0(\mathrm{H}) =$

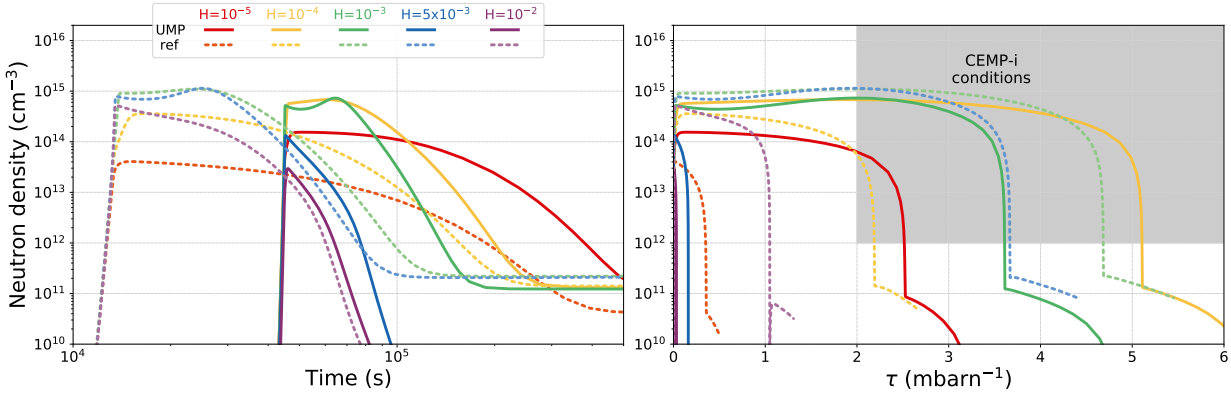

Figure 5.13: **Neutron-density evolution for the simulations using the CHeF-trajectory.** Same as Figure 5.9 but for the simulations with the CHeF-trajectory.

10^{-3} and $X_0(\mathrm{H}) = 10^{-4}$, respectively. These are also the simulations which yield the highest i-process neutron exposures of $\tau_\mathrm{i} = 3.6\,\mathrm{mbarn}^{-1}$ and $\tau_\mathrm{i} = 5.1\,\mathrm{mbarn}^{-1}$, respectively. In comparison to the simulations with the Stars-trajectory, these maximum n_max and τ_i are reached at lower $X_0(\mathrm{H})$ for the CHeF-trajectory. In fact, similar behaviours of the neutron-density evolution from a simulation with the Stars-trajectory can be found among the simulations with the CHeF-trajectory with a respectively lower $X_0(\mathrm{H})$, which includes similar n_max, similar τ_i, and even a similar shape of the neutron density evolution over time. E.g., the simulation with $X_0(\mathrm{H}) = 5 \times 10^{-3}$ using the Stars-trajectory shows almost the same behaviour as the simulation with $X_0(\mathrm{H}) = 10^{-3}$ using the CHeF-trajectory: after reaching the maximum temperature and density both simulations show a plateau-like phase with a slight decline in neutron density caused by additional ^{14}N production through neutron-recycling reactions, followed by a "bump" in the neutron density when the ^{14}N is depleted at a higher rate than the ^{13}C neutron source (see previous discussions in Chapter §3 and §4). This neutron-density bump is responsible for yielding the highest n_max amongst the other simulations with the same trajectory, although it is followed by a relatively fast decline of the neutron density such that the τ_i remain lower than in simulations with a higher $X_0(\mathrm{H})$ for the same trajectory. Even the n_max and τ_i of these two simulations show very similar results with just a few percent deviation between the simulation with $X_0(\mathrm{H}) = 5 \times 10^{-3}$ using the Stars-trajectory and $X_0(\mathrm{H}) = 10^{-3}$ using the CHeF-trajectory.

The way in which pairs of simulations with the Stars-trajectory and the CHeF-trajectory can be associated with one-another (and where the $X_0(\mathrm{H})$ of the simulation with the Stars-trajectory is higher than the one of the associated CHeF-trajectory simulation) is not coincidental. In fact, this similar behaviour is driven by the proton-to-carbon fraction $Y_\mathrm{p}/Y(^{12}\mathrm{C})$ of each simulation (see Section §4.2.2 for a discussion of the importance of the $Y_\mathrm{p}/Y(^{12}\mathrm{C})$ ratio). The proton-ingestion episode triggered by the CHeF happens in an environment where even less ^{12}C has been produced than can be found in the intershell of a low-metallicity AGB star in its first few thermal pulses. In our case here, the $X_0(^{12}\mathrm{C})$ for the CHeF-trajectory is ca. four-times lower than the standard composition used in the reference simulations. Therefore, the same $Y_\mathrm{p}/Y(^{12}\mathrm{C})$ occurs for ingested proton fractions which are also four-times lower for the CHeF-trajectory compared to the Stars-trajectory. As a consequence the CHeF-trajectory is also the only of the considered trajectories

where large enough i-process neutron exposures and significant heavy-element nucleosynthesis occur at ingested proton fractions as low as $X_0(\mathrm{H}) = 10^{-5}$.

There are still differences in the neutron-density evolution between the CHeF- and the Stars-trajectory, even for a pair of simulations with a similar $Y_\mathrm{p}/Y(^{12}\mathrm{C})$ ratio. Altogether, the maximum neutron densities reached by the simulations with the CHeF-trajectory are lower than those of the Stars-trajectory. Even though very similar conditions in terms of composition can be found in the pairs of simulations using the CHeF- and the Stars-trajectory with the same $Y_\mathrm{p}/Y(^{12}\mathrm{C})$, e.g. almost the same $^{13}\mathrm{C}/^{14}\mathrm{N}$ ratios, the different temperatures and densities at the bottom of the convective region still result in different neutron densities. For the resulting heavy-element abundance patterns in the simulations with the UMP initial conditions this small difference is negligible, as the effects of the higher densities and lower temperatures at the bottom of the convective region in the CHeF- compared to the Stars-trajectory almost even out each other.

Figure 5.14 shows the heavy-element abundances produced in the simulations with the CHeF-trajectory and UMP initial abundances at the respective final τ_i. For comparison we also show the heavy elements produced in the simulation with $X_0(\mathrm{H}) = 5 \times 10^{-3}$ using the Stars-trajectory, which is the model most similar to the CHeF-simulation with $X_0(\mathrm{H}) = 10^{-3}$ in terms of their $Y_\mathrm{p}/Y(^{12}\mathrm{C})$ ratios and neutron density evolution. The CHeF-simulations with low ingested proton fractions of $X_0(\mathrm{H}) \leq 10^{-3}$ have low proton-to-carbon ratios of $Y_\mathrm{p}/Y(^{12}\mathrm{C}) \leq 0.24$ which yields the highest τ_i and the most evolved i-proton heavy-element abundance patterns. These simulations with low $Y_\mathrm{p}/Y(^{12}\mathrm{C})$ all show very comparable heavy-element production, in contrast to the other two CHeF-simulations with high ingested proton fractions of $X_0(\mathrm{H}) = 5 \times 10^{-3}$ and $X_0(\mathrm{H}) = 10^{-2}$ (i.e., $Y_\mathrm{p}/Y(^{12}\mathrm{C}) = 1.2$ and $Y_\mathrm{p}/Y(^{12}\mathrm{C}) = 2.4$, respectively) which show no significant enhancements of heavy-element abundances. We have already seen in Chapter §3 that the regime of low $Y_\mathrm{p}/Y(^{12}\mathrm{C}) \lesssim 0.2$ can produce comparable heavy-element abundances from a range of neutron exposures due to the different neutron densities at which the i-process neutron exposure builds up. In the case of the CHeF-simulations there is a large i-process exposure difference of $\Delta\tau_\mathrm{i} = 2.6\,\mathrm{mbarn}^{-1}$ between the simulation with $X_0(\mathrm{H}) = 10^{-5}$ and $X_0(\mathrm{H}) = 10^{-4}$ but the abundance enhancements for the majority of the elements between the second s-process peak and the Pb-peak are almost identical.

Nevertheless, the differences in neutron-densities and exposures between the simulations leave imprints on the abundance patterns, which still become evident from a closer look at the heavy-element enhancements: the simulation with $X_0(\mathrm{H}) = 10^{-5}$ experiences only half of the i-process exposure of the simulation with $X_0(\mathrm{H}) = 10^{-4}$ and as a consequence the Pb-peak in this simulation is less enhanced causing an abundance difference of ca. 1 dex between the two simulations. A further difference between the two simulations is the actual neutron density at which the majority of the exposure builds up and develops the abundance pattern: the simulation with $X_0(\mathrm{H}) = 10^{-4}$ reaches neutron densities which are about five-times higher than the neutron densities in the simulation with $X_0(\mathrm{H}) = 10^{-5}$, which is, e.g., reflected in their $n_\mathrm{max} = 6.8 \times 10^{14}\,\mathrm{cm}^{-3}$ and $n_\mathrm{max} = 1.5 \times 10^{14}\,\mathrm{cm}^{-3}$, respectively. At the lower neutron density, the abundance pattern produced by the simulation with $X_0(\mathrm{H}) = 10^{-5}$ shows higher abundances of elements around the first peak and leading up to the second peak, where abundance differences of ca. 1dex occur for Sn, Sb, and Te (with atomic numbers $Z = 50$, 51, and 52). Combining both of these effects that the different neutron-density histories have on the abundance patterns for the simulations with $X_0(\mathrm{H}) = 10^{-5}$ and $X_0(\mathrm{H}) = 10^{-4}$, one can find deviations of the relative peak heights of the Pb- to the first s-process-peak that show

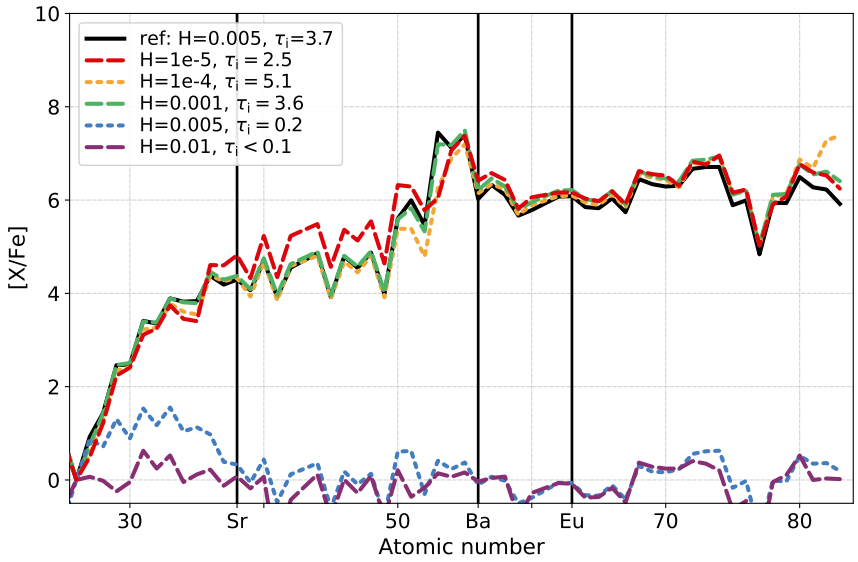

Figure 5.14: **Heavy-element abundances for the models with the CHeF-trajectory**. We show the abundance patterns for various ingested proton fractions at the time of $\tau_{\rm i}$. For comparison we also show the abundances produced by the reference simulation with the Stars-trajectory and $X_0({\rm H}) = 5 \times 10^{-3}$. The $\tau_{\rm i}$ of each model is given in the label in units of mbarn^{-1}.

abundance differences exceeding 1 dex, e.g., [Pb/Sr] ≈ 1.3 dex, while the abundances of elements of the second-peak and leading up to the Pb-peak only show abundance variations of ca. 0.1 dex.

In summary, in this section we present a third stellar-evolution scenario that hosts proton-ingestion episodes and i-process nucleosynthesis: the core helium flash in a low-mass, ultra metal-poor star. We use the stellar evolution model of a $0.8\,{\rm M}_\odot$ star with metallicity of $Z = 2 \times 10^{-6}$ to extract the temperature-density trajectory and abundance information at the time of the proton-ingestion episode for our i-process simulations. The CHeF provides a denser environment than found in the previously considered trajectories with slightly lower temperatures at the bottom of the convective region. More importantly, the abundances of ^{12}C are lower in this CHeF scenario compared to the proton-ingestion episodes in later evolutionary stages during the AGB or post-AGB phase of a star's life. As a consequence, lower ingested proton fractions compared to the previous reference simulations lead to similar proton-to-carbon ratios $Y_{\rm p}/Y(^{12}{\rm C})$, which then causes similar nucleosynthesis behaviour. Already at $X_0({\rm H}) = 10^{-5}$ significant neutron production and i-process nucleosynthesis occurs with an i-process neutron exposure of $\tau_{\rm i}$ =2.5 mbarn^{-1}. Sufficient i-process neutron exposures for heavy-element nucleosynthesis are achieved at low enough $Y_{\rm p}/Y(^{12}{\rm C}) \lesssim 0.2$ provided by the simulations with ingested proton fractions up to $X_0({\rm H}) = 10^{-3}$, and the maximum i-process neutron exposure of $\tau_{\rm i} = 5.1\,{\rm mbarn}^{-1}$ is reached at $X_0({\rm H}) = 10^{-4}$. At the respective $\tau_{\rm i}$ of each simulation, the produced abundance enhancements of the elements around the second peak and up to the Pb-peak show very little variation among the simulations with different ingested proton fractions (or even compared to a reference simulation with the Stars-trajectory and a similar $Y_{\rm p}/Y(^{12}{\rm C})$) despite significant differences in $\tau_{\rm i}$. In contrast, we find more traces of the individual neutron-density histories and i-process neutron exposures of each simulation in the abundances of the elements located around first peak and particularly between the first and second peak, as well as the Pb-peak elements.

5.4 Summary

In this chapter we compared the conditions of three different i-process host sites and how they influence the i-process neutron production and heavy-element nucleosynthesis: (*i*) the early thermal pulse of a low-mass, low-metallicity AGB, which we tested with two different temperature density trajectories from two stellar models of a $1\,M_\odot$ and a $1.3\,M_\odot$ star both with a metallicity of $Z = 10^{-4}$ computed with independent stellar evolution codes, (*ii*) a model of a very late thermal pulse in a post-AGB star at higher metallicity ([Fe/H] $= -1.3$) representative of the progenitors of the Pb-poor Magellanic post-AGB stars (Lugaro et al., 2015), and (*iii*) a model of a core helium flash in a $0.8\,M_\odot$ ultra metal-poor ($Z = 2 \times 10^{-6}$) star (Campbell, S. W. 2020, private communication).

The temperature-density trajectory for the post-AGB star model has the highest maximum temperature at the bottom of the convective region and reaches these conditions in the shortest time. As a consequence, only short but intense neutron bursts with neutron densities as high as $10^{16}\,\mathrm{cm}^{-3}$ are produced in the instantaneous proton ingestion modelled in our simulations. These short intense bursts alone appear not sufficient to produce abundance patterns as observed in the Pb-poor Magellanic post-AGB stars. However, the abundances can be reproduced when considering further extended neutron exposure in the neutron-density tail after the ^{13}C source is depleted. We expect these simulations with the post-AGB-star trajectory to be the most affected by the limitations of our models, particularly by not including the effects of mixing and only considering an instantaneous instead of a prolonged proton-ingestion episode.

The temperature-density trajectories for the second model of the AGB thermal pulse and the core helium flash model both reach their maximum conditions slower than the reference simulations. Differences in the physical conditions can cause variations of $n_{\max}$ and τ_{i}, but for low proton-to-carbon ratios of $Y_{\mathrm{p}}/Y(^{12}\mathrm{C}) \lesssim 0.2$ the achieved i-process neutron exposures produce significant heavy-element nucleosynthesis with robust abundance enhancements for the elements between the second s-process peak and the Pb-peak. Depending on the actual neutron-density history, a combination of the i-process neutron exposure and the neutron-density at which this exposure has built up, we find abundance variations of the Pb-peak elements, the first s-process peak elements, and particularly of the elements between the first and second s-process peak (i.e., elements between Zr and Ba).

When comparing the abundances from our simulations to those of CEMP-i stars, only few abundance measurements for elements between Zr and Ba exist to constrain i-process model predictions. We find different models which predict nearly identical abundance patterns for the other heavy-elements but deviate in their predictions for the abundance enhancements of these elements between the first and second s-process peak. We even find the possibility of reproducing observed CEMP-i abundance patterns with some models where further heavy-element nucleosynthesis occurs after the main i-process event at lower neutron densities and on longer time scales in the neutron-density tail. Altogether, more complete heavy-element abundance patterns, including observational constraints on the enhancements of elements between the s-process peaks, may be able to help distinguish between different i-process histories.

> *Science progresses best when observations force us to alter our preconceptions.*
>
> — Vera Rubin

Chapter 6

Abundance signatures of the i process

In this section we are going to summarise a few selected signatures of i-process nucleosynthesis to identify what sets the abundance patterns from the i process apart from other nucleosynthetic pathways. Of particular interest are abundance ratios of elements and isotopes that can distinguish "typical s-process signatures" from "typical i-process signatures".

The first task on this endeavour is to define what "typical" s- and i-process abundance patterns look like, which already brings the first difficulties with it: what are the best definitions for *s process* and *i process* in the first place? When does a neutron-capture process stop being *slow* and starts being *intermediate*? Is there even a clear diving line between these two processes? Or is the transition between the s and i process a continuum?

From a theoretical point of view, the neutron number density is typically used as the quantity to distinguish between the different regimes of neutron-capture nucleosynthesis. It also is the neutron number density that lead Cowan & Rose (1977) to identify the nucleosynthesis process in their models as i process in the first place, since the neutron densities of $n \approx 10^{15}$ cm^{-3} in their calculations of proton-ingestion episodes fell *intermediate* to the classical s- and r-process regimes with $n \approx 10^{7}$ cm^{-3} and $n \approx 10^{23}$ cm^{-3}.

However, there are s-process models that can reach high peak neutron densities. For example, Fishlock et al. (2014) present a $5\,M_\odot$ AGB model with [Fe/H] $= -1.2$ which reaches peak neutron densities of $n \approx 10^{13}\,\mathrm{cm}^{-3}$ and maintains $n > 10^{12}\,\mathrm{cm}^{-3}$ for approximately 30 days in each thermal pulse. Is this an s- or i-process model? The neutron density is in the regime of what we consider as i-process models throughout this thesis. Yet, we would argue here that it is not the neutron density alone that determines the heavy-element production. Reaching a high peak neutron density for a short amount of time does not influence the final heavy-element abundance pattern in the same way as an extended neutron exposure at that high neutron density does. Arguably, trying to define an objective measure for how long at what neutron density which fraction of exposure needs to be built up to then name the process slow or intermediate may not be the best way to think about the s- versus i-process distinction.

From an observational point of view, the i process is of interest as a nucleosynthetic process that can produce observed abundance patterns, which cannot be explained as originating from the s process, the r process, or a combination of both. Such observations motivating and constraining the work in this thesis are the abundance patterns of CEMP stars, with overabundances of Ba and Eu. The abundance patterns of this subclass of CEMP stars were not previously reproducable with s-process models or a combination of s- and r-process models (e.g., Jonsell et al., 2006; Bisterzo et al., 2012; Lugaro et al., 2012; Abate et al., 2015b, 2016; Cristallo et al., 2016). So the better, or at least an alternative, starting point to approach the question of what a "typical i-process" abundance pattern looks like may be to focus on the common features of the CEMP-i stars as a group. We will use these observations here as the basis to reiterate the characteristics incompatible with s-process nucleosynthesis and to emphasize the features that i-process nucleosynthesis predicts.

6.1 The sample and subclasses of CEMP stars

For CEMP stars there is a variety of different definitions of subclasses available in the literature, based on the presence or absence of elemental overabundances. Typically, an observed overabundance of Ba is used as indicator of s-process nucleosynthesis, whereas Eu is used as tracer of

r-process nucleosynthesis. Additionally, we now consider the overabundance of both Ba and Eu as indicator of i-process nucleosynthesis. However, the exact definitions vary amongst authors and even additional abundances are considered in the literature to group CEMP stars according to their formation history. Already the variety of definitions as well as the evolution of the nomenclature indicates that there is no single absolute definition of what counts as s-, i-, and r-process signature.

To avoid confusion as best as possible, we want to briefly review a few common classification schemes used in the litereature. The early classifications for CEMP stars that have influenced the nomenclature used in the community are defined in the review of Beers & Christlieb (2005). Here the definitions of *metal-poor* and *carbon-enhanced* have an upper threshold of $[\mathrm{Fe/H}] = -1$ and a lower threshold of $[\mathrm{C/Fe}] = 1$ and stars exceeding those limits (i.e., a lower Fe content but a higher C enhancement relative to that Fe content) are classified as CEMP stars. Amongst those CEMP stars, a Eu enhancement of $[\mathrm{Eu/Fe}] > 1$ defines a star as r-process rich (CEMP-r). In contrast, if a star shows a strong Ba enhancement of $[\mathrm{Ba/Fe}] > 1$ and a strong enough overabundance of Ba relative to Eu of $[\mathrm{Ba/Eu}] > 0.5$ it is identified as CEMP-s stars. Stars which are enhanced in Ba and Eu but do not show a strong dominating Ba signature to indicate a pure s-process origin (i.e., their relative Ba to Eu ratio is $[\mathrm{Ba/Eu}] < 0.5$) are called CEMP-r/s. Stars without notable Ba enhancements (defined as $[\mathrm{Ba/Fe}] < 0$) are categorised as CEMP-no stars.

Multiple modifications to these definitions have emerged, motivated by different stellar evolution and nucleosynthesis considerations. E.g., mixing of processed material from the interior of the star to its surface, affects the carbon composition of the star: the CNO-cycle reactions in the star's interior reduce the C abundance. As a consequence of mixing this processed material to the surface evolved giant stars show lower C abundances than in earlier stages of their life. To take this evolutionary affect into account Aoki et al. (2007) propose a revised criterion for CEMP stars based on their luminosity: less evolved stars with $\log(L/\mathrm{L}_\odot) \leq 2.3$ need to have $[\mathrm{C/Fe}] \geq 0.7$ to classify as CEMP star, whereas giant stars with $\log(L/\mathrm{L}_\odot) > 2.3$ only need to meet a reduced threshold the more luminous they are, which is defined by $[\mathrm{C/Fe}] \geq 3 - \log(L/\mathrm{L}_\odot)$. A slightly different modification to the stricter $[\mathrm{C/Fe}] > 1$ definition was adopted by Masseron et al. (2010). Here the idea behind revising the threshold value of $[\mathrm{C/Fe}]$ stems from the community's shift to adopting new reference values of the solar composition by Asplund et al. (2009). To keep the sample consistent with previously classified CEMP stars a threshold of $[\mathrm{C/Fe}] > 0.9$ is used.

Particularly the definitions of the heavy-element signatures have undergone modifications as well. While a negative $[\mathrm{Ba/Eu}]$ abundance ratio does point to an r-process origin, some s-process models predict less dominant Ba signatures than the originally required $[\mathrm{Ba/Eu}] > 0.5$ (see, e.g., models from Lugaro et al., 2012; Abate et al., 2015b). A commonly adopted classification scheme to identify s-process enhancement is therefore $[\mathrm{Ba/Eu}] > 0$ (e.g., Jonsell et al., 2006; Lugaro et al., 2009; Masseron et al., 2010; Abate et al., 2015b, 2016). While Ba and Eu are most commonly used to categorise CEMP stars, some authors adopt enhancements of La as indicator for s-process nucleosynthesis (e.g., Bisterzo et al., 2011, 2012; Frebel, 2018; Karinkuzhi et al., 2021).

The CEMP subclass which may have undergone the most evolution is the one classically referred to as CEMP-rs, CEMP-sr, CEMP-s/r, CEMPs+r, or some similar name that involves the letters s and r. In this case the evolution does not just concern the definition of abundance thresholds but the interpretation of the abundance pattern: instead of an abundance pattern that originates from a combination of separate s- and r-process events the heavy element signatures can be better

explained with an i-process origin. The quest for the origin of the CEMP-i stars has seen some new re-classification schemes, which propose to move away from the current standard of comparing the s- and r-process contributions by focussing on the relative abundances of the s-process elements Ba or La compared to the representative r-process element Eu. Instead, other abundance signatures have been focused on, which identify CEMP-i stars exactly as not being the mixture of s- and r-processed material. For example, CEMP-i stars show high abundance ratios between elements of the heavy s-process peak (hs) to those of the light s-process peak (ls), which are incompatible with an s-process origin. We will focus on this abundance signature in the next section, but want to already mention here for completeness that new classification schemes based on relative ratios between typical s-process elements Ba and Y (Hollek et al., 2015) or Ba and Sr (Hansen et al., 2019) have been propsed. Additionally, Frebel (2018) suggest to use relative ratios of Hf to Ir for the definition of CEMP-i stars, although these abundances have not been measured in many CEMP stars yet.

For the remainder of this chapter we use the following criteria to select and classify a sample of CEMP stars from the SAGA database[1] (Suda et al., 2008, 2017):

- **Carbon enhancement:** [C/Fe] > 0.9
- **CEMP-no:** [Ba/Fe] ≤ 0.5
- **CEMP-s:** [Ba/Fe] > 0.5, [Ba/Eu] ≥ 0, and [Eu/Fe] ≤ 1
- **CEMP-i:** [Ba/Fe] > 0.5, [Ba/Eu] ≥ 0, and [Eu/Fe] > 1
- **CEMP-r:** [Ba/Fe] > 0.5, [Ba/Eu] < 0, and [Eu/Fe] > 1

In Figure 6.1 we show the Ba and Eu abundances of our compiled sample of CEMP stars. Stars with available Ba and Eu measurements are classified based on the described classification scheme. Where only a Ba abundance measurement is available and an upper limit exists for the Eu abundance, we include the star in Figure 6.1. However, since a subclassification is not really possible without a measured Eu abundance we exclude these stars from our sample for further discussions.

6.2 [hs/ls] ratios

By definition the higher abundance of Eu sets CEMP-i stars apart from CEMP-s stars. But this is not the only distinctive abundance feature between these two CEMP subclasses. Also the enhancements of the light and heavy s-process peak (ls and hs, respectively) elements show different signatures between CEMP-s and CEMP-i stars. Typical s-process models, even with enhanced Eu abundances from r-process pre-enhancement, have difficulties to reproduce the high [hs/ls] ratios

[1] We use the recommended abundances from the SAGA database version updated on April 7, 2021. For consistency with the compilations used in Abate et al. (2015b) we adopt the same determination of abundances and uncertainties: where multiple abundance measurements of one element are given for one object we use the average abundance and the larger uncertainty if all measurements agree with the average abundance within this uncertainty. Otherwise we adopt a larger uncertainty given by the discrepancy between the measurements and the average abundance. We adopt a minimum uncertainty of 0.1 dex.

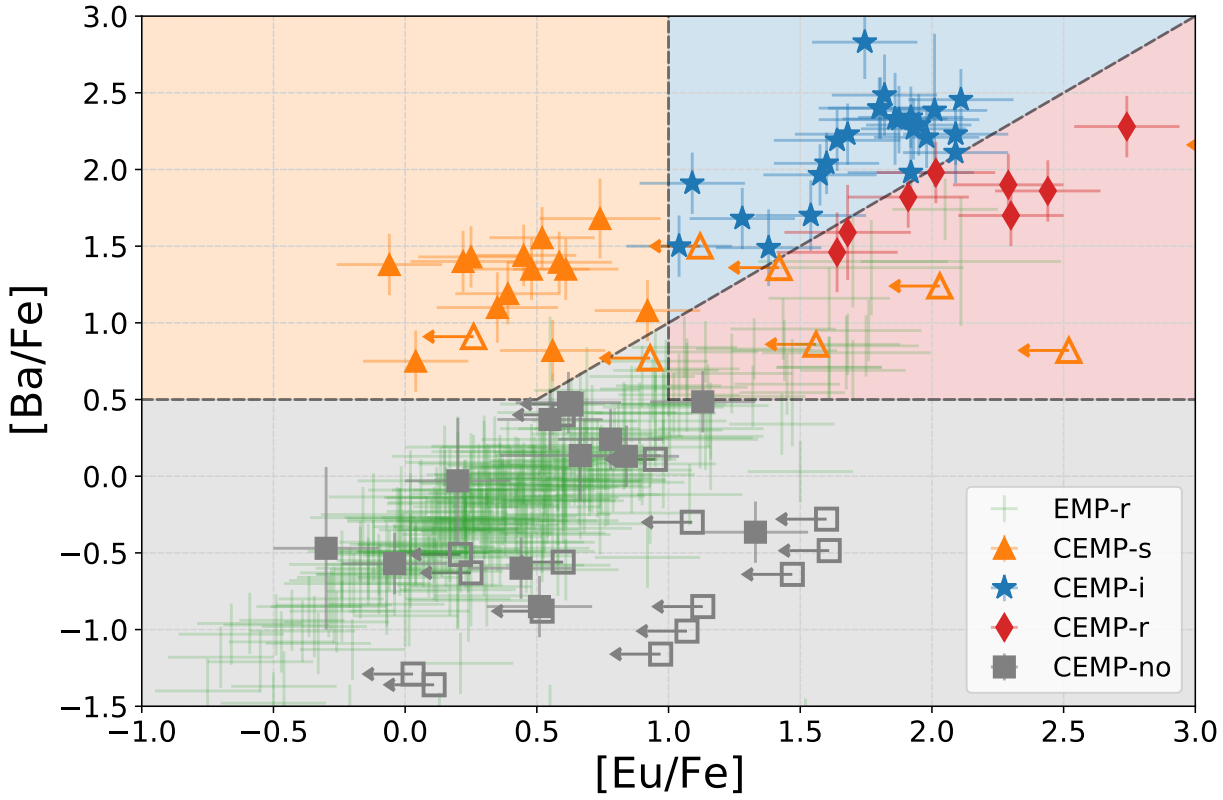

Figure 6.1: **Subclassification of CEMP stars based on their Ba and Eu abundances.** Additionally, the Ba and Eu abundances of (carbon-normal) rI and rII stars are shown. The lines and shaded regions indicate the different CEMP subclasses and their divides at [Ba/Fe] = 0.5, [Eu/Fe] = 1, and [Ba/Eu] = 1. Where available CEMP-s and CEMP-no stars with upper limits on [Eu/Fe] are shown as open symbols, whereas stars without Eu and Ba measurements are not considered in the sample.

observed in CEMP-i stars (e.g., Jonsell et al., 2006; Lugaro et al., 2012; Bisterzo et al., 2012; Abate et al., 2015b; Cristallo et al., 2016). The distinctly high [hs/ls] ratios of CEMP-i stars have also been considered as observables for a new CEMP classification scheme (Hollek et al., 2015; Hansen et al., 2019; Goswami et al., 2021).

Representative elements of the ls peaks which are often measurable in stellar spectra are Sr, Y, and Zr. In our sample 24 CEMP-i and 14 CEMP-s stars have reported measurements of Sr abundances, which are more stars than those with Y and Zr measurements. Therefore we focus on Sr as representative of the ls elements in this section. Since Ba is the element whose abundance measurement we require for a CEMP classification in the first place, all stars in our sample have a reported Ba measurement which we will use as representative hs element.

In Figure 6.2 we show the [Ba/Sr] abundance ratios of the CEMP stars from our sample as a function of their [Eu/Ba] abundance ratios. In general, CEMP-i stars have higher [Ba/Sr] ratios than CEMP-s stars with average values of $[\mathrm{Ba/Sr}]_{\mathrm{CEMP-i}} = 1.3$ and $[\mathrm{Ba/Sr}]_{\mathrm{CEMP-s}} = 0.7$, respectively. The [Eu/Ba] ratio separates the CEMP-r stars from the CEMP-s and -i stars, where CEMP-r stars by definition have a positive [Eu/Ba] ratio, whereas CEMP-s and -i stars have negative [Eu/Ba] ratios. Among the CEMP-s and -i stars, CEMP-i stars tend to have higher [Eu/Ba] ratios than CEMP-s stars with average values of $[\mathrm{Eu/Ba}]_{\mathrm{CEMP-i}} = -0.4$ and $[\mathrm{Eu/Ba}]_{\mathrm{CEMP-s}} = -0.8$, respectively, although both groups show a large spread with individual outliers as far away as $\Delta\,[\mathrm{Eu/Ba}] = 0.6$.

For comparison with the abundances in CEMP stars, in Figure 6.2 we also show the results from simulations of stellar evolution models with various initial masses between $0.9\,\mathrm{M}_\odot$ and $6\,\mathrm{M}_\odot$ at a metallicity of $Z = 10^{-4}$ (Lugaro et al., 2012). These model predictions of s-process nucleosynthesis fall into the abundance range around $[\mathrm{Eu/Ba}]_{\mathrm{AGB}} \approx -1$ and $[\mathrm{Ba/Sr}]_{\mathrm{AGB}} \approx 0.7$ in general agreement with the abundances observed in CEMP-s stars. However, all of the models presented by Lugaro et al. (2012) predict $[\mathrm{Ba/Sr}]_{\mathrm{AGB}} < 1$ and cannot produce high enough abundance ratios to explain the [Ba/Sr] ratios in CEMP-i stars.

As Lugaro et al. (2012) discuss in their study, a limit to the maximum [Ba/Sr] abundance ratio is given by the nuclear physics properties of the isotopes along the neutron-capture path of the process producing the heavy elements. In particular, the neutron-capture cross sections of the involved species determine a maximum [Ba/Sr] equilibrium abundance ratio. In Figure 6.2 we also show the equilibrium abundances of our single-zone nuclear-network simulations with constant neutron densities. At constant neutron densities of $n = 10^7\,\mathrm{cm}^{-3}$ to $10^9\,\mathrm{cm}^{-3}$ (typical s-process neutron densities) the equilibrium abundance ratio remains below $[\mathrm{Ba/Sr}] < 1$ in good agreement with the maximum abundance ratios from the models presented by Lugaro et al. (2012). However, as the neutron density increases the equilibrium abundance ratios of both [Ba/Sr] and [Eu/Ba] increase as well.

While the [Ba/Sr] ratio keeps increasing with neutron density, the [Eu/Ba] ratio reaches a maximum of $[\mathrm{Eu/Ba}] = -0.3$ at $n = 2 \times 10^{13}\,\mathrm{cm}^{-3}$. This interesting effect is a consquence of increased Ba production through decays of ^{135}I, which becomes the dominantly produced isotope with magic neutron number $N = 82$ at neutron densities between approximately $10^{13}\,\mathrm{cm}^{-3} \lesssim n \lesssim 10^{15}\,\mathrm{cm}^{-3}$. Since ^{135}I is unstable it decays into ^{135}Ba after the neutron source ceases and is also responsible for other unique features of i-process abundance patters, which we will discuss in the next sections.

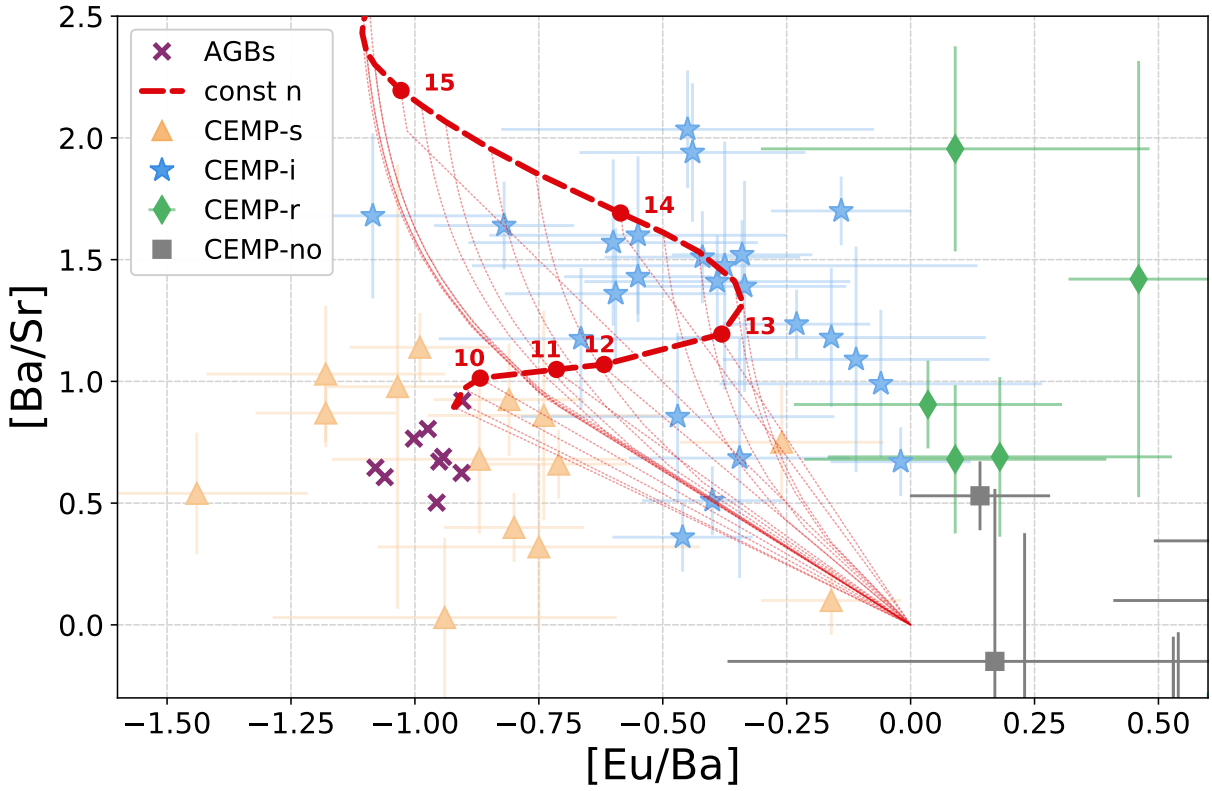

Figure 6.2: **Observed [Ba/Sr] ratios of CEMP stars as function of their [Ba/Eu] ratios.** Additionally, we indicate the abundance ratios predicted by the s process in metal-poor AGB stars (Lugaro et al., 2012). Equilibrium abundances of i-process calculations at constant neutron densities are shown along with their dilution lines. Discrete magnitudes of neutron densities are highlighted by red points and labelled with the respective $\log(n)$ value of the calculation.

As Figure 6.2 shows, the i-process equilibrium abundance ratios extend into the regime in the [Ba/Sr]-[Eu/Ba] abundance plane where the CEMP-i observations are located, particularly for constant neutron densities in the range of approximately $10^{12}\,\mathrm{cm}^{-3} \lesssim n \lesssim 5 \times 10^{14}\,\mathrm{cm}^{-3}$. In Figure 2.1 (Hampel et al., 2019) we show that these [Ba/Sr] ratios are already reached after an exposure of $\tau = 2\,\mathrm{mbarn}^{-1}$ to $3\,\mathrm{mbarn}^{-1}$. Therefore it is not surprising that the constant neutron densities of $n = 10^{13}\,\mathrm{cm}^{-3}$ and $10^{14}\,\mathrm{cm}^{-3}$ in Chapter §2 (Hampel et al., 2019) provide the majority of best fits to the abundance patterns of individual CEMP-i stars.

6.3 The hs peak abundances

Ultimately, the differences in heavy-element abundance patterns from neutron-capture processes at different neutron densities arise from the fact that isotopes are produced along different neutron-capture paths. Each neutron-capture path is determined by the balance of the reaction time scales and rates between neutron-capture reactions and β-decays. As the neutron density increases the i process can create more neutron-rich isotopes further away from the valley of stability than the s process can and the i-process neutron-capture path reaches species with magic neutron numbers at lower atomic numbers. This causes a shift of the positions of typical abundance peaks associated with the enhanced production of these magic species, which act like bottlenecks along the neutron-capture path. As a result the abundance ratios of typical s-process elements within the ls and hs peak get significantly altered by i-process nucleosynthesis in comparison to s-process nucleosynthesis.

In Figure 6.3 we show the abundance ratios of Ba to La and of La to Eu observed in CEMP stars. We also show the predicted s-process abundance ratios from the AGB models from Lugaro et al. (2012), as well as the equilibrium abundance ratios from i-process models at various constant neutron densities. In general, the CEMP-r and CEMP-no stars have lower [Ba/La] and [La/Eu] ratios than the CEMP-i and CEMP-s stars.

Our sample of CEMP-i and CEMP-s stars has average abundance ratios of $[\mathrm{Ba/La}]_{\mathrm{CEMP-i}} = 0.06$ and $[\mathrm{Ba/La}]_{\mathrm{CEMP-s}} = 0.21$, respectively, with a relatively large spread of $\sigma \sim 0.2$ dex for both CEMP classes. The CEMP-i and CEMP-s stars separate more clearly in the abundance space of the [La/Eu] ratio. Here the CEMP-i stars show lower average abundances of $[\mathrm{La/Eu}]_{\mathrm{CEMP-i}} = 0.37$ than the CEMP-s stars with $[\mathrm{La/Eu}]_{\mathrm{CEMP-s}} = 0.69$, although the spread of abundance ratios among the stars of each class is similarly high as for the [Ba/La] ratios.

Typical s-process models predict approximately equal Ba and La enhancements (i.e. $[\mathrm{Ba/La}] \approx 0$) and high relative La to Eu ratios of $[\mathrm{La/Eu}] \approx 1$, as shown in Figure 6.3 by both the AGB models from Lugaro et al. (2012) and the equilibrium abundance ratios from our models at constant neutron densities of $n \leq 10^{10}\,\mathrm{cm}^{-3}$. Although the average abundance ratio between La and Eu of CEMP-s stars is [La/Eu] = 0.7 some s-process models struggle to reproduce this abundance ratio, let alone abundance ratios of [La/Eu] < 0.7 as observed in many CEMP-s stars and almost all CEMP-i stars. A similar problem arises for the abundance ratios between Ba and La, where the s process cannot reproduce abundance ratios where Ba is significantly more enhanced than La — a limitation given by the relative neutron-capture cross sections of these two neighbouring elements. The observation of high [Ba/La] ratios raise a significant discrepancy between the observed and modelled nucleosynthesis because the r process produces negative [Ba/La] ratios.

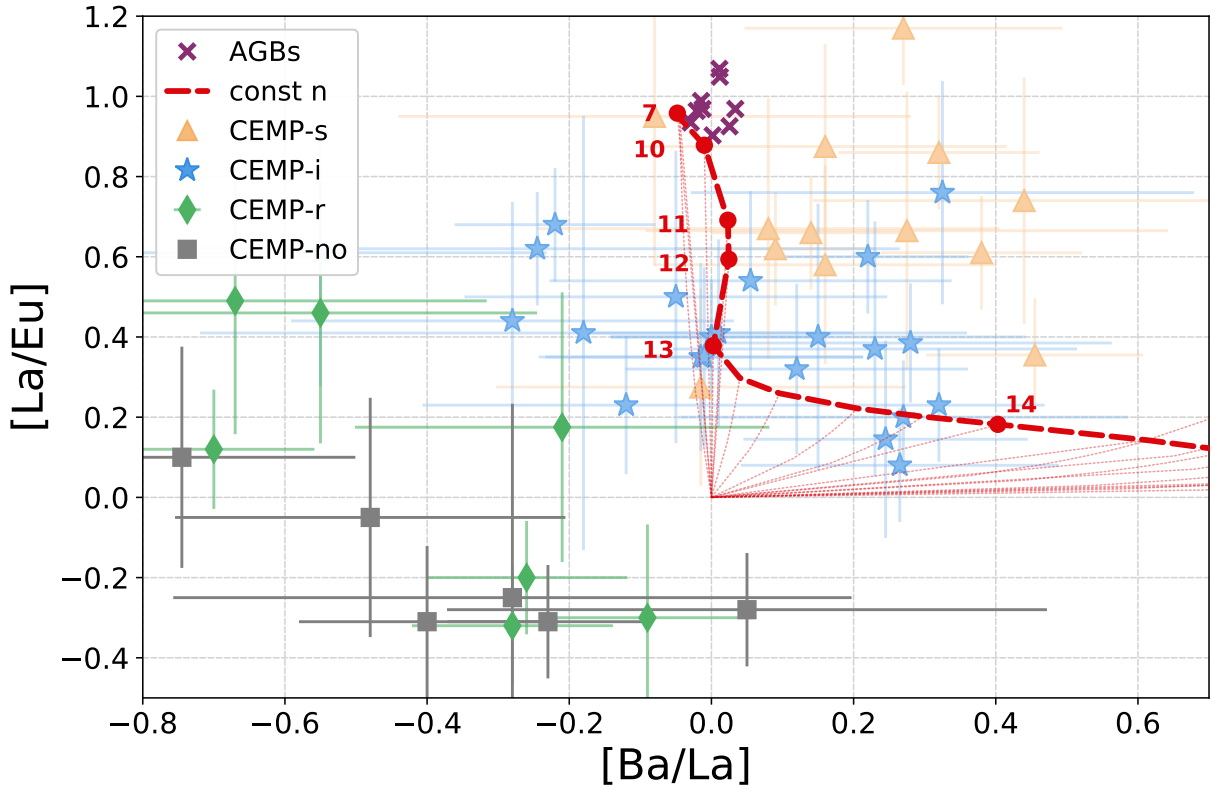

Figure 6.3: **Observed [La/Eu] ratios of CEMP stars as function of their [Ba/La] ratios.** Additionally, we indicate the abundance ratios predicted by the s process in metal-poor AGB stars (Lugaro et al., 2012). Equilibrium abundances of i-process calculations at constant neutron densities are shown along with their dilution lines. Discrete magnitudes of neutron densities are highlighted by red points and labelled with the respective $\log(n)$ value of the calculation.

Therefore, high [Ba/La] ratios cannot be reproduced by a mixture of s- and r-processed material.

The s-process models struggle to explain low [La/Eu] ratios just as much as they struggle to explain the characteristic low [Ba/Eu] abundance ratios of CEMP-i stars (and we remind the reader that both ratios are used in the literature to define CEMP-s versus CEMP-i stars). The i process does a much better job at reproducing the observed abundance ratios between La and Eu as well. Figure 6.3 shows how the equilibrium abundance ratios of the models with constant neutron density predict lower and lower ratios of [La/Eu] as the neutron density increases. Up to neutron densities of approximately $n = 10^{13}\,\mathrm{cm}^{-3}$ the abundance ratios of the predicted [Ba/La] ratios are not much affected and remain around [Ba/La] ≈ 0. This is because at higher n the shift of the neutron-capture path which produces isotopes with magic neutron numbers at lower atomic numbers affects the production of the typical s-process isotopes ^{138}Ba and ^{139}La almost equally.

Once the constant neutron densities reach $n > 10^{13}\,\mathrm{cm}^{-3}$ the [Ba/La] ratio starts to increase rapidly. This sudden increase of Ba production at neutron densities of $n > 10^{13}\,\mathrm{cm}^{-3}$ was already mentioned in the previous section where the increased Ba production became obvious as an onset of a decrease in the evolution of the [Eu/Ba] ratio (see Figure 6.2). Positive [Ba/La] abundance ratios are another manifestation of the same typical i-process behaviour: neutron densities in the approximate range of $10^{13}\,\mathrm{cm}^{-3} \lesssim n \lesssim 10^{15}\,\mathrm{cm}^{-3}$ produce a significant amount of ^{135}I, which later decays into ^{135}Ba.

^{135}I has an atomic number of $Z = 53$ and a magic neutron number of $N = 82$. As the neutron-capture path moves further away from the valley of stability with increasing neutron density, the i-process is able to produce significant amounts of ^{135}I instead of the typical hs isotopes ^{138}Ba and ^{139}La. ^{135}I is such a strong bottleneck for neutron-capture nucleosynthesis because of its particularly low neutron-capture cross section. Compared to the $^{134}\mathrm{I}(\mathrm{n},\gamma)^{135}\mathrm{I}$ reaction by which ^{135}I is produced the rate of its destruction via the $^{135}\mathrm{I}(\mathrm{n},\gamma)^{136}\mathrm{I}$ reaction has a ca. 300 to 400 times lower cross section in the temperature range around $T = 2 \times 10^8\,\mathrm{K}$ and $3 \times 10^8\,\mathrm{K}$. In Figure 6.4 we show a nuclear reaction flow chart in the region around ^{135}I for the constant neutron densities of $n = 10^{13}\,\mathrm{cm}^{-3}$ and $10^{15}\,\mathrm{cm}^{-3}$. It can be seen that the neutron-capture path is a few isotopes away from the valley of stability in this neutron-density range. The particular nuclear physics properties of the isotopes in the shown region shape the final i-process heavy-element patterns: the xenon isotopes ^{134}Xe and ^{136}Xe are stable isotopes and are the main products of the neutron-capture reactions that create the magic isotopes with mass numbers $A = 134$ and 136 (^{134}Xe is produced through the decays of ^{134}Te but does not decay further into Ba and ^{136}Xe has a magic neutron number itself). But most importantly, the xenon isotope ^{135}Xe is unstable with a half life of $T_{1/2} = 9.1\,\mathrm{hr}$. This allows for the decay of the magic isotope ^{135}I via ^{135}Xe and ^{135}Cs into ^{135}Ba, which increases the abundances of in the typical s-process element Ba without having this same enhancing impact on the other hs elements.

The i-process models shown in Figure 6.3 only represent the equilibrium abundance patterns at constant neutron densities. In Figure 6.5 we show how the [La/Eu] and [Ba/La] abundance ratios develop in our simulations with various ingested proton fractions using the different thermodynamic trajectories discussed in Chapter §4. The time evolution of the abundance ratios is indicated by the shading of each line, while the colours represent the ingested proton fraction in each simulation. Thin lines indicate the abundance evolution at subsequent neutron exposures below i-process neutron densities at $n < 10^{12}\,\mathrm{cm}^{-3}$. Dilution lines to the initial solar-scaled abundance ratios are also

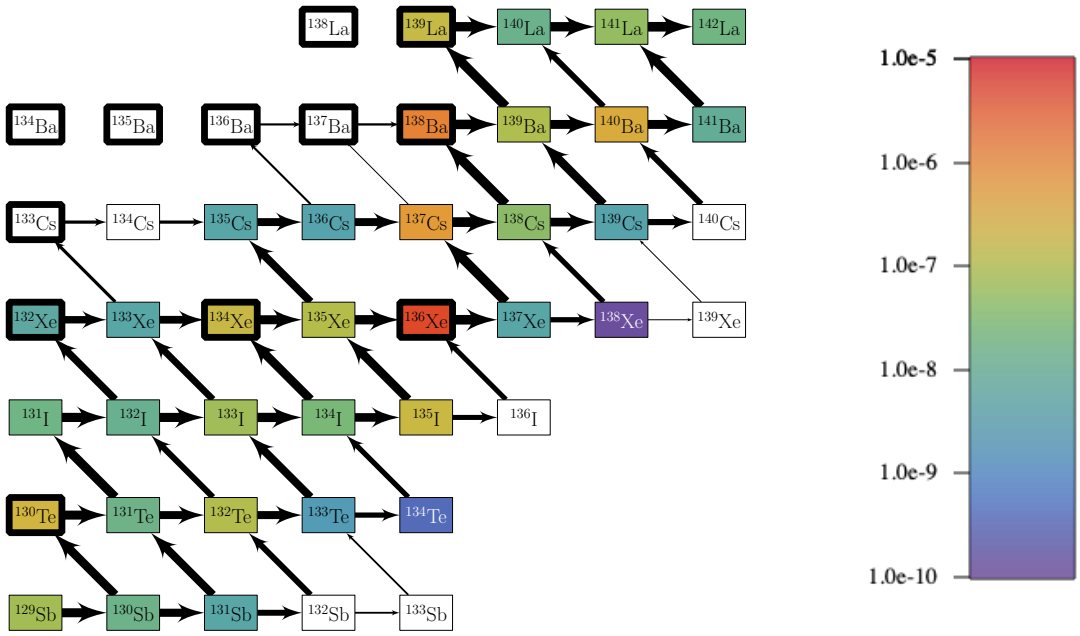

(A) Constant neutron density $n = 10^{13}\,\mathrm{cm}^{-3}$.

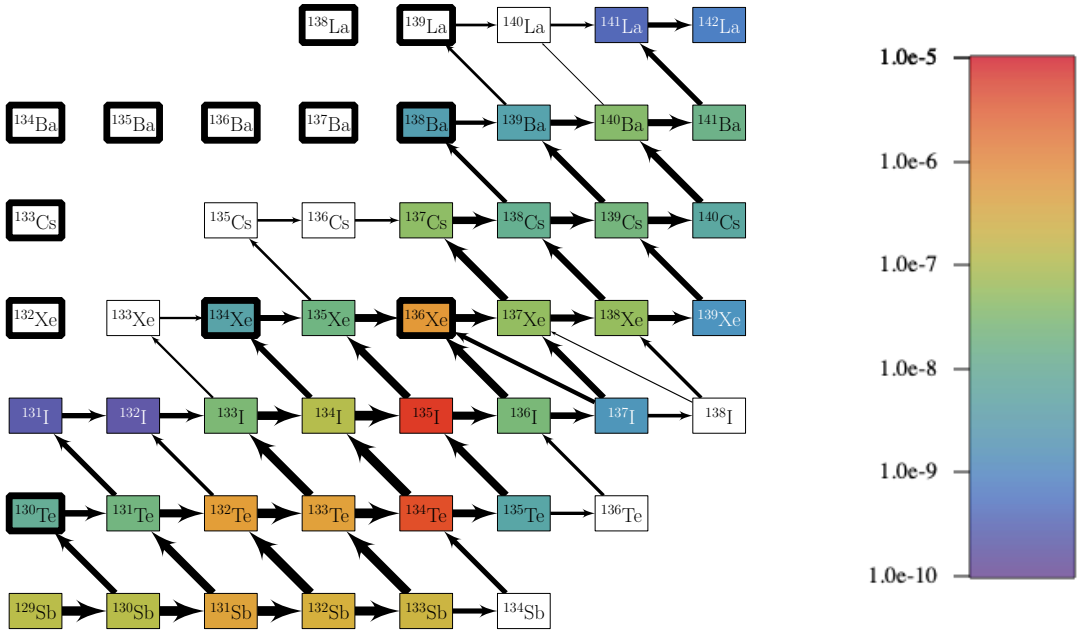

(B) Constant neutron density $n = 10^{15}\,\mathrm{cm}^{-3}$.

Figure 6.4: **Flow charts of neutron-capture reactions in the region of isotopes with magic neutron number $N = 82$.** Reaction flows for the simulations with constant neutron densities $n = 10^{13}\,\mathrm{cm}^{-3}$ (panel a) and $n = 10^{15}\,\mathrm{cm}^{-3}$ (panel b) at the time of a neutron exposure of $\tau = 2.5\,\mathrm{mbarn}^{-1}$. The colour of each isotope represents its mass fractions in the range of $10^{-10} \leq X \leq 10^{-5}$ and the size of the arrow scales logarithmically with the reaction flow. Stable isotopes are highlighted by bold black borders.

shown. Note that we only show times in our model when exposures of $\tau > 1\,\mathrm{mbarn}^{-1}$ are reached and significant heavy-element production has started. In contrast to Figure 6.3 we only focus on the regimes with positive abundance ratios and show a wider abundance scale. For comparison we also show the same equilibrium abundances of our models with constant neutron densities in all panels.

There is some general common behaviour which the models in Figure 6.5 display. At the beginning of the shown time evolution, which is for most models when the neutron density is at its maximum, high abundance ratios of [Ba/La] $\gtrsim 1.5$ are produced with simulatenous enhancement of the [La/Eu] abundance ratios. As time progresses and the neutron densities decline (see the according Figures in Chapter §5, which show the neutron density evolution for these models) the evolution of the [Ba/La] abundance ratio turns around and starts declining as well. Most models also show a decrease in their [La/Eu] abundance ratio in this phase with the exception of the models with the pAGB-trajectory. For the models using the thermodynamic trajectories from the other stellar sites another phase of increasing [La/Eu] ratios can be seen towards the end of the i-process nucleosynthesis evolution (shown with the darkest shading of the evolution lines in Figure 6.5) just before the model's respective τ_i is reached. In this phase the nucleosynthesis is most similar to s-process nucleosynthesis (although usually on shorter time scales) and has stopped producing significant amounts of ^{135}I. Accordingly, the abundance ratios show an increase of the [La/Eu] ratio with less significant influence on the [Ba/La] abundances, as typical for s-process nucleosynthesis.

The abundance ratios of each model at the time of τ_i vary between the models with different trajectories as well as with different ingested proton fractions. Depending on each model's individual neutron density evolution the abundance ratios at the time of τ_i can in some cases show a spread of several tenth of a dex. These abundance ratios at the time of τ_i can be significantly altered again, when subsequent nucleosynthesis in the neutron-densitiy tails with $n < 10^{12}\,\mathrm{cm}^{-3}$ over longer time scales is considered as well. In Figure 6.5 this subsequent evolution is shown as a continuation of the discussed shaded lines. The result is an increase in the [La/Eu] abundance ratio and a decrease in the [Ba/La] ratio which moves the abundance ratios closer to the predictions by the s-process models and does not necessarily preserve the signatures of its previous i-process history.

From Figure 6.5 we can conclude that models, which experience a neutron-density variation over time show a complex abundance evolution, which affects the evolution of the abundance ratios within the hs peak in particular. This shows that expected physical variations, such as the ingested proton fractions, can already explain a relatively wide spread of observed abundance ratios. There is no reason to expect that the abundance pattern of two CEMP stars should look exactly identical and we explore in this thesis how some physical parameters change the individual neutron density evolution of our models. Hence it is only reasonable to expect a variety of individual histories for the neutron density evolution, even among a population of otherwise similar stars, and already relatively small variations of the neutron density evolution can cause a spread of abundance ratios of the hs elements.

We want to point out that Figure 6.3 also shows (*i*) that it is not just CEMP-i stars, which have high [Ba/La] abundance ratios. The observed [Ba/La] abundances in CEMP-s stars have similarly high [Ba/La] ratios as the CEMP-i stars, which is incompatible with our current understanding of pure s-process nucleosynthesis. Yet, some of our models in Figure 6.5 show a

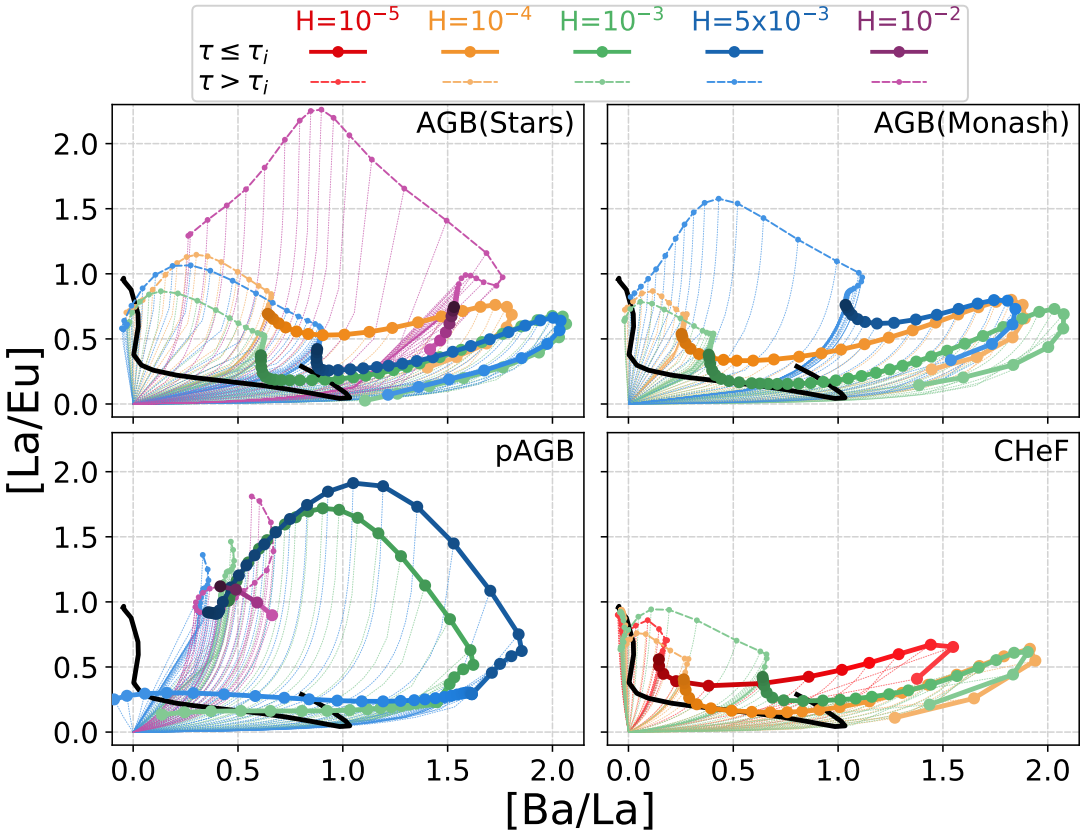

Figure 6.5: **Evolution of the [La/Eu] vs [Ba/La] ratios for various i-process models.** A separate panel for each of the four discussed temperature-density trajectories shows the results of the models with various ingested proton fractions. The time series of the evolution of the abundance ratios is shown where the colour identifies the initial proton fraction and the shading indicates the direction of the time evolution from light to dark. The lightest shading corresponds to the time of $\tau = 1\,\mathrm{mbarn}^{-1}$ when the main heavy-element production starts and the darkest shading corresponds to the time of τ_i when the neutron density in the simulation has dropped to $n = 10^{12}\,\mathrm{cm}^{-3}$. The further abundance-ratio evolution at lower neutron densities is indicated by small points on a thin dashed line. Even thinner, lighter, dotted lines are the dilution lines, which connect each point with (0, 0), the initial solar-scaled abundance ratio. For comparison, the black line represents the equilibrium abundance ratios from the simulations at constant neutron densities between $n = 10^{7}\,\mathrm{cm}^{-3}$ and $10^{16}\,\mathrm{cm}^{-3}$.

coverage of the [Ba/La] and [La/Eu] abundance space of the observed CEMP-s abundance ratios if subsequent heavy-element nucleosynthesis below i-process neutron-density levels is considered for longer times scales. (*ii*) There are some CEMP-i stars with negative [Ba/La] ratios. In our i-process models enhanced Ba production through ^{135}I decay is expected, which leads to a positive [Ba/La] abundance ratio, higher than in s- or r- process models. Therefore, we do not encounter negative [Ba/La] ratios in our models of i-process nucleosynthesis.

A further aspect that generally limits the predictions of i-process abundance ratios are uncertainties in the nuclear reaction rates. We discuss in Chapter 4.1 how reaction-rate uncertainties in the neutron-producing reactions can influence the evolution of the neutron density. However, for the prediction of heavy-element abundances the neutron-capture rates of the involved isotopes are of particular importance. For most isotopes, particularly the neutron-rich unstable nuclei, the neutron-capture cross sections are determined theoretically, which can lead to major uncertainties. Bertolli et al. (2013) study how abundance predictions from i-process nucleosynthesis vary when (n,γ) reaction rates from separate theoretical codes are compared. In some cases the resulting [La/Eu] abundances can vary up to 0.5 dex and the maximum variations in the [Ba/La] abundance ratio can even reach close to 1 dex. Recent studies by Denissenkov et al. (2021) study the reaction-rate uncertainties affecting the i-process nucleosynthesis of isotopes in the region of the magic neutron number $N = 82$, which we discussed in this section. They identify the nuclear reactions that have the largest effect on the produced heavy-element abundances and find, for example, that the production of Ba is most closely correlated with the neutron-capture reaction rates of ^{135}I at neutron densities of $n = 3.16 \times 10^{14}\,\mathrm{cm}^{-3}$, which re-emphasises the importance of the ^{135}I production for the i-process abundance signatures.

6.4 Barium isotopic ratios

The production of ^{135}I and its subsequent decay into ^{135}Ba is a firm prediction from i-process nucleosynthesis models at neutron densities in the range of $10^{13}\,\mathrm{cm}^{-3} \lesssim n \lesssim 10^{15}\,\mathrm{cm}^{-3}$. In general, Ba enhancements are commonly interpreted as signatures of the s process, but in the case of s-process nucleosynthesis it is the stable isotope ^{138}Ba with a magic neutron number of $N = 82$, which is responsible for predictions of enhanced Ba abundances. Therefore, the isotopic ratios of ^{135}Ba/^{138}Ba potentially hold a lot of information about the nucleosynthetic process responsible for the production of Ba.

The abundance ratios of Ba isotopes are commonly reported as the fraction of the Ba abundance, which is provided by Ba isotopes with an odd mass number. In general, Ba has 5 stable isotopes ^{134}Ba, ^{135}Ba, ^{136}Ba, ^{137}Ba, and ^{138}Ba. The odd-isotope fraction of Ba is defined as $f_{\mathrm{odd,Ba}} = [N(^{135}\mathrm{Ba}) + N(^{137}\mathrm{Ba})]/N(\mathrm{Ba})]$, where $N(^{135}\mathrm{Ba})$, $N(^{137}\mathrm{Ba})$, and $N(\mathrm{Ba})$ are the number densities of the isotopes ^{135}Ba, ^{137}Ba and of the total elemental Ba abundance, respectively. Commonly used reference values for $f_{\mathrm{odd,Ba}}$ are the predicted odd-isotope fractions for the contributions to the Solar System abundance of Ba, where the Solar System has $f_{\mathrm{odd,Ba}} = 0.18$, the pure r-process contribution has $f_{\mathrm{odd,Ba}} = 0.46$, and the pure s-process contribution has $f_{\mathrm{odd,Ba}} = 0.11$ (Arlandini et al., 1999).

In Figure 6.6 we show the evolution of $f_{\mathrm{odd,Ba}}$ as predicted by our models with constant neutron densities. Initially, approximately for a neutron exposure up to $\tau \approx 1\,\mathrm{mbarn}^{-1}$ or $2\,\mathrm{mbarn}^{-1}$

depending on the neutron density (compare Figure 2.1), there is a phase in which isotopic rearrangements due to the neutron exposures occur, but the neutron-capture path has not yet reached the isotopes with magic neutron number $N = 82$. After this initial phase each model shows a characteristic $f_{\mathrm{odd,Ba}}$ which increases with increasing neutron density. The lowest $f_{\mathrm{odd,Ba}} = 0.06$ results from the simulation with a constant neutron density of $n = 10^7\,\mathrm{cm}^{-3}$, which is reasonably close to the ratio of the Solar System s-process contribution. It is not surprising that s-process nucleosynthesis is associated with a particularly low $f_{\mathrm{odd,Ba}}$ since the Ba isotope predominantly produced by the s process is ^{138}Ba with an even mass number.

The significance of the production of the magic s-process isotope ^{138}Ba becomes less as neutron densities increase and the neutron-capture path moves away from the valley of stability. When the neutron density reaches levels above $n \approx 10^{13}\,\mathrm{cm}^{-3}$ the main production of Ba occurs via decays of ^{135}I into ^{135}Ba, which results in significantly higher values of $f_{\mathrm{odd,Ba}}$. In fact, for constant neutron densities of $n = 10^{14}\,\mathrm{cm}^{-3}$ and $10^{15}\,\mathrm{cm}^{-3}$ the Ba abundance is almost entirely composed of the odd isotope ^{135}Ba resulting in $f_{\mathrm{odd,Ba}} \gtrsim 0.9$.

Although the i process predicts a clear signature of high $f_{\mathrm{odd,Ba}}$, even higher than a combination of just s- and r-process nucleosynthesis can achieve, it is not a prediction that is easily verifiable through observations. The measurement of $f_{\mathrm{odd,Ba}}$ either relies on measuring the asymmetry in observed Ba line profiles caused by the line's hyperfine structure (Cowley & Frey, 1989; Magain & Zhao, 1993) or by comparing very accurate abundance measurements of several absorption lines with non-local thermodynamic equilibrium model atmospheres (Mashonkina et al., 1999). Despite the difficulties of the required measurements, the determination of $f_{\mathrm{odd,Ba}}$ in metal-poor stars has been attempted in multiple studies, although the results are not always conclusive and tend to have relatively large uncertainties (e.g., Magain, 1995; Lambert & Allende Prieto, 2002; Mashonkina & Zhao, 2006; Collet et al., 2009; Gallagher et al., 2010, 2012, 2015; Meng et al., 2016; Cui et al., 2018).With respect to our sample of CEMP-i stars, Meng et al. (2016) reported the odd-isotope fraction of Ba in CEMP-i star HE 0338-3945 as $f_{\mathrm{odd,Ba}} = 0.23 \pm 0.12$, which is close to the Solar System ratio but does not confirm an exceptionally large $f_{\mathrm{odd,Ba}}$ as a pure i-process signature would predict.

6.5 Summary and conclusions

In summary, i-process neutron densities create their own, distinct heavy element abundance patterns. It is tempting to think of the *intermediate* neutron-capture process as a process that simply combines and reproduces characteristics of the s and r process in some merged, mashed-up way maybe similar to mixing s- and r-processed matter. After all, its neutron density is intermediate to the s- and r-process neutron densities, its neutron-capture path lies in between the s- and r-process neutron-capture path, and even observationally CEMP-i stars are the "s/r" class which stand out by showing overabundances of both the s-process element Ba and the r-process element Eu.

However, thinking that the i process creates abundance patterns that resemble a combination of an s- and r-process abundance pattern is not correct. In fact, the i process and CEMP-i stars show characteristics that are incompatible with a mix of s- and r-processed material. Since the i-process neutron-capture path runs along its own set of isotopes, the nuclear physics properties of these isotopes and their decay products determine the final abundance pattern.

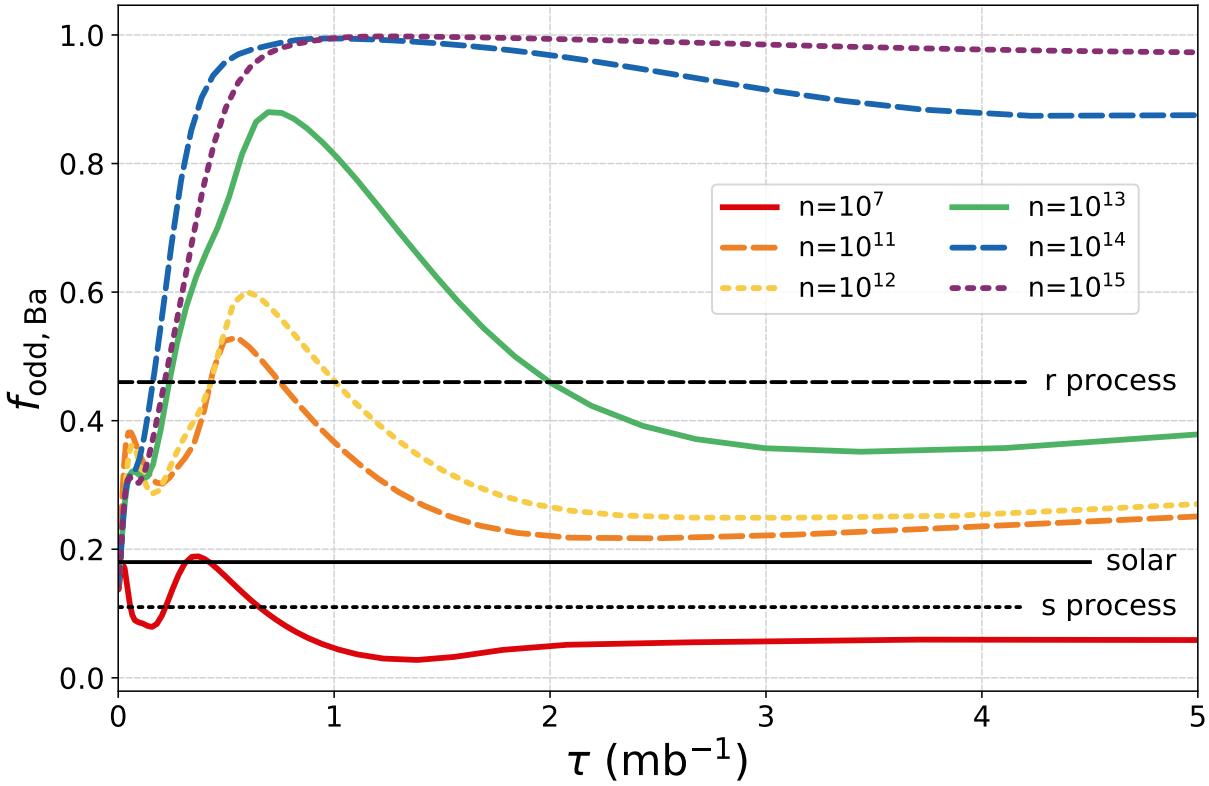

FIGURE 6.6: **Barium odd-isotope fractions $f_{\mathrm{odd,Ba}}$ predicted by the i-process models with constant neutron densities.** The evolution with neutron exposure is shown. For comparison the odd isotopes fractions of a pure r process $f_{\mathrm{odd,Ba}} = 0.46$, a pure s process $f_{\mathrm{odd,Ba}} = 0.11$, and for the Solar System $f_{\mathrm{odd,Ba}} = 0.18$ (Arlandini et al., 1999) are shown.

The isotopes that play a major role in shaping the final abundance patterns are the nuclei with magic neutron numbers along the neutron-capture path. With increasing neutron densities the neutron-capture path runs further away from the valley of stability where it encounters the bottleneck isotopes with magic neutron numbers at lower atomic numbers. Transitioning from an s- to an i-process neutron density means that both the ls and hs peak shift to lower Z and the noble gases Kr and Xe are produced significantly. Unfortunately, it is hard if not even impossible to observe these noble gases in stellar atmospheres. However, observations of some planetary nebulae or measurements of pre-solar meteoric grains may hold some elemental or isotopic i-process information for us.

An important feature of the i process is that it opens up the branching points that allow a large production of ^{135}I at neutron densities around $10^{13}\,\mathrm{cm}^{-3} \lesssim n \lesssim 10^{15}\,\mathrm{cm}^{-3}$. ^{135}I is such a strong bottleneck for neutron-capture nucleosynthesis because of its particularly low neturon-capture cross section compared to its neighbouring isotopes. It's significance for i-process abundance patterns arises from the fact that it is unstable and decays into ^{135}Ba. Therefore, ^{135}I offers a pathway of enhanced Ba production without simultaneously producing the same overenhancements of the other typical s-process elements.

The high production of ^{135}Ba through the i process leads to a few (potentially) observable characteristics, which are unique to i-process nucleosynthesis and cannot be reproduced by a superposition of s- and r-process nucleosynthesis. In particular, the i process produces very high odd-to-even isotopic barium ratios, which can exceed $f_{\mathrm{odd,Ba}} > 0.9$ in undiluted material and is much higher than the predictions from pure s- and r-process nucleosynthesis. The extra production of Ba through the decays from ^{135}I also leaves its signature on the elemental ratios of the classical hs-peak elements. While the s and r process produce either similar overabundances of Ba and La or even negative [Ba/La] ratios, the i-process operating at neutron densities $n > 10^{13}\,\mathrm{cm}^{-3}$ produces positive [Ba/La] abundance ratios. In addition, the i process also predicts higher [hs/ls] ratios, particularly of the typical representative observables such as [Ba/Sr] or [Ba/Y] which distinguish CEMP-i from CEMP-s stars and have even been suggested for a revised CEMP classification scheme.

Although not explicitly presented in this chapter but discussed in Chapter §2 (Hampel et al., 2019), we want to highlight again, that the i process can also reproduce high relative abundance ratios of Eu to other r-process elements such as Tb, Dy, and Ho. These elements are typically considered as tracers of r-process nucleosynthesis and the fractions of their Solar System abundances have an r-process origin of 98 %, 94 %, 88 %, and 93 %, respectively (Sneden et al., 2008). Due to their common r-process origin it is difficult to explain large variations in their relative abundances. In the CEMP-i star CS31062-050 the observed abundances of Eu/Tb are almost twice as large as the r-process predictions, and with an even smaller abundance ratio predicted by s-process nucleosynthesis a combination of s- and r-process cannot account for these observations (for details on the measurements in CEMP-i star CS 31062-050 see Johnson & Bolte, 2004). As discussed in Chapter §2 (Hampel et al., 2019) the enhanced Eu production by the i process naturally predicts higher [Eu/Tb, Dy, Ho] abundance ratios than explainable by s- or r-process nucleosynthesis or a combination of both.

Finally, for readers turning to this section for information on abundance-signatures to look for in future observations of CEMP stars, we would like to reiterate that the elements between the light

and heavy s-process peaks (between Zr and Ba) potentially hold information to constrain i-process nucleosynthesis models. Additionally, we also hope that Chapter §2 (Hampel et al., 2019) shows that observations of Pb are always interesting contributors to the story an abundance pattern tells about its origin, whether it is by providing answers and constraints or by raising more puzzling questions.

> *I never am really satisfied that I understand anything; because, understand it well as I may, my comprehension can only be an infinitesimal fraction of all I want to understand*
>
> — Ada Lovelace

Chapter 7

Summary and concluding remarks

In this thesis we presented nuclear-network simulations to study the nucleosynthesis of the *intermediate* neutron-capture process. Neutron-capture processes are the main nucleosynthesis pathways for the creation of the majority of *heavy elements*, elements heavier than iron. While the classical picture of two separate neutron capture processes, a *slow* and a *rapid* neutron capture process (s and r process, respectively) is successful in reproducing the main characteristics of the heavy-element abundance pattern in our Sun, there also is a growing number of observations, particularly of metal-poor stars, which cannot be explained as results of s- or r-process nucleosynthesis or even a combination of both.

The description of neutron-capture processes being either slow or rapid refers to the time scale of neutron-capture reactions relative to β-decay time scales of the produced neutron-rich, unstable isotopes. The neutron-capture reaction rates depend on the available neutron densities n, where low neutron densities of $n \approx 10^7\,\mathrm{cm}^{-3}$ lead to conditions for s-process nucleosynthesis, while the r process requires high neutron densities of $n \gtrsim 10^{20}\,\mathrm{cm}^{-3}$. The neutron-capture process and heavy-element production at conditions *intermediate* (i process) to the s and r process are the subject of study in this thesis.

Typical i-process neutron densities of $10^{13}\,\mathrm{cm}^{-3}$ to $10^{15}\,\mathrm{cm}^{-3}$ create their own distinct heavy-element abundance patterns which have been successful at reproducing some of the observed mysterious heavy-element abundance patterns that could not previously be explained by just s- and r-process components. In particular, it is a subclass of carbon-enhanced metal-poor (CEMP) stars with simultaneous overenhancements of the typical s-process element barium (Ba) and the r-process element europium (Eu), which are now believed to owe their heavy-element abundances to the production via i-process nucleosynthesis (CEMP-i stars).

Although the high neutron densities for i-process heavy-element production were first encountered decades ago in stellar evolution models by Cowan & Rose (1977), the quest for a stellar i-process host site (or sites?) is still ongoing. A variety of stellar evolution scenarios are believed to be able to provide conditions for the i process in proton-ingestion episodes, where protons are mixed into a helium convective region and can lead to the production of i-process neutron densities. Among the proposed scenarios are the first thermal pulse(s) of metal-poor AGB stars, the core He-flash in metal-poor and metal-free low-mass stars, very late thermal pulses in post-AGB stars, super-AGB stars, rapidly accreting white dwarfs, or even low-metallicity massive stars.

With the main stellar i-process site(s) still unidentified, we set out to investigate systematically what story observed i-process abundance patterns can tell about the conditions under which they have been produced and how the heavy-element abundances relate to the parameters of the physical environments in which they were created.

In **Chapter 2** we presented single-zone nuclear-reaction network calculations at various constant neutron densities. This study was an extension of earlier work presented in Hampel et al. (2016) and focused on constraining the time scales and neutron exposures required to reproduce observed i-process abundance patterns. A key feature of s- and i-process nucleosynthesis which we utilised for this study is the continuous production of Pb-peak elements. While other elements reach equilibrium abundances between one another, the elements at the end of the neutron-capture path, and Pb in particular, only get produced in larger and larger quantities the longer the neutron-capture process operates for. We used the observed abundances of Pb in CEMP-i stars to constrain that neutron exposure of $\tau > 2\,\mathrm{mbarn}^{-1}$ at neutron densities of $n = 10^{13}\,\mathrm{cm}^{-3}$ and $10^{14}\,\mathrm{cm}^{-3}$ are

required to reproduce the majority of abundance patterns of CEMP-i stars. This means that it only takes the i process time scales as short as weeks or even just days at these high neutron-densities to produce the observed i-process heavy-element abundances.

Additionally, we investigated the Pb abundances in Magellanic post-AGB stars, which are puzzlingly low for an s-process origin. Pb is one of the main s-process products and particularly with decreasing metallicity large enhancements of Pb are expected to be produced. Yet these Magellanic post-AGB stars, whose progenitors were low-mass stars of approximately $1\,M_\odot$ to $1.5\,M_\odot$, do not show the expected Pb overabundances. In our simulations we find that constant neutron densities of $n = 10^{11}\,\mathrm{cm}^{-3}$ and $10^{12}\,\mathrm{cm}^{-3}$ can reproduce the observed low Pb abundances after neutron exposures of $\tau = 1\,\mathrm{mbarn}^{-1}$ to $1.3\,\mathrm{mbarn}^{-1}$.

In **Chapter 3** we started focusing on the neutron-production process during proton-ingestion episodes. When protons are mixed into He convective regions the reaction chain $^{12}\mathrm{C}(\mathrm{n},\gamma)^{13}\mathrm{N}(\beta^+\nu)^{13}\mathrm{C}(\alpha,\mathrm{n})^{16}\mathrm{O}$ leads to the production of neutrons. However, the ingested protons also get captured through other CNO and hot CNO cycle reactions which produce the neutron poison ^{14}N, e.g., via $^{13}\mathrm{C}(\mathrm{p},\gamma)^{14}\mathrm{N}$ or $^{13}\mathrm{N}(\mathrm{p},\gamma)^{14}\mathrm{O}(\beta^+\nu)^{14}\mathrm{N}$. We present single-zone nuclear network calculations that take into account that material experiences increasingly hot and dense conditions as it moves downwards through the convective region. Once the produced ^{13}C makes it to the hottest regions at the bottom of the convective zone, we focus on this thin layer in the star where i-process neutron densities can be produced and heavy-element nucleosynthesis can take place. By testing various ingested proton fractions we were able to lay out the fundamental sequence of neutron-producing and -recycling reactions, which only lead to neutron exposures sufficient for heavy-element production in cases of ingested proton fractions less than approximately 10^{-3}.

In **Chapter 4** we investigated how the produced neutron density evolution for i-process nucleosynthesis is affected by variations of underlying physical conditions and uncertainties. When testing how the reaction-rate uncertainties of the charged-particle reactions impact the evolution of the neutron density we found that the reaction-rate uncertainties of the $^{12}\mathrm{C}(\mathrm{n},\gamma)^{13}\mathrm{C}$ reaction, the $^{13}\mathrm{C}(\alpha,\mathrm{n})^{16}\mathrm{O}$ reaction, and the $^{14}\mathrm{N}(\mathrm{n},\mathrm{p})^{14}\mathrm{C}$ reactions can cause heavy-element abundance spreads of several tenths of a dex. We found similar and even larger heavy-element abundance variations as a consequence of varying the initial ^{12}C abundances in the He convective zone. Even for simulations with the same ratio of protons to ^{12}C, which is usually regarded as the determining parameter that shapes the neutron and heavy-element production in s-process nucleosynthesis studies, we find that differences in the neutron-recycling reactions occur. These differences can influence how quickly or slowly the high i-process neutron densities decrease after they reached their maximum n_{max}. Finally we tested different convective velocities in the convective region, which influence how quickly our parcel of material experiences the rise in temperature and density as it moves downwards through the He convective region. Here we found that the main aspect affecting the neutron production is the time that the produced ^{13}N needs to decay into ^{13}C. If substantial amounts of ^{13}N are still present when reaching the highest temperatures at the bottom of the convective region, then ^{13}N can alter the neutron-recycling processes, although the details of how the neutron production and neutron density evolution is affected is a complex interplay with various dependencies, such as the ingested proton fraction and the abundance variations of ^{13}N.

In **Chapter 5** we tested different temperature-density trajectories which are adapted from the stellar structure during proton-ingestion episodes of different stellar evolution models. Our reference

simulations from the previous chapters were based on a proton-ingestion episode in an early thermal pulse of a $1\,M_\odot$ AGB model with metallicity $Z = 10^{-4}$. In this chapter we presented a new stellar evolution model of a heavier $1.3\,M_\odot$ AGB star at the same metallicity computed with a different stellar evolution code to test the variations in conditions that could reasonably be expected from different models of the same i-process site and how these differences of thermodynamic properties affect the i-process nucleosynthesis. Additionally, we also presented i-process models with various ingested proton fractions using temperature-density trajectories adapted from the very late thermal pulse of a $1.3\,M_\odot$ post-AGB star and the core helium flash of an ultra metal-poor $0.8\,M_\odot$ star. In comparison of the various i-process nucleosynthesis models to observed abundance patterns we found that significantly different abundances of the elements between the typical light and heavy s-process peaks (elements between Zr and Ba with atomic numbers $40 < Z < 56$) were predicted. These abundances are mostly unconstrained in the observations and more complete observational abundance patterns can potentially provide valuable constraints for different i-process scenarios.

In **Chapter 6** we pointed out some i-process signatures, which can help to distinguish heavy-element abundance patterns created by the s process from those of the i process. By definition of the subclasses of CEMP-s and CEMP-i stars, CEMP-i stars show high abundance ratios of typical s- and r-process elements and therefore have typically lower [Ba/Eu] and [La/Eu] ratios than predicted by the s-process alone, which can be reproduced by i-process nucleosynthesis. We also showed how the i process is able to reproduce higher abundance ratios between the heavy and light s-process peak elements [Ba/Sr] than predicted by the s process, which is a distinguishing feature between CEMP-i and CEMP-s stars. Additionally, we showed that unique i-process abundance features arise from the enhanced production of ^{135}I with magic neutron number $N = 82$ at neutron densities between approximately $10^{13}\,\mathrm{cm}^{-3}$ and $10^{15}\,\mathrm{cm}^{-3}$. The unstable ^{135}I decays into ^{135}Ba which produces signatures of high [Ba/La] ratios as well as high odd-isotope fractions for Ba which can reach $f_{\mathrm{odd,Ba}} > 0.9$ in pure i-process material. Interestingly, CEMP-s stars show similar high observed abundance ratios of [Ba/La] as CEMP-i stars, which are incompatible with an s-process origin. On the other hand, there are also some CEMP-i stars with observed negative [Ba/La] abundance ratios, which cannot be explained with our i-process models.

Although single-zone nuclear-reaction network calculations only present a simplified picture of the complex physics responsible for i-process nucleosynthesis, they provide a powerful and computationally inexpensive tool to quickly test a broad parameter range systematically. Given their simplicity, they can reproduce observed abundance patterns surprisingly well. Choplin et al. (2021) investigated i-process nucleosynthesis in a proton-ingestion episode in a detailed stellar evolution model of a low-mass, low-metallicity AGB star and found fits to the abundance patterns of CEMP-i stars, which are surprisingly similar to the fits we presented in Chapter §2 (Hampel et al., 2019) with a much more simplistic model.

One of the effects that cannot be modelled well in simplistic models, or not at all with our single-zone models, are important but uncertain mixing effects. Unfortunately, our understanding and modelling of these mixing processes remains poor, particularly because 1D stellar evolution codes cannot provide adequate descriptions of inherently 3D mixing phenomena. The situation becomes worse from a theoretical point of view, since the interplay between convective mixing and nuclear reactions occurs on similar time scales. To top things off, the high i-process neutron densities create fairly neutron-rich, unstable isotopes of the heavy elements, which requires large

nuclear networks to adequately study the i-process heavy-element production with the number of involved nuclear species of the order of a thousand or more, as well as multiple thousand reactions between them. Often these nuclear reactions are just theoretically predicted and come with large reaction rate uncertainties. Finally, there is a whole set of challenges and uncertainties associated with measuring the heavy-element abundances in metal-poor stars in the first place, which we will leave for future generations of PhD students to discuss and hopefully solve.

With many uncertainties in our models of i-process nucleosynthesis there is still a long way to go until we can fully understand all the effects and the underlying physics responsible for the heavy-element production at *intermediate* neutron densities. Particularly with the long list of potential i-process sites but no clear narrative of when and how much i-process nucleosynthesis happened throughout the history of the Universe, there are still many gaps in our understanding of the origin of the elements. To conclude this thesis, we want to repeat some of the major open questions about i-process nucleosynthesis, which we first posed in the introduction some 100 pages ago:

Where did the i process nucleosynthesis occur and what was the nature of its host site? Is there a dominant i-process site or are multiple different stellar evolution scenarios hosting i-process nucleosynthesis? What can we learn about the underlying nuclear and stellar physics from observed i-process patterns? Compared to CEMP-s stars, CEMP-i stars do not appear to be particularly rare. Is i-process nucleosynthesis a common occurrence? Did the i process play a significant role in galactic chemical evolution?

With the ongoing improvements and combined efforts of nuclear physics studies, observational abundance measurements, and theoretical modelling we will hopefully continue to get closer to the answer to some of those questions and continue to put together the individual puzzle pieces that will ultimately lead us to a complete picture of the origin of the elements.

Bibliography

C. Abate, et al. "Carbon-enhanced metal-poor stars: a window on AGB nucleosynthesis and binary evolution. I. Detailed analysis of 15 binary stars with known orbital periods." *A&A*, 576:A118, 2015a.

C. Abate, et al. "Carbon-enhanced metal-poor stars: a window on AGB nucleosynthesis and binary evolution. II. Statistical analysis of a sample of 67 CEMP-s stars." *A&A*, 581:A22, 2015b.

C. Abate, et al. "How plausible are the proposed formation scenarios of CEMP-r/s stars?" *A&A*, 587:A50, 2016.

C. Abate, et al. "Understanding the orbital periods of CEMP-s stars." *A&A*, 620:A63, 2018.

B. P. Abbott, et al. "GW170817: Observation of Gravitational Waves from a Binary Neutron Star Inspiral." *Phys. Rev. Lett.*, 119(16):161101, 2017.

A. Abohalima & A. Frebel. "JINAbase—A Database for Chemical Abundances of Metal-poor Stars." *ApJS*, 238:36, 2018.

D. M. Allen, et al. "Elemental abundances and classification of carbon-enhanced metal-poor stars." *A&A*, 548:A34, 2012.

C. Angulo, et al. "A compilation of charged-particle induced thermonuclear reaction rates." *Nucl. Phys. A*, 656(1):3–183, 1999.

W. Aoki, et al. "Detection of Lead in the Carbon-rich, Very Metal-poor Star LP 625-44: A Strong Constraint on S-Process Nucleosynthesis at Low Metallicity." *ApJ*, 536:L97–L100, 2000.

W. Aoki, et al. "Neutron Capture Elements in s-Process-Rich, Very Metal-Poor Stars." *ApJ*, 561:346–363, 2001.

W. Aoki, et al. "A Subaru/High Dispersion Spectrograph Study of Lead (Pb) Abundances in Eight s-Process Element-rich, Metal-poor Stars." *ApJ*, 580:1149–1158, 2002a.

W. Aoki, et al. "Subaru/HDS Study of the Extremely Metal-Poor Star CS 29498-043: Abundance Analysis Details and Comparison with Other Carbon-Rich Objects." *PASJ*, 54:933–949, 2002b.

W. Aoki, et al. "Carbon-enhanced Metal-poor Stars: Osmium and Iridium Abundances in the Neutron-Capture-enhanced Subgiants CS 31062-050 and LP 625-44." *ApJ*, 650:L127–L130, 2006.

W. Aoki, et al. "Carbon-enhanced Metal-poor Stars. I. Chemical Compositions of 26 Stars." *ApJ*, 655:492–521, 2007.

W. Aoki, et al. "Carbon-Enhanced Metal-Poor Stars. III. Main-Sequence Turnoff Stars from the SDSS SEGUE Sample." *ApJ*, 678:1351–1371, 2008.

Wako Aoki, et al. "Chemical Composition of Carbon-Rich, Very Metal-Poor Subgiant LP 625-44 Observed with the Subaru/HDS." *PASJ*, 54:427–449, 2002c.

C. Arlandini, et al. "Neutron Capture in Low-Mass Asymptotic Giant Branch Stars: Cross Sections and Abundance Signatures." *ApJ*, 525:886–900, 1999.

M. Arnould & S. Goriely. "Astronuclear Physics: A tale of the atomic nuclei in the skies." *Progress in Particle and Nuclear Physics*, 112:103766, 2020.

M. Asplund, et al. "The rapid evolution of the born-again giant Sakurai's object." *A&A*, 343:507–518, 1999.

M. Asplund, et al. "The Chemical Composition of the Sun." *ARA&A*, 47:481–522, 2009.

Australian Academy of Science. "Australia in the era of global astronomy: the decadal plan for australian astronomy 2016–2025." 2015.

P. Banerjee, et al. "New Neutron-capture Site in Massive Pop III and Pop II Stars as a Source for Heavy Elements in the Early Galaxy." *ApJ*, 865:120, 2018.

B. Barbuy, et al. "New analysis of the two carbon-rich stars CS 22948-27 and CS 29497-34: Binarity and neutron capture elements." *A&A*, 429:1031–1042, 2005.

P. S. Barklem, et al. "The Hamburg/ESO R-process enhanced star survey (HERES). II. Spectroscopic analysis of the survey sample." *A&A*, 439:129–151, 2005.

T. C. Beers & N. Christlieb. "The Discovery and Analysis of Very Metal-Poor Stars in the Galaxy." *ARA&A*, 43:531–580, 2005.

T. C. Beers, et al. "Near-Infrared Spectroscopy of Carbon-Enhanced Metal-Poor Stars. I. A SOAR/OSIRIS Pilot Study." *AJ*, 133:1193–1203, 2007.

M. G. Bertolli, et al. "Systematic and correlated nuclear uncertainties in the i-process at the neutron shell closure N = 82." *ArXiv e-prints*, page arXiv:1310.4578, 2013.

S. Bisterzo, et al. "The s-process in low-metallicity stars - II. Interpretation of high-resolution spectroscopic observations with asymptotic giant branch models." *MNRAS*, 418:284–319, 2011.

S. Bisterzo, et al. "The s-process in low-metallicity stars - III. Individual analysis of CEMP-s and CEMP-s/r with asymptotic giant branch models." *MNRAS*, 422:849–884, 2012.

E. Böhm-Vitense. "Über die Wasserstoffkonvektionszone in Sternen verschiedener Effektivtemperaturen und Leuchtkräfte. Mit 5 Textabbildungen." *ZAp*, 46:108, 1958.

E. M. Burbidge, et al. "Synthesis of the Elements in Stars." *Reviews of Modern Physics*, 29:547–650, 1957.

M. Busso, et al. "Nucleosynthesis in Asymptotic Giant Branch Stars: Relevance for Galactic Enrichment and Solar System Formation." *ARA&A*, 37:239–309, 1999.

A. G. W. Cameron. "Nuclear Reactions in Stars and Nucleogenesis." *PASP*, 69(408):201, 1957a.

A. G. W. Cameron. "On the origin of the heavy elements." *AJ*, 62:9–10, 1957b.

S. W. Campbell. "private communication." 2020.

S. W. Campbell & J. C. Lattanzio. "Evolution and nucleosynthesis of extremely metal-poor and metal-free low- and intermediate-mass stars. I. Stellar yield tables and the CEMPs." *A&A*, 490:769–776, 2008.

S. W. Campbell, et al. "Evolution and nucleosynthesis of extremely metal-poor and metal-free low- and intermediate-mass stars. II. s-process nucleosynthesis during the core He flash." *A&A*, 522:L6, 2010.

R. C. Cannon. "Massive Thorne-Żytkow Objects - Structure and Nucleosynthesis." *MNRAS*, 263:817, 1993.

Georgeann R. Caughlan & William A. Fowler. "Thermonuclear Reaction Rates V." *Atomic Data and Nuclear Data Tables*, 40:283, 1988.

A. Choplin, et al. "Are some CEMP-s stars the daughters of spinstars?" *A&A*, 607:L3, 2017.

A. Choplin, et al. "The intermediate neutron capture process. I. Development of the i-process in low-metallicity low-mass AGB stars." *A&A*, 648:A119, 2021.

O. Clarkson & F. Herwig. "Convective H-He interactions in massive population III stellar evolution models." *MNRAS*, 500(2):2685–2703, 2021.

O. Clarkson, et al. "Pop III i-process nucleosynthesis and the elemental abundances of SMSS J0313-6708 and the most iron-poor stars." *MNRAS*, 474:L37–L41, 2018.

Donald D. Clayton. *Principles of stellar evolution and nucleosynthesis*. 1968.

J. G. Cohen, et al. "Abundance Analysis of HE 2148-1247, A Star with Extremely Enhanced Neutron Capture Elements." *ApJ*, 588:1082–1098, 2003.

J. G. Cohen, et al. "Abundances In Very Metal-Poor Dwarf Stars." *ApJ*, 612:1107–1135, 2004.

J. G. Cohen, et al. "Carbon Stars in the Hamburg/ESO Survey: Abundances." *AJ*, 132:137–160, 2006.

J. G. Cohen, et al. "Normal and Outlying Populations of the Milky Way Stellar Halo at [Fe/H] <-2." *ApJ*, 778:56, 2013.

R. Collet, et al. "The Barium Isotopic Abundance in the Metal-Poor Star HD140283." *PASA*, 26(3):330–334, 2009.

Thomas Constantino, et al. "On the Necessity of Composition-dependent Low-temperature Opacity in Models of Metal-poor Asymptotic Giant Branch Stars." *ApJ*, 784(1):56, 2014.

B. Côté, et al. "The Origin of r-process Elements in the Milky Way." *ApJ*, 855:99, 2018.

Benoit Côté, et al. "Neutron Star Mergers Might Not Be the Only Source of r-process Elements in the Milky Way." *ApJ*, 875(2):106, 2019.

J. J. Cowan & W. K. Rose. "Production of C-14 and neutrons in red giants." *ApJ*, 212:149–158, 1977.

John J. Cowan, et al. "Origin of the heaviest elements: The rapid neutron-capture process." *Reviews of Modern Physics*, 93(1):015002, 2021.

Charles R. Cowley & Madai Frey. "Hyperfine Structure in the Barium Resonance Line: Curves of Growth for Solar and r-Process Isotopic Mixtures." *ApJ*, 346:1030, 1989.

S. Cristallo, et al. "Asymptotic-Giant-Branch Models at Very Low Metallicity." *PASA*, 26:139–144, 2009.

S. Cristallo, et al. "Constraints of the Physics of Low-mass AGB Stars from CH and CEMP Stars." *ApJ*, 833:181, 2016.

M. A. Cruz, et al. "S-process in extremely metal-poor, low-mass stars." *A&A*, 559:A4, 2013.

W. Cui, et al. "The odd-isotope fractions of Barium in the strongly r-process enhanced (r-II) stars." *arXiv e-prints*, page arXiv:1801.07919, 2018.

W. Y. Cui, et al. "The Hamburg/ESO R-process Enhanced Star survey (HERES). VIII. The r+s star HE 1405-0822." *A&A*, 558:A36, 2013.

R. H. Cyburt, et al. "The JINA REACLIB Database: Its Recent Updates and Impact on Type-I X-ray Bursts." *ApJS*, 189:240–252, 2010.

L. Dardelet, et al. "i process and CEMP-s+r stars." In *XIII Nuclei in the Cosmos (NIC XIII)*, page 145. 2014.

O. De Marco & R. G. Izzard. "Dawes Review 6: The Impact of Companions on Stellar Evolution." *PASA*, 34:e001, 2017.

K. De Smedt, et al. "Post-AGB stars in the SMC as tracers of stellar evolution: the extreme s-process enrichment of the 21 μm star J004441.04-732136.4." *A&A*, 541:A67, 2012.

K. De Smedt, et al. "The lead discrepancy in intrinsically s-process enriched post-AGB stars in the Magellanic Clouds." *A&A*, 563:L5, 2014.

K. De Smedt, et al. "Chemical abundance study of two strongly s-process enriched post-AGB stars in the LMC: J051213.81-693537.1 and J051848.86-700246.9." *A&A*, 583:A56, 2015.

K. De Smedt, et al. "Detailed homogeneous abundance studies of 14 Galactic s-process enriched post-AGB stars: In search of lead (Pb)." *A&A*, 587:A6, 2016.

P. Denissenkov, et al. "The impact of (n, γ) reaction rate uncertainties of unstable isotopes near N = 50 on the i-process nucleosynthesis in He-shell flash white dwarfs." *Journal of Physics G Nuclear Physics*, 45(5):055203, 2018.

P. A. Denissenkov, et al. "i-process Nucleosynthesis and Mass Retention Efficiency in He-shell Flash Evolution of Rapidly Accreting White Dwarfs." *ApJ*, 834:L10, 2017.

Pavel A. Denissenkov, et al. "The i-process yields of rapidly accreting white dwarfs from multicycle He-shell flash stellar evolution models with mixing parametrizations from 3D hydrodynamics simulations." *MNRAS*, 488(3):4258–4270, 2019.

Pavel A. Denissenkov, et al. "The impact of (n,γ) reaction rate uncertainties of unstable isotopes on the i-process nucleosynthesis of the elements from Ba to W." *MNRAS*, 503(3):3913–3925, 2021.

I. Dillmann, et al. "KADoNiS- The Karlsruhe Astrophysical Database of Nucleosynthesis in Stars." In *Capture Gamma-Ray Spectroscopy and Related Topics*, editors A. Woehr & A. Aprahamian, volume 819 of *American Institute of Physics Conference Series*, pages 123–127. 2006.

C. L. Doherty, et al. "Super- and massive AGB stars - IV. Final fates - initial-to-final mass relation." *MNRAS*, 446:2599–2612, 2015.

H. W. Duerbeck, et al. "The Rise and Fall of V4334 Sagittarii (Sakurai's Object)." *AJ*, 119(5):2360–2375, 2000.

C. K. Fishlock, et al. "Evolution and Nucleosynthesis of Asymptotic Giant Branch Stellar Models of Low Metallicity." *ApJ*, 797:44, 2014.

A. Frebel. "From Nuclei to the Cosmos: Tracing Heavy-Element Production with the Oldest Stars." *Annual Review of Nuclear and Particle Science*, 68:237–269, 2018.

Ken Freeman & Joss Bland-Hawthorn. "The New Galaxy: Signatures of Its Formation." *ARA&A*, 40:487–537, 2002.

Urs Frischknecht, et al. "s-process production in rotating massive stars at solar and low metallicities." *MNRAS*, 456(2):1803–1825, 2016.

C. A. Frost & J. C. Lattanzio. "On the Numerical Treatment and Dependence of the Third Dredge-up Phenomenon." *ApJ*, 473:383, 1996.

M. Y. Fujimoto, et al. "Helium flashes and hydrogen mixing in low-mass population III stars." *ApJ*, 349:580–592, 1990.

M. Y. Fujimoto, et al. "The Origin of Extremely Metal-poor Carbon Stars and the Search for Population III." *ApJ*, 529:L25–L28, 2000.

A. J. Gallagher, et al. "The barium isotopic mixture for the metal-poor subgiant star HD 140283." *A&A*, 523:A24, 2010.

A. J. Gallagher, et al. "The barium isotopic fractions in five metal-poor stars." *A&A*, 538:A118, 2012.

A. J. Gallagher, et al. "A three-dimensional hydrodynamical line profile analysis of iron lines and barium isotopes in HD 140283." *A&A*, 579:A94, 2015.

R. Gallino, et al. "Evolution and Nucleosynthesis in Low-Mass Asymptotic Giant Branch Stars. II. Neutron Capture and the S-Process." *ApJ*, 497:388–403, 1998.

S. Goriely & N. Mowlavi. "Neutron-capture nucleosynthesis in AGB stars." *A&A*, 362:599–614, 2000.

S. Goriely, et al. "Improved predictions of nuclear reaction rates with the TALYS reaction code for astrophysical applications." *A&A*, 487(2):767–774, 2008.

A. Goswami & W. Aoki. "HD 209621: abundances of neutron-capture elements*." *MNRAS*, 404:253–264, 2010.

A. Goswami, et al. "A high-resolution spectral analysis of three carbon-enhanced metal-poor stars." *MNRAS*, 372:343–356, 2006.

Partha Pratim Goswami, et al. "Spectroscopic study of CEMP-(s & r/s) stars. Revisiting classification criteria and formation scenarios, highlighting i-process nucleosynthesis." *A&A*, 649:A49, 2021.

B. Guo, et al. "New Determination of the $^{13}C(\alpha, n)^{16}O$ Reaction Rate and its Influence on the s-process Nucleosynthesis in AGB Stars." *ApJ*, 756(2):193, 2012.

A. S. Hamers, et al. "Population synthesis of triple systems in the context of mergers of carbon-oxygen white dwarfs." *MNRAS*, 430:2262–2280, 2013.

M. Hampel, et al. "The Intermediate Neutron-capture Process and Carbon-enhanced Metal-poor Stars." *ApJ*, 831:171, 2016.

Melanie Hampel, et al. "Learning about the Intermediate Neutron-capture Process from Lead Abundances." *ApJ*, 887(1):11, 2019.

C. J. Hansen, et al. "Abundances and kinematics of carbon-enhanced metal-poor stars in the Galactic halo. A new classification scheme based on Sr and Ba." *A&A*, 623:A128, 2019.

T. Hansen, et al. "An Elemental Assay of Very, Extremely, and Ultra-metal-poor Stars." *ApJ*, 807:173, 2015.

T. T. Hansen, et al. "The role of binaries in the enrichment of the early Galactic halo. III. Carbon-enhanced metal-poor stars - CEMP-s stars." *A&A*, 588:A3, 2016.

F. Herwig. "The evolution of AGB stars with convective overshoot." *A&A*, 360:952–968, 2000.

F. Herwig. "Evolution of Asymptotic Giant Branch Stars." *ARA&A*, 43:435–479, 2005.

F. Herwig, et al. "Convective-reactive Proton-^{12}C Combustion in Sakurai's Object (V4334 Sagittarii) and Implications for the Evolution and Yields from the First Generations of Stars." *ApJ*, 727:89, 2011.

F. Herwig, et al. "Global Non-spherical Oscillations in Three-dimensional 4π Simulations of the H-ingestion Flash." *ApJ*, 792:L3, 2014.

J. K. Hollek, et al. "The Chemical Abundances of Stars in the Halo (CASH) Project. III. A New Classification Scheme for Carbon-enhanced Metal-poor Stars with s-process Element Enhancement." *ApJ*, 814:121, 2015.

D. Hollowell, et al. "Hydrogen burning and dredge-up during the major core helium flash in a Z = 0 model star." *ApJ*, 351:245–257, 1990.

Jr. Iben, I., et al. "On the evolution of those nuclei of planetary nebulae that experiencea final helium shell flash." *ApJ*, 264:605–612, 1983.

Carlos A. Iglesias & Forrest J. Rogers. "Updated Opal Opacities." *ApJ*, 464:943, 1996.

C. Iliadis, et al. "Charged-particle thermonuclear reaction rates: II. Tables and graphs of reaction rates and probability density functions." *Nucl. Phys. A*, 841(1-4):31–250, 2010a.

C. Iliadis, et al. "Charged-particle thermonuclear reaction rates: III. Nuclear physics input." *Nucl. Phys. A*, 841(1-4):251–322, 2010b.

C. Iliadis, et al. "Charged-particle thermonuclear reaction rates: IV. Comparison to previous work." *Nucl. Phys. A*, 841(1-4):323–388, 2010c.

C. Iliadis, et al. "Bayesian Estimation of Thermonuclear Reaction Rates." *ApJ*, 831(1):107, 2016.

Christian Iliadis, et al. "Statistical methods for thermonuclear reaction rates and nucleosynthesis simulations." *Journal of Physics G Nuclear Physics*, 42(3):034007, 2015.

G. Imbriani, et al. "S-factor of ^{14}N(p,γ)^{15}O at astrophysical energies*." *European Physical Journal A*, 25(3):455–466, 2005.

I. I. Ivans, et al. "Near-Ultraviolet Observations of CS 29497-030: New Constraints on Neutron-Capture Nucleosynthesis Processes." *ApJ*, 627:L145–L148, 2005.

N. Iwamoto, et al. "Flash-Driven Convective Mixing in Low-Mass, Metal-deficient Asymptotic Giant Branch Stars: A New Paradigm for Lithium Enrichment and a Possible s-Process." *ApJ*, 602:377–388, 2004.

J. A. Johnson & M. Bolte. "The s-Process in Metal-Poor Stars: Abundances for 22 Neutron-Capture Elements in CS 31062-050." *ApJ*, 605:462–471, 2004.

S. Jones, et al. "H ingestion into He-burning convection zones in super-AGB stellar models as a potential site for intermediate neutron-density nucleosynthesis." *MNRAS*, 455:3848–3863, 2016.

K. Jonsell, et al. "The Hamburg/ESO R-process enhanced star survey (HERES). III. HE 0338-3945 and the formation of the r + s stars." *A&A*, 451:651–670, 2006.

A. Jorissen & M. Arnould. "Proton mixing in He-rich layers - The C-13(alpha,n)O-16 neutron source and associated nucleosynthesis." *A&A*, 221(1):161–179, 1989.

A. Jorissen, et al. "Binary properties of CH and carbon-enhanced metal-poor stars." *A&A*, 586:A158, 2016.

D. Kamath, et al. "Evolution and Nucleosynthesis of Asymptotic Giant Branch Stars in Three Magellanic Cloud Clusters." *ApJ*, 746(1):20, 2012.

D. Kamath, et al. "Optically visible post-AGB stars, post-RGB stars and young stellar objects in the Large Magellanic Cloud." *MNRAS*, 454:1468–1502, 2015.

F. Käppeler, et al. "The s process: Nuclear physics, stellar models, and observations." *Reviews of Modern Physics*, 83:157–194, 2011.

A. I. Karakas. "Updated stellar yields from asymptotic giant branch models." *MNRAS*, 403:1413–1425, 2010.

A. I. Karakas. "Helium enrichment and carbon-star production in metal-rich populations." *MNRAS*, 445:347–358, 2014.

A. I. Karakas & J. C. Lattanzio. "The Dawes Review 2: Nucleosynthesis and Stellar Yields of Low- and Intermediate-Mass Single Stars." *PASA*, 31:e030, 2014.

A. I. Karakas, et al. "Nucleosynthesis in Helium-enriched Asymptotic Giant Branch Models: Implications for Heavy Element Enrichment in ω Centauri." *ApJ*, 784:32, 2014.

D. Karinkuzhi, et al. "Low-mass low-metallicity AGB stars as an efficient i-process site explaining CEMP-rs stars." *A&A*, 645:A61, 2021.

C. D. Kilpatrick, et al. "Electromagnetic evidence that SSS17a is the result of a binary neutron star merger." *Science*, 358:1583–1587, 2017.

C. Kobayashi, et al. "Low-Metallicity Inhibition of Type IA Supernovae and Galactic and Cosmic Chemical Evolution." *ApJ*, 503:L155–L159, 1998.

Chiaki Kobayashi, et al. "The Origin of Elements from Carbon to Uranium." *ApJ*, 900(2):179, 2020.

A. J. Koning, et al. "Talys: a nuclear reaction program, nrg-report 21297/04.62741/p." 2004.

A. J. Koning, et al. *Nuclear Data for Science and Technology,*. 211. O. Bersillon et al. (EDP Sciences), 2008.

D. K. Lai, et al. "Abundances of Extremely Metal-poor Star Candidates." *AJ*, 128:2402–2419, 2004.

D. K. Lai, et al. "Carbon and Strontium Abundances of Metal-poor Stars." *ApJ*, 667:1185–1195, 2007.

David L. Lambert & Carlos Allende Prieto. "The isotopic mixture of barium in the metal-poor subgiant HD 140283." *MNRAS*, 335(2):325–334, 2002.

John Lattanzio. "AGB Stars: Remaining Problems." *IAU Symposium*, 343:3–8, 2019.

John C. Lattanzio. "The Asymptotic Giant Branch Evolution of 1.0–3.0 M_{sun} Stars as a Function of Mass and Composition." *ApJ*, 311:708, 1986.

J. M. Lattimer & D. N. Schramm. "Black-hole-neutron-star collisions." *ApJ*, 192:L145–L147, 1974.

H. H. B. Lau, et al. "The evolution of low-metallicity asymptotic giant branch stars and the formation of carbon-enhanced metal-poor stars." *MNRAS*, 396:1046–1057, 2009.

Z. H. Li, et al. "N13(d,n)O14 reaction and the astrophysical N13(p,γ)O14 reaction rate." *Phys. Rev. C*, 74(3):035801, 2006.

Zhihong Li, et al. "Determination of the ^{12}C(p, γ)^{13}N reaction rates from the ^{12}C(^{7}Li,^{6}He)^{13}N reaction." *Science China Physics, Mechanics, and Astronomy*, 53(4):658–663, 2010.

K. Lodders. "Solar System Abundances and Condensation Temperatures of the Elements." *ApJ*, 591:1220–1247, 2003.

R. Longland, et al. "Charged-particle thermonuclear reaction rates: I. Monte Carlo method and statistical distributions." *Nucl. Phys. A*, 841(1-4):1–30, 2010.

S. Lucatello, et al. "The Binary Frequency Among Carbon-enhanced, s-Process-rich, Metal-poor Stars." *ApJ*, 625:825–832, 2005.

M. Lugaro, et al. "s-Process Nucleosynthesis in Asymptotic Giant Branch Stars: A Test for Stellar Evolution." *ApJ*, 586:1305–1319, 2003.

M. Lugaro, et al. "The Mystery of CEMPs+r Stars and the Dual Core-Flash Neutron Superburst." *PASA*, 26:322–326, 2009.

M. Lugaro, et al. "The s-process in Asymptotic Giant Branch Stars of Low Metallicity and the Composition of Carbon-enhanced Metal-poor Stars." *ApJ*, 747:2, 2012.

M. Lugaro, et al. "Post-AGB stars in the Magellanic Clouds and neutron-capture processes in AGB stars." *A&A*, 583:A77, 2015.

Maria Lugaro, et al. "Reaction Rate Uncertainties and the Production of ^{19}F in Asymptotic Giant Branch Stars." *ApJ*, 615(2):934–946, 2004.

P. Magain. "Heavy elements in halo stars: the r/s-process controversy." *A&A*, 297:686, 1995.

P. Magain & G. Zhao. "Barium isotopes in the very metal-poor star HD 140283." *A&A*, 268:L27–L29, 1993.

R. A. Malaney. "Neutron synthesis in AGB and post-AGB stars of low mass." *MNRAS*, 223:683–707, 1986.

P. Marigo & B. Aringer. "Low-temperature gas opacity. ÆSOPUS: a versatile and quick computational tool." *A&A*, 508:1539–1569, 2009.

L. Mashonkina & G. Zhao. "Barium even-to-odd isotope abundance ratios in thick disk and thin disk stars." *A&A*, 456(1):313–321, 2006.

L. Mashonkina, et al. "Barium abundances in cool dwarf stars as a constraint to s- and r-process nucleosynthesis." *A&A*, 343:519–530, 1999.

T. Masseron, et al. "A holistic approach to carbon-enhanced metal-poor stars." *A&A*, 509:A93, 2010.

T. Masseron, et al. "Lithium Abundances in Carbon-enhanced Metal-poor Stars." *ApJ*, 751:14, 2012.

E. Matrozis, et al. "High-Resolution Spectroscopy of Cool Carbon-Rich and Metal-Poor Star HD 209621." *Baltic Astronomy*, 21:399–420, 2012.

John E. McKay, et al. "The impact of (n,γ) reaction rate uncertainties on the predicted abundances of i-process elements with $32 \leq Z \leq 48$ in the metal-poor star HD94028." *MNRAS*, 491(4):5179–5187, 2020.

A. McWilliam, et al. "Spectroscopic Analysis of 33 of the Most Metal Poor Stars. II." *AJ*, 109:2757, 1995.

X. Y. Meng, et al. "The odd-isotope fractions of barium in CEMP-r/s star HE 0338-3945 and r-II star CS 31082-001." *A&A*, 593:A62, 2016.

B. Meyer. "WEBNUCLEO.org." In *Nuclei in the Cosmos (NIC XII)*, page 96. 2012.

B. S. Meyer. "Decompression of initially cold neutron star matter - A mechanism for the r-process?" *ApJ*, 343:254–276, 1989.

B. S. Meyer. "The r-, s-, and p-Processes in Nucleosynthesis." *ARA&A*, 32:153–190, 1994.

M. M. Miller Bertolami, et al. "New evolutionary calculations for the born again scenario." *A&A*, 449(1):313–326, 2006.

M. Mocák, et al. "The core helium flash revisited. III. From Population I to Population III stars." *A&A*, 520:A114, 2010.

N. Nishimura, et al. "The r-process Nucleosynthesis in the Various Jet-like Explosions of Magnetorotational Core-collapse Supernovae." *ApJ*, 810:109, 2015.

N. Nishimura, et al. "The Intermediate r-process in Core-collapse Supernovae Driven by the Magneto-rotational Instability." *ApJ*, 836:L21, 2017.

K. Nomoto, et al. "Thermal Stability of White Dwarfs Accreting Hydrogen-rich Matter and Progenitors of Type Ia Supernovae." *ApJ*, 663:1269–1276, 2007.

J. E. Norris, et al. "Extremely Metal-poor Stars. IV. The Carbon-rich Objects." *ApJ*, 488:350–363, 1997.

M. Ono, et al. "Explosive Nucleosynthesis in Magnetohydrodynamical Jets from Collapsars. II — Heavy-Element Nucleosynthesis of s, p, r-Processes." *Progress of Theoretical Physics*, 128:741–765, 2012.

Bill Paxton, et al. "Modules for Experiments in Stellar Astrophysics (MESA)." *ApJS*, 192(1):3, 2011.

Bill Paxton, et al. "Modules for Experiments in Stellar Astrophysics (MESA): Planets, Oscillations, Rotation, and Massive Stars." *ApJS*, 208(1):4, 2013.

Bill Paxton, et al. "Modules for Experiments in Stellar Astrophysics (MESA): Binaries, Pulsations, and Explosions." *ApJS*, 220(1):15, 2015.

Bill Paxton, et al. "Modules for Experiments in Stellar Astrophysics (MESA): Convective Boundaries, Element Diffusion, and Massive Star Explosions." *ApJS*, 234(2):34, 2018.

Bill Paxton, et al. "Modules for Experiments in Stellar Astrophysics (MESA): Pulsating Variable Stars, Rotation, Convective Boundaries, and Energy Conservation." *ApJS*, 243(1):10, 2019.

Cecilia Helena Payne. *Stellar Atmospheres; a Contribution to the Observational Study of High Temperature in the Reversing Layers of Stars.* Ph.D. thesis, RADCLIFFE COLLEGE., 1925.

Ilenia Picardi, et al. "Evolution and Nucleosynthesis of Primordial Low-Mass Stars." *ApJ*, 609(2):1035–1044, 2004.

M. Pignatari, et al. "The Weak s-Process in Massive Stars and its Dependence on the Neutron Capture Cross Sections." *ApJ*, 710:1557–1577, 2010.

M. Pignatari, et al. "NuGrid Stellar Data Set. I.Stellar Yields from H to Bi for Stars with Metallicities Z = 0.02 and Z = 0.01." *ApJS*, 225(2):24, 2016.

V. M. Placco, et al. "Metal-poor Stars Observed with the Magellan Telescope. I. Constraints on Progenitor Mass and Metallicity of AGB Stars Undergoing s-process Nucleosynthesis." *ApJ*, 770:104, 2013.

N. Prantzos, et al. "Chemical evolution with rotating massive star yields - I. The solar neighbourhood and the s-process elements." *MNRAS*, 476(3):3432–3459, 2018.

Y.-Z. Qian & G. J. Wasserburg. "Stellar Sources for Heavy r-Process Nuclei." *ApJ*, 588:1099–1109, 2003.

C. M. Raiteri, et al. "S-process nucleosynthesis in massive stars and the weak component. II - Carbon burning and galactic enrichment." *ApJ*, 371:665–672, 1991.

D. A. Rastegaev. "Multiplicity and Period Distribution of Population II Field Stars in Solar Vicinity." *AJ*, 140:2013–2024, 2010.

D. Reimers. "Circumstellar absorption lines and mass loss from red giants." *Memoires of the Societe Royale des Sciences de Liege*, 8:369–382, 1975.

I. U. Roederer, et al. "A Search for Stars of Very Low Metal Abundance. VI. Detailed Abundances of 313 Metal-poor Stars." *AJ*, 147:136, 2014.

I. U. Roederer, et al. "The Diverse Origins of Neutron-capture Elements in the Metal-poor Star HD 94028: Possible Detection of Products of I-Process Nucleosynthesis." *ApJ*, 821:37, 2016.

A. L. Sallaska, et al. "STARLIB: A Next-generation Reaction-rate Library for Nuclear Astrophysics." *ApJS*, 207(1):18, 2013.

H. Schlattl, et al. "On the Helium Flash in Low-Mass Population III Red Giant Stars." *ApJ*, 559(2):1082–1093, 2001.

T. Sivarani, et al. "First stars IV. CS 29497-030: Evidence for operation of the s-process at very low metallicity." *A&A*, 413:1073–1085, 2004.

C. Sneden, et al. "Binary Blue Metal-poor Stars: Evidence for Asymptotic Giant Branch Mass Transfer." *ApJ*, 592:504–515, 2003.

C. Sneden, et al. "Neutron-Capture Elements in the Early Galaxy." *ARA&A*, 46:241–288, 2008.

R. J. Stancliffe, et al. "Three-dimensional Hydrodynamical Simulations of a Proton Ingestion Episode in a Low-metallicity Asymptotic Giant Branch Star." *ApJ*, 742:121, 2011.

E. Starkenburg, et al. "Binarity in carbon-enhanced metal-poor stars." *MNRAS*, 441:1217–1229, 2014.

David Stephens, et al. "3D1D hydro-nucleosynthesis simulations. I. Advective-reactive post-processing method and its application to H ingestion into He-shell flash convection in rapidly accreting white dwarfs." *arXiv e-prints*, arXiv:2001.10969, 2020.

O. Straniero, et al. "Radiative 13C Burning in Asymptotic Giant Branch Stars and s-Processing." *ApJ*, 440:L85, 1995.

T. Suda & M. Y. Fujimoto. "Evolution of low- and intermediate-mass stars with [Fe/H] <= - 2.5." *MNRAS*, 405(1):177–193, 2010.

T. Suda, et al. "Stellar Abundances for the Galactic Archeology (SAGA) Database — Compilation of the Characteristics of Known Extremely Metal-Poor Stars." *PASJ*, 60:1159–1171, 2008.

Takuma Suda, et al. "Stellar Abundances for Galactic Archaeology Database. IV. Compilation of stars in dwarf galaxies." *PASJ*, 69(5):76, 2017.

L.-S. The, et al. "s-Process Nucleosynthesis in Advanced Burning Phases of Massive Stars." *ApJ*, 655:1058–1078, 2007.

F. Thielemann, K., et al. "Neutron Star Mergers and Nucleosynthesis of Heavy Elements." *Annual Review of Nuclear and Particle Science*, 67:annurev-nucl-101916-123246, 2017.

O. Trippella, et al. "s-Processing in AGB Stars Revisited. II. Enhanced 13C Production through MHD-induced Mixing." *ApJ*, 818:125, 2016.

E. van Aarle, et al. "Detailed abundance study of four s-process enriched post-AGB stars in the Large Magellanic Cloud." *A&A*, 554:A106, 2013.

S. van Eck, et al. "Discovery of additional lead-rich stars." *Nuclear Physics A*, 718:521–523, 2003.

H. van Winckel. "Post-AGB Stars." *ARA&A*, 41:391–427, 2003.

E. Vassiliadis & P. R. Wood. "Evolution of low- and intermediate-mass stars to the end of the asymptotic giant branch with mass loss." *ApJ*, 413:641–657, 1993.

George Wallerstein, et al. "Synthesis of the elements in stars: forty years of progress." *Reviews of Modern Physics*, 69(4):995–1084, 1997.

A. Wallner, et al. "Accelerator mass spectrometry measurements of the ^{13}C (n ,γ)^{14}C and ^{14}N(n ,p)^{14}C cross sections." *Phys. Rev. C*, 93(4):045803, 2016.

S. Wanajo, et al. "Enrichment of Very Metal Poor Stars with Both r-Process and s-Process Elements from 8-10 M_{solar} Stars." *ApJ*, 636:842–847, 2006.

Darach Watson, et al. "Identification of strontium in the merger of two neutron stars." *Nature*, 574(7779):497–500, 2019.

A. Weiss, et al. "Models for extremely metal-poor halo stars." *A&A*, 422:217–223, 2004.

C. Winteler, et al. "Magnetorotationally Driven Supernovae as the Origin of Early Galaxy r-process Elements?" *ApJ*, 750:L22, 2012.

Paul R. Woodward, et al. "Hydrodynamic Simulations of H Entrainment at the Top of He-shell Flash Convection." *ApJ*, 798(1):49, 2015.

A. A. Zijlstra. "Low-mass supernovae in the early Galactic halo: source of the double r/s-process enriched halo stars?" *MNRAS*, 348:L23–L27, 2004.